

N7615595



NASA CR-134886

ER75-4368



# MICROWAVE POWER TRANSMISSION SYSTEM STUDIES

VOLUME II INTRODUCTION, ORGANIZATION,  
ENVIRONMENTAL AND SPACEBORNE  
SYSTEMS ANALYSES

RAYTHEON COMPANY  
EQUIPMENT DIVISION  
ADVANCED DEVELOPMENT LABORATORY  
SUDBURY, MASS. 01776

prepared for  
NATIONAL AERONAUTICS AND SPACE ADMINISTRATION

NASA Lewis Research Center  
Contract NAS 3-17835

1. Report No. NASA CR-134886	2. Government Accession No.	3. Recipient's Catalog No.
4. Title and Subtitle MICROWAVE POWER TRANSMISSION SYSTEM STUDIES Volume II - Introduction, Organization, Environmental and Spaceborne Systems Analysis (Sections 1 through 7)		5. Report Date December 1975
7. Author(s) O. E. Maynard, W. C. Brown, A. Edwards, J. T. Haley, G. Meltz, J. M. Howell - Raytheon Co.; A. Nathan - Grumman Aerospace Corp.		6. Performing Organization Code
9. Performing Organization Name and Address Raytheon Company Equipment Division 528 Boston Post Road Sudbury, Massachusetts 01776		8. Performing Organization Report No. ER75-4368
12. Sponsoring Agency Name and Address National Aeronautics and Space Administration Washington, D. C. 20546		10. Work Unit No.
15. Supplementary Notes Mr. Richard M. Schuh NASA Lewis Research Center Cleveland, Ohio 44135		11. Contract or Grant No. NAS 3-17835
16. Abstract -- A study of microwave power generation, transmission, reception and control was conducted as a part of the NASA Office of Applications' joint Lewis Research Center/Jet Propulsion Laboratory five-year program to demonstrate feasibility of power transmission from geosynchronous orbit. This volume (2 of 4) is comprised of Sections 1 through 7 which present introduction, organization, analyses, conclusions and recommendations for each of the spaceborne subsystems. Section 1 presents the introduction, task definitions, conclusions and recommendations, with discussion of the associated subsystems technologies. It is concluded with a discussion of the report approach and organization. Section 2 presents the organization and approach to the study. Section 3 presents the environmental effects - propagation analyses with appendices covering radio wave diffraction by random ionospheric irregularities, self-focusing plasma instabilities and ohmic heating of the D-region. Section 4 presents the analyses of dc to rf conversion subsystems and system considerations for both the amplatron and the klystron with appendices for the klystron covering cavity circuit calculations, output power of the solenoid-focused klystron, thermal control system, and confined flow focusing of a relativistic beam. Section 5 presents the photovoltaic power source characteristics as they apply to interfacing with the power distribution flow paths, magnetic field interaction, dc to rf converter protection, power distribution including estimates for the power budget, weights and costs. Section 6 presents analyses for the transmitting antenna considering aperture illumination and size, with associated efficiencies and ground power distributions. Analyses of subarray types and dimensions, attitude error, flatness, phase error, subarray layout, frequency tolerance, attenuation, waveguide dimensional tolerances, mechanical including thermal considerations are included. Implications associated with transportation, assembly and packaging, attitude control and alignment are discussed. Section 7 presents analyses for the phase front control subsystem, including both ground based pilot signal driven adaptive and ground command approaches with their associated phase errors.		13. Type of Report and Period Covered Contractor Report
17. Key Words (Suggested by Author(s)) Microwave power transmission; power from space; satellite power transmission; phased array power transmission; rectifying antenna (rectenna).		14. Sponsoring Agency Code
19. Security Classif. (of this report) Unclassified		18. Distribution Statement Unclassified - Unlimited
20. Security Classif. (of this page) Unclassified		

PRICES SUBJECT TO CHANGE

\* For sale by the National Technical Information Service, Springfield, Virginia 22161

## TABLE OF CONTENTS

### VOLUME I - EXECUTIVE SUMMARY

<u>Section</u>	<u>Page</u>
1. Introduction	2
2. DC to RF Conversion	4
3. Transmitting Antenna and Phase Front Control	9
4. Mechanical Systems	16
5. Flight Operations	22
6. Receiving Antenna	25
7. Systems Analysis and Evaluation	28
8. Critical Technology	34
9. Critical Technology and Test Program	37
10. Recommendations for Additional Studies	42

### VOLUME II - Sections 1 through 7 with Appendices A through G

	<u>Page</u>
1. INTRODUCTION, CONCLUSIONS AND RECOMMENDATIONS	
1.1 Introduction	1-1
1.2 Conclusions and Recommendations	1-3
1.2.1 General	1-3
1.2.2 Subsystems and Technology	1-5
1.2.2.1 Environmental Effects - Propagation	1-5
1.2.2.2 DC-RF Conversion	1-5
1.2.2.3 Power Interface and Distribution (Orbital)	1-7
1.2.2.4 Transmitting Antenna	1-7
1.2.2.5 Phase Front Control	1-8
1.2.2.6 Mechanical Systems and Flight Operations	1-9
1.2.2.7 Receiving Antenna	1-10
1.2.2.8 Radio Frequency Interference and Allocation	1-11
1.2.2.9 Risk Assessment	1-12
1.2.3 System Analysis and Evaluation	1-15

## TABLE OF CONTENTS -- Continued

	<u>Page</u>
1.2.4 Technology Development and Test Programs	1-16
1.2.4.1 Technology Development and Ground Test Program	1-16
1.2.4.2 Technology Development and Orbital Test Program	1-16
1.2.5 Additional Studies	1-17
1.3 Report Approach and Organization	1-17
<b>2. ORGANIZATION AND APPROACH</b>	
2.1 Organization	2-1
2.2 Approach	2-3
<b>3. ENVIRONMENTAL EFFECTS - PROPAGATION</b>	
3.1 Introduction	3-1
3.2 Atmospheric Attenuation and Scattering	3-2
3.2.1 Molecular Absorption	3-2
3.2.2 Scattering and Absorption by Hydrometeors	3-4
3.3 Ionosphere Propagation	3-12
3.3.1 Ambient Refraction	3-12
3.3.2 Scintillations Due to Ambient Fluctuations and Self-Focusing Instabilities	3-13
3.4 Ionospheric Modification By High Power Irradiation	3-19
3.5 Faraday Rotation Effects	3-21
3.5.1 Introduction	3-21
3.5.2 Diurnal and Seasonal Changes	3-21
3.5.3 Midlatitude Geomagnetic Storms	3-22
3.6 Conclusions and Recommendations	3-24
<b>4. DC-RF CONVERSION</b>	
4.1 Amplitron	4-1
4.1.1 RF Circuit	4-2
4.1.2 Pyrolytic Graphite Radiator	4-4
4.1.3 Magnetic Circuit	4-4
4.1.4 Controlling the Output of Amplitrons	4-5
4.1.5 Weight	4-5



TABLE OF CONTENTS -- Continued

	<u>Page</u>
4.1.6 Cost	4-7
4.1.7 Noise and Harmonics	4-7
4.1.8 Parameters Versus Frequency	4-9
4.1.9 Parameters Versus Power Level	4-15
4.2 Klystron	4-16
4.2.1 Periodic Permanent Magnetic Focusing	4-17
4.2.2 Circuit Efficiency	4-20
4.2.3 Klystron Efficiency With Solenoidal Focusing	4-25
4.2.4 Heat Dissipation and Beam Collection	4-27
4.2.5 Variations of Supply Voltages	4-34
4.2.6 Noise, Gain and Harmonic Characteristics	4-37
4.2.7 Tube Designs	4-40
4.2.8 Tube Lifetime	4-43
4.2.9 Weight and Cost	4-43
4.2.10 Conclusions	4-46
4.3 System Considerations	4-48
4.3.1 Amplitron Gain and Efficiency	4-48
4.3.2 Cascaded Vs Parallel Configurations	4-50
4.3.3 Cascaded Amplitron Gain	4-56
4.3.4 Amplifier Noise	4-56
4.3.5 Klystron Power Level	4-61
4.3.6 Converter Filter Requirements	4-64
4.4 Conclusions and Recommendations	4-69
5. POWER SOURCE INTERFACE AND DISTRIBUTION	
5.1 Power Source Characteristics	5-1
5.2 Power Source-Converter Interface	5-3
5.3 Power Distribution Flow Paths	5-6
5.4 Magnetic Interaction	5-12
5.5 DC to RF Converter Protection	5-15
5.6 Power Distribution System	5-19
5.7 Power Distribution Cost and Weight	5-23
5.8 Power Budget	5-24
5.9 Conclusions and Recommendations	5-24

TABLE OF CONTENTS -- Continued

	<u>Page</u>
6. TRANSMITTING ANTENNA	
6.1 Aperture Illumination and Size	6-1
6.2 Array Types	6-10
6.3 Subarray Types	6-16
6.4 Subarray Dimensions	6-16
6.5 Subarray Layout	6-20
6.6 Tolerance and Attenuation	6-26
6.6.1 Frequency Tolerance	6-26
6.6.2 Waveguide Dimensional Tolerances	6-27
6.6.3 Waveguide Attenuation	6-28
6.7 Mechanical Design and Analysis	6-29
6.7.1 Thermal Analysis and Configuration	6-29
6.7.2 Materials	6-38
6.7.3 Transportation, Assembly and Packaging	6-43
6.8 Attitude Control and Alignment	6-47
6.9 Conclusions and Recommendations	6-49
7. PHASE FRONT CONTROL	
7.1 Adaptive Phase Front Control	7-4
7.2 Command Phase Front Control	7-10
7.2.1 Phase Estimation	7-10
7.2.2 Bit Wiggle	7-14
7.3 Conclusions and Recommendations	7-14
APPENDIX A - RADIO WAVE DIFFRACTION BY RANDOM IONOSPHERIC IRREGULARITIES	
A.1 Introduction	A-1
A.2 Model for Electron Density Irregularities	A-2
A.3 Phase Fluctuations and Their Spatial Correlation at the Diffracting Screen	A-3
A.4 Phase and Amplitude Fluctuations and Their Spatial and Temporal Correlation Functions on an Observational Plane	A-4

TABLE OF CONTENTS -- Continued

	<u>Page</u>
APPENDIX B - SELF-FOCUSING PLASMA INSTABILITIES	B-1
APPENDIX C - OHMIC HEATING OF THE D-REGION	C-1
APPENDIX D - CAVITY CIRCUIT CALCULATIONS	
D. 1 Input Impedance	D-1
D. 2 Input Power and Gain at Saturation	D-2
D. 3 Intermediate- and Output-Gap Voltages	D-3
D. 4 Cavity Tunings	D-3
D. 5 Output Cavity and Circuit Efficiency	D-4
APPENDIX E - OUTPUT POWER OF THE SOLENOID-FOCUSED KLYSTRON	E-1
APPENDIX F - KLYSTRON THERMAL CONTROL SYSTEM	
F. 1 Heat Conduction	F-1
F. 2 Temperature, Area and Weight of Radiators	F-2
F. 2.1 Collector	F-3
F. 2.2 Collector Reflector and Heat Shield	F-4
F. 2.3 Body Radiator	F-4
F. 2.4 Body Reflector and Heat Shield	F-5
F. 3 Weight of Heat Pipes	F-5
APPENDIX G - CONFINED-FLOW FOCUSING OF A RELATIVISTIC BEAM	G-1
 <u>VOLUME III - MECHANICAL SYSTEMS AND FLIGHT OPERATIONS</u> (Section 8)	
	<u>Page</u>
1. INTRODUCTION	1-1
2. SUMMARY	
2.1 Task 1 - Preliminary Design	2-1
2.1.1 Control Analysis	2-1
2.1.2 Thermal/Structural Analysis	2-1
2.1.3 Design Options and Groundrules for Task 2 Concept Definition	2-5

## TABLE OF CONTENTS -- Continued

	<u>Page</u>
2.2 Task 2 - Concept Definition	2-9
2.2.1 Mission Analysis	2-9
2.2.2 Antenna Structural Definition	2-9
2.2.3 Configuration Analysis	2-14
2.2.4 Assembly	2-21
2.2.5 Cost	2-31
2.3 Recommendations	2-33
3. TECHNICAL DISCUSSION	
3.1 Mission Analysis	3.1-1
3.1.1 SSPS Configuration and Flight Mode Descriptions	3.1-1
3.1.2 Transportation System Performance	3.1-1
3.1.3 Altitude Selection	3.1-8
3.1.4 SEPS (Ion Engine) Sizing	3.1-14
3.2 Antenna Structural Concept	3.2-1
3.2.1 General Arrangement	3.2-1
3.2.2 Rotary Joint	3.2-1
3.2.3 Primary/Secondary Antenna Structure	3.2-15
3.2.4 Structure/Waveguide Interface	3.2-15
3.2.5 Antenna Weight and Mass Properties	3.2-18
3.3 Configuration Analysis	3.3-1
3.3.1 Control Analysis	3.3-1
3.3.2 Thermal Evaluation	3.3-9
3.3.3 Structural Analysis	3.3-41
3.4 Assembly and Packaging	3.4-1
3.4.1 Detail Parts	3.4-1
3.4.2 Structural Assembly	3.4-9
3.5 Cost	3.5.1
3.5.1 Task 1 - Preliminary Design Results	3.5-1
3.5.2 Task 2 - Concept Definition Results	3.5-5
3.5.3 MPTS Structural Costs	3.5-19

TABLE OF CONTENTS -- Continued

	<u>Page</u>
4. TECHNOLOGY ISSUES	
4.1 Control System	4-1
4.1.1 Evaluation of Alternate Power Transfer and Drive Devices	4-1
4.1.2 Detailed Control System Analysis	4-2
4.2 Structural System	4-3
4.2.1 Composite Structures and Assembly Techniques	4-3
4.2.2 Tension Brace Antenna Feasibility Assessment	4-4
4.2.3 Local Crippling Stress Evaluation	4-4
4.2.4 Design Environments	4-5
4.2.5 Optimum Antenna Structures	4-5
4.2.6 Finite Element Model Development	4-6
4.2.7 Composite Waveguide	4-6
4.3 Thermal System	4-7
4.3.1 Maximum Temperature	4-7
4.3.2 Transient Analysis	4-8
4.4 Assembly	4-9
4.4.1 Assembly Cost	4-9
4.4.2 Man's Role in Assembly and Maintenance	4-10
5. REFERENCES	5-1

VOLUME IV - Sections 9 through 14 with Appendices H through K

	<u>Page</u>
9. RECEIVING ANTENNA	
9.1 Microwave Rectifier Technology	9-1
9.2 Antenna Approaches	9-9
9.3 Topology of Rectenna Circuits	9-14
9.4 Assembly and Construction	9-21
9.5 ROM Cost Estimates	9-21
9.6 Power Interface Estimates	9-25
9.6.1 Inverter System	9-30
9.6.2 Power Distribution Costs	9-30
9.6.3 System Cost	9-31
9.7 Conclusions and Recommendations	9-31

TABLE OF CONTENTS -- Continued

	<u>Page</u>
10. FREQUENCY INTERFERENCE AND ALLOCATION	10-1
10.1 Noise Considerations	10-3
10.1.1 Amplitron	10-3
10.1.2 Klystron	10-4
10.1.3 Interference Limits and Evaluation	10-6
10.2 Harmonic Considerations	10-6
10.3 Conclusions and Recommendations	10-12
11. RISK ASSESSMENT	
11.1 Technology Risk Rating and Ranking	11-1
11.2 Technology Assessment Conclusions and Recommendations	11-16
12. SYSTEM ANALYSIS AND EVALUATION	12-1
12.1 System Geometry	12-1
12.2 Parametric Studies	12-3
12.2.1 System Relationships	12-3
12.2.2 Efficiency, Weight and Cost	12-8
12.2.3 Converter Packing	12-12
12.2.4 Capital Cost Vs Power and Frequency Results	12-13
12.2.5 Ground Power Density and Power Level Selection	12-19
12.2.6 Frequency Selection	12-22
12.2.7 Characteristics of 5 GW and 10 GW Systems	12-22
12.2.8 Energy Cost	12-36
12.3 Final System Estimates	12-41
12.3.1 Cost and Weight	12-41
12.3.2 Efficiency Budget	12-43
12.3.3 Capital Cost and Sizing Analyses	12-45
12.4 Conclusions and Recommendations	12-45
13. CRITICAL TECHNOLOGY AND GROUND TEST PROGRAM	
13.1 General Objectives	13-1
13.2 Detailed Ground Test Objectives	13-2
13.3 Implementation - Ground Test	13-3
13.3.1 Summary	13-3

TABLE OF CONTENTS -- Continued

	<u>Page</u>
13.3.2 Phase I	13-5
13.3.3 Phase II	13-5
13.3.4 Phase III	13-9
13.3.5 Alternate Phase I Converter Implementation	13-11
13.4 Critical Technology Development	13-14
13.4.1 Amplitron	13-14
13.4.2 Klystron	13-14
13.4.3 Phase Control	13-14
13.5 Schedule and Cost	13-15
13.6 Conclusions and Recommendations	13-17
<b>14. CRITICAL TECHNOLOGY AND ORBITAL TEST PROGRAM</b>	
14.1 Orbital Test Objectives	14-1
14.2 Implementation	14-3
14.2.1 Geosatellite (Mission 1)	14-4
14.2.2 Shuttle Sorties (Missions 2 through 11)	14-4
14.2.3 Orbital Test Facility	14-23
14.3 Cost and Schedule	14-25
14.4 Conclusions and Recommendations	14-30
<b>APPENDIX H - ESTIMATED ANNUAL OPERATIONS AND MAINTENANCE COST (5 GW System)</b>	<b>H-1</b>
<b>APPENDIX I - ANNUAL OPERATIONS AND MAINTENANCE COST (10 GW System)</b>	<b>I-1</b>
<b>APPENDIX J - SYSTEM ANALYSIS EXAMPLES</b>	
J.1 Introductory Analysis of Initial Operational System With Minimum Size Transmitting Antenna	J-1
J.2 Analysis of the Final Operational System and Their Goals	J-10
J.3 Analysis of the Initial Operational System Based On the Final System Configuration	J-21
J.4 Weight and Cost Analysis for the Initial and Final Operational Systems	J-25
J.5 Energy Cost	J-27

TABLE OF CONTENTS -- Continued

	<u>Page</u>
APPENDIX K - DETAILS OF GROUND AND ORBITAL TEST PROGRAM	
K. 1    Introduction	K-1
K. 2    Objectives Implementation Equipment and Characteristics	K-1
K. 3    Implementation of Objectives H1, H2, D1 and D2 Using Low Earth Orbit Sortie Missions	K-3
K. 4    Defining an MPTS Orbital Test Facility Program	K-13
K. 4. 1    Assumptions	K-13
K. 4. 2    Sizing the Phased Array Antennas	K-14



## LIST OF ILLUSTRATIONS

<u>Figure</u>		<u>Page</u>
2-1	Microwave Power Transmission Systems Study Program Organization	2-2
2-2	Work Breakdown Structure	2-4
2-3	MPTS Schedule	2-5
3-1	Atmospheric Absorption by the 1.35-cm Line of Water Vapor for a Mean Absolute Humidity of $7.75 \text{ g/m}^3$ and by the 0.5 cm Line of Oxygen at a Temperature of $20^\circ\text{C}$ and a Pressure of One Atmosphere	3-3
3-2	Zenith Attenuation Versus Frequency	3-4
3-3	Comparison of Gaseous Absorption and Rain Attenuation	3-5
3-4	Transmission Efficiency - Molecular Absorption and Rain	3-8
3-5	Rainfall Rate in a Thunderstorm, North-South Section	3-9
3-6	Rainfall Rate in a Thunderstorm, East-West Section	3-10
3-7	Transmission Through Very Heavy Rain (Elevation 40 Degree Angle)	3-10
3-8	Phase Scintillations	3-14
3-9	Typical Gaussian Model Results of Density Correlation	3-15
3-10	Path of a Straight Line Ray from a Geostationary Satellite to a Midlatitude Receiving Site	3-22
3-11	Diurnal and Seasonal Variation in Faraday Rotation $\Omega$ and Polarization Mismatch "Loss" $\eta_p$	3-23
3-12	Variation in Total Electron Content During a Magnetic Storm	3-25
4-1	Amplitron Assembly	4-3
4-2	5 kW Amplitron Parameters	4-3
4-3	Amplitron Current and Voltage Levels for Various Magnetic Field Levels	4-6
4-4	Power Level Versus Frequency	4-10
4-5	Amplitron Weight/Cost/Efficiency Versus Frequency	4-10
4-6	Anode Radiator Diameter Versus Frequency	4-11
4-7	Anode Radiator Weight Versus Frequency	4-12
4-8	Tube Dimensions Versus Frequency	4-12
4-9	Magnetic Field Intensity Versus Frequency	4-13
4-10	Dissipated Power Density Versus Frequency	4-13

LIST OF ILLUSTRATIONS -- Continued

<u>Figure</u>		<u>Page</u>
4-11	Temperature Drop Across Vanes Versus Frequency	4-14
4-12	DC Current Versus Frequency	4-14
4-13	Amplitron Weight and Cost Versus Power	4-15
4-17	Klystron Bunching with PPM Focusing	4-18
4-18	Radial Beam Spreading with PPM Focusing	4-18
4-19	Klystron Output Gap with PPM Focusing	4-19
4-20	Klystron Bunching with PPM Focusing, Shorter Magnet Period and Increased Voltage at Gap 1	4-21
4-21	Graphical Analysis of the Collector Depression	4-22
4-22	Klystron Power Summary	4-23
4-23	Effect of Temperature on Output-Circuit Efficiency	4-24
4-24	Effect of Temperature on $Q_u$ in the Klystron Output Cavity	4-24
4-25	Efficiency Vs Output Power for Solenoid-Focused Klystron	4-26
4-26	Body Heat Versus Saturated Output Power	4-29
4-27	Output Cavity of 43 kW Klystron (Longitudinal Cross Section)	4-31
4-28a	Outline of the PPM Klystron	4-32
4-28b	Outline of the 48 kW Solenoid Klystron	4-33
4-29	Klystron Voltage Control	4-36
4-30	Gain and Noise in PPM-Focused Klystron	4-39
4-31	Computed Noise Characteristic of the PPM Klystron	4-40
4-32	Summary of Design Parameters	4-41
4-33	Weight and Cost Analysis of the PPM Klystron with 5.57 kW Output	4-44
4-34	Weight and Cost Analysis of an EM Klystron with 16 kW Output	4-45
4-35	Weight and Cost Analysis of an EM Klystron with 48 kW Output	4-46
4-36	Comparison of Tube Types	4-47
4-37	Amplitron Gain and Efficiency	4-49
4-38	Cascaded Amplifier Configuration Phase Characteristics	4-52
4-39	Parallel Feed Amplifier Considerations Phase Characteristics	4-53
4-40	Cascaded Amplifier Chain	4-54
4-41	Parallel Amplifier Chain	4-55
4-42	Amplitrons in Cascade	4-57
4-43	Amplifier Noise	4-58

LIST OF ILLUSTRATIONS -- Continued

<u>Figure</u>		<u>Page</u>
4-44	Noise Output of Preamplifier Stages	4-59
4-45	Amplifier - Noise Power Output	4-60
4-46	Klystron Parameters for 60 kW Beam	4-62
4-47	Waveguide Losses Vs RF Power Per Tube	4-63
4-48	Power Divider	4-64
4-49	Klystron Parameters (Electronic Efficiency = 84%)	4-65
4-50	Total Efficiency with Waveguide Losses	4-66
4-51	Klystron System Efficiency Including Waveguide Losses	4-67
4-52	Klystron Equivalent Filter Characteristic	4-68
4-53	Amplitron Equivalent Filter Characteristics ( $f_o = 2450$ MHz)	4-70
5-1	Typical Solar Cell Characteristics Based on 1985 Cell With No Concentrators	5-2
5-2	Source Voltage Characteristics Solar Cell	5-4
5-3	Total Source Characteristics	5-4
5-4	Klystron-Solar Cell Interface	5-5
5-5	Klystron Operation Available Power Usage	5-6
5-6	Amplitron-Solar Cell Interface	5-7
5-7	Quadrant of Microwave Platform Divided Into Areas of Equal Power	5-8
5-8	Circular Power Flow	5-9
5-9	Power Distribution Lateral Power Flow	5-10
5-10	Distribution System Weight Estimate (15 GW Input Power)	5-12
5-11	Microwave Array - Magnetic Torque - Lateral Power Flow	5-13
5-12	Microwave Array - Magnetic Torque - Radial Power Flow	5-14
5-13	Amplitron Failure Modes and Probable Results	5-16
5-14	Klystron Failures and Probable Results	5-17
5-15	Concept for Converter/Crowbar Interface	5-18
5-16	Crowbar and Switchgear Distribution	5-21
5-17	Power Distribution System Short Circuit Currents	5-22
5-18	Simplified Diagram - HVDC Interrupter	5-24
5-19	Power Distribution Cost Summary (9 GW Power Source)	5-26
5-20	Power Distribution Weight Summary (9 GW Power Source)	5-26
5-21	Typical Microwave Array, Power Usage	5-27

## LIST OF ILLUSTRATIONS -- Continued

<u>Figure</u>		<u>Page</u>
6-1	Fraction of Total Power in Sectors of Prescribed Radii	6-2
6-2	Sidelobe Level and Beamwidths	6-3
6-3	Pattern Efficiency for Uniform Illumination (0 dB Taper)	6-5
6-4	Pattern Efficiency for Uniform Illumination (5 dB Taper)	6-5
6-5	Pattern Efficiency for Uniform Illumination (10 dB Taper)	6-6
6-6	Pattern Efficiency for Uniform Illumination (15 dB Taper)	6-6
6-7	Taper Effect on Pattern and Efficiency	6-7
6-8	First Sidelobe Level Vs Truncated Gaussian Taper	6-8
6-9	Antenna Sizes for Truncated Gaussian Tapers	6-9
6-10	Array-Subarray Organization	6-10
6-11	Beam Efficiency - Truncated Gaussian Distribution (5 dB Edge Taper)	6-11
6-12	Beam Efficiency - Truncated Gaussian Distribution (10 dB Edge Taper)	6-11
6-13	Relative Sidelobes - Truncated Gaussian Distribution (5 dB Edge Taper)	6-12
6-14	Relative Sidelobes - Truncated Gaussian Distribution (10 dB Edge Taper)	6-12
6-15	Outage of a Single DC Filter	6-13
6-16	MPTS Concept	6-13
6-17	Alternative Array Types	6-14
6-18	Space Fed Array	6-15
6-19	Feed Illumination (Array Focused at Feed)	6-15
6-20	Subarray Types	6-17
6-21	Subarray Types	6-17
6-22	Subarray Size Considerations	6-18
6-23	SPS Incremental Cost Vs Subarray Size	6-20
6-24	Three Subarray Layout Approaches	6-21
6-25	Subarray Right End Termination Approaches	6-23
6-26	Two Slotted Waveguide Designs	6-25
6-27	Amplitron Thermal Model	6-30
6-28	Amplitron Thermal Analysis	6-31
6-29	6 kW Klystron Configuration	6-33

LIST OF ILLUSTRATIONS -- Continued

<u>Figure</u>		<u>Page</u>
6-30	Klystron Configuration Temperature Distribution	6-34
6-31	Subarray Deflection Vs Size	6-36
6-32	Subarray Deflection Vs Size	6-36
6-33	Subarray Configuration (Using 6061-T6 Al. Waveguide)	6-37
6-34	Subarray Layout	6-39
6-35	Thermal Stability at 260°C of Various Adhesives	6-40
6-36	Thermal Stability at 177°C of Epoxy and Epoxy-Phenolic Adhesives	6-41
6-37	Comparison of High Temperature Strength of Various Types of Adhesives	6-42
6-38	Transportation Alternative A	6-44
6-39	Transportation Alternative B	6-45
6-40	Transportation Alternative C	6-46
6-41	Waveguide Weight and Packaging Density	6-47
7-1	Effect of rms Phase Errors on Beam Efficiency	7-2
7-2	Command and Adaptive Phase Front Control Concepts	7-3
7-3	MPTS Phase Front Control Approaches	7-3
7-4	Phase Front Control Approach Comparison	7-4
7-5	Reference Distribution Systems	7-5
7-6	Ground Pilot and Phase Distribution	7-6
7-7	Subarray Phase Control Block Diagram	7-8
7-8	Quadratic Phase Error Example	7-12
7-9	Curved Array Example	7-12
7-10	Phase Estimation Example	7-13
7-11	Bit Wiggle Approach	7-15
A-1	The Geometry Used in the Diffraction Calculations	A-5
B-1	Self-Focusing Instability	B-2
B-2	Self-Focusing Instability Threshold Power Density	B-6
B-3	Growth Rate Versus Transverse Wavelength (Night Time Conditions)	B-7
B-4	Growth Rate Versus Transverse Wavelength (Daytime Conditions)	B-8

LIST OF NON-STANDARD TERMS

AFCRL	Air Force Cambridge Research Laboratory
ATC	Air Traffic Control
ATS	Applications Technology Satellite
CFA	Crossed Field Amplifier
CPU	Central Processor Unit
GaAs	Gallium Arsenide
HLLV	Heavy Lift Launch Vehicle
Met	Meteorological
MPTS	Microwave Power Transmission System
MW	Microwave
N. F.	noise factor
PPM	periodic permanent magnet
ROM	Rough Order of Magnitude
SCR	Silicon Controlled Rectifier
SEPS	Solar Electric Propulsion Stage
Sm-Co(SMCO)	Samarium Cobalt
SPS	Satellite Power System
SSPS	Satellite Solar Power Station
TDRS	Tracking and Data Relay Satellite
TEC	Total Electron Content

## SECTION 1

### INTRODUCTION, CONCLUSIONS, AND RECOMMENDATIONS

#### 1.1 INTRODUCTION

The concept of an orbiting electric power generating station that transmits power through space to earth leads to a potential source of comparatively pollution-free power. The basic elements of the concept are an extraterrestrial power source, e.g., a nuclear reactor or a solar-powered device, and a transmission system to condition the power, transmit it to earth, and again condition it for distribution.

This study concerned the use of microwave technology for the transmission system, an approach which has the potential for high efficiency, large power handling capability and controllability. The transmitting antenna would be in geosynchronous equatorial orbit on a fixed line of sight to the ground receiving and rectifying antenna (rectenna).

Microwaves can traverse the atmosphere with low attenuation, and advances in microwave power technology have been considerable since the first demonstration of appreciable microwave power transfer by Brown<sup>(1)</sup>. The combination of a solar photovoltaic power source in geosynchronous orbit with microwave transmission to earth was first proposed by Glaser<sup>(2)</sup>. This Satellite Solar Power Station (SSPS) concept received increasing attention<sup>(3, 4)</sup> and led to a feasibility study conducted by a team consisting of Arthur D. Little, Inc., Grumman Aerospace Corp., Raytheon Co., and Textron, Inc. under NASA sponsorship<sup>(5)</sup>. Results were sufficiently promising to warrant support of more detailed studies in the technologies involved.

The National Aeronautics and Space Administration (NASA), Office of Applications, as part of a joint Lewis Research Center/Jet Propulsion Laboratory five-year program to demonstrate feasibility of power transmission from space, has included a Microwave Power Transmission System Study. The Lewis Research Center, under a competitive procurement, awarded a cost plus fixed fee contract to the Raytheon Company's Advanced Development Laboratory to undertake the program tasks as follows:

Task I - Preliminary Analysis: To identify potential high efficiency, low cost and low weight in orbit system configurations.

Task II - Conceptual Design: To estimate in greater detail and accuracy than in Task I selected systems cost, weight and performance.

Task III - Technical and Economic Evaluation of Systems: To compare the conceptual designs on the basis of such considerations as cost, weight, reliability, development risk, and to select one concept for further study.

Task IV - Development of Ground Test Program: To define a ground test program with its associated technology development and to estimate the cost of the program.

Task V - Development of Orbital Test Program: To develop a program for a series of orbital tests associated with technology development and to scope the schedule and cost of the program.

Task VI - Reporting: To provide periodic technical, financial and schedule reporting and to provide a final report.

The study concentrated on the microwave power transmission system (MPTS) for transmitting power from space to earth, and as such the results are independent of the power source selected. For example, a solar thermal converter or a nuclear reactor in orbit could be considered in place of a solar photovoltaic power source. Nevertheless, the solar photovoltaic source remains the best known and studied of alternatives, and so was used for purposes of illustration where required.

The study examined system performance, including efficiency and cost and component size and weights as a function of ranges of variables for the Microwave Power Transmission System (MPTS) which included:

- Ground Power Output
- Operating Frequency
- DC-RF Converter Power Level
- DC-RF Converter Type - Amplitron
  - Klystron
- Transmitting Antenna Subarray Size
- Transmitting Antenna Subarray Power Levels



Technique for Cooling Transmitter Tubes  
Beam Control Techniques  
Transmitting Antenna Illumination Pattern  
Peak Receiving Antenna Power Density

A broad range of Satellite Power System (SPS) considerations were investigated to ascertain their impact on the MPTS. These included the following:

Socio-Economic Considerations  
Power Source  
Operations and Maintenance  
Flight Operations  
    Transportation System  
    Re-Supply  
    SPS Flight Mechanics  
    Orbital Assembly System  
Assurance Technologies  
    Reliability  
    Safety  
    Environmental Impact

The study did not evaluate resource utilization and energy payback. These were addressed in reference 5, however they should be further investigated in the course of maturing the detail design features.

## 1.2 CONCLUSIONS AND RECOMMENDATIONS

### 1.2.1 GENERAL

The recommended transmitting antenna is a planar phased array about 1 km in diameter constructed of aluminum or composites and weighing about  $6 \times 10^6$  kg. It consists of 18M x 18M slotted waveguide subarrays which are electronically controlled to direct the power beam at the ground receiving antenna which results in an rms error of about 10M. The subarrays use groups either of 5 kW amplitrons in series or 50 kW klystrons in parallel to convert input dc power to microwave power. The receiving antenna is an array about 10 km in diameter consisting of dipole elements each integrated with a solid state diode and filters which convert microwave power back to dc power.

The recommended operating frequency of 2.45 GHz in the USA industrial band results in near optimum efficiency, avoids brownouts in rain and should have minimal problems in radio frequency interference and allocation. A recommended 5 GW ground power output level provides economy of scale while limiting the peak microwave power density in the center of the beam at earth to about 20 mW/cm<sup>2</sup>. Microwave system transmission efficiency is about 60% and cost is about 500 \$/kW including orbital assembly and transport of the transmitting antenna from the ground to geosynchronous orbit at 200 \$/kg.

The orbital transportation and assembly cost should not exceed about 200 \$/kg if a satellite power system is to have energy costs comparable with projections for ground based nuclear plants. The recommended flight plan is transport to low earth orbit using a reusable heavy lift launch vehicle, assembly in low earth orbit and then transport to synchronous orbit using a solar electric propulsion stage. Emphasis should be placed on orbital manufacture and assembly to achieve favorable launch vehicle packaging densities.

The critical technology items of the MPTS needing early development are the dc to microwave converters, materials, electronic phase control subsystems, transmitting antenna waveguide including its interface with the microwave converters, and structures.

A six-year, three-phase critical technology development and ground test program is recommended at a rough order of magnitude cost of \$27M. The ground test involves transmitting and receiving antennas to obtain data on beam controllability and radio frequency interference, which will provide design confidence for orbital tests.

The planned orbital test program implements defined objectives and relies on the Shuttle transportation system to develop and demonstrate orbital assembly techniques and to establish learning for cost and schedule projections. In order to accomplish all defined objectives it culminates in an orbital test facility which could be the nucleus for a pilot plant in geosynchronous orbit. The objectives and their implementation are subject to change and should be reassessed periodically as further in-depth studies are completed and technology developments are matured. The rough order of magnitude cost for the currently indicated flight test and associated technology development is \$3500M.

## 1.2.2 SUBSYSTEMS AND TECHNOLOGY

A summary set of conclusions and recommendations in each of the major technical areas is provided at the end of each of the Sections 3 through 14. These are collected in the following paragraphs.

### 1.2.2.1 Environmental Effects - Propagation

For the atmosphere at frequencies below 3 GHz:

- a. Absorption and scattering effects are small except for wet hail.
- b. Refraction changes and gradients cause negligible displacement or dispersion of the high power beam and do not degrade significantly a ground based pilot beam phase front as seen at the transmitting antenna.

For the ionosphere at frequencies above 1 GHz:

- c. Refraction changes and gradients cause negligible displacement or dispersion of the high power beam, and do not degrade significantly a ground based pilot beam phase front as seen at the transmitting antenna.
- d. Absorption and scattering effects are negligible.
- e. Faraday rotation has only a small effect for a linearly polarized receiving antenna.
- f. Changes in electron density caused by power densities of  $20 \text{ mW/cm}^2$  and above at 2.45 GHz need to be investigated for possible effects on other ionosphere users.
- g. Possibility of harmonic radiation from the ionosphere (radio frequency interference effects) should be investigated.

### 1.2.2.2 DC-RF Conversion

For the amplatron concept:

- a. Cold pure metal cathode (platinum) for long life.
- b. Pyrolytic graphite radiator for cathode and anode for light, efficient waste heat radiation.
- c. Samarium cobalt permanent magnet for light weight and low cost.

- d. Operating frequency 1.5 GHz to 3.0 GHz; 2.45 GHz preferred.
- e. Power added 5 kW to 10 kW per tube; 5 kW preferred.
- f. Efficiency with rf noise and harmonic filters is conservative 85%; improvement to 90% is a realistic goal.
- g. Cascade configuration because of low gain characteristics.
- h. Regulation of constant current or constant phase by movable pole piece or impulse magnet technique for high efficiency.
- i. Open tube construction, possibly with contaminant baffle, for higher reliability, simple thermal control and lower weight.

For the klystron concept:

- j. Hot cathode design used in study, but a cold cathode development desirable for longer life.
- k. Pyrolytic graphite radiators for efficient heat radiation.
- l. Heat pipes needed for transfer of heat to the radiator surface; study and development required.
- m. Operating frequency can be 1 GHz - 30 GHz; 2.45 GHz is good.
- n. Solenoid focusing and power outputs of 48 kW or greater, with output power dividers to the waveguide.
- o. Collector depression needed for highest efficiency; requires further study to determine practicality of reaching 80%.
- p. Five-stage design including a second harmonic bunching cavity to reduce noise bandwidth.
- q. Open tube construction, possibly with contaminant baffle, for higher reliability, simple thermal control and lower weight.
- r. Parallel configuration.

#### 1.2.2.3 Power Interface and Distribution (Orbital)

- a. Lateral power flow for minimum weight.
- b. Recycling switchgear (crowbar) needed for protection against tube arcing.
- c. Power source and slip rings to be sectored into a minimum of eight independent units to permit a practical switchgear design by limiting maximum short circuit current.
- d. Cost and weight can be scaled by the square root of input power for system tradeoff studies.
- e. Magnetic interaction effects are negligible in attitude control system design.

For the amplitron:

- f. Constant current regulation at the converter to maximize power output and minimize phase shift variations with voltage changes.
- g. Cascade configuration because of low gain characteristic.
- h. Power source voltage should be 20 kVdc.

For the klystron:

- i. Unregulated operation to maximize power output.
- j. Parallel operation to minimize failure effects and simplify compensation for phase shift variations with voltage changes.
- k. Power source voltage should be 40 kVdc.

#### 1.2.2.4 Transmitting Antenna

- a. The transmitting antenna will be a circular, planar, active phased array on the order of 1 km in diameter.
- b. Antenna illumination will be truncated Gaussian with tapers of 5 dB to 10 dB, which can be quantized into about five regions of uniform power.
- c. The antenna will be sectored into subarrays of nominal dimensions 18M x 18M.

d. Subarrays consist of slotted waveguide radiators providing a high overall beam formation and interception efficiency of at least 95 percent for a contiguous rectenna within the main lobe.

e. Waveguide wall thickness nominally is 0.5 mm, but additional investigation may show this can be reduced; width is 12 cm and depth is 6 cm. Cross sections other than rectangular should be included in future detailed investigations.

f. Aluminum, graphite epoxy, and graphite polyimide are candidate materials for the slotted array waveguides.

g. Aluminum configurations require structural segmenting of the subarrays and variation of operating frequency to compensate for longitudinal thermal distortions.

h. Graphite polyimide configurations offer the highest temperature margin with minimal distortion, but all composites must be evaluated for stability and outgassing properties.

i. Waveguide manufacture and subarray assembly on orbit is recommended to achieve favorable launch vehicle packaging density.

j. Microwave interferometers are recommended for MPTS and SPS attitude control, and for initial and periodic alignment of subarrays using screwjack actuators on each subarray.

#### 1.2.2.5 Phase Front Control

- a. Adaptive (retrodirective) approach needed for maximum efficiency.
- b. Command approach needed for safety and back-up.
- c. Calibrated transmission line and/or subarray-to-subarray transfer of reference phase data for adaptive phase control mechanization.
- d. Phase estimation for command mechanization.
- e. Investigate bit wiggle technique as diagnostic tool.
- f. Detailed investigations should be conducted to minimize phase control electronics costs, weight, and blockage for each subarray.

#### 1.2.2.6 Mechanical Systems and Flight Operations

The following summarizes significant conclusions for the mechanical systems and flight operations.

- a. Rectangular grid structural arrangement with triangular hat section is recommended for basic members of the transmitting antenna structure.
- b. Aluminum, graphite epoxy, and graphite polyimide are recommended candidate materials.
- c. Aluminum materials result in the probable lowest cost and development risk program with thermal limits being their most critical area.
- d. Composites are attractive for low thermal distortion and high temperature operation (polyimide), but ultra-violet compatibility, and outgassing leading to rf generator contamination need investigation.
- e. Assuming the Shuttle as the transportation system, low altitude assembly is recommended. The associated transportation and assembly cost for \$10.5M/launch is estimated to be near 600 \$/kg.
- f. Advanced transportation system needed for low cost of large payloads to low earth orbit at relatively low launch packaging densities for the payload. Low cost advanced transportation system required to transport assembled or partially assembled systems from low earth orbit to geosynchronous equatorial orbit.
- g. Orbital assembly requires remote controlled manipulators.
- h. Maximum on orbit manufacturing and assembly will be necessary when using the Shuttle transportation or other options with small volume capacity requiring high launch packaging densities to achieve payload performance.

Technology issues for mechanical systems are listed and discussed in Section 4 of Section 8 (Mechanical Systems and Flight Operations). This listing identifies areas in technology where more work needs to be done and suggests approaches for accomplishing these tasks. The following simplified list is incorporated here as recommendations for further detailed investigation.

- i. Evaluate alternate power transfer and drive devices for the rotary joint.
- j. Conduct detailed control system analysis.
- k. Conduct detailed investigations of composite structures and assembly techniques.
  - l. Investigate tension-brace concepts and compare them with the built-up section approach.
  - m. Evaluate the local crippling stress characteristics of the basic thin material elements of the structure.
  - n. Establish the design environments for launch into low earth orbit, transfer to synchronous orbit as well as those associated with fabrication and assembly.
  - o. Continue investigation of near optimum antenna structural design approaches as environments, geometry, and characteristics with respect to manufacturing, assembly, maintenance, and life are matured.
  - p. Investigate techniques to limit the maximum temperature experienced by the structural elements at the same time achieving high power output for the transmitting antenna.
  - q. Conduct detailed investigation of transient thermal effects.
  - r. Continue detailed investigation of approaches to establish and limit cost of assembly.
  - s. Continue detailed investigation of transport, assembly, positioning, and maintenance operations to define man's role and to define the equipment needed for effective support.

#### 1.2.2.7 Receiving Antenna

- a. An array of small independent elements able to collect and rectify incident microwave power is required for low cost and high efficiency.
- b. A linearly polarized dipole with GaAs Schottky barrier diode is recommended.



c. Development of rectifying antenna elements including diodes for low power density is needed.

d. Rectenna collection and conversion efficiency is 84% and a realistic development goal is 90%.

e. Support structure is major cost item requiring further in-depth study as types of terrain, soils mechanics, and environments are established.

f. Power interface to the user network needs development to reach 92% and greater efficiency.

#### 1.2.2.8 Radio Frequency Interference and Allocation

For both amplitron and klystron:

a. 2.45 GHz is recommended as the operating frequency.

b. Harmonic filters at the rf generators are needed to meet commercial service regulations.

c. Radio astronomy and similar sensitive receiving systems will need notch filters to protect against MPTS harmonics.

d. Multiple SPS installations require further in-depth investigation.

For the amplitron:

e. A bandpass filter is needed to improve performance relative to radio astronomy noise regulations.

f. Noise level with filter added is estimated to exceed radio astronomy isotropic regulations between 2.3 GHz and 2.7 GHz, and to exceed radio astronomy 60 dB antenna regulations above 1.9 GHz. Early development of the amplitron and filters is required to establish noise characteristics.

For the klystron:

g. Noise level exceeds radio astronomy isotropic regulations only in USA industrial band of 2.4 GHz to 2.5 GHz.

h. Noise level exceeds radio astronomy 60 dB antenna regulations between 2.1 GHz and 2.85 GHz.

#### 1.2.2.9 Risk Assessment

The highest risk items in an SPS were identified and ranked according to their relative importance in impacting MPTS equipment design, development and operation. They were ranked as follows:

1. DC-RF Converters and Filters
2. Materials
3. Phase Control Subsystems
4. Waveguide
5. Structure
6. Manufacturing Modules
7. Remote Manipulators
8. Biological
9. Attitude Control
10. Ionosphere
11. Power Transfer
12. Switchgear
13. Radio Frequency Interference and Allocation
14. Support Modules
15. Orbital Assembly Operations
16. Reliability
17. Solar Electric Propulsion System (SEPS)
18. Transportation Operations
19. SPS Flight Mechanics (Stationkeeping)
20. Operations and Maintenance
21. Power Source
22. Heavy Lift Launch Vehicle (HLLV)
23. Socio-Economic Considerations
24. Re-Supply

The following are recommended as considerations for risk assessment in developing the system concept, technology development, ground test and flight test.

a. The microwave power transmission system can be configured in such a manner as to not require invention or technology breakthrough, however, continuing efforts should be made to take advantage of applicable breakthroughs as they might be developed over the years.

b. There are 24 items having significant technology risk for the MPTS which require aggressive development programs before high confidence can be established in their implementation.

c. The first five most critical items needing technology development in order of priority are: DC-RF Converters and Filters, Materials, Phase Control Subsystems, Waveguides, and Structures.

d. Although Manufacturing Modules and Remote Manipulators are in the critical technology category, significant advancement cannot be undertaken until certain characteristics associated with the technology of the first five items are established.

e. General existing developments leading to the understanding of biological effects of low and high microwave power densities are important. In addition, specific investigations must be undertaken which are site dependent to a large extent. These should be undertaken as the development and operational sites are identified.

f. Attitude control technologies for the operational system interact with beam efficiency, safety and depending on the approach they may result in dynamic loads and materials that will impact the microwave system and components. For flight test systems operating at low orbital altitudes, high angular rates and accelerations lead to significantly more complex implementation than is required for the operational system. These require further in-depth investigation as flight test objectives and their implementation are progressively and more firmly established.

g. Ionospheric effects on the microwave power transmitting system will probably be small. Effects of the system on the ionosphere and on its other users may be significant. The flight test system, in particular the size of the system, may be established by ionospheric effects demonstration test requirements. Further in-depth analysis and tests are required before establishing the requirements firmly.

h. Power transfer at high power levels across flexing and rotary joints constitute a large scale technology development problem.

i. Switchgear including protective elements must be developed for the high power spaceborne application.

j. When it has been established that power from space can be a significant part of the solution to national and international power needs, detailed radio frequency interference investigations must be undertaken and frequency allocations must be established. Radio astronomy users must be major participants in this activity.

k. Support modules and orbital assembly techniques for space flight operations must be developed as the requirements are established in detail.

l. Reliability as well as operations and maintenance considerations to assure long life in space and on the ground will be critical to the operational acceptability of the system. Both mechanically passive and active elements are involved. The maintenance equipment may well be more complex than the functional equipment and a thorough tradeoff of competitive approaches is required.

m. Solar electric propulsion stages, transportation operations, heavy lift launch vehicles, SPS flight mechanics and the power source will have characteristics that impact the design of the microwave power transmission system and its equipments. Thorough understanding of these characteristics and perhaps associated constraints must be established as technology development and concept formulation progresses.

n. Socio-economic considerations will become most important as the total concept formulation is established. How the considerations of environmental impact (favorable and unfavorable) interact with design, operations and economics are yet to be established in the required detail.

o. Re-supply of the space station, particularly of gases and fluids, will impact the system and equipment design. Operations must be established such as to assure an acceptable level of contamination of sensitive components such as the open elements of the many rf generators.

p. Progressive technology risk assessments and rankings must be established as the technology developments mature and the system concept is established. This will play an important part in technology development, ground test and flight test program definition and re-definition as well as in the details of the overall concept.

### 1.2.3 SYSTEM ANALYSIS AND EVALUATION

The system analysis and evaluation section incorporates and reflects the subsystem and technology study results in arriving at the following:

- a. Capital specific cost decreases as ground power output increases.
- b. At higher power levels, cost is lowest near 2 GHz.
- c. Frequency of 2.45 GHz in the industrial band is the recommended choice.
- d. System configurations having ground bus power levels above 5 GW exceed  $20 \text{ mW/cm}^2$  peak ground power density which is beginning to affect the ionosphere and so 5 GW is currently recommended as the maximum for planning purposes. Further in-depth analysis and testing is required to understand these effects more thoroughly and perhaps relax the constraint.
- e. Overall MPTS efficiency is expected to be about 54%-56% initially with improvement potential to about 63%-67% for amplitron configurations; klystron configurations would be 49%-52% to 56%-59%.
- f. Amplitrons result in lower cost systems than do klystrons.
- g. Aluminum results in potentially lower cost but more complex systems than do graphite composites.
- h. Dominant cost factors for SPS are the power source and transportation.
- i. As a guide, the power source parameters should not exceed the combination of 350 \$/kW with 1.0 kg/kW or possibly 250 \$/kW with 1.5 kg/kW where the power is as delivered to the transmitting antenna.
- j. As a guide, transportation and orbital assembly should not exceed 200 \$/kg.

k. As a guide, build and deploy cycle for SPS should not exceed 3 years to limit interest charges.

1. For the aluminum-amplitron configuration, near optimum transmitting antenna and receiving antenna sizes are 0.9 km and 10 km respectively, and transmitting antenna weight is about  $6 \times 10^6$  kg.

#### 1.2.4 TECHNOLOGY DEVELOPMENT AND TEST PROGRAMS

The recommended critical technology developments in support of both the integrated ground test program and the orbital test program are as proposed in Sections 13 and 14. The integrated ground test program and orbital test programs are based on the level of detail established to date in studies including the current status of technology development. It is recommended that they be re-evaluated in terms of both the objectives and their implementation as further detail study is conducted and technology developments are matured.

##### 1.2.4.1 Technology Development and Ground Test Program

a. Initial technology development is needed for dc-rf converter, materials, and phase control subsystem.

b. Test program will provide data on controllability and radio frequency interference.

c. Transmitting antenna phased array and rectenna are required for integrated ground testing.

d. Rough order of magnitude costs are \$4M for technology and \$23M for the integrated ground test.

##### 1.2.4.2 Technology Development and Orbital Test Program

a. Orbital test is needed to develop and demonstrate dc-rf converter startup and operation, zero 'g' assembly and operations, and learning with respect to projected costs and schedule.

b. Requirements are satisfied by a geosynchronous test satellite and by a series of Shuttle sortie missions that lead to an orbital test facility.

c. A low earth orbital test facility can be sized to determine the effects on the upper ionosphere of high microwave power densities.

d. Modified ground based facilities such as at Arecibo are best suited to determine the effects on the lower ionosphere of high microwave power densities.

e. Technology development is needed in not only the "critical" areas but in essentially all MPTS areas in order to support a progressive program to demonstrate readiness to proceed to significant scale for a pilot plant or prototype.

f. Rough order of magnitude costs are \$318M for critical technology development, and \$96M for the geosatellite, and to accomplish all identified objectives \$3052M for the sorties and orbital test facility.

#### 1.2.5 ADDITIONAL STUDIES

Recommendations for early further in-depth studies complementing the technology development programs are:

a. Analyze transient thermal effects on the transmitting antenna structure, waveguide and electronics as it passes in and out of eclipse to determine impact on controllability and materials selection.

b. Analyze power beam ionospheric effects to estimate impact on other users and provide a detail model for phase front control simulation.

c. Model closed loop phase front control to better estimate error budget and performance under transient conditions.

d. Determine special requirements for multiple ( 100) stations relating to spacing in orbit and on the ground, control, frequency selection and interference.

e. Detail alternate uses and intermediate benefits of MPTS and potential impact on its design and development.

f. Investigate ways of reducing transportation and assembly costs by a better (higher level of detail) synthesis of launch vehicle, assembly and equipment technologies.

#### 1.3 REPORT APPROACH AND ORGANIZATION

This report presents the final results and the techniques leading to those results that evolved through the course of the study. There is no deliberate attempt to present a chronological record or documentation of the evolution through intermediate steps, except where it might serve a useful tutorial function.

This report is organized in four volumes with the Executive Summary comprising Volume I. The sequence in Volume II begins with a discussion of the study organization and approach. This is followed by the section on propagation which introduces important background material affecting choices of operating frequency, control approach and power level.

The remainder of Volume II is concerned with the orbital portions of MPTS, beginning with the section on dc-rf conversion. This provides the background for a discussion of the power interface. The transmitting antenna and phase front control sections, and appropriate appendices complete Volume II.

Volume III is devoted entirely to mechanical systems and flight operations. This is the final report of Grumman Aerospace Corporation for preliminary analysis and conceptual design tasks. It was submitted at the end of the latter phase, and it contains material, particularly in preliminary analysis, that later was modified as a result of subsequent system analysis and evaluation by Raytheon. This aspect is noted in the preface to Volume III.

Volume IV begins with the ground portion of the MPTS, the receiving antenna, and proceeds through sections relating to system aspects -- frequency interference, system analysis, risk assessment, critical technology and test programs -- which evaluate and draw conclusions from the subsystem material presented earlier.



## REFERENCES (SECTION 1)

1. W. C. Brown, "Experiments in the Transportation of Energy by Microwave Beam", 1964 IEEE Int. Conv. Rec., Vol. 12, pp. 8-17.
2. P. E. Glaser, "Power From the Sun: Its Future", Science, Vol. 162, pp. 857-861, November 22, 1968.
3. J. Microwave Power, "Satellite Solar Power Station and Microwave Transmission to Earth", Vol. 5, Devenber 1970.
4. W. C. Brown, "Satellite Power Stations: A New Source of Energy?", IEEE Spectrum, Vol. 10, No. 3, pp. 38-47, March 1973.
5. P. E. Glaser, O. E. Maynard, J. Mockovciak Jr., L. E. Ralph, "Feasibility Study of a Satellite Solar Power Station", NASA Contractor Report CR-2357, NASA, Washington, D. C., February 1974.

## SECTION 2

### ORGANIZATION AND APPROACH

#### 2.1 ORGANIZATION

The organization that was structured to conduct the study is shown in Figure 2-1. Management was centered in the Space Systems Department of Raytheon's Equipment Division's Advanced Development Laboratory, headed by Dr. R. B. Campbell, Jr. The Space Systems Department, headed by Mr. O. E. Maynard, was responsible for all of the Equipment Division space microwave power activities including the construction of a Reception Conversion Subsystem (Rectenna) for the Jet Propulsion Laboratory under JPL Contract No. 953968. Mr. A. Edwards was responsible on a full-time basis for technical and financial management of the MPTS program.

Task Managers Messrs. H. Rowland, L. Doyan, A. Greene, and G. Meltz were resident in the Advanced Development Laboratory. The study drew upon other elements of the Equipment Division to obtain the specialized knowledge of Mr. J. Howell for the Transmitting Antenna and Phase Front Control, and of Mr. J. Haley for the Power Source Interface and DC to RF Conversion. Raytheon's Microwave and Power Tube Division was assigned to support the effort in three areas: rectenna, transmitting antenna, and amplitrons. Mr. W. C. Brown, a pioneer in the microwave power transmission field, headed the activity in these areas and for the amplitron effort reported through Mr. Haley.

An extensive search to obtain the best possible group to study the klystron culminated in the selection of Shared Applications, Inc. of Ann Arbor, Michigan. This firm is headed by Dr. J. E. Rowe who is a recognized authority in the field of linear beam devices and was Chairman of the Electrical Engineering Department at the University of Michigan.

The Grumman Aerospace Corporation, Bethpage, New York was selected to perform the study tasks related to mechanical systems and flight operations because of their extensive experience in these areas related to the microwave power transmission system. They had participated in the earlier feasibility study sponsored by Lewis Research Center under NAS3-16804, contract to Arthur D. Little Inc.

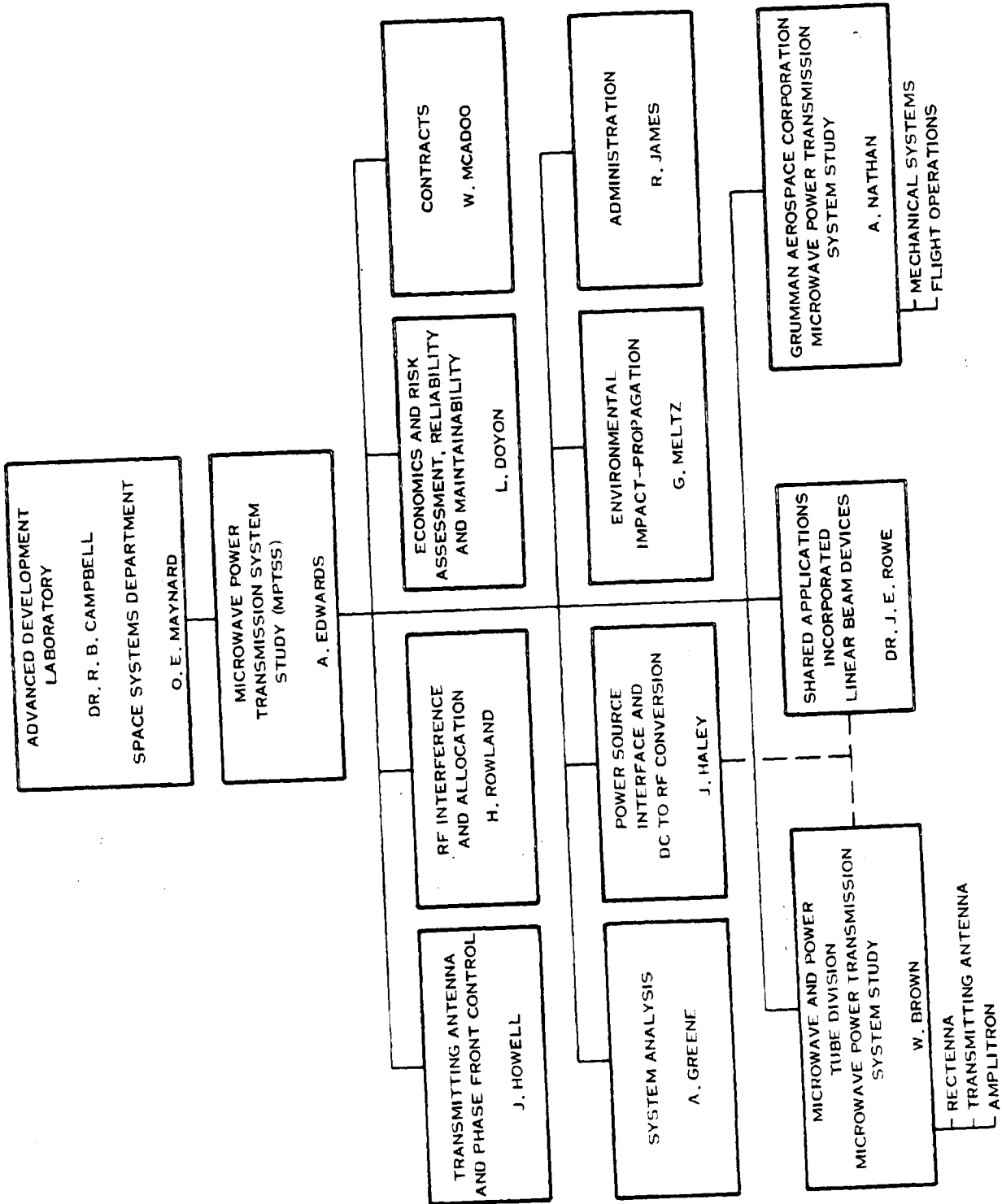


Figure 2-1. Microwave Power Transmission Systems Study Program Organization

ORIGINAL PAGE IS  
OF POOR QUALITY

## 2.2 APPROACH

The Work Breakdown Structure (WBS) for the study is shown in Figure 2-2. This was the basic vehicle for managing the technical aspects of the program and controlling the cost. The first level breakdown conforms to the tasks described in Section 1. The second level tasks are the key activities in the program for which task managers were assigned with both financial and technical responsibilities. The man hours expended at the first level breakdown are noted in Figure 2-2 to indicate the study emphasis.

The schedule for the study is shown in Figure 2-3. There were frequent reviews conducted by Lewis Reserach Center throughout the program, coordinated with the key decision and planning dates. Contributors at several reviews included representatives from NASA Headquarters' Office of Applications, Johnson Space Center, and the Jet Propulsion Laboratory.

As shown in the schedule the Grumman Aerospace Corporation effort was reinitiated to support the Orbital Test Program development effort, and work on the final report was carried forward during the period between completion of planning for the Ground Test Program and contractual authorization to proceed on the Orbital Test Program studies.

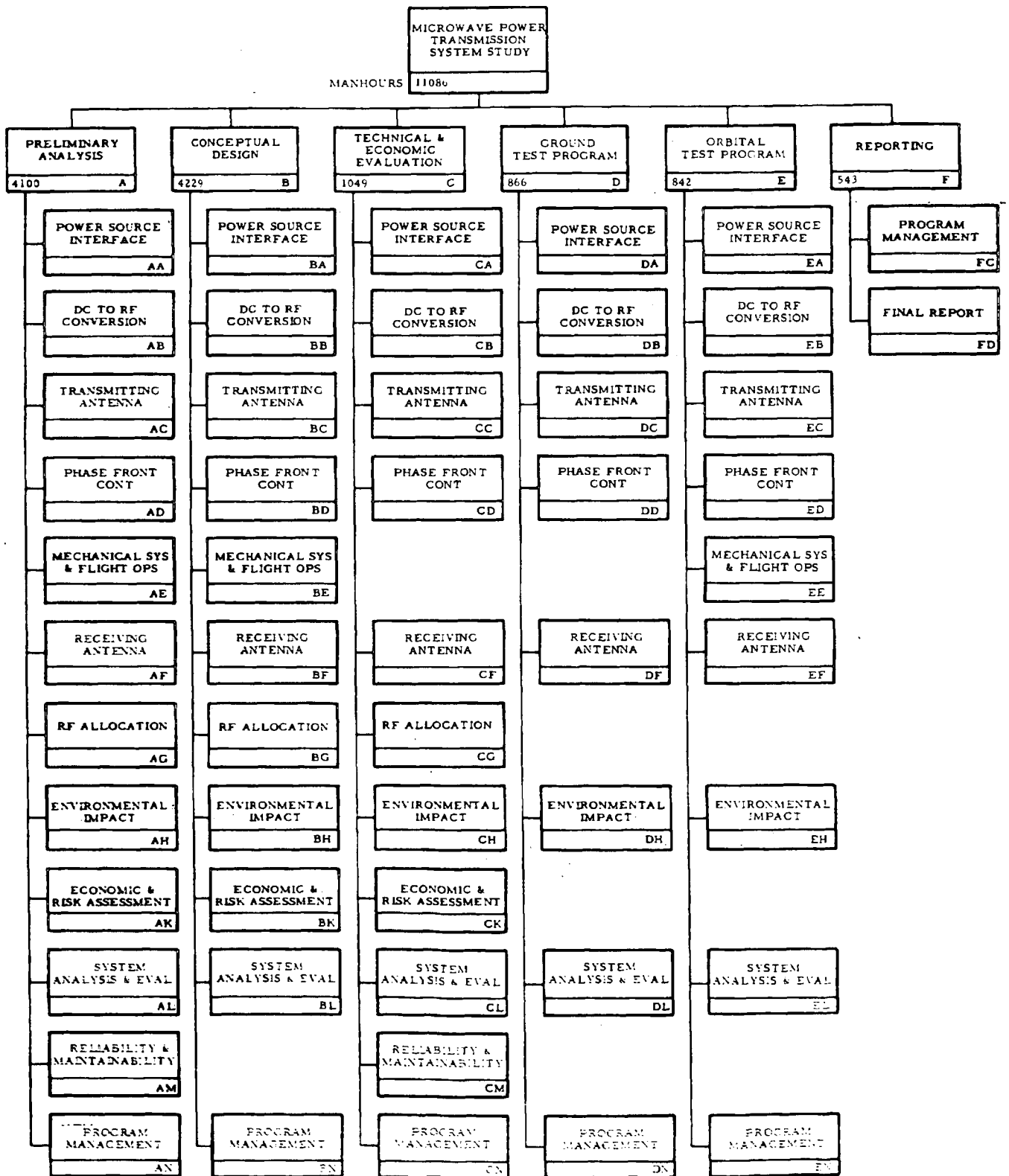


Figure 2-2. Work Breakdown Structure

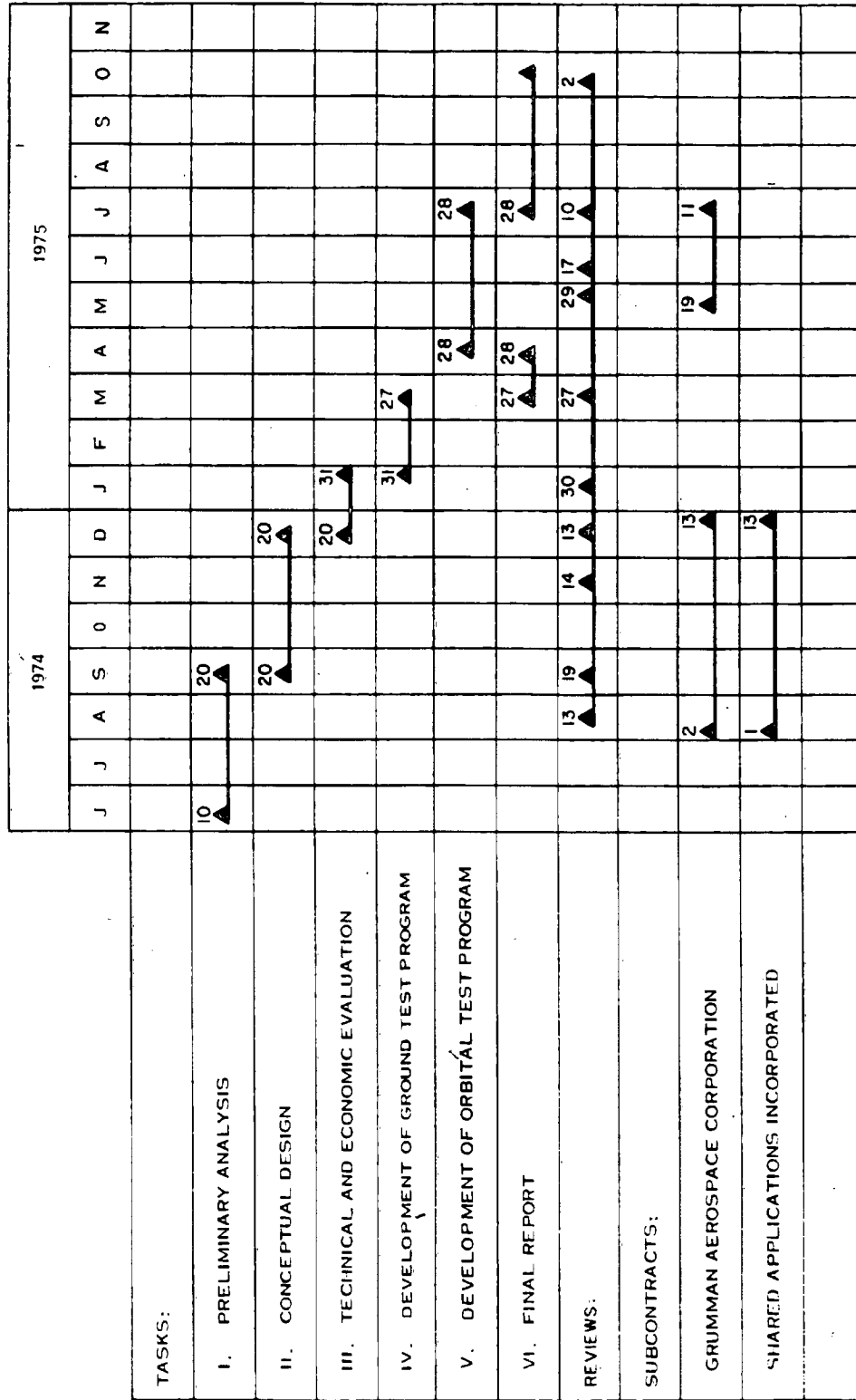


Figure 2-3. MPTS Schedule

## SECTION 3

### ENVIRONMENTAL EFFECTS - PROPAGATION

#### 3.1 INTRODUCTION

In the Satellite Power Station concept a large amount of microwave power is transmitted to the earth from a large phased array antenna. It is received and rectified by a large ground antenna. Control of the high power beam is maintained by both a command system and a self-phasing system. The command system senses deviations from the desired power density distribution on the ground and telemeters phase corrections to the array. The self-phasing or adaptive system uses a pilot signal or control beam radiated from the ground to adjust the array phase distribution to focus the power on the receiving antenna. This section describes the effects of the atmosphere and ionosphere on the transmission and control of the high power beam. It also identifies possible effects of the high power beam on the natural environment of the ionosphere and atmosphere.

The physics of molecular absorption by oxygen and water vapor and the theory of scattering and absorption by hydrometeors, such as rain, cloud droplets, snow and hail, are reviewed in Paragraph 3.2 and applied to estimating the atmospheric transmission efficiency as a function of frequency from 1 to 30 GHz and for various meteorological conditions. Paragraph 3.3 deals with the power beam displacement and dispersion due to refraction and ionospheric irregularities as well as the control beam phase and amplitude noise due to ambient and self-induced electron density fluctuations. Paragraph 3.4 provides a brief discussion of ionospheric modification due to microwave heating. Additional in-depth work will be required in this area to determine the effects of power fluxes in excess of  $20 \text{ mW/cm}^2$ . Detailed derivations and discussions of the various ionospheric propagation factors are provided in Appendices A, B and C.

The effects of atmospheric absorption are to attenuate the transmitted power significant but limited amounts which are minimal for frequencies below 3 GHz (2 percent attenuation nominally and 4 percent in most severe cloud and rain conditions).

The effects of tropospheric refraction, turbulence and index of refraction gradients across clouds or weather fronts are to produce negligible displacement or dispersion of the high power beam for frequencies of 3 GHz and below. Their effects on the pilot signal are such as to not degrade the signal or the shape of the associated reference phase front significantly.

The effects of the high power beam at power densities between 10 and 100 mW/cm<sup>2</sup> on portions of certain layers of the ionosphere (D, E and F layers) may be significant in terms of increasing electron temperature and modifying (both increasing and decreasing) the plasma density. This in turn may be significant in modifying the performance of systems involving the F layer such as Over the Horizon Radars, HF communications, UHF radar (backscatter clutter and measurement accuracy). Also systems involving the D layer such as VLF (Omega and LORAN) navigation systems may be effected.

### 3.2 ATMOSPHERIC ATTENUATION AND SCATTERING

Estimates of atmospheric transmission efficiency are developed in this section as a function of frequency for various meteorological conditions. Gaseous absorption and attenuation by hydrometeors, such as rain, cloud droplets, snow, and hail, are the principal sources of propagation loss.

#### 3.2.1 MOLECULAR ABSORPTION

Attenuation of decimeter and centimeter radiation in clear air is due to the excitation of collision broadened rotational lines in water vapor and oxygen. <sup>(1, 2, 3, 4)</sup> Absorption occurs because these molecules have permanent dipole moments that couple the electric or magnetic components of the microwave field to rotational energy levels. Most of the absorption is due to the 1.35 cm (22 GHz) line of water vapor and the 0.5 cm (60 GHz) line of oxygen. The strength of the interaction, and hence the frequency dependence is a function of the inherent line shape and the line width of the induced transition, which are in turn functions of the atmospheric model. Battan <sup>(4)</sup> contains a figure that illustrates the variation of the attenuation coefficient with frequency (and wavelength) for O<sub>2</sub> and uncondensed H<sub>2</sub>O. This figure is duplicated in Figure 3-1 to point out the rapid rise in absorption above 10 GHz and the weak dependence on water vapor content in the decimeter range of the spectrum. The same variation with frequency is seen, of course, in the



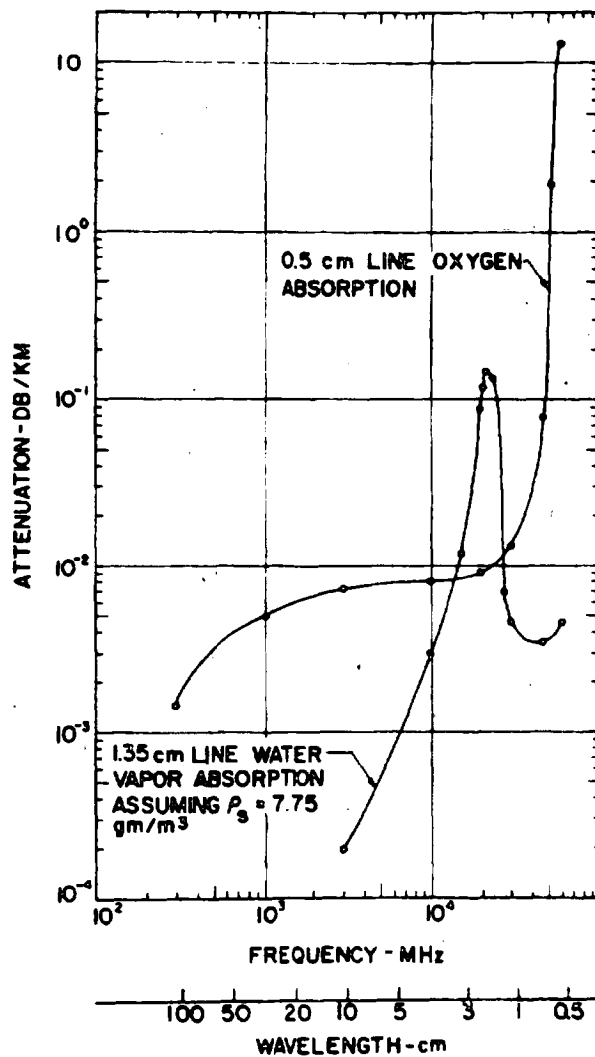


Figure 3-1. Atmospheric Absorption by the 1.35-cm Line of Water Vapor for a Mean Absolute Humidity of  $7.75 \text{ g/m}^3$  and by the 0.5-cm Line of Oxygen at a Temperature of  $20^\circ\text{C}$  and a Pressure of One Atmosphere. After Bean and Dutton (1968).

integrated zenith attenuation as shown by the curves in Figure 3-2, due to Crane and reproduced from reference (2). There is little variation in attenuation below 10 GHz between the extremes of a totally dry and saturated atmosphere. The curve labeled M corresponds to a representative model atmosphere for summer conditions at a temperate latitude. The estimates of molecular absorption for power transmission are based on this result, but scaled by the cosecant of the

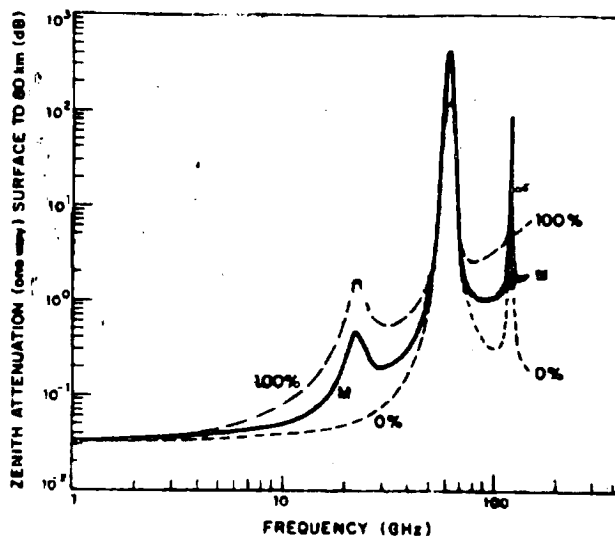


Figure 3-2. Zenith Attenuation Versus Frequency

elevation angle to adjust for the longer path. Figure 3-3 compares the integrated gaseous attenuation at a representative northeast (power beam elevation above horizontal  $\theta_e = 20^\circ$ ) and southwest ( $\theta_e = 50^\circ$ ) location with the total attenuation along a 10 km path through a moderately heavy rainfall\*. It can be seen that below 10 GHz the attenuation resulting from molecular absorption is approximately 0.1 dB or less, depending on the elevation angle. At frequencies less than 3 GHz, gaseous attenuation greatly exceeds the atmospheric loss due to a typical rainfall.

### 3.2.2 SCATTERING AND ABSORPTION BY HYDROMETEORS

Attenuation by particles of condensed and solidified water vapor results from both absorption and scattering and depends on the size, shape, statistical distribution and composition. (2, 4, 5) Generally, dry ice, snow, and hail produce much less attenuation than rain at an equivalent rate. However, wet snow, melting precipitation, and water-coated ice particles can cause significant loss which may be comparable to, and under some circumstances, larger than an equivalent rainfall.

\*The probability that rainfall rate equals or exceeds 5 mm/hr is less than 1 percent.

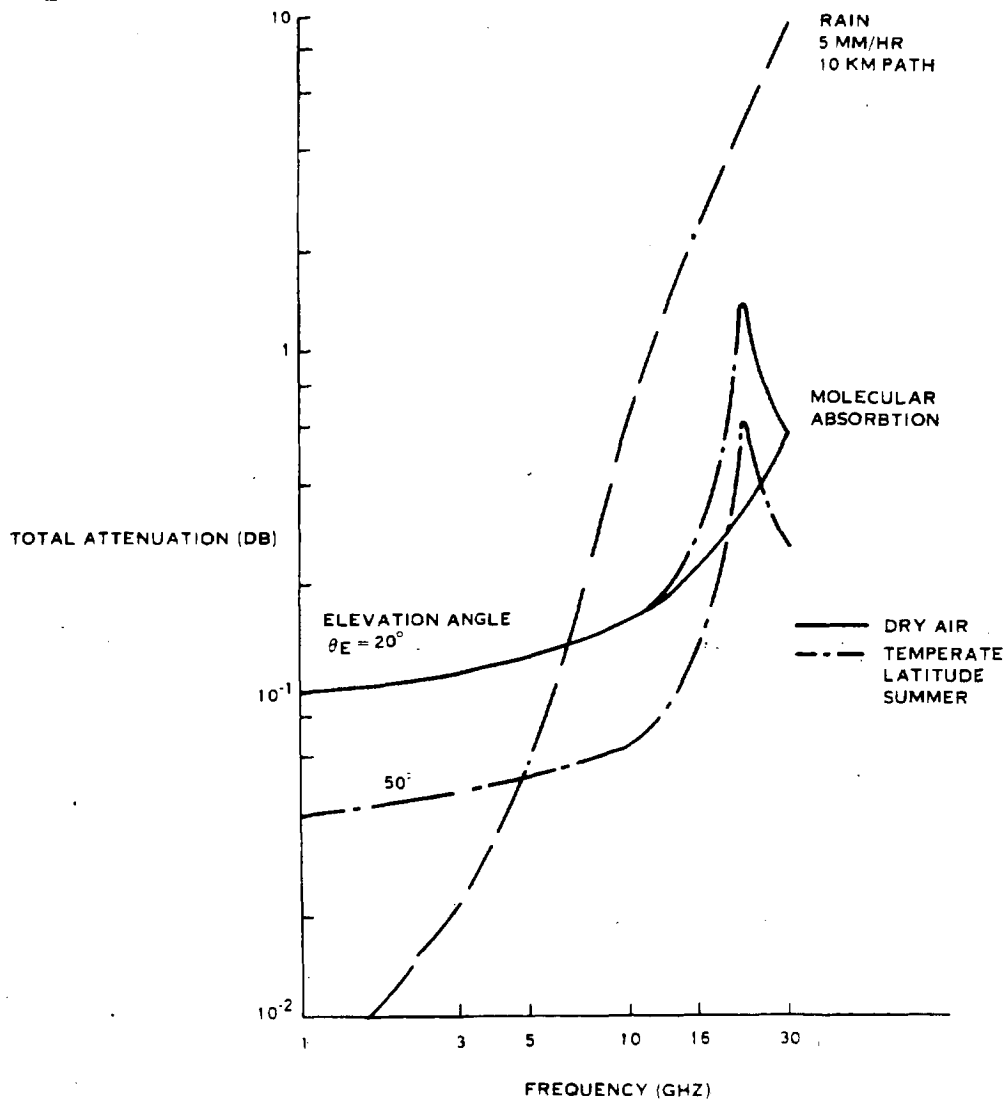


Figure 3-3. Comparison of Gaseous Absorption and Rain Attenuation

The theory of attenuation by hydrometeors is based on the exact results first obtained by Mie for scattering from large dielectric spheres. If the particles are small compared to wavelength, an assumption which is valid for wavelengths greater than 10 cm and all precipitation except hail, then the Rayleigh approximations can be used to simplify the expression for the total cross-section  $Q_t$ :

$$Q_t = Q_a + Q_s \quad (3-1)$$

$$Q_s = 1.31 \times 10^4 a^6 / \lambda^4 |K|^2 \quad (3-2)$$

$$Q_a = 79 a^3 / \lambda \operatorname{Im}(-K) \quad (3-3)$$

$$K = (m^2 - 1) / (m^2 + 2) \quad (3-4)$$

Where  $Q_a$  and  $Q_s$  are the absorption and scattering cross-sections, respectively,  $a$  is the particle radius and  $m$  is the complex index of refraction of the hydrometeor.  $\operatorname{Im}$  denotes the imaginary part of the complex quantity  $-K$ . The attenuation coefficient  $A$  is directly expressible in terms of  $Q_t$  and the drop size distribution per unit volume  $n(a)$ .

$$A = 0.4343 \int_0^{\infty} n(a) Q_t(a) da \text{ (dB/km)} \quad (3-5)$$

Where  $Q_t$  and  $a$  are in cgs units and  $n(a)$  is in mixed units  $\text{cm}^{-1}/\text{m}^3$ . If the droplets are sufficiently small, then the attenuation can be re-expressed in terms of the water content. This is the usual practice in estimating decimeter attenuation due to water clouds.

The drop distribution of rainfall is highly variable, contributing to a large spread in the estimate of  $A$  for a given surface rainfall rate.<sup>6</sup> Marshall and Palmer<sup>7</sup> formulated an empirical distribution of the form

$$n(a) = 8 \times 10^4 \exp(-82 R^{-0.2} a) (\text{cm}^{-1}/\text{m}^3) \quad (3-6)$$

with  $R$ , the rainfall rate, given in mm/hr. This distribution fits observations and nearly coincides with the classical Laws and Parsons distribution (which is based on three years of measurements near Washington, D. C.) over the range of drop diameters that determine decimeter and centimeter attenuation. Substituting Equation (3-6) in (3-5) and carrying out the integration we obtain:

$$A = 1.2 \times 10^{-2} |K|^2 R^{1.4} / \lambda^4 + 3.3 \times 10^{-1} \operatorname{Im}(-K) R^{0.8} / \lambda \quad (3-7)$$

The imaginary part of the dielectric factor  $K$  depends on the temperature and phase of the hydrometeor and the microwave frequency. Dry ice is at least an order of magnitude less lossy than water. This is important since most of the attenuation of decimeter radiation is due to absorption. Wet ice or water-coated hail will be nearly as lossy as a raindrop.

The exact Mie theory must be used for wavelengths less than 10 cm; however, the Rayleigh approximation is useful between 10 and 30 cm and is accurate for wavelengths 30 cm and greater. Table 3-1 compares the attenuation coefficient obtained from Equation (3-7) with the distribution of values computed by Schell et al.<sup>6</sup> (using measured drop size distributions and Mie theory) and the Log Regression fits to attenuation versus rainfall rate scattergrams given by Crane.<sup>(2)</sup> Also shown are the results of computations based on Equation (3-6) and the exact Mie expressions for  $Q_s$ .

TABLE 3-1  
ATTENUATION BY HEAVY RAIN (dB/km)  
R = 25 mm/hr      T = 10°C

Estimate	Frequency (GHz)			
	2.80	3	9.15	10
Rayleigh Approximation		$3 \times 10^{-3}$		0.05
Log Regression	$9.9 \times 10^{-3}$		0.30	
Measured Drop Distribution				
Minimum	$6 \times 10^{-3}$		0.14	
Lower	$8 \times 10^{-3}$		0.23	
Mean	$9 \times 10^{-3}$		0.35	
Upper	$10 \times 10^{-3}$		0.54	
Maximum	$26 \times 10^{-3}$		1.12	
Marshall - Palmer and Mie Theory (Battan <sup>(4)</sup> )		$11 \times 10^{-3}$	0.33	

Estimates of the transmission efficiency for propagation through a uniform rainfall are based on the Log Regression model and the mean value of the set of estimates obtained from measured drop distributions at six heavy rain locations.<sup>(2)</sup> The results are expressed in terms of one-way path attenuation and

plotted in Figure 3-3, and combined with estimates of clear air gaseous absorption and plotted in Figure 3-4 for two elevation angles. Also shown in Figure 3-4 are transmission efficiency estimates for propagation through an extremely heavy rainfall (50 mm/hr) in a 4 km high cloud and a severe thunderstorm.<sup>(8)</sup> The latter results are based on the measured rainfall rates<sup>(9)</sup> shown in Figures 3-5 and 3-6. A Laws and Parsons distribution and Mie theory were used to compute the attenuation coefficient. The variation in efficiency with frequency for four different propagation paths through the thunderstorm are depicted in Figure 3-7. The curve in Figure 3-4 corresponds to path ① through the storm center. Note the height and lateral extent of the storm and the variation in efficiency with distance from the region of peak rainfall. A more accurate estimate would take into account the variation in loss across the beam cross-section. The results presented herein provide a lower bound on the transmission efficiency.

Based on the results in Figure 3-4, it is concluded that atmospheric attenuation due to molecular absorption and heavy rain is tolerable at frequencies below 3 GHz. Under the most severe conditions it is found that  $\eta_{tt} = 0.96$  at 3 GHz.

In the 10 to 30 cm band, attenuation due to clouds is less than one-half percent. Attenuation due to dry snow is also negligible in this band as can be seen by evaluating Equation (3-5), using the Rayleigh approximation to the cross-section and an empirical particle size distribution (see Table 6.4, pg. 74, in Battan).

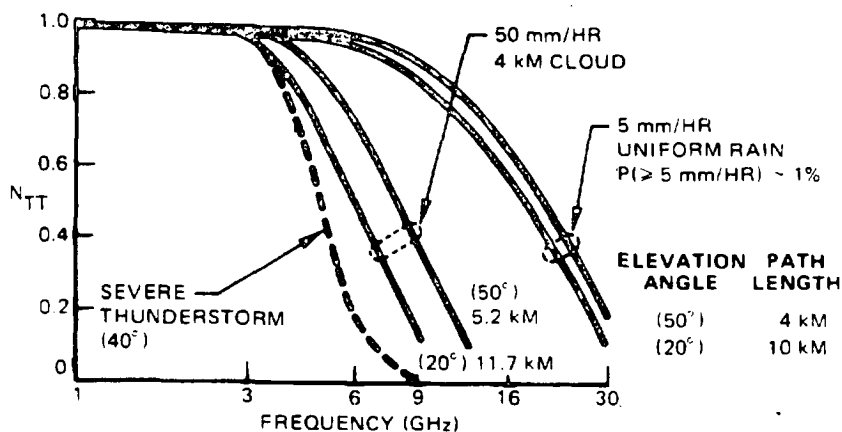


Figure 3-4. Transmission Efficiency - Molecular Absorption and Rain

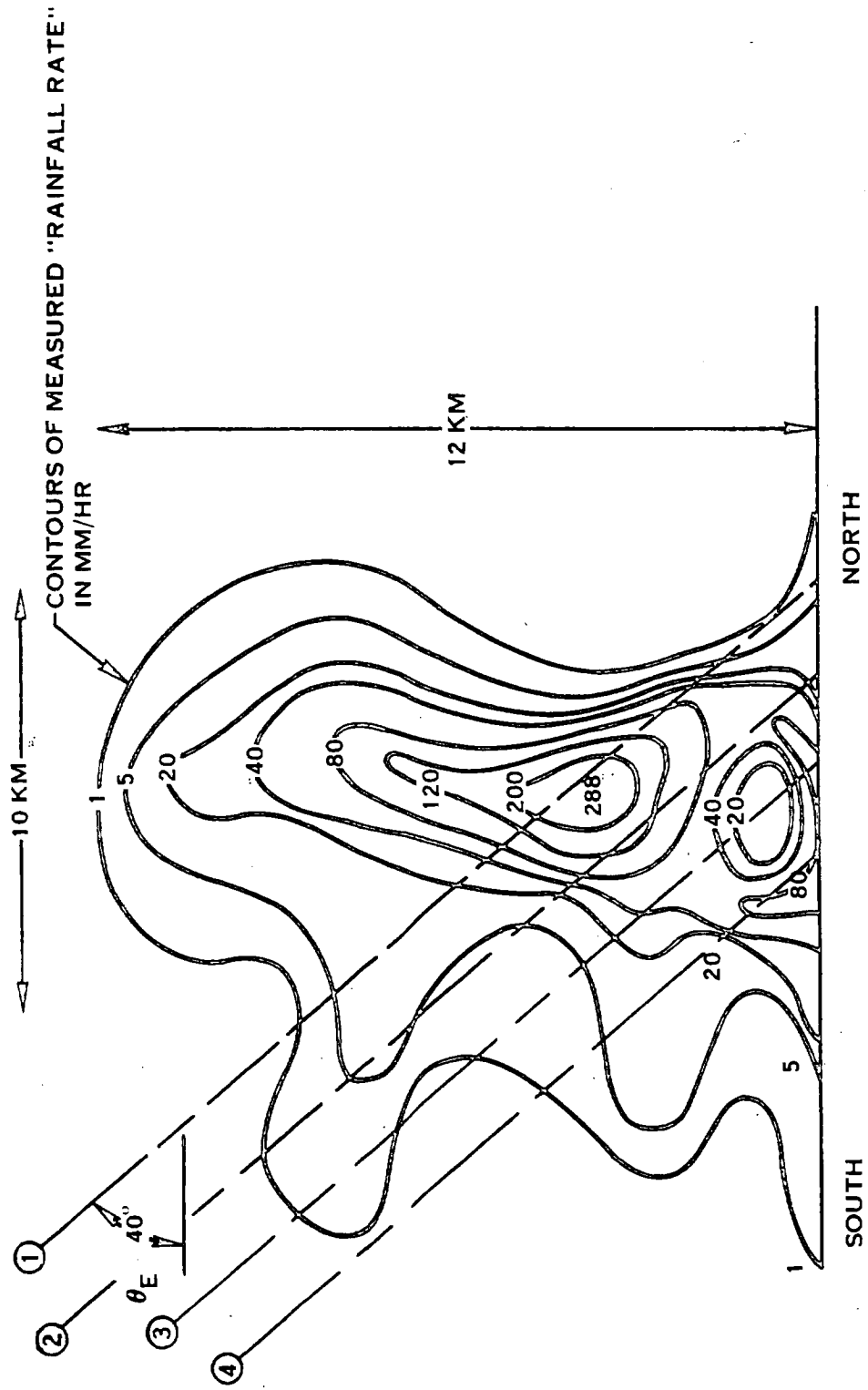


Figure 3-5. Rainfall Rate in a Thunderstorm, North-South Section

Wet snowflakes may produce much larger attenuation because a thin coating of water can cause a small ice particle to have a total cross-section nearly the same as an all water particle. The shape of the snowflake and the orientation of its principal axes with respect to the polarization of the microwave beam could also influence the amount of attenuation produced by snow in the melting layer below the 0°C isotherm.

Attenuation due to water-coated hail can be quite severe, although infrequent because of the low probability of hail. Very few measurements are available; however, we can get an estimate of the expected loss from computations made by Battan.<sup>(4)</sup> Table 3-2 lists attenuation coefficients for 10 cm propagation through dry and wet hail. Results are shown for three exponential particle-size distributions with different maximum particle sizes. The attenuation produced by a 1 km path through 25 mm/hr rain is shown for comparison. A one kilometer path through wet hail could result in transmission efficiency at 3 GHz of 0.87.

TABLE 3-2

3 GHz ATTENUATION IN dB/km FOR SPHERICAL HAIL

Distribution	Maximum Size (cm)	Water-Shell Thickness (cm)			
		Dry	0.01	0.05	0.10
I	0.97	$2 \times 10^{-3}$	$51 \times 10^{-3}$	$58 \times 10^{-3}$	$80 \times 10^{-3}$
II	1.93	$17 \times 10^{-3}$	0.15	0.34	0.89
III	2.89	$34 \times 10^{-3}$	0.19	0.60	1.18
Rain (25 mm/hr)	Marshall Palmer Distribu- tion	$11 \times 10^{-3}$			

If the receiving array is to be located at a site where hail or snowfall is likely, then closer examination of the transmission loss associated with propagation through these precipitates is needed.

Forward scattering by rain and particularly by hail will increase the field intensity outside the main beam. This problem has received recent attention because of the possible interference between satellite downlinks and microwave



trans-horizon communication. To estimate the scattered power density, we will assume that the hydrometeor scatters isotropically. This is not quite accurate since we know that Rayleigh scattering has an angular dependence of  $1/2 (1 + \cos^2 \chi)$ , where  $\chi$  is the scattering angle. Nevertheless, isotropic scattering is a reasonable first approximation. Consider a unit volume at a height  $h$  illuminated by the microwave beam. If the incident power density is  $S_i$ , then the scattered power density  $dS_r$  at a range  $r$  is given by:

$$dS_r = S_i \sum Q_s / 4\pi r^2 \quad (3-8)$$

where the summation extends over all particles (hydrometeors) in a unit volume. The scattered power density is obtained by integrating Equation (3-8) over the volume containing hail and contributing to a point at an average range  $\bar{r}$  from the scattering region. If  $d$  is the height of the storm cell that contains large diameter hail, then

$$S_r = P_t / (4\pi \bar{r}^2) \eta d \quad (3-9)$$

where  $\eta$  is a reflectivity or scattering cross-section per unit volume. A 5 GW system at 3 GHz would scatter 3 mW nearly isotropically, if  $d$  is 1 km. Thus, at a range of 10 km the scattered power density would be about  $2 \times 10^{-4}$  mW/cm<sup>2</sup>. We conclude, therefore, that scattering from the hail will not significantly increase sidelobe levels or broaden the main beam.

### 3.3 IONOSPHERE PROPAGATION

#### 3.3.1 AMBIENT REFRACTION

The lateral displacement of the power beam due to ionospheric refraction is given by<sup>(10)</sup>

$$d = 4.5 \times 10^{-12} \frac{\cos \theta_e}{\sin^2 \theta_e} N \lambda^2 \text{ [m]} \quad (\lambda \text{ in meters}) \quad (3-10)$$

where  $N$  is the total electron content in a vertical column, measured in electrons/cm<sup>2</sup>, and  $\theta_e$  is the elevation angle. For  $N = 5 \times 10^{13}$  e/cm<sup>2</sup>, probably an upper bound at midlatitudes, and  $\theta_e = 20^\circ$ ,  $d = 41$  m with  $\lambda = 15$  cm. Thus, the displacement is entirely negligible. Horizontal gradients are also expected to produce displacement that are less than 100 meters. <sup>(10)</sup>

### 3.3.2 SCINTILLATIONS DUE TO AMBIENT FLUCTUATIONS AND SELF-FOCUSING INSTABILITIES

Electron density fluctuations in the upper ionosphere will cause correlated random differential phase shifts across the wave front of a microwave beam as it propagates through the irregularities. As a result, a spherical wavefront becomes corrugated (Figure 3-8) and the ensuing diffraction produces phase and amplitude scintillations at some distant surface. Assuming that the correlation function of index of refraction fluctuations is Gaussian with scale length  $r_0$ , then the correlation length of phase fluctuations along the wavefront of a control\* beam at the transmitting antenna face will be given approximately by  $r'_0 = r_0 \times (Z_2/Z)$ , where  $Z_2$  is the distance to the location (or mean location) of the irregularities and  $Z$  is the distance to the satellite. It follows that only small scale lengths contribute to phase noise across the array. One expects that these small scale (50 meters and less) irregularities will be weak and therefore not produce a large phase shift.

The theory of phase and amplitude fluctuations due to propagation through ionospheric irregularities is developed in Appendix A. Temporal decorrelation occurs when density irregularities drift through a correlation length (see Appendix A-32 and A-33). A computer program has been written to compute phase and amplitude correlation functions at the transmitting antenna in terms of the power spectrum of the electron density fluctuations. In addition, the program determines the rms phase deviations and amplitude fades and the temporal correlation function for phase changes. Typical results are given in Figure 3-9 for a Gaussian model of the density correlation function and a frequency of 1 GHz. The rms phase fluctuation  $\phi_{rms}$  scales inversely with frequency.

A double Gaussian distribution provides a better fit (see Appendix A) to nonlinear self-induced density fluctuations<sup>(11)</sup>, assuming that a self-focusing plasma instability (Appendix B) causes irregularities at microwave frequencies that are similar to those observed during high power HF heating of the ionosphere. Results of this model are tabulated in Table 3-3).

---

\* Used in self-phasing adaptive phase control method.

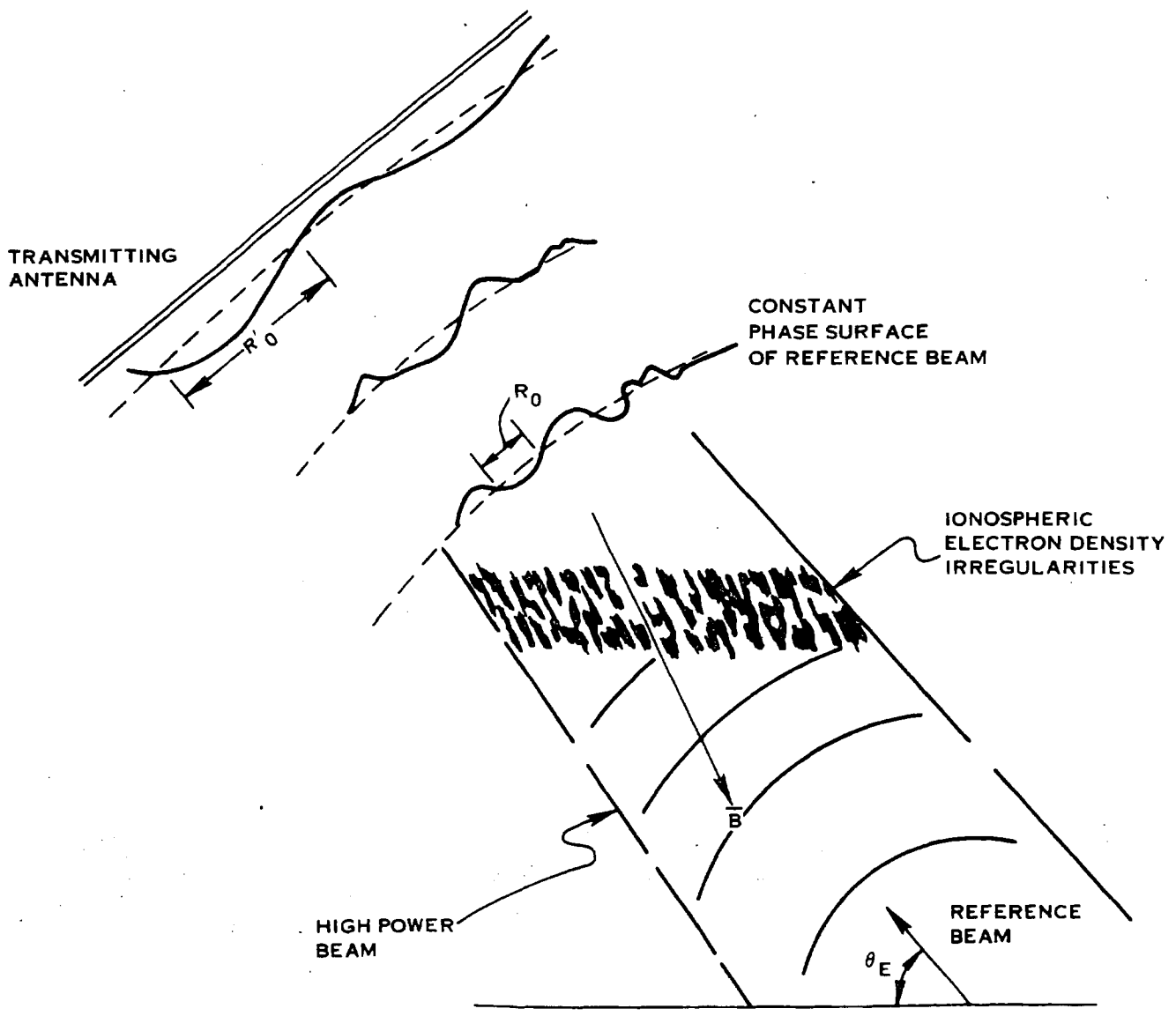
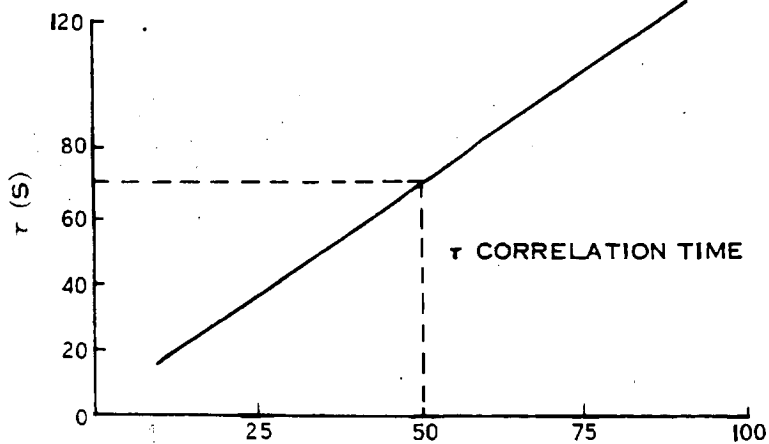
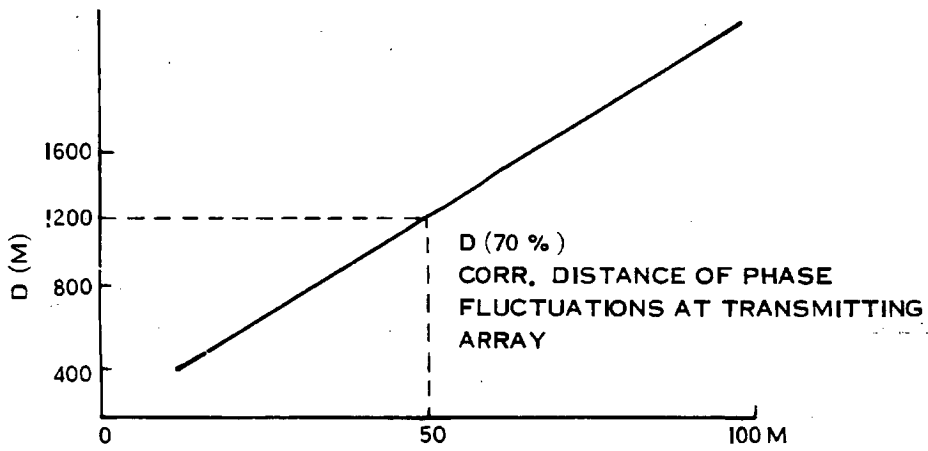
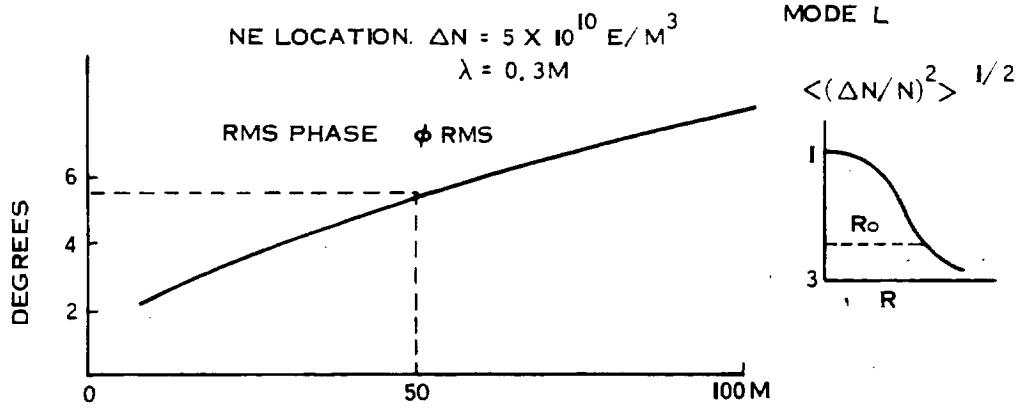


Figure 3-8. Phase Scintillations



$R_0$  CORR. LENGTH OF DENSITY FLUCTUATIONS (M)

Figure 3-9. Typical Gaussian Model Results of Density Correlation

TABLE 3-3

## SCINTILLATION CHARACTERISTICS AT 1 GHz DUE TO HIGH POWER INTERACTIONS

Location	$\phi$ rms	$(\Delta A/A)^2$	Correlation Coeff. Spatial Temporal	
			D(m)	$\tau$ (s)
NE (20°)	5.9	0.10	400	23
SW (50°)	6.6	0.11	900	23

The correlation scale size D is the distance at which the correlation drops to 70 percent.

Nonlinear induced density irregularities will be confined to some fraction of beamwidth; namely, those regions where the power density exceeds the instability threshold (see Appendix B). Because of the finite lateral extent of the unstable region only phase fluctuations with wavelengths  $\lambda_q$  greater than  $Z_o/D_r$  will contribute to the field of the reference beam at the transmitting antenna face (where  $Z_o$  is the distance to irregularity region or equivalent phase screen and  $D_r$  is the transverse dimension of the unstable region). For example, if  $D_r = 2$  km,  $\lambda = 0.15$  m and  $Z_o = 300$  km then

$$\lambda_q > 23 \text{ m} \quad (3-11)$$

These results can be summarized stating that ionospheric irregularities, self-induced or ambient, will cause phase fluctuations of less than 10 degrees across the wavefront of a reference beam propagated from the center of the ground antenna to the transmitting antenna face. The random phase variations (and amplitude fades) will decorrelate over lengths of a few hundred meters and in tens of seconds.

Propagation through the density fluctuations will cause some power beam spreading by diffraction. The increase in beamwidth is estimated by "paired-echo" theory applied to Fresnel diffraction of a wave-field modulated by a thin phase screen. At microwave frequencies the refractive index of the ionosphere is given by:

$$\mu = 1 - \frac{\lambda^2 r_e n_e}{2\pi} \quad (3-12)$$

Where  $r_e$  is the classical radius of the electron,  $2.818 \times 10^{-15}$  m, and  $n_e$  is the electron density. Phase fluctuations (in radians) along a path length  $\ell$  are given by:

$$\varphi = k_o \int_0^{\ell} \Delta\mu ds = -\lambda r_e \int_0^{\ell} \Delta n ds \quad (3-13)$$

A 1 percent fluctuation in total content along the propagation path causes a phase fluctuation of:

$$\varphi = -\lambda r_e 0.01 N_o \quad (3-14)$$

where  $N_o$  is the mean total content. For example if  $\lambda = 15$  cm and  $N_o = 10^{13}$  electron/cm<sup>2</sup>,  $\varphi = 0.42$  radians. Now consider a sinusoidal phase fluctuation with amplitude  $\varphi/2$  and wavelength  $\Omega$ . Let  $\mathbf{U}_i(x_1, y_1)$  be the field incident on the ionosphere. The coordinates  $x_1$  and  $y_1$  are in a plane perpendicular to the boresight direction. After propagating through the ionosphere the field distribution will take the form:

$$\mathbf{U}(x_1, y_1) = \mathbf{U}_i(x_1, y_1) \cdot t(x_1, y_1) \quad (3-15)$$

where  $t(x_1, y_1)$  is a phase modulation due to scattering (diffraction) by the density irregularities. A simple sinusoidal irregularity gives rise to a phase modulation

$$\begin{aligned} t(x_1, y_1) &= \exp [j \varphi/2 \sin (2\pi/\Omega x_1)] \\ &= \sum_{q=-\infty}^{\infty} j^q J_q(\varphi/2) \exp (j2\pi/\Omega q x_1) \end{aligned} \quad (3-16)$$

The latter Bessel function expansion is the Fourier series representation of the modulation.

Fresnel diffraction theory shows that the field at some distant plane  $(x_o, y_o)$  is given by:

$$\begin{aligned}
\dot{U}(x_0, y_0) &= \frac{\exp(jkz)}{j\lambda z} \exp\left[j\frac{k}{2z}(x_0^2 + y_0^2)\right] \\
&\cdot \iint_{-\infty}^{\infty} \left\{ (x_1, y_1) \exp\left[j\frac{k}{2z}(x_1^2 + y_1^2)\right] \right\} \\
&\cdot \sum_{q=-\infty}^{\infty} j^q J_q(\varphi/2) \exp\left[-jk(x_0/z - q\lambda/\Omega)x_1 - jk(y_0/z)y_1\right] dx_1 dy_1.
\end{aligned} \tag{3-17}$$

It can be seen by inspection, that the field at the  $(x_0, y_0)$  plane,  $z$  units away from the  $(x_1, y_1)$  plane, consists of the unperturbed field distribution reduced in amplitude by  $J_0(\varphi/2)$  plus an infinite sum of "paired echos" or replicas of the unperturbed field distribution laterally displaced by  $\pm |q|(\lambda/\Omega)z$ .

For a typical set of parameters,  $\lambda = 15$  cm,  $\varphi = 0.42$  radians, and  $z = 200$  km, the lowest order echo is displaced by:

$$d = \pm 0.15 \times 200/\Omega \tag{3-18}$$

with

$$\Omega = 0.2, 2 \text{ km,}$$

$$d = \pm 150 \text{ m, } 15 \text{ m,} \tag{3-19}$$

respectively. Thus to lowest order in  $\varphi$ , the intensity distribution is:

$$\begin{aligned}
U(x_0, y_0) U^*(x_0, y_0) &\approx J_0^2(\varphi/2) G^2(x_0, y_0) + J_1^2(\varphi/2) \\
&\cdot \left\{ G[(x_0 - d), y_0] + G[(x_0 + d), y_0] \right\}^2
\end{aligned} \tag{3-20}$$

where  $G(x_0, y_0)$  is the unperturbed field distribution on the  $(x_0, y_0)$  plane. If the  $G(x_0, y_0) = \exp[-\alpha(x_0^2 + y_0^2)]$ , which is the radiation field of an untruncated Gaussian aperture distribution, then the intensity distribution:

$$I(x_0, y_0) \equiv U U^* \approx \exp[-2\alpha(x_0^2 + y_0^2)] \cdot [J_0^2 + 4J_1^2 \cosh^2(2\alpha x_0 d)] \tag{3-21}$$

and for  $\alpha = (2 \text{ km})^{-2}$ ,  $d = 200$  m

$$I(1/\sqrt{\alpha}, y_0) = 1.15 G^2(x_0, y_0) \quad (3-22)$$

and

$$I(4/\sqrt{\alpha}, y_0) = 1.27 G^2 \quad (3-23)$$

These results suggest that power beam dispersion due to ionospheric density fluctuations, ambient or nonlinearly induced, will be such as to increase field intensity at the edges of the beam by 15 to 27 percent, which at the low nominal power densities does not contribute to significant loss.

### 3.4 IONOSPHERIC MODIFICATION BY HIGH POWER IRRADIATION

Ionospheric modification experiments conducted during the last three years at Platteville, Colorado and Arecibo, Puerto Rico have shown that relatively modest HF power fluxes can produce significant changes in the thermal energy of the plasma in the D ( $\approx 60$  to 90 km), E ( $\approx 90$  to 150 km) and F ( $\approx 150$  to 340 km) regions. <sup>(12)</sup> Moreover, one finds that incident power fluxes intense enough to modify the ionospheric energy balance through ohmic heating can also cause self-focusing instabilities which produce substantial field-aligned density perturbations and an overall F-layer electron density depletion of several percent. Results of recent D-region experiments also suggest, although not conclusively, that HF heating can reduce recombination and thereby increase the electron density during the day (see Appendix C).

One can attempt to estimate the effects of high power microwaves by noting that ohmic dissipation scales as the reciprocal of the square of the electromagnetic frequency. At radio wave frequencies (2 to 10 MHz), fluxes of 10 - 100  $\mu\text{W}/\text{m}^2$  at F-layer heights and 800 - 1600  $\mu\text{W}/\text{m}^2$  in the D and E regions produce significant changes. Therefore, one would expect that microwave ( $< 5.0$  GHz) power densities of 10 - 100  $\text{mW}/\text{cm}^2$  might produce similar effects. The direct effect on high power microwave transmission is likely to be small since the absorption at these frequencies remains negligible even if we expect an order of magnitude increase in electron temperature and density. However, power densities in excess of 100  $\text{mW}/\text{cm}^2$  could produce large horizontal electron density gradients that could cause significant beam displacement and dispersion.



Although only a small fraction of the beam power is absorbed, it is still significant compared to the natural thermal input into the ionosphere. A rough estimate of the degree of ionospheric modification can be obtained by comparing the electron heat content in the volume of ionospheric plasma where the bulk of the power is absorbed, about  $10^2 \text{ km}^2 \times 100 \text{ km}$ , to the energy dissipated in an electron-ion thermal time constant. Thermal equilibrium is reached in about 50 seconds. For a 5 GW system, 0.2 mW-sec are absorbed during this interval compared to a heat content of 1 mW-sec. For an incident flux of  $20 \text{ mW/cm}^2$ , the ratio of the ohmic loss to the natural input due to photoelectrons and heat conduction in typical ionospheres ranges from 10 to 40 in daytime and 40 to 160 at night. Thus, one expects significant changes in ionospheric properties as a result. These changes will probably be local and reversible but they nevertheless should be quantified, particularly with regard to sustained operations. Non-local disturbances could occur at high power densities through the generation of acoustic-gravity waves (low frequency sound waves whose behavior is influenced by the earth's gravitational force). Changes in the neutral composition are unlikely, although the ionic chemistry of the D layer could be altered by high power transmission.

It is expected that decimeter radiation with power densities in excess of  $20 \text{ mW/cm}^2$  will cause major changes in the properties of the plasma in the D, E and F regions of the ionosphere. A flux of  $100 \text{ mW/cm}^2$  could double the F region electron temperature and cause a 10 to 50 percent local reduction in the electron density. Microwave heating in the D region and the lower E layer will probably reduce the recombination rate and thereby lead to substantial increases in the plasma density (see Appendix C). For example, calculations of D-region heating (see Appendix C) show that a flux of  $70 \text{ mW/cm}^2$  will raise the ambient electron temperature tenfold. This will slow down the dissociative recombination rate by a factor of ten and therefore increase the D-region electron density by as much as 3-4 times the ambient value.<sup>(17)</sup>

### 3.5 FARADAY ROTATION EFFECTS

#### 3.5.1 INTRODUCTION

The total polarization twist  $\Omega$  of a linearly polarized wave is related to the total columnar electron content (TEC) of the ionosphere by the following equation:

$$\Omega = (K/f^2) \int B \cos \theta \sec \chi N dh \quad (3-24)$$

where

$$K = 2.36 \times 10^{-5}$$

f = frequency in Hertz

B = magnetic field strength in gammas

$\theta$  = propagation angle

$\chi$  = zenith angle

N = local electron density in  $\text{el}/\text{m}^3$

and the limits of the integral extend from the lower boundary of the ionosphere to the satellite height. The geometry is shown in Figure 3-10.

A useful engineering approximation is obtained by introducing a suitable average value  $\overline{M}$  for the factor  $B \cos \theta \sec \chi$ . Titheridge<sup>(14)</sup> has shown that accurate ( $\pm 5\%$ ) results can be obtained by evaluating the M factor at 420 km. This approximation holds under a wide range of model ionospheres and satellite locations. Thus the equation can be rewritten in a simplified form that permits direct scaling of  $\Omega$  with TEC:

$$\Omega = (K/f^2) \overline{M} (\text{TEC}) \quad (3-25)$$

Variations in  $\Omega$ , seasonal, diurnal, during a magnetic storm and as a result of solar activity, can all be inferred directly from the associated changes in electron content.

#### 3.5.2 DIURNAL AND SEASONAL CHANGES

Comprehensive, synoptic observations of midlatitude electron content have been compiled from Faraday rotation measurements made by Hawkins and Klobuchar<sup>(15)</sup> at the AFCRL station at Sagamore Hill, Massachusetts,  $70^\circ .82\text{W}$ ,  $42^\circ .63\text{N}$ . The data were collected over a 6 year span from 1967 to 1973 by monitoring the received polarization of 136 MHz cw signals from the geostationary

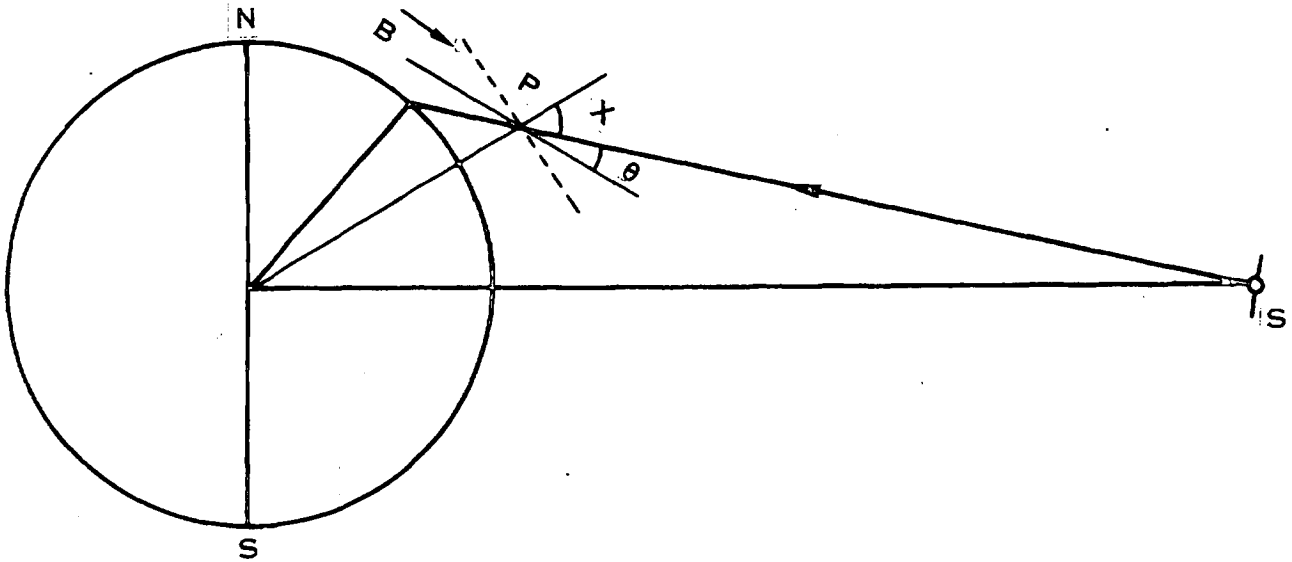


Figure 3-10. Path of a Straight Line Ray from a Geostationary Satellite to a Midlatitude Receiving Site

satellite ATS-3. Throughout the period of observation the elevation angle was close to 41 degrees.

The daily variation of solar radiation gives rise to a typical variation in TEC which changes slowly with month and season. However, under geomagnetically disturbed conditions marked departure can occur from the usual diurnal change. The Faraday rotation at a midlatitude rectenna site under quiet conditions will also follow the same cyclical pattern as the TEC. Estimates of  $\rho$  and the polarization "loss", based on mean monthly diurnal TEC measurements, are shown in Figure 3-11 for a typical Northeast ( $40^{\circ}\text{N}$ ) location. The polarization loss  $\eta_p$  occurs if the rectenna dipoles (Section 9) are not aligned with the incident direction of the electric field. It is computed by assuming that the cross-polarized component is totally reflected or scattered by the rectenna structure. It is clear that Faraday rotation under geomagnetically quiet conditions produces insignificant polarization losses.

### 3.5.3 MIDLATITUDE GEOMAGNETIC STORMS

AFCL has also compiled an atlas of TEC variations during geomagnetically disturbed periods.<sup>(16)</sup> A particularly severe storm has been selected to estimate the maximum polarization loss under disturbed conditions. As the result of a magnetic storm on 8 March 1970 a sudden enhancement of 66 percent above the

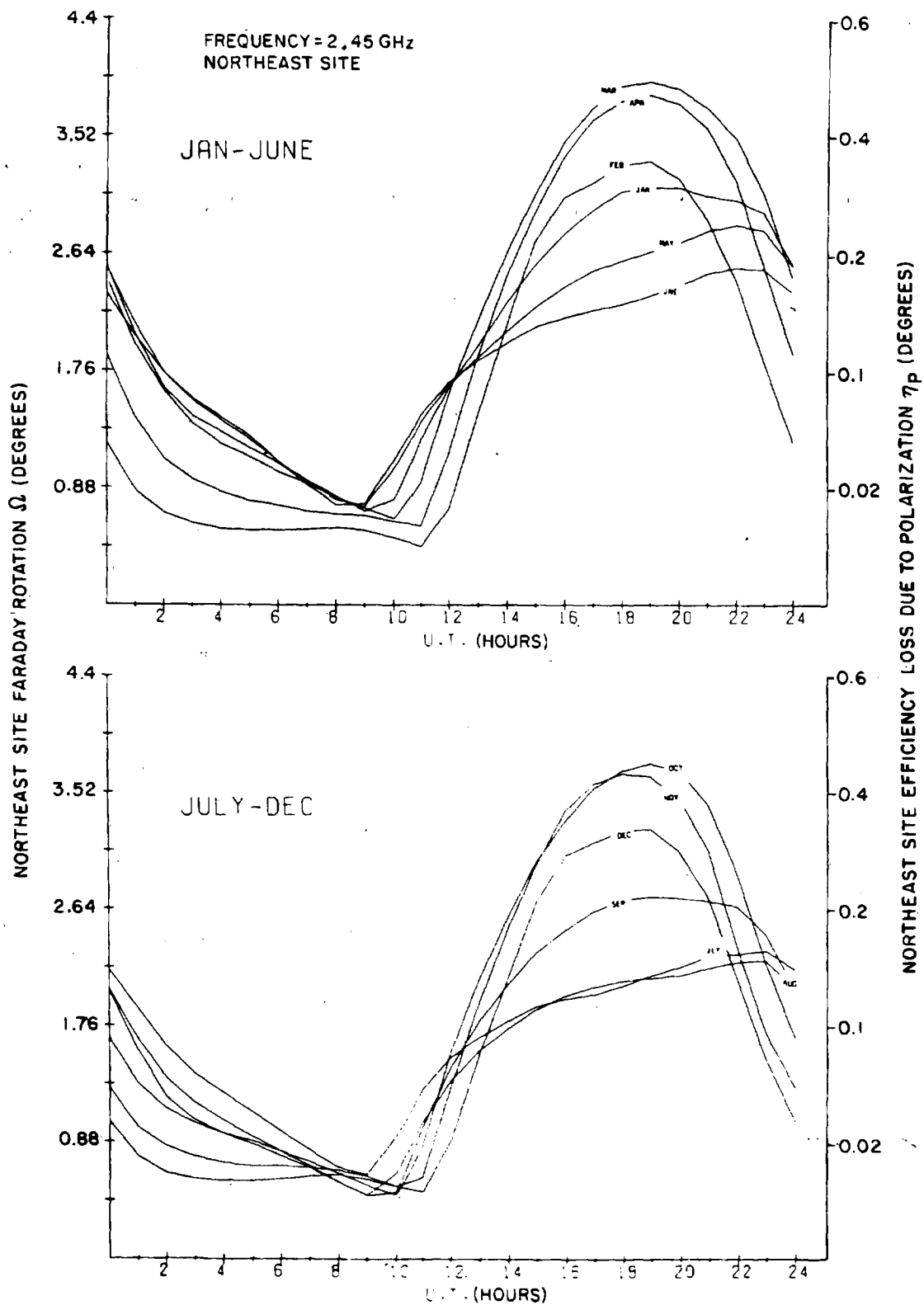


Figure 3-11. Diurnal and Seasonal Variation in Faraday Rotation  $\Omega$  and Polarization Mismatch "Loss"  $\eta_p$

preceding 7 day mean TEC was observed at Hamilton, Massachusetts (42.6°N, 70.8°W). The variation in TEC during the storm (proportional to  $\rho$ ) and the subsequent response of the ionosphere is shown in Figure 3-12. The maximum TEC was  $8.47 \times 10^{17}$  el/m<sup>2</sup>. The corresponding predicted Faraday rotation and polarization loss for the Northeast and Southwest sites are as follows:

Latitude	Site	$\rho$ (degrees)	Loss for Linearly Polarized Rectenna $\eta_p$ (percent)
40°	Northeast	9.3	3.0
30°	Southwest	7.4	1.7

If the receiving antenna is aligned to compensate for the mean rotation under quiet conditions then an inspection of the TEC records in the AFCRL storm atlas shows a 1 percent loss could be expected 3 times a year.

### 3.6 CONCLUSIONS AND RECOMMENDATIONS

For the atmosphere at frequencies below 3 GHz:

- a. Absorption and scattering effects are small except for wet hail.
- b. Refraction changes and gradients cause negligible displacement or dispersion of the high power beam, and do not significantly degrade a ground based pilot phase front as seen at the orbital power transmitting antenna.

For the ionosphere at frequencies above 1 GHz:

- a. Refraction changes and gradients cause negligible displacement or dispersion of the high power beam, and do not significantly degrade a ground based pilot phase front as seen at the transmitting antenna.
- b. Absorption and scattering effects are negligible.
- c. Faraday rotation has only a small effect for a linearly polarized receiving antenna.
- d. Changes in electron density caused by power densities of 20 mW/cm<sup>2</sup> and above at 2.45 GHz need to be investigated for possible effects on other ionosphere users.
- e. Possibility of noise and harmonic radiation (radio frequency interference effects) should be investigated.

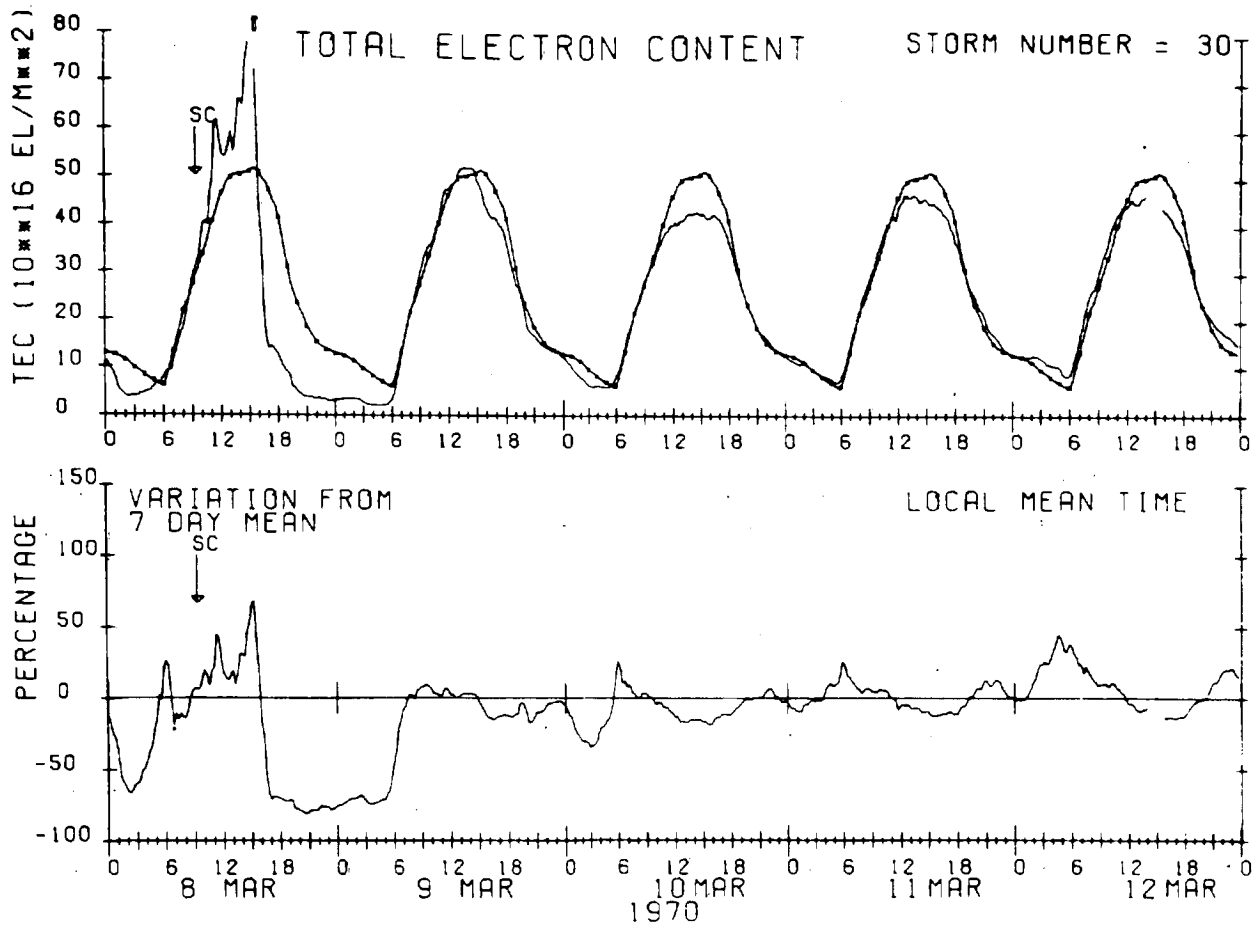


Figure 3-12. Variation in Total Electron Content during a Magnetic Storm (from AFCRL-TR-74-0065, 6 February 1974)

### REFERENCES (SECTION 3)

- (1) Van Vleck, J. H., and Weisskopf, V. F., Rev. Mod. Phys. 17:227 (1945).
- (2) Crane, R. K., Proc. IEEE 59:173 (1971).
- (3) Falcone, V. J., J. Microwave Power 5:270 (1970).
- (4) Battan, L. J., Radar Observation of the Atmosphere, University of Chicago Press, 1973.
- (5) Proceedings of the IUCRM Colloquium on the Fine Scale Structure of Precipitation and EM Propagation, Nice, 23-31 October 1973.
- (6) Schell, A. C., R. K. Crane, R. J. Donaldson, R. M. Dyer and R. A. Lawheren, AFCRL Special Report, No. 141, 15 June 1972.
- (7) Marshall, J. S. and Palmer, W. M. K., J. Meteor 5:165-66 (1948).
- (8) Falcone, V. J., unpublished computations, 1974.
- (9) Atlas, D., J. of Meteor. 10:486 (1953).
- (10) Goubau, G., J. of Microwave Power 5:224 (1970).
- (11) Bowhill, S. A., E. E. Mendenhall and D. R. Ward, Experiments and Models in Prairie Smoke, RADC-TR-73-210 (April 1973).
- (12) Radio Science Vol. 9, Special Issue on Ionospheric Modification (Nov. 1974).
- (13) L. H. Holway, Jr., and G. Meltz, Response of Gravity Waves to Slowly-Varying Ionospheric Heating (Technical Memo), 1973.
- (14) J. E. Titheridge, Planet. Space Sci., 20, pp. 353-369.
- (15) G. S. Hawkins and J. A. Klobuchar, Seasonal and Diurnal Variations in the Total Electron Content of the Ionosphere at Invariant Latitude 45 Degrees, AFCRL-TR-74-0294, June 1974.
- (16) M. Mendillo and J. A. Klobuchar, An Atlas of the Midlatitude F-Region Response to Geomagnetic Storms, AFCRL-TR-74-0065, February 1974.
- (17) M. T. Lev, M. A. Biondi, and R. Johnson, Measurements of the Recombination of Electrons with  $H_3O^+ \cdot (H_2O)_n$ - Series Ions, Phys. Rev. A, 7, pp. 292-298 (1973).

## SECTION 4

### DC-RF CONVERSION

#### 4.0 INTRODUCTION

The primary candidates for dc to rf conversion are the amplatron and klystron. They are each separately examined for the MPTS application in Sections 4.1 and 4.2 respectively. System level considerations for them both are examined in Section 4.3 while conclusions and recommendations for both are given in Section 4.4.

#### 4.1 AMPLITRON

The baseline design is a 5 kW, radiation-cooled amplatron operating at 2450 MHz at 85 percent efficiency. Characteristics at other operating frequencies and power levels are also determined. The amplatron is a backward wave, crossed field amplifier (CFA). Reference 1 provides a survey of CFA concepts and state of the art. This discussion covers only the special aspects of the MPTS application.

A basic consideration in the design of the continuous wave (cw) amplatron for the satellite power station system is high reliability and long life. Cathode life is a major limitation for most electron tubes. In the cw amplatron, the long life requirement is met by designing it with a pure metal, secondary emitting platinum cathode. Platinum makes a nearly ideal cathode for amplitrons. It is a noble metal with very low vapor pressure and no inherent wearout mechanism. It has demonstrated good life under very high power operating conditions.

The rf circuit of the amplatron consists of only 17 sections which are relatively large and rugged. The structure is solidly supported by the shell of the tube and is connected by a short thermal path to the pyrolytic graphite radiator. Heat associated with losses in the amplatron is radiated into space through the cooling fins.

The amplatron is particularly desirable for space applications because of its high efficiency. Efficiencies between 80 and 90 percent have been obtained at S-band. Lightweight magnetic circuits can be used to obtain these high efficiencies by means of samarium-cobalt magnet material.



High efficiency is very desirable for the satellite power station system design. It not only reduces the amount of dc power which must be provided but also reduces the problems associated with dissipation of the waste heat. Increasing tube efficiency from 60 to 90 percent reduces the amount of heat that must be dissipated from the tube by a factor of  $6/1$ . It also reduces the dc power required by a factor of  $1/3$ . The high efficiency of the cw amplatron enables the tube to be cooled by conduction and radiation only.

A factor which makes the cw amplatron desirable for high reliability applications is the relative simplicity of the structure required. Figure 4-1 shows the complete tube assembly. Other features such as cooling radiators, input and output rf connections, and magnetic circuit are included. A control system is also shown which enables variation of the static magnetic field which is imposed on the tube. The power input to the amplatron will be controlled by changing the value of the magnetic field. In the amplatron, the major portion of the power which is not converted to rf appears as heat when electrons strike the surface of the anode. A smaller amount of power is dissipated at the cathode surface. Some cathode back-bombarding electrons are useful because they provide the mechanism for the release of secondary electrons.

As shown in Figure 4-2, for an efficiency of 85 percent and an average power added of 5 kW, the input power will be 5747 watts. About 3.5 percent of the power (199 watts) will be dissipated in the cathode as electron bombardment, and most of the rest (548 watts) will be dissipated in the anode. However, the vanes are not bombarded equally. The vanes near the output receive about 1.5 times the average power. The average temperature drop across the vanes is only  $64^{\circ}\text{C}$  and probably  $94^{\circ}\text{C}$  near the output. The temperature drop across the cathode is about  $75^{\circ}\text{C}$ .

#### 4.1.1 RF CIRCUIT

The  $I^2R$  losses for the rf structure including vanes and straps were calculated using a temperature of  $400^{\circ}\text{C}$ . The calculations for an operating amplatron utilize equations where the current is injected into each vane and power builds up along the network. Actual operating circuit losses are low because the bulk of the

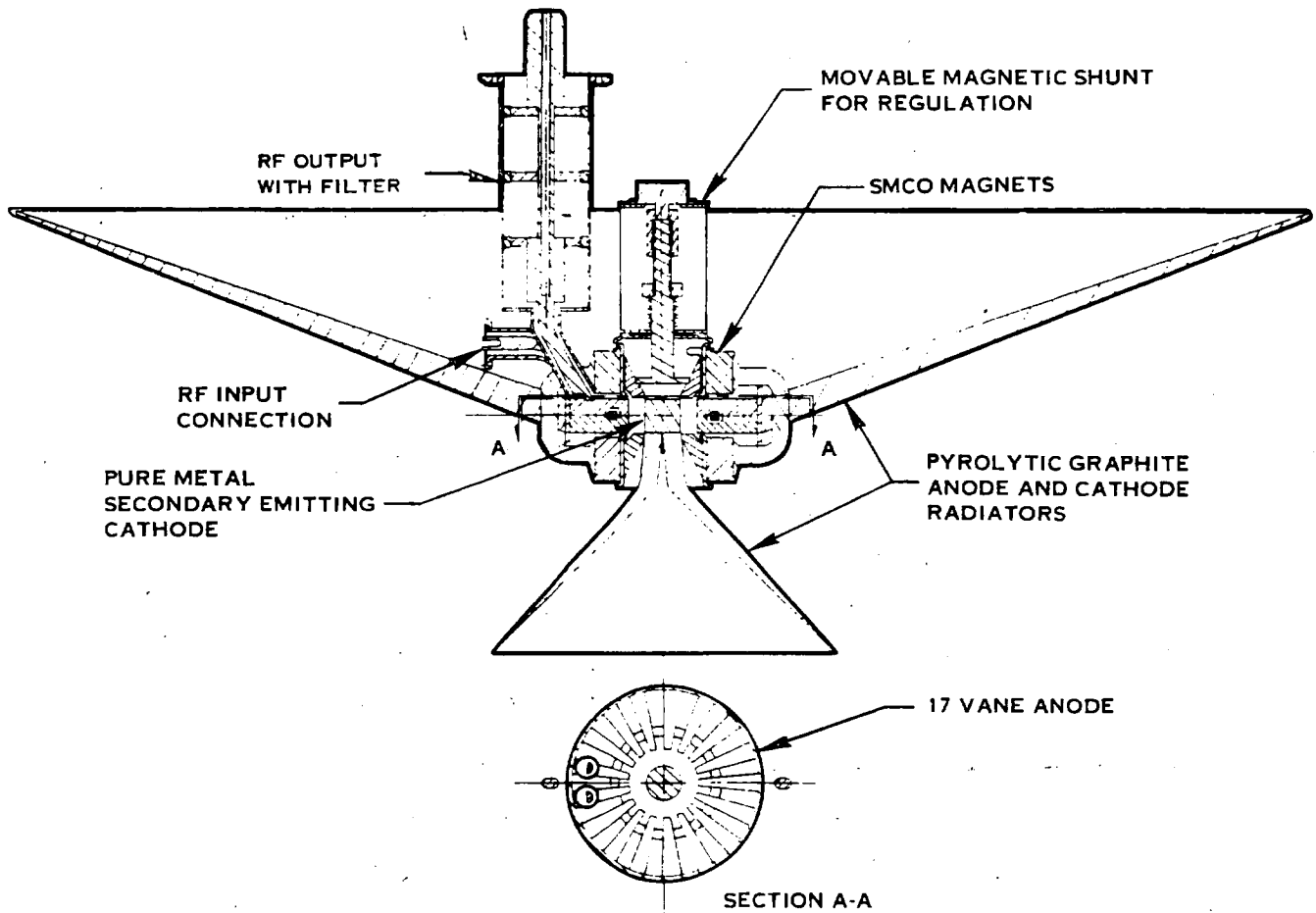


Figure 4-1. Amplitron Assembly

ANODE	108 GRAMS	RF POWER ADDED	5000 WATTS
ANODE RADIATOR	1000	ANODE ELECTRON BOMBARDMENT	371
CATHODE	9	ANODE CIRCUIT LOSSES	177
CATHODE RADIATOR	71	CATHODE DISSIPATION	199
MAGNET	260	DC INPUT POWER	5747 WATTS
POLES	100	GROSS EFFICIENCY	87%
INPUT AND OUTPUT	40	OUTPUT FILTER DISSIPATION	125 WATTS
MOTOR AND DRIVE	30	NET EFFICIENCY	85%
	1618 GRAMS - 3.56 LB		
SPECIFIC WEIGHT	0.33 g/w		
SPECIFIC COST	0.018 \$/w		

Figure 4-2. 5 kW Amplitron Parameters

ORIGINAL PAGE IS  
OF POOR QUALITY

power generated is near the output of the device. The circuit losses were determined to be 2.7 percent when operating with an rf gain of 7 dB and generating 5000 watts of power output.

The slow-wave network in the MPTS amplatron is similar to that used in other Raytheon amplitrons and circuit losses of approximately 3 percent have been measured in hot test. The QK1224 amplatron, for example, utilized a similar circuit in which all the components were water cooled, and the power dissipated in the various tube components were measured. When operating QK1224 model #8 at the 425 kW level the useful rf power output and various dissipated powers were proportioned as follows:

RF power added	375 kW	72.1%
Anode dissipation	105 kW	20.2%
Cathode dissipation	25 kW	4.8%
Anode circuit losses	<u>15 kW</u>	<u>2.9%</u>
	520 kW	100.0%

The circuit losses can be related to mechanical as well as electrical properties of the slow-wave structure. Special fabrication techniques are required to produce circuits with high circuit efficiency. These techniques must suppress multipactor.

#### 4.1.2 PYROLYTIC GRAPHITE RADIATOR

Radiating fins of pyrolytic graphite heat fins are made as tapered cones, so during heating and cooling cycles they can bend slightly without setting up undue stresses.

#### 4.1.3 MAGNETIC CIRCUIT

A Raytheon computer program was used to design a Sm-Co magnetic circuit for the amplatron at a frequency of 2450 MHz. The design of the magnetic circuit is important in achieving a lightweight tube.

Radially-gaussed samarium-cobalt magnets are to be used on the amplatron. This magnetic circuit develops the required 2940 gauss in the interaction region with 167 grams of Sm-Co magnet. A pole piece is employed for field shaping, and a steel flux return path is used.

#### 4.1.4 CONTROLLING THE OUTPUT OF AMPLITRONS

In the MPTS application, a large number of microwave generators must receive their dc power input from a common bus, and their microwave power output and electrical phases must be held closely to preset levels so that the subsections of the transmitting antenna which they feed are properly excited. It is necessary, therefore, to insert some form of regulation in each microwave generator.

The output power and phase of the amplatron are determined by the applied dc voltage and by the value of the magnetic field which is imposed on the tube. Two approaches are discussed to control by magnetic means.

The first concept is to use a movable pole piece which enables variations of the static magnetic field imposed on the tube. It is shown in Figure 4-1. The value of the magnetic field will be changed in this approach by changing the gap between the magnet poles. Figure 4-3 shows the current and voltage of the amplatron for various magnetic field levels. The pole gap can be controlled by a dc brushless motor driving a recirculating ball, differential screw. DC brushless motors have been proven satisfactory in space applications. Ball bearings are necessary for high vacuum use where no lubrication is available. The rotating anodes used in Raytheon's X-ray tubes use vacuum ball bearing supports which have been life tested to 10,000 hours at 3000 rpm without failure. In the MPTS application, the revolutions will be lower and the motor would be used infrequently, which may create stiction problems which should be investigated in the technology development program. The dc brushless motor will be used to adjust the pole gap as a vernier control only. The main force of the magnetic pull will be counter-balanced with a spring. The motor will weigh about 30 grams and will use only one watt of power. It can supply a force of 35 pounds and change the gauss level by over 20 percent in about one second. With the motor power off, the permanent magnet rotor will lock onto one set of stator poles to prevent any movement of the pole.

#### 4.1.5 WEIGHT

The majority of the weight is in three components: (a) the pyrolytic graphite heat radiators, (b) the magnetic circuit, and (c) the anode. A breakdown is given in Figure 4-2.

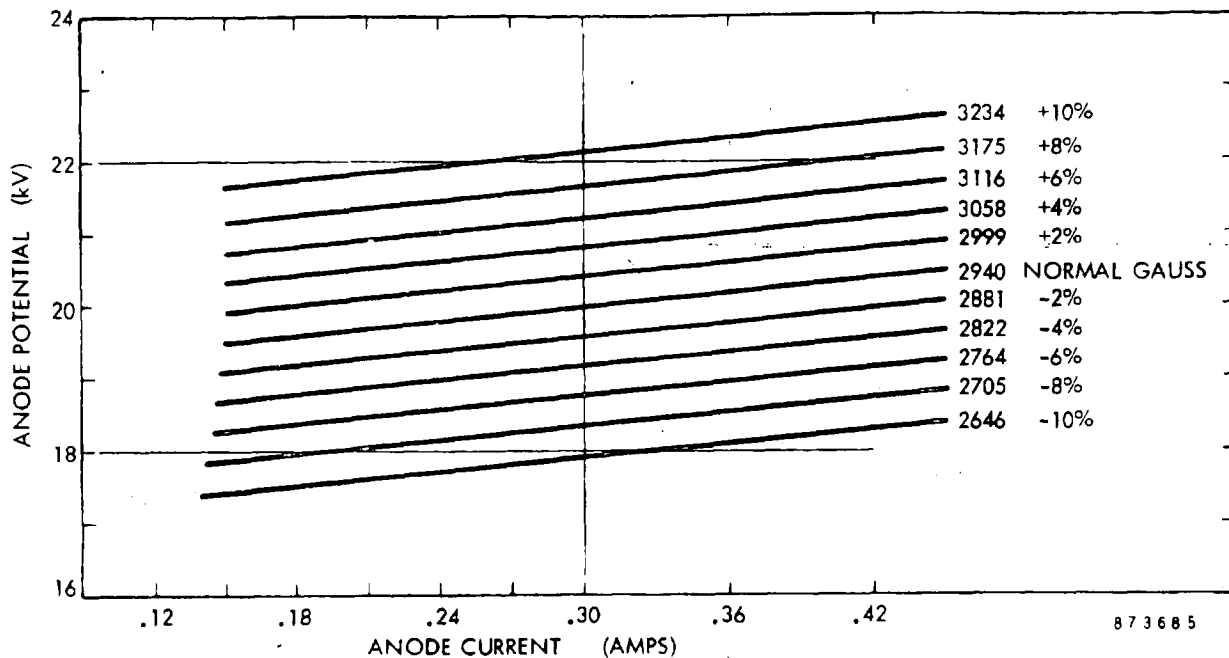


Figure 4-3. Amplitron Current and Voltage Levels for Various Magnetic Field Levels

a. The pyrolytic graphite radiators are the heaviest part of the tube. However, the density of pyrolytic graphite is only one fourth that of copper and its thermal conductivity is about twice as high as that of copper. Heat pipes, able to withstand the pressure involved and filled with a working fluid, are heavier than pyrolytic graphite. A radiating surface of course would still be required. Over one half of the weight, 1000 grams, is in the anode pyrolytic graphite radiator and another 71 grams are in the cathode radiator.

b. The radially gaussed Sm-Co magnetic circuit makes a very efficient design. It presents a wide surface area and short depth of magnetic material to make efficient use of the very high coercive force of Sm-Co. It also has a short return path to conserve pole weight and reduce leakage flux. The nearly 3000 gauss is obtained with only 260 grams of Sm-Co and 100 grams of pole material. An energy product of  $15 \times 10^6$  gauss-oersted was used in the design.

c. The anode is made of solid copper. This is needed to conduct the heat from the vane face out to the pyrolytic graphite heat radiator. In the baseline design, the anode weighs 108 grams.

The RF input and output and the output filter will be made of thin-wall material and should weigh about 40 grams total. The dc brushless motor and the differential screw weigh 30 grams. The cathode only weighs 9 grams. The extra hardware involved, mounting flange, spring, etc., bring the total tube weight up to 1618 grams.

#### 4.1.6 COST

A tube cost of \$91 for the baseline design has been estimated using many inputs. The raw materials are based on 1975 prices. Parts fabrication and assembly are based on actual costs of large production quantities of the similarly constructed microwave oven magnetron. The estimated cost of the amplatron is about twice the current cost of the magnetron. The production rate of the amplatron will be many times higher than that of the magnetron, so this estimate is conservative.

The pyrolytic graphite cost figure of \$25 for the baseline design was arrived at in a discussion with personnel at Raytheon's Research Division who operated Raytheon's pyrolytic graphite facility. It includes the use of semiautomated equipment and the use of a carbon fiber mandrel. Their experience was with very expensive machined graphite mandrels and non-automated equipment. For high-volume production, this figure should be conservative.

Thermal bonding of the pyrolytic graphite radiators to the anode and cathode will be one of the major subjects of the technology development program.

#### 4.1.7 NOISE AND HARMONICS

In the MPTS the generated noise outside a guard band (background noise) is of concern along with the harmonics of the main signal.

Measurements and observations have shown that background noise in crossed-field devices is caused partially by oscillations in the space charge in the region immediately surrounding the cathode. In the MPTS the gain requirement for the amplatron is only five. This small gain along with a proper interaction space design and a cold cathode should result in a well controlled space charge to reduce the background noise. Another factor that effects space-charge instabilities is the magnetic field. A recently developed Raytheon computer program provides a more desirable magnetic field shape to improve space-charge control.

Experiments have shown that there is a relationship between noise output and tube gas pressure. Lowering the pressure of the tubes has produced noticeable changes in the noise levels. At the present, the vacuums utilized are not much better than  $10^{-8}$  torr. The improved vacuum of space might reduce the overall spurious noise output.

Since the application is narrowband, the background noise bandwidth may be reduced by narrowing the passband of the tube. A bandpass filter may also be used to suppress the background noise.

Bandpass filters have been attached to the output of magnetrons to reduce the harmonic output. The information obtained on noise reduction will be described because the magnetron is similar to the amplatron and utilizes the same means of converting dc into microwave power. The measurements of the noise generated by the magnetron with a cold cathode are therefore similar to those which will be obtained from the amplatron. The noise measurements to be described are on a pulsed tube with a hot cathode, and it would be expected that the noise characteristics of a cw tube, such as the type to be used in the MPTS, would be better than those of a pulsed tube.

The standard production model RK6344 magnetron has a second harmonic power output typically about 50 dB below the main signal power level. The third harmonic is approximately 45 dB down. The background noise is 80 to 90 dB below the main signal level as measured over a 3 MHz band. This signal-to-noise ratio is therefore 85 to 95 dB/MHz.

A waffle-iron waveguide filter was attached to the output of an RK6344 magnetron. With the filter on the output of the tube, the second harmonic was 90 dB below the carrier level, which represented a reduction of 40 dB as compared with the standard tube. The third harmonic level was 80 dB below the carrier, indicating a reduction of 35 dB.

From the background noise measurements of the RK6344 magnetron, it is concluded that the cw amplatron to be used for the MPTS would have a signal-to-noise ratio of 85 dB/MHz. For this single frequency application, filters may be coupled to the tube. The output signal of the amplatron, therefore, would pass through a filter before reaching the tube's waveguide output system. This will

offer advantages which could greatly reduce the harmonic amplitude along with the bandwidth of the background noise. Details of amplatron filter design and performance are covered in a later section. The cold cathode for the amplatron should result in yet lower noise generation.

Low noise and harmonics will be a major objective of the technology development program.

#### 4.1.8 PARAMETERS VERSUS FREQUENCY

The baseline design of a 5 kW power gain amplatron operating with high efficiency at 2450 MHz was frequency scaled to four other frequency levels from 1.0 to 6.0 GHz. The designs were then current scaled to give the estimated optimum power at each frequency. The main criterion was maximum power for the least overall system weight and cost. For scaling, the maximum temperature drop across the vane was held constant at 95°C (at 6.0 GHz, 125°C was allowed).

The parametric design was not carried above 6 GHz. The previous section on propagation has shown that rain attenuation makes the range above 6 GHz of little interest from a system point of view, and in addition:

- a. In a crossed-field device, the rf currents are on the microwave circuit so that the  $I^2R$  losses increase with frequency.
- b. The structure size varies inversely with frequency, so the tube gets very small at X-band and above. For the same current density, therefore, output power per unit decreases.
- c. The small size of the tube would increase the cooling problem. Above approximately 6 GHz, the cathode would require some auxiliary liquid or vapor cooling.
- d. As the size decreases, the voltage gradients increase, and this increases the chance for arcing.

The power levels investigated for each frequency are shown in Figure 4-4. This is the power added per tube. All have a 7 dB gain and will operate at 20 kV.

The specific weight and cost are shown in Figure 4-5. From these curves, it is seen that the range from 1.5 to 2.5 GHz should yield the least overall tube weight and cost. Radiator size and weight data are shown in Figures 4-6 and 4-7.



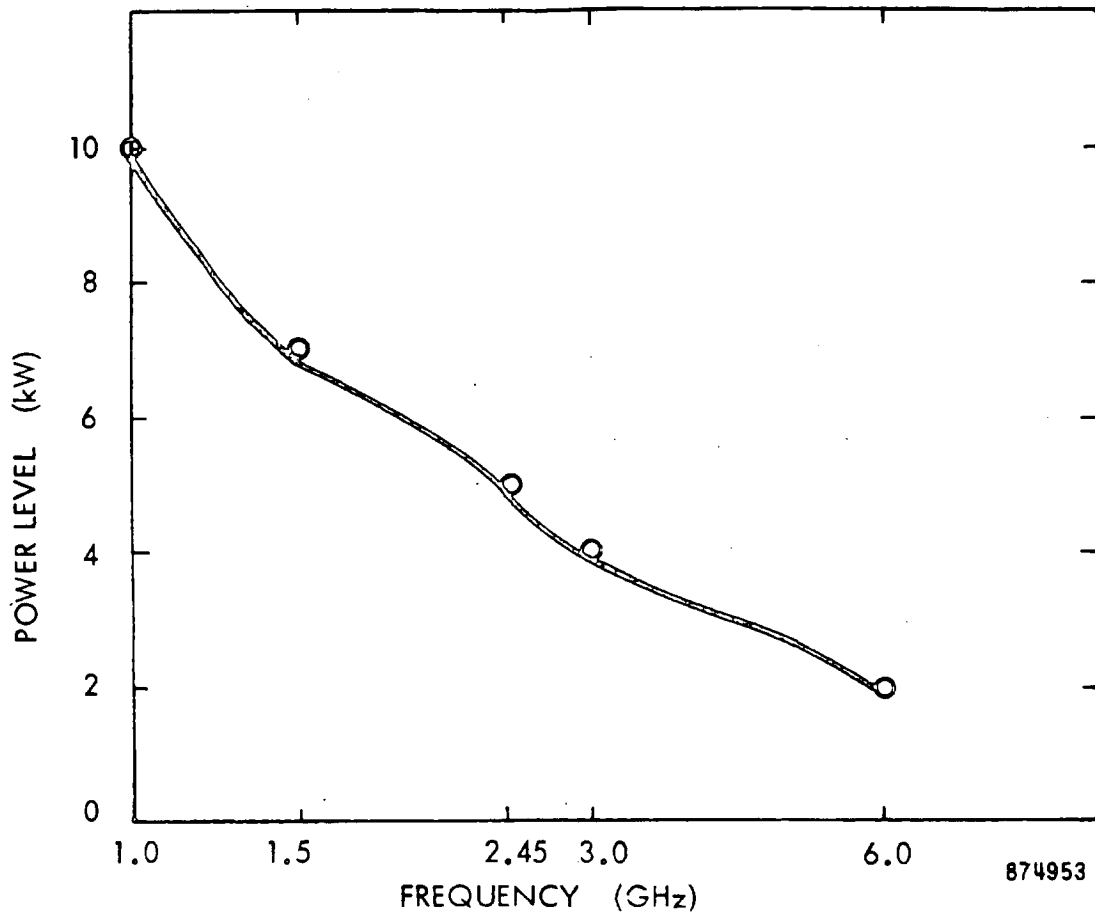


Figure 4-4. Power Level versus Frequency

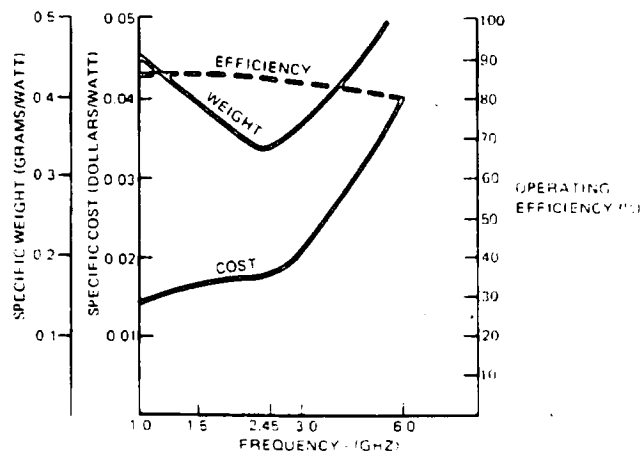


Figure 4-5. Amplitron Weight/Cost/Efficiency versus Frequency

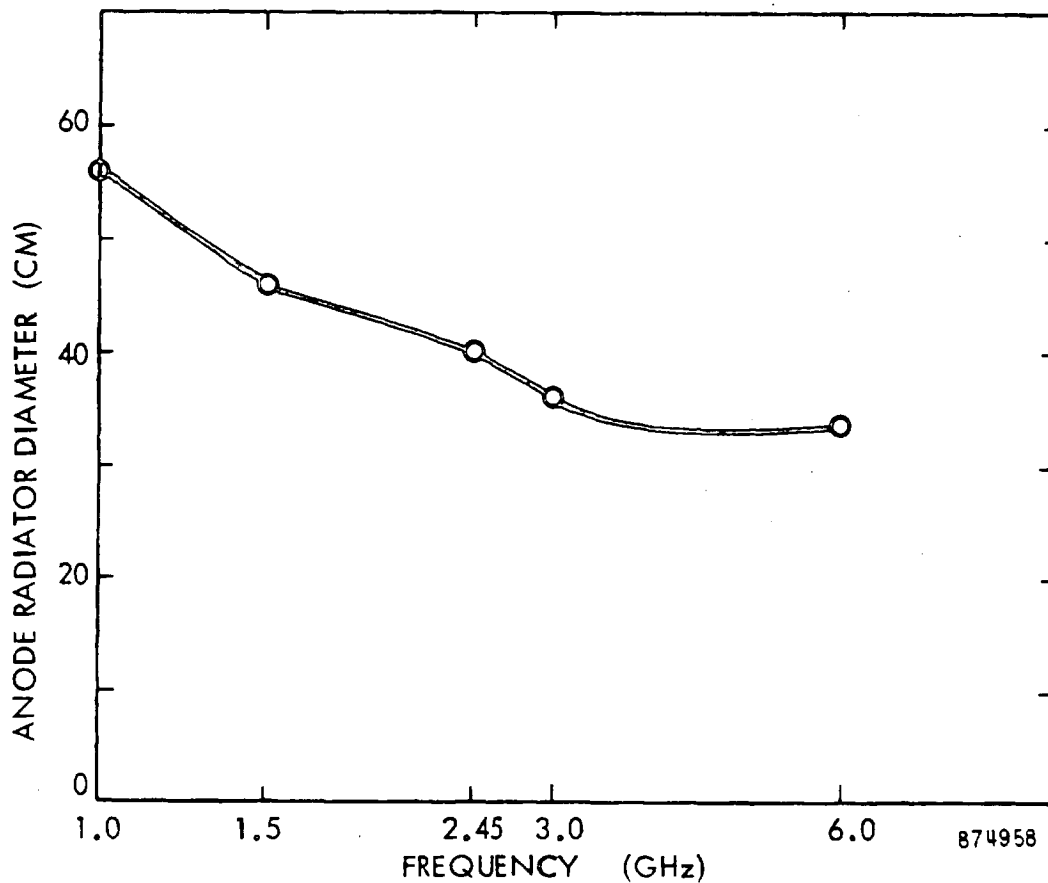


Figure 4-6. Anode Radiator Diameter versus Frequency

In the frequency range of 1.5 to 2.5 GHz, the radiator diameter is 40-46 cm and the weight varies from 600 to 1000 grams. This was later changed to 48 cm and 1000 grams at 2.45 GHz based on system studies described in Section 6. The large variation in radiator weight is due to larger power generation at the lower frequency. The radiator size is important because it limits the packing density of the tubes near the center of the array.

Other tube parameters that vary with frequency such as size, magnetic field intensity, operating current, dissipated power density, and temperature drop across the vanes, are shown in Figures 4-8 through 4-12.

Since high efficiency is of prime importance, tubes operating at the lower frequencies are more desirable. However, below 2.5 GHz the larger tube dimensions increase the specific weight. At the higher frequencies, the magnetic field intensity becomes quite high. Therefore, the information obtained from these figures further shows that 1.5 to 2.5 GHz is a desirable frequency range.

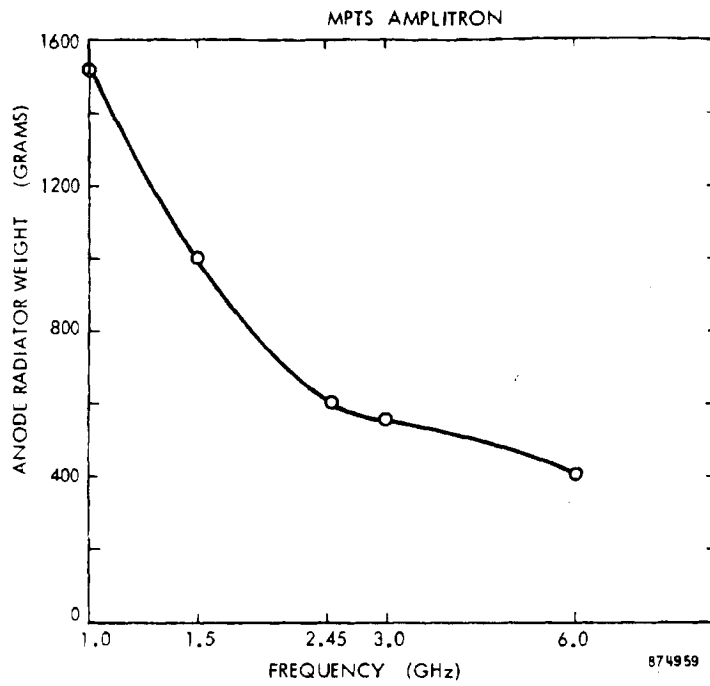


Figure 4-7. Anode Radiator Weight versus Frequency

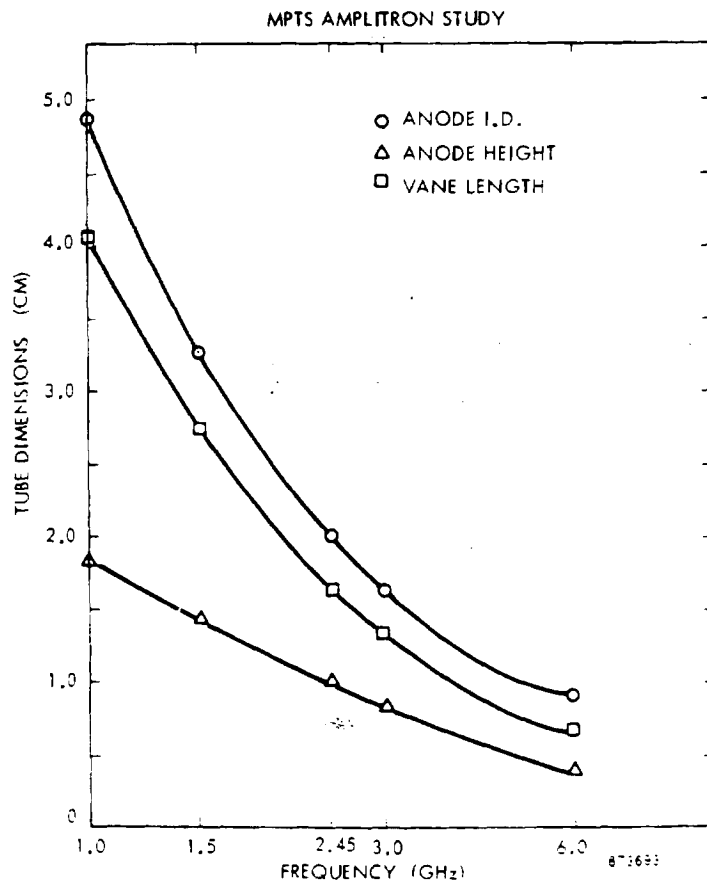


Figure 4-8. Tube Dimensions versus Frequency

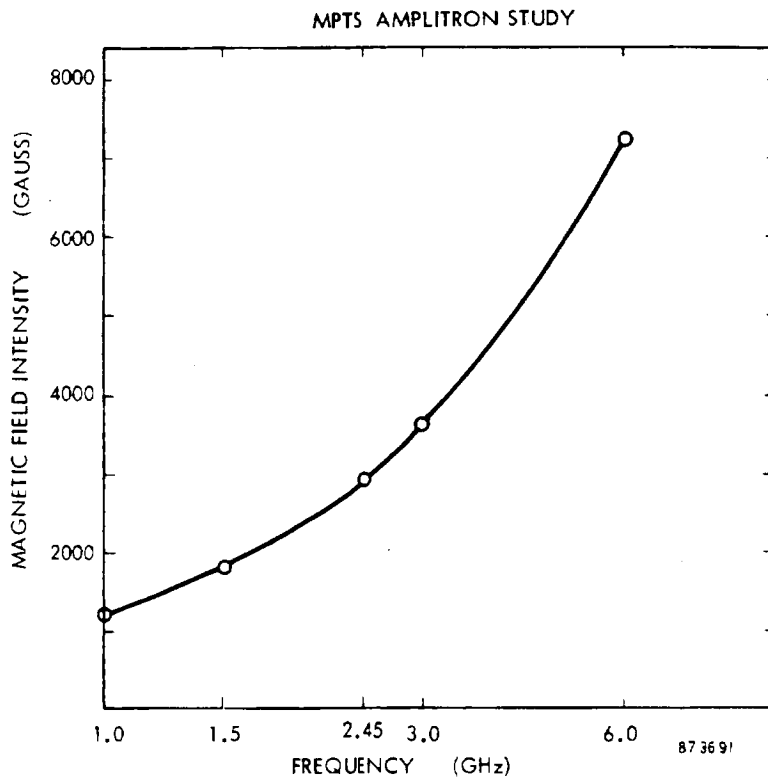


Figure 4-9. Magnetic Field Intensity versus Frequency

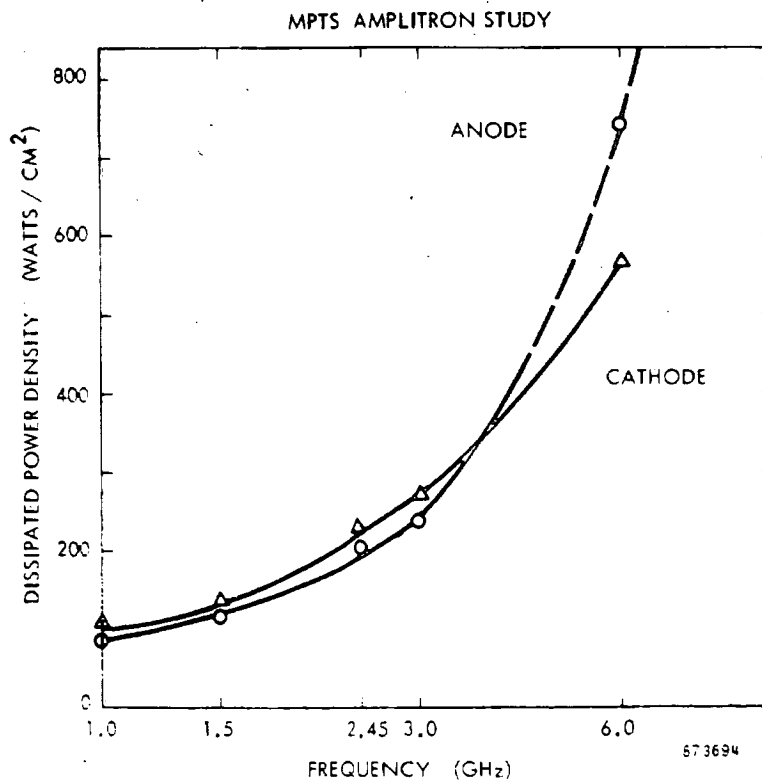


Figure 4-10. Dissipated Power Density versus Frequency

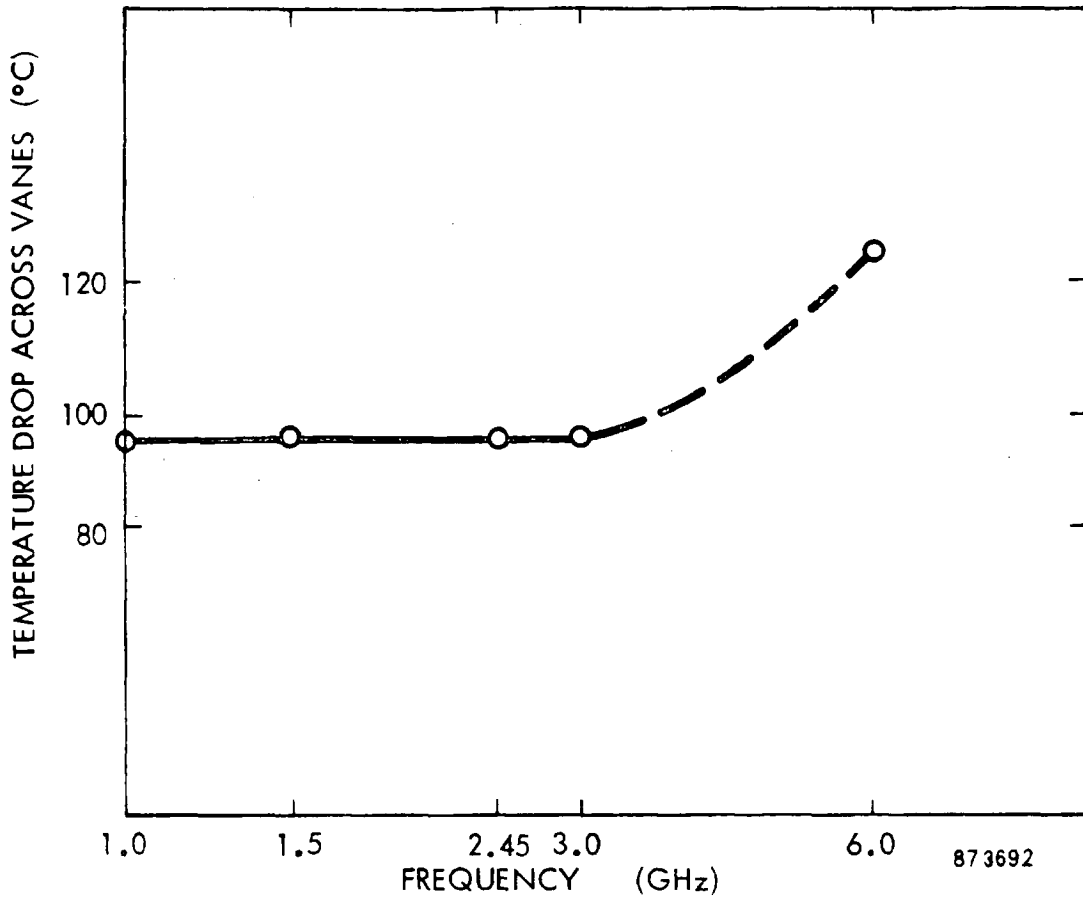


Figure 4-11. Temperature Drop Across Vanes versus Frequency

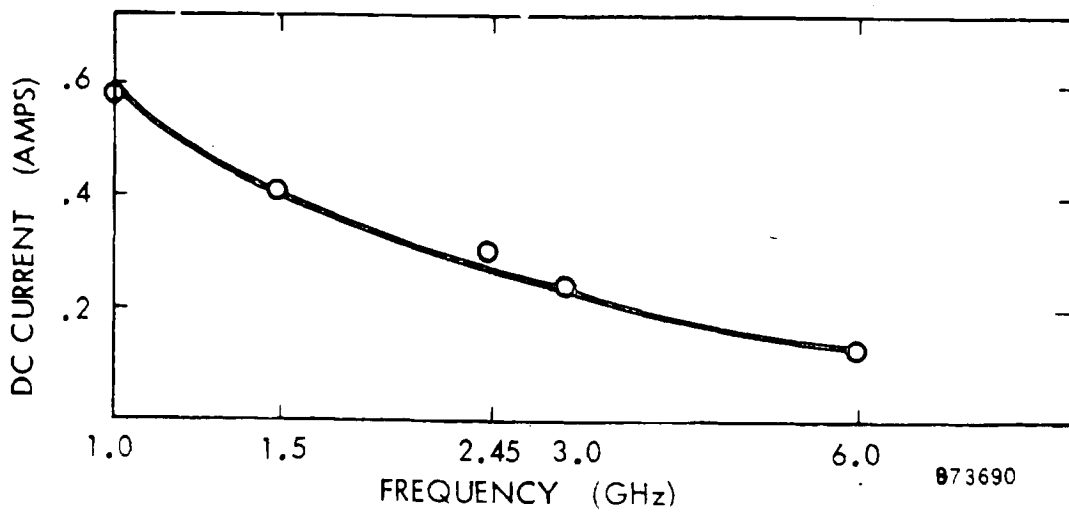


Figure 4-12. DC Current versus Frequency

#### 4.1.9 PARAMETERS VERSUS POWER LEVEL

The 2.45 GHz tube including the passive thermal radiator was scaled to power levels from 2 to 20 kW. The optimum power appears to be in the 5 to 10 kW region. The summary data are shown in Figure 4-13.

Higher power levels could be obtained only with a great increase in specific weight or by the use of liquid cooling. The high temperature of operation, 300°C or higher, rules out the use of normal coolant such as water or oil. Liquid mercury could be considered, but it is heavy and undesirable for a long life tube.

Heat pipes are another alternative for cooling. They have an extraordinarily high thermal conductivity, but they are limited in maximum power density to only a few tens of watts per square centimeter, and would use liquid metals which would reduce the reliability of the system by risk of leakage and widespread arcing.

Discussion of the two basic contributors to specific weight and cost is important to understand why the near minima occur as shown.

a. The core elements (cathode, anode, vanes, and magnets) weight and cost are functions of size which in turn is a function of wavelength. For a fixed wavelength or frequency = 2.45 GHz the weight and cost of the core elements are essentially established so that specific weight and cost would increase as power level decreases.

b. The thermal control system weight and cost, for a fixed core size, increases non-linearly with increasing power to be dissipated.

The sum of these two contributors results in minimum specific weight and cost occurring as shown in Figure 4-13.

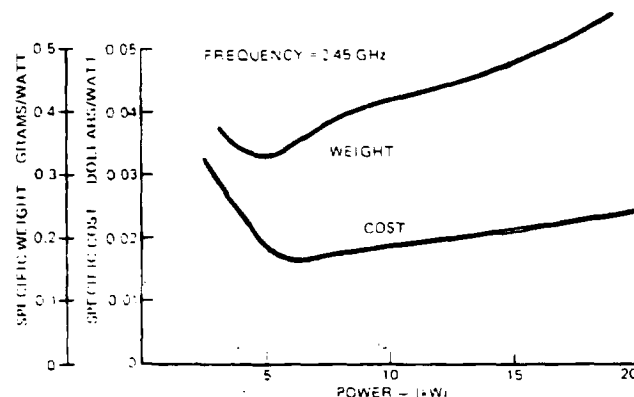


Figure 4-13. Amplitron Weight and Cost versus Power

## 4.2 KLYSTRON

The study of the klystron, a linear beam device, for the MPTS application was conducted by Shared Applications, Inc., of Ann Arbor, Michigan under sub-contract. Raytheon provided assistance in thermal analysis, magnetic design, weight and cost estimating as well as overall technical direction. In addition, the suggestions of Dr. Henry Kosmahl of Lewis Research Center were important factors in maximizing klystron capabilities for MPTS.

The preliminary analysis indicated klystron designs could be implemented over ranges of 1-30 GHz and power to 150 kW with heat pipe cooling, and with powers to 10 kW with passive cooling. This resulted in initial design efforts centering on low power to achieve the simplicity of passive cooling. However, further study showed heat pipes would be needed at all powers, and design effort then was applied to higher power versions to reach maximum efficiency. Detailed design was undertaken at the nominal 2.45 GHz frequency.

Included in the study is a comparison of periodic permanent magnet (PPM) and solenoid, or electromagnetically (EM) focused klystrons. Simulations by computer have been used to determine the power capability and the efficiency of the PPM tube. Heat dissipation limits the power of both PPM and EM focused tubes, and heat-pipe cooling will be necessary for the body; indeed existing tubes are cooled by water or forced air when generating kilowatts of average power. The EM klystron is the clear choice for output power levels of 16 kW or more. It has higher efficiency, and at least three times the power output of the PPM tube for the same degree of body heating. Furthermore, the weight and cost per kilowatt generated fall appreciably with increasing power per tube. A nominal maximum of 43 kW initially was selected for the analysis, and this later was set at 48 kW, but the ultimate limit will depend on the extent of developments in heat-pipe technology.

Previous research, published by the General Electric Company<sup>(2)</sup> and by Varian Associates<sup>(3)</sup>, has been directed at obtaining 7.5 kW or less of continuous-wave output power per tube.

The competing amplifron is recommended at 5 kW per tube. Thus, on the order of 1.3 million such tubes would be needed for a 5 GW system. The high-power klystron provides an alternative system requiring, for example, only

160,000 40 kW tubes or 32,000 200 kW tubes. It would be a significant technological advance to successfully apply tubes of these power levels in space.

#### 4.2.1 PERIODIC PERMANENT MAGNETIC FOCUSING

The focusing system for the electron beam constitutes a major portion of the weight of an electron tube; for low power space applications periodic permanent magnets give a distinct saving in comparison with either a single permanent magnet or a solenoid. Samarium cobalt magnets are particularly attractive,<sup>(4)</sup> requiring much less magnetic material for a given focusing field. PPM focusing has been used in satellite traveling-wave tubes of up to 125 kW peak pulsed and 10 kW average output power at S-band,<sup>(5)</sup> as well as in an X-band broadband klystron.<sup>(4,6)</sup> This study evaluates the klystrons' capabilities in more detail.

For calculation of the efficiency and the cooling requirements a nominal beam power of 10 kW is chosen. The magnetic period must be as small as the magnetic material can supply in order to focus the beam sufficiently well, but must be at least twice the length of one klystron cavity to allow space for pole pieces around the cavities. Accordingly a magnet period of one-half the free space wavelength corresponds to quarter-wavelength cavities. According to preliminary computations on the spreading of ideal electron beam bunches, a beam perveance as low as  $10^{-7}$  is necessary to reduce the radial space-charge forces sufficiently for good transmission. The outline design is described in paragraph 4.2.4 and the tube layout is illustrated in Figure 4-28(a).

Under low-level modulation the focusing and stability of the beam may be described analytically,<sup>(7,8)</sup> but a large signal computer model is necessary to predict beam interception and efficiency under saturated rf drive. A program developed by Shared Applications, Inc., uses the "deformable-disc model"<sup>(8,9)</sup> in which sixteen or more electron "discs" per period are followed in phase through the bunching cavities. The calculation is relativistically accurate and treats the rippling, spreading and interception of the beam under large-signal rf conditions. The plotted trajectories (Figures 4-17 to 4-19) show the results. In Figure 4-17 the three drift lengths contain respectively three, three, and two magnetic focusing periods. As the beam forms bunches it expands radially (Figure 4-18), and as a result 1.3 percent (130 watts) of the beam power is computed to be intercepted in



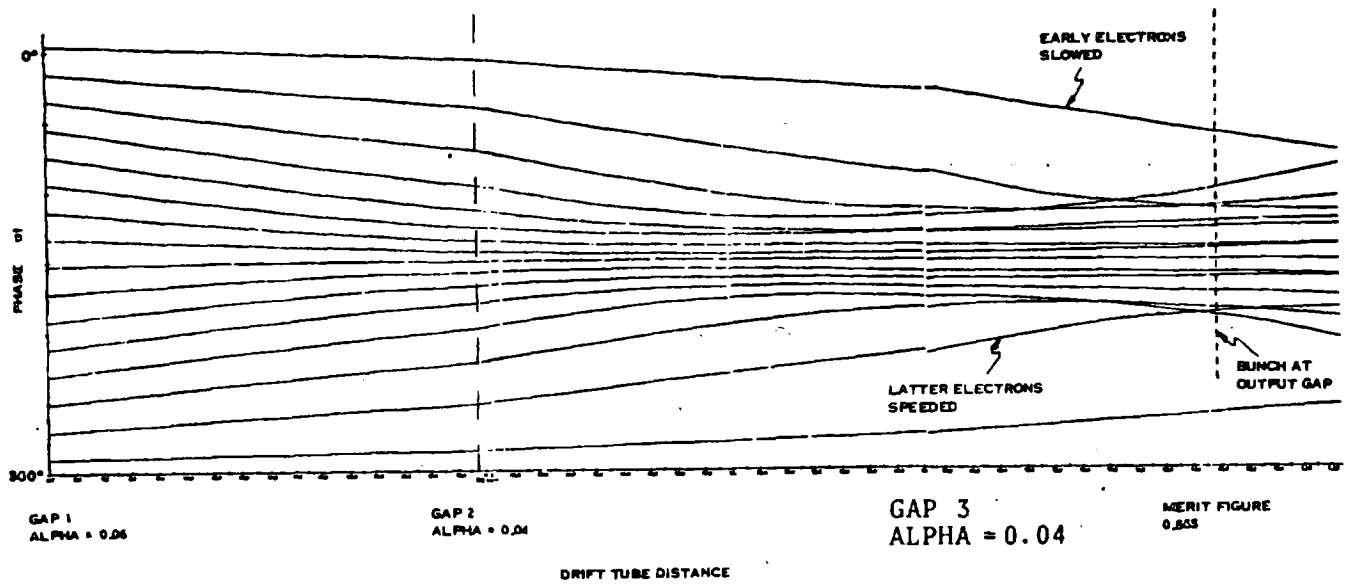
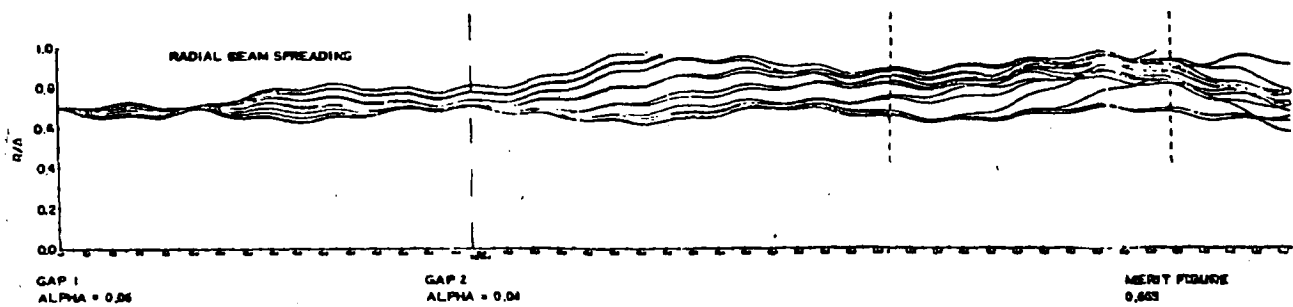


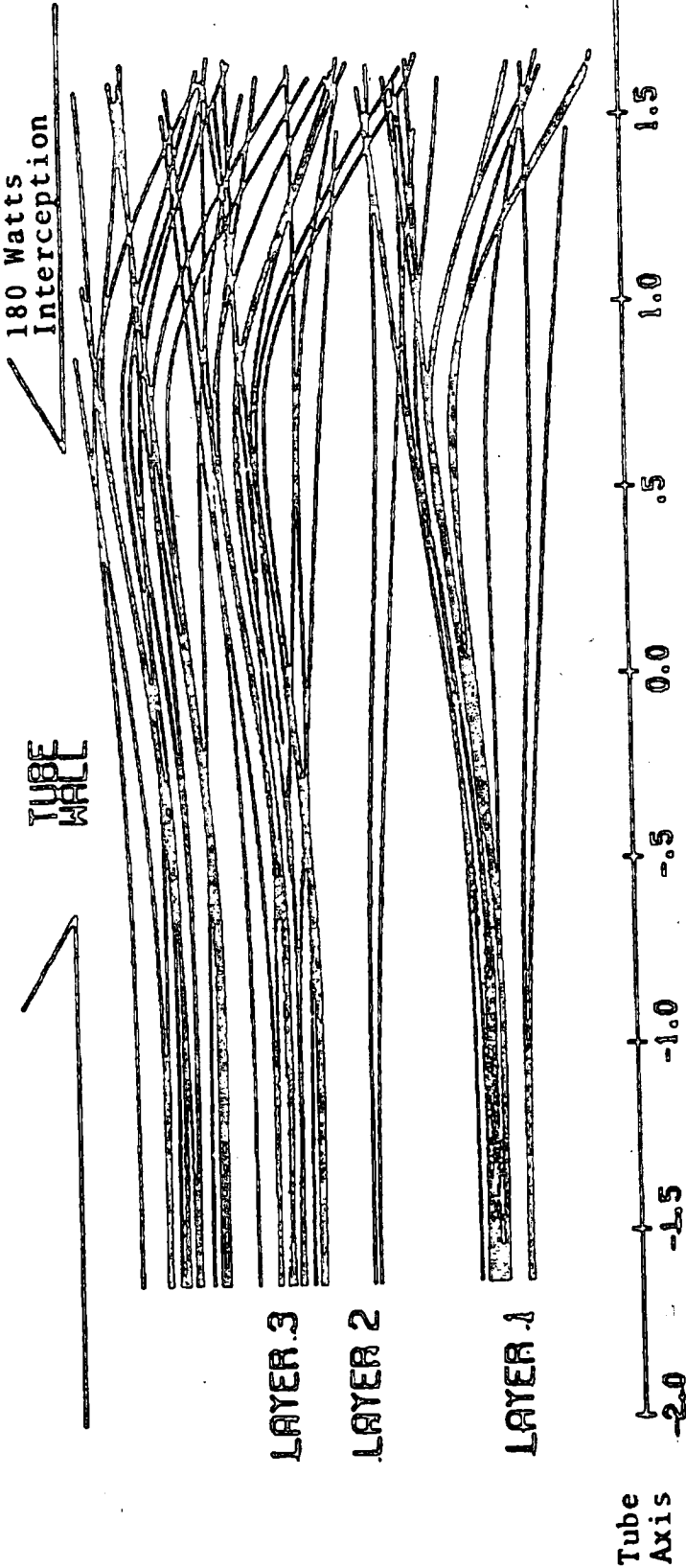
Figure 4-17. Klystron Bunching with PPM Focusing



Electronic Efficiency	64%	Net Efficiency		Beam Power	10 kW
Transmission Efficiency	97%	Undepressed	55%	Microperveance	0.1
Circuit Efficiency	87%	Maximum Depressed		Output Power	5.5 kW
		Collector Efficiency	74%		

Figure 4-18. Radial Beam Spreading with PPM Focusing

10 kW Beam Power



DISTANCE/TUBE RADIUS  
ELECTRONIC EFFICIENCY 64 PERCENT

Figure 4-19. Klystron Output Gap with PPM Focusing

the second drift tunnel. In the output gap (Figure 4-19) each disc is divided into three radial ring layers, and the realistic nonuniform cavity fields are used to calculate the motion and the induced circuit current. The resulting electronic efficiency is 64 percent; power of 180 watts is lost through collisions with the exit tunnel tip. This interception occurs mainly during the accelerating half-cycle, and the average energy of the lost electrons is about  $0.45 eV_0$ , where  $V_0 = 25$  kV for the main beam. Here the amplitude of rf beam current is only 1.37 times the beam current  $I_0$ . In a confined-flow beam increases of the rf gap voltages could yield up to  $1.8 I_0$ . However, the PPM tube shows increasing interception as the gap voltage is raised. The bunching of Figure 4-20, for example, gives 4 percent interception, even though the magnet period has been reduced from 0.5 to 0.4 times the free-space wavelength by shortening the cavities.

Collector depression can recover some of the power (about 33 percent of the total) remaining in the spent beam. The energies are computed for the beam elements following the output-gap interaction of Figure 4-19 and are used in a graphical analysis. The sixteen elements in Figure 4-21 cover one period, and the shaded area represents the recovered power, which is about 70 percent of that entering the collector. The net dc to rf conversion efficiency using a four-stage collector is then:

$$\frac{\text{rf power to output cavity}}{(\text{input beam power}) - (\text{power recovered at collector})}, \text{ i. e.,}$$

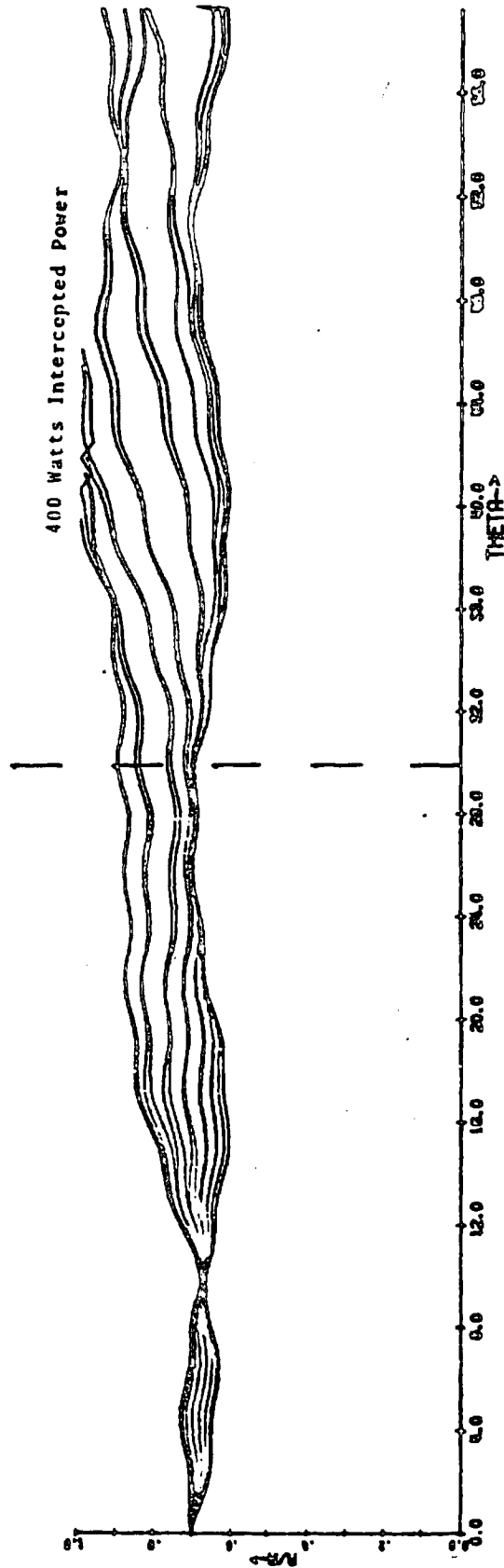
$$\frac{0.64}{1 - 0.33 \times 0.7} \text{ or 83 percent}$$

The klystron power summary of Figure 4-22 shows that approximately 12 percent of the rf power is dissipated as heat in the output cavity, so that the net efficiency is 71.9 percent; in comparison, a confined-flow tube should yield 70.7 percent efficiency without collector depression.

#### 4.2.2 CIRCUIT EFFICIENCY

The design of a cooling system for the tube body is largely determined by the quantity of heat dissipated in the walls of the output cavity. The circuit efficiency, defined as:

$$1 - \frac{\text{heat dissipated in output cavity}}{\text{total RF power delivered to output cavity}}$$



GRF 1  
RUP10-03

GRF 2  
RUP10-04

Figure 4-20. Klystron Bunching with PPM Focusing, Shorter Magnet Period and Increased Voltage at Gap 1

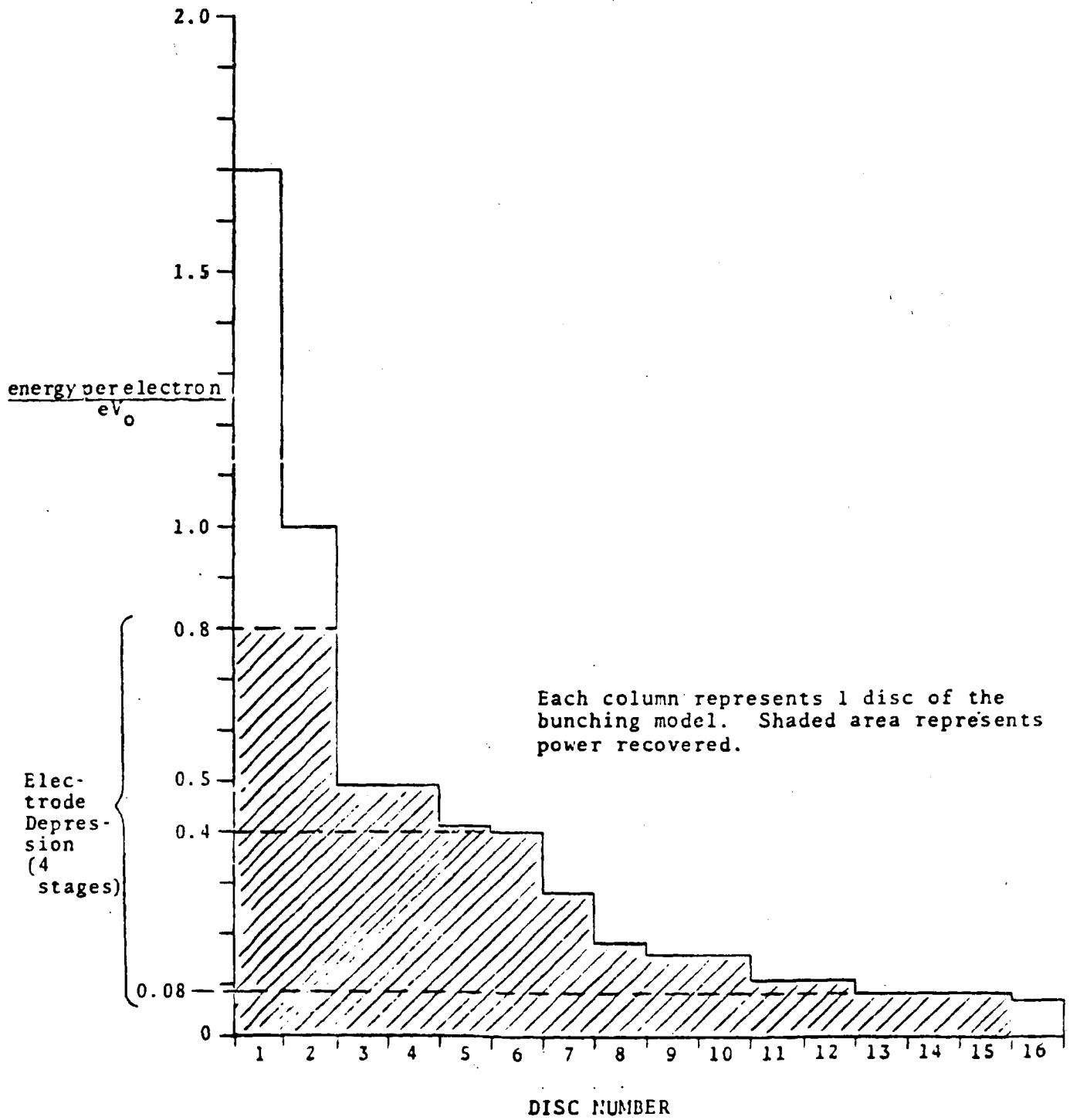


Figure 4-21. Graphical Analysis of the Collector Depression

	PPM	PPM with Collector Depression	High-Power Confined Flow (with Solenoid)
Output Power	5574	5574	43180 (assuming 75% electronic efficiency and no collector depression)
Output Cavity Losses:			
Skin Losses	826	826	1820
Interception	180	180	600
Interception in Drift Tunnel	130	130	600
Buncher Cavity Skin Losses	5	5	120
Collector Dissipation	3285	978.5	13680
Total Beam Power	10000	7693.5	60000
Heater Power	60	60	60
Solenoid Power	---	---	100
Total Input	10060	7753.5	61060
Net Efficiency	55.4%	71.9%	70.7%

Figure 4-22. Klystron Power Summary (Watts)

and calculated in Appendix F, is typically 0.97 or larger in a high-power water-cooled tube. It is highest when the electronic efficiency, beam power, beam perveance and the cavity parameters  $R/Q$  and  $Q_u$  are all large.  $Q_u$  is proportional to the square root of the electrical conductivity of the copper walls<sup>(10)</sup> and hence falls with increasing cavity temperature. Since a passively cooled tube requires a heat radiator of area and weight proportional to (temperature)<sup>-4</sup>, the body temperature must be as high as mechanical rigidity and magnetic focusing permit; 300°C is about the maximum.

Calculated circuit efficiencies and  $Q_u$  values are shown in Figures 4-23 and 4-24 for both PPM- and EM- (solenoid) focused tubes. Accounting for losses in the iris output coupling, at 20°C a  $Q_u$  of about 6115 is realistic at 2.45 GHz.

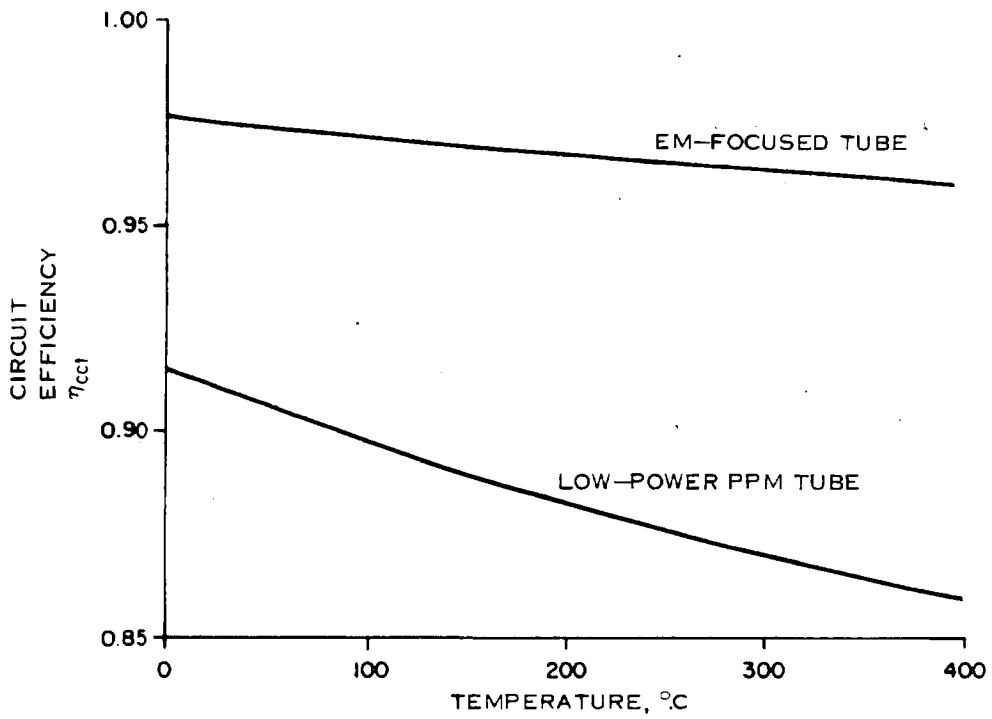


Figure 4-23. Effect of Temperature on Output-Circuit Efficiency

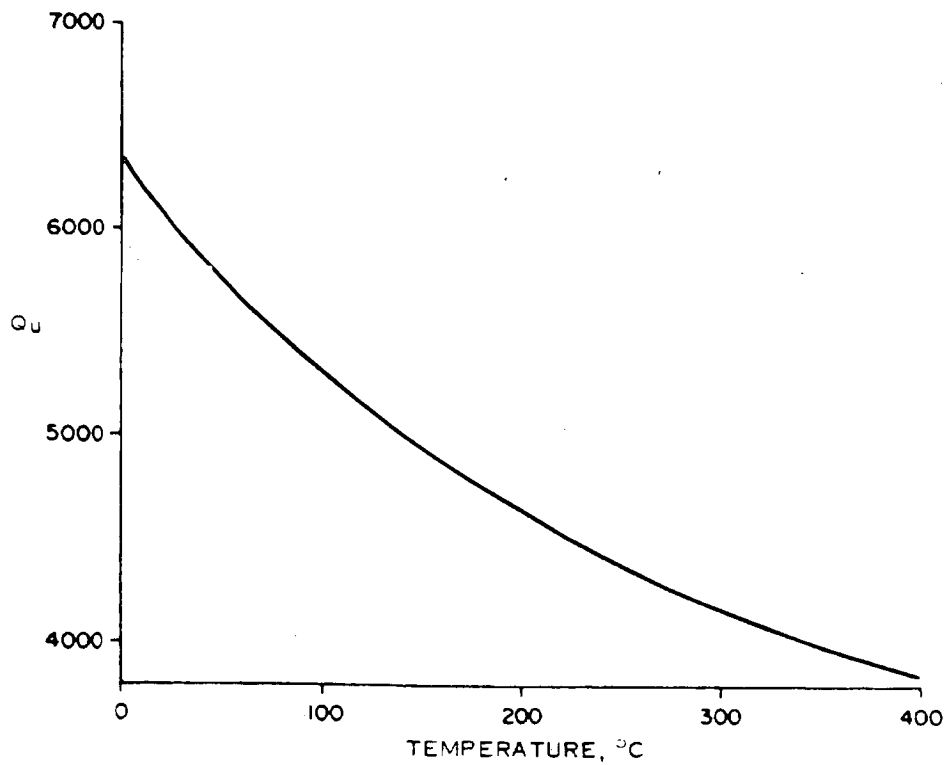


Figure 4-24. Effect of Temperature on  $Q_u$  in the Klystron Output Cavity

( $Q_u$  is proportional to  $1/\sqrt{\text{frequency}}$  through the skin depth of copper.) A temperature change from 20 to 300°C increases the heat losses by a factor of 1.5, reducing the net efficiency of the PPM tube (with depressed collector) from 76 to 72 percent and that of the EM tube from 72 to 71 percent. However, the weight of the body radiator is reduced by more than 93 percent. The PPM tube has a lower circuit efficiency because the lower bunching level produces less rf output voltage for a given output-gap voltage, while the latter determines the heat lost.

#### 4.2.3 KLYSTRON EFFICIENCY WITH SOLENOIDAL FOCUSING

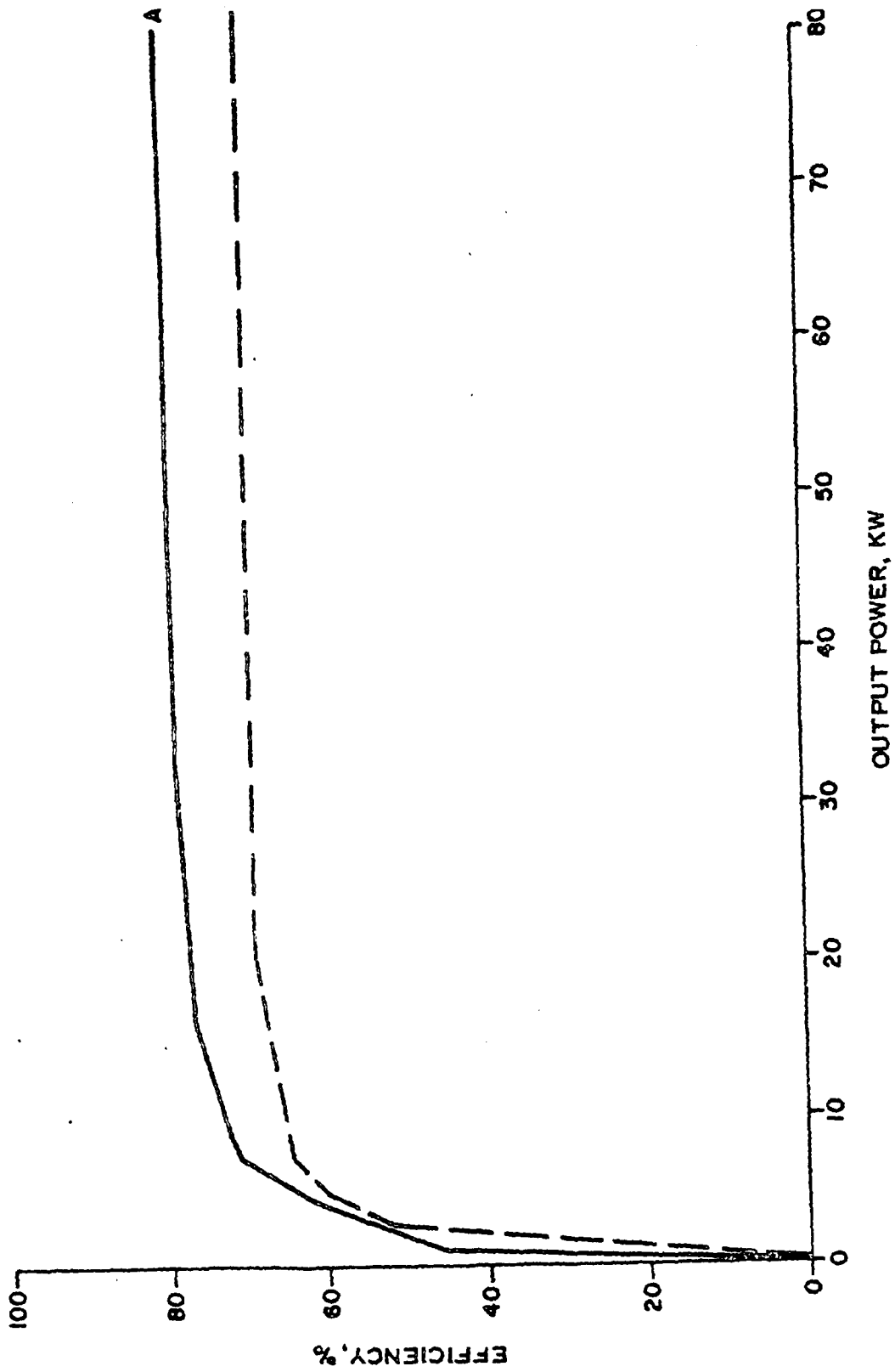
For high efficiency, full advantage can be gained from narrowband operation at the single specified frequency. For example, a 50 kW water-cooled klystron has demonstrated up to 74 percent conversion efficiency (the Varian VKS-7773)<sup>(4, 11)</sup> at 2.45 GHz, using confined-flow focusing and two second-harmonic bunching cavities.

While the Varian tube uses a 0.5-microperveance beam, a reduction of perveance should further increase electronic efficiency.<sup>(12)</sup> Accounting also for the fall of circuit efficiency, as in Appendix E (Equation (E-12) and Table E-1)), a conversion efficiency of 80 percent should be attainable with a microperveance of 0.2, and a cavity temperature of 300°C.

A permanent magnet of the size needed for a 2.45 GHz tube would weigh at least eight times as much as a solenoid, even if using samarium cobalt instead of the conventional alnico which can halve the weight. The additional power consumed by a solenoid is relatively small with more than 16 kW output. Figure 4-25 shows the resulting efficiency with a nominal solenoid power of 1 kW. (Appendix E details the calculations used to derive the output power.) The power summary (Figure 4-22) compares the PPM- and EM-focused tubes; the net efficiency of the PPM tube is 15 percent less before collector depression. Note that average efficiencies may be a few percent lower because of the time-varying supply voltage (see Paragraph 4.2.5): the design parameters correspond only to maximum power.

To further increase efficiency, voltage bias across or just before the output gap has been proposed:<sup>(13)</sup> however, no recent studies have been published. Voltage bias is not recommended for the following reasons:





60 kW Beam Power  
 1 kW Solenoid Power  
 60 W To Cathode, Heater  
 }  
 A - ASSUME 84 PERCENT ELECTRONIC EFFICIENCY  
 B - ASSUME 75 PERCENT ELECTRONIC EFFICIENCY

a. A voltage bias across the output gap produces an outward radial field at the far end of the gap, where the rf field has slowed the electrons. This may increase interception and also cause additional thermal problems.

b. Reduction of space-charge forces and output velocity spread is the major effect of bias just before the output gap. However, in a low perveance beam these are already small. Further, part of the extra energy supplied by the bias will be lost as increased energy of intercepted electrons and the remainder must either be recovered at the collector or entirely converted to rf power if net improvement is to result. Even without a detailed design it is clear that this would be difficult, particularly in a tube of varying beam voltage.

c. To apply a bias without loss of transmission, the drift tunnel must be severed over a distance shorter than the tube radius; with a voltage of 30 kV or more this could produce insulation problems.

Collector depression is well developed<sup>(14-16)</sup> for tubes of low electronic efficiency (30 to 40 percent). If a collector can recover 70 percent of the energy in the spent klystron beam, electronic efficiencies of 85 to 90 percent are attainable. However, the many slow electrons leaving the output gap may present difficulties when the basic electronic efficiency is already 70 percent or higher, and a further feasibility study is recommended. Existing computer programs are capable of the analysis; 100 or more representative particles would give a realistic velocity spread. Ultimately the cost and weight of such a collector must be compared with the cost and weight of the power sources that are eliminated.

#### 4.2.4 HEAT DISSIPATION AND BEAM COLLECTION

A high-power klystron generates considerable heat through beam interception and high-frequency skin losses in the cavities. A calculation of the heat that must be removed is the first stage in the design of a thermal control system. This study shows that the confined-flow tube, with better beam transmission and higher circuit efficiency, can produce about three times as much useful rf power for the same body heating as the PPM tube.

Figure 4-26 shows both the body heat and the output-cavity heat as calculated (using Equations (E-11 through E-16), Appendix E) for tubes of output power up to 43 kW. The output cavity alone produces a kilowatt or more both in the 5.6 kW PPM tube and in a confined-flow tube of output exceeding 16 kW. While this power may be dissipated at a density of more than 100 watts/sq. cm., it must be radiated into space at about 0.4 watt/sq. cm. (depending on the radiator temperature). At the start of this study it was hoped to use conduction cooling as in the amplitron. Unfortunately, solid conduction is impractical at these power levels (see Appendix G) and, in this space application, forced air or water cooling are unsuitable because of their weight and reliability. However, heat pipes can transfer kilowatts of power from source to radiator surface with temperature drops of only a few degrees (reference 2, pp. 121-125).<sup>(17-19)</sup>

The output gap and particularly the tunnel tips present the major problems, as experience with actual tubes has shown.<sup>(20)</sup> In the PPM tube, the heat must be transferred past the focusing magnets and pole pieces, which are less effective heat conductors than the copper cavity walls and can operate only at 300°C or less. Even with heat pipes between the cavity walls and the magnets, the available power is seriously restricted in such a tube with passive cooling. The results in Figure 4-26 show that a 16 kW confined-flow tube is at least as good as the 5.6 kW PPM tube; the latter produces relatively more heat from the beam before collector depression, while the lower perveance requires a higher voltage at the output gap and hence there are higher skin losses there.

Large-signal computer studies yield useful information on both the quantity and the distribution of the heating of the klystron body. For example, beam interception in the PPM tube dissipates 120 watts halfway along the second drift tunnel (see Figure 4-18), and a further 180 watts are distributed over the inside of the tunnel wall at the end of the output gap (see Figure 4-19). Skin losses are calculated from the gap voltages (Equation (E-12), Appendix E) where each bunching cavity of the PPM tube loses about 5 watts, while the 43 kW tube would lose about 120 watts per cavity. While the field pattern in the cavity determines the actual distribution of this heat over the walls, a simple model<sup>(21)</sup> treats two-thirds as uniformly spread over the two re-entrant tunnel walls (inside the drift tunnel) and the rest over the inside of the cavity.

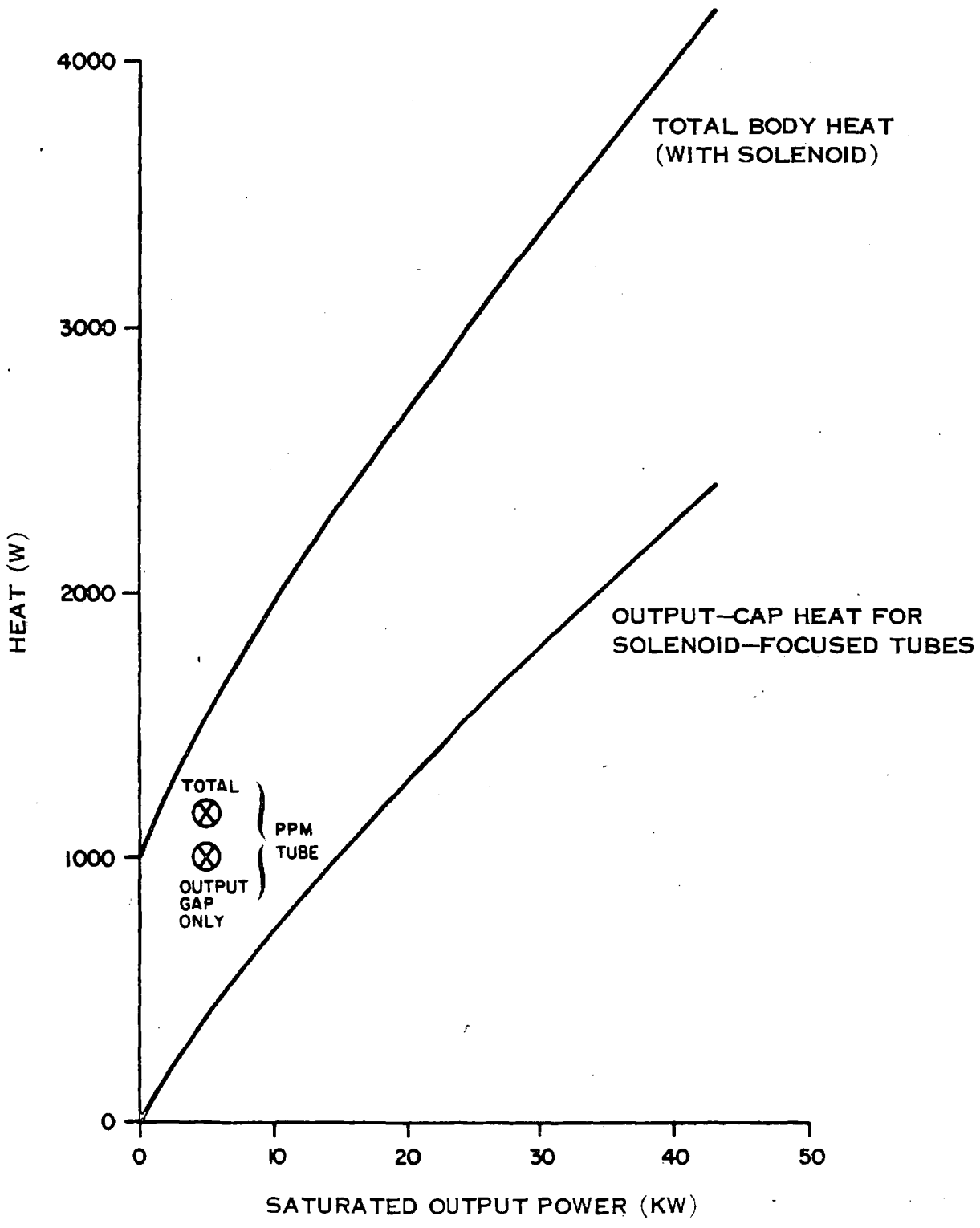


Figure 4-26. Body Heat versus Saturated Output Power

The confined-flow tube should contain a heat pipe around the entire drift tunnel and penetrate to the tips of the cavities as shown in Figure 4-27, in order to maintain a uniform temperature. This minimizes possible mechanical stress due to the periodic changes in body heat with supply power. "Dowtherm A" (Reference 2, p. 124) or cesium are suitable liquids for the heat pipes. "Dispersion hardened copper", which contains zirconium oxide or aluminum oxide, has 95 percent of the electrical and thermal conductivities of pure copper but can withstand temperatures of 500°C or higher. It may be possible to use thin and light cavity walls surrounded by the copper mesh wick of the heat-pipe evaporator.

Linear scaling from Branch and Mihran's design for an 11 GHz, 5 kW tube (Reference 2, pp. 137, 141) suggests that the 43 kW tube described here (48 kW for the higher electronic efficiency) is feasible, one criterion being the maximum power that a heat pipe can remove. However, a more detailed thermal model of the output cavity will determine the ultimate power capability.

If a solenoid is used, it should be wound directly on the heat pipe used to cool the drift tunnel and cavities, and should therefore be capable of operation at 300°C or higher. The outer surface of the solenoid can radiate directly; for example, a black body cylinder 60 cm long by 6 cm radius at 300°C radiates sideways 1430 watts. The PPM klystron and solenoid klystron are shown respectively in Figures 4-28(a) and 4-28(b).

The size and weight of body radiators are calculated in Appendix G. A surface temperature of 250°C allows for 50°C rise between radiator and heat source, and the sizes allow for a "view factor" between body and collector and for radiation that is absorbed when the collector points directly at the sun. Heat pipes must line the backs of the radiators in order to reduce the thickness and weight required for effective conduction. The collector serves both to complete the circuit of cathode, beam and anode and to dissipate the unconverted power remaining in the beam after the output cavity. To minimize weight for space application it should radiate directly from its electrodes, and only the heat remaining when the tube is under saturated RF drive need be removed.

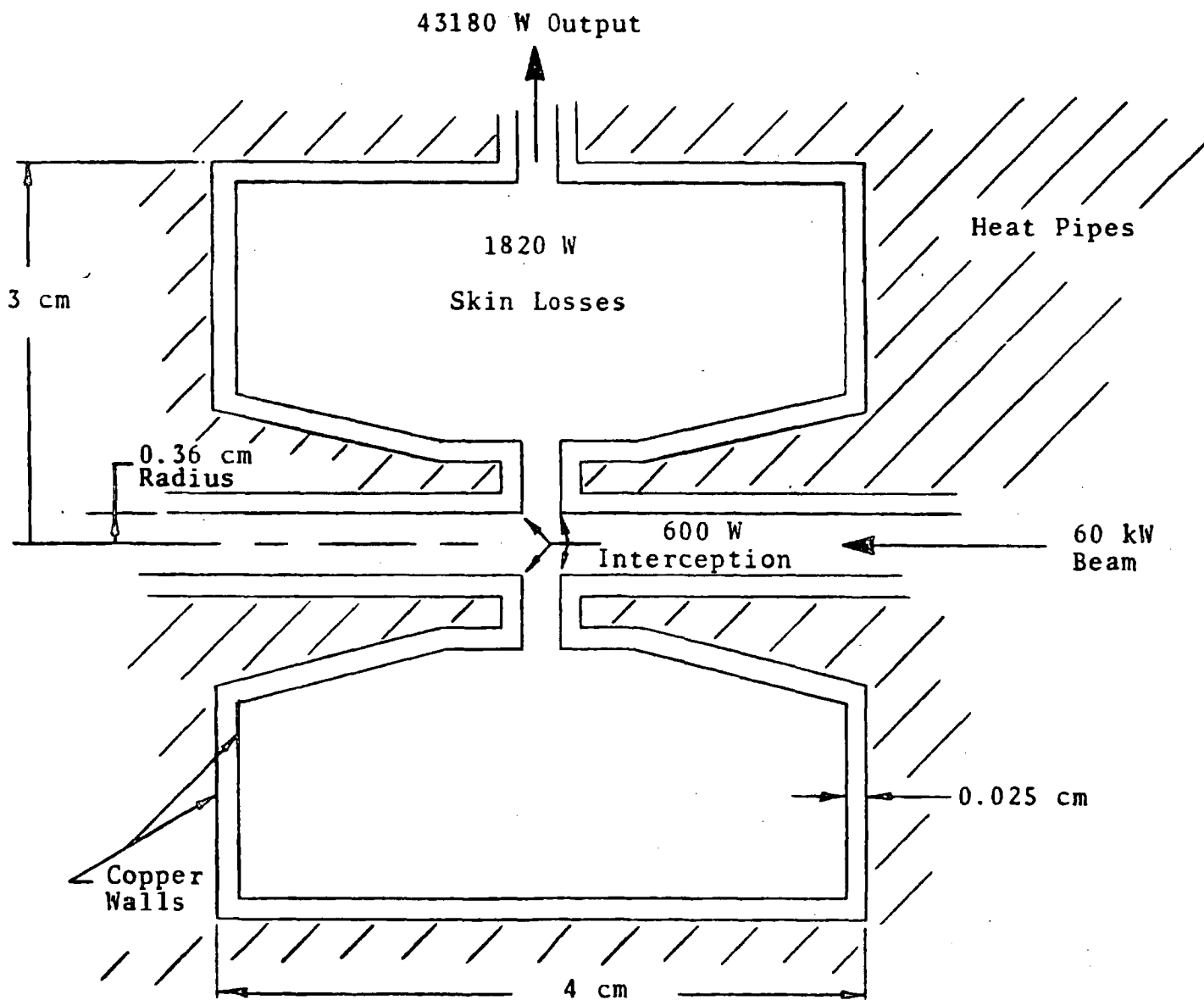
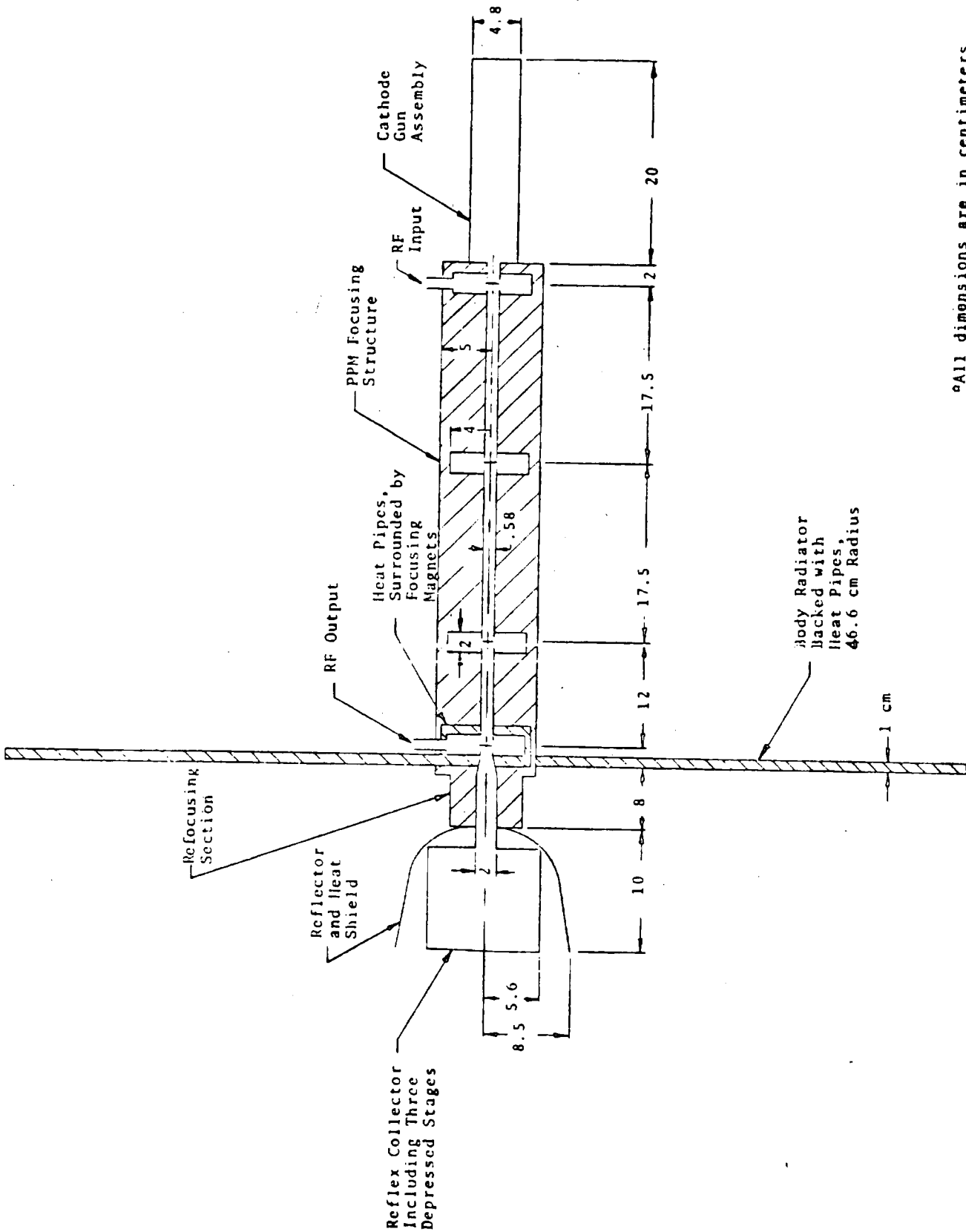


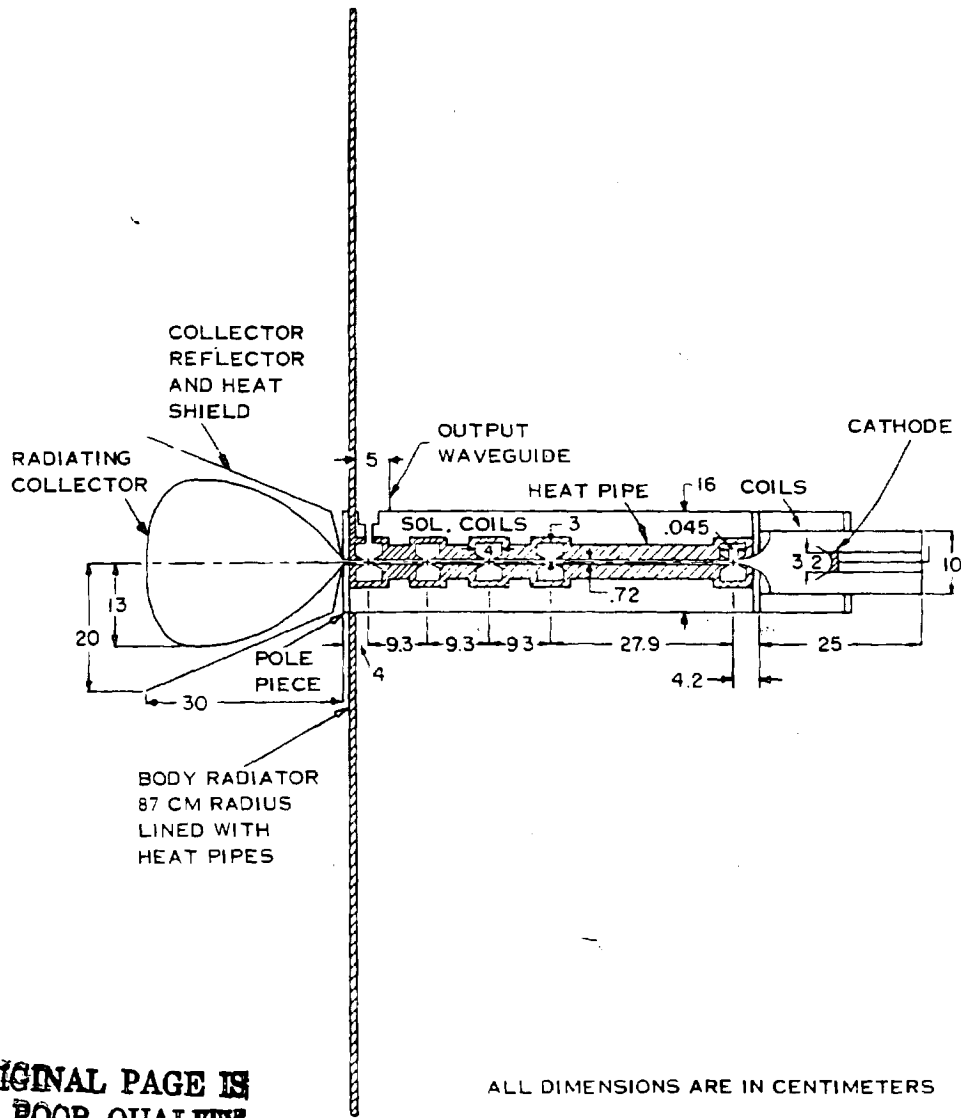
Figure 4-27. Output Cavity of 43 kW Klystron (Longitudinal Cross-Section)



All dimensions are in centimeters

Figure 4-28(a). Outline of the PPM Klystron

ORIGINAL PAGE IS  
OF POOR QUALITY



ORIGINAL PAGE IS  
OF POOR QUALITY

Figure 4-28(b). Outline of the 48 kW Solenoid Klystron



For an undepressed collector the simplest design is an envelope of tungsten or graphite foil as patented by Lien<sup>(22)</sup> (see also Reference 3, Appendix E). The vacuum window is convenient for initial tests, but is unnecessary when the tube is opened to space. Although the radiant emissivity is only 0.55, the radiating temperature may be 1400°C or higher, restricted primarily by sublimation of the envelope material. A molybdenum reflector backed by a heat shield then protects the body of the tube, which has a separate radiator to "see past" this shield. The tube drawing (as shown in Figures 4-28(a) and 4-28(b) shows the size required for a 43 kW (or 48 kW) tube; the dimensions and weight are calculated in Appendix C for tubes of output power 16 kW and 43 kW. Since existing high-power collectors are generally liquid- or air-cooled, additional development of this design may be needed. The Varian VKS-7773 klystron<sup>(4, 11)</sup> appears to be a suitable test vehicle.

For increased efficiency with several depressed stages the reflex collector<sup>(15)</sup> eliminates backstreaming to the drift tunnel by reversing the electron motion before collection. A magnetic refocusing section<sup>(16)</sup> allows the beam to spread in a linearly decreasing axial magnetic field between output gap and collector, and reduces both charge density and radial velocities. In addition, the power density can be reduced enough to allow the electrodes to radiate directly; flat pyrolytic graphite electrodes backed by copper may be suitable. Of course, the recovered power leads to savings of area and weight, but at the expense of a more complex design.

#### 4.2.5 VARIATIONS OF SUPPLY VOLTAGES

While the tubes are designed here for a maximum supply voltage, in practice the voltage and available power from solar cells, for example, may fall by 5.3 percent of the maximum in an annual cycle, and by a further 6.6 percent over a 25-year lifetime. Three alternative control schemes proposed for the klystron are as follows:

- a. No regulation. Here the current is controlled by the electron gun under space-charge-limited operation. This produces the largest variation in output power but is the simplest and most stable method.
- b. Constant current. This requires a gridded gun, which is undesirable in a long-life tube.

c. Constant power output and depressed collector of varying potential. At maximum voltage, the excess power is then dissipated as heat in the collector. This has the disadvantages of increasing the required weight of the radiator, and using the collector efficiently only at minimum voltage. At peak source voltage the collector is undeepressed and efficiency is at its minimum.

Figure 4-29 summarizes the alternatives. The unregulated klystron has a clear overall advantage.

When the source voltage falls by 5 percent, 7-1/2 percent of the available source power is unused. Tubes designed for 5.6 kW, 16 kW and 43 kW maximum output power, respectively, will have annual minima of 4.9 kW, 14 kW and 37.5 kW. A grid-controlled tube maintains constant current so that beam power varies only directly with the source voltage.

Under imperfect focusing conditions the beam ripples about an equilibrium radius<sup>(8)</sup>. The cathode magnetic field and the gun must be designed for a fixed voltage; simple estimates (Reference 8, Appendices G and H) suggest that an 11 percent voltage reduction may increase the ratio of beam-to-tunnel radius from 0.65 to 0.74, with ripple to 0.83, accounting for the fall of solenoid power in an unregulated tube. Current regulation increases the charge density in the beam and may cause instability. The effects of saturated drive are best determined by actual measurement in order to decide whether solenoid power must be regulated.

Electronic efficiency depends both on the beam size and on the normalized gap voltages ( $V_1/V_0$ ), which can be optimized at only one beam voltage. An estimated efficiency loss of one-half percent for each percent fall of voltage may occur through the fall of output-gap voltage below optimum, but, as several mechanisms are involved, experimental measurements should be made on existing tubes to confirm this. The cavity loadings and tunings must, of course, be fixed as the voltage varies so as to simulate the conditions in the satellite tube.

At the input cavity the impedance and resonant frequency are partly determined by the beam-loading impedance, which changes with beam voltage (Appendix E). However, the effects are small. The voltage standing-wave ratio increases from unity by about 0.0025 for each percent fall of beam voltage, while the resonant frequency changes by only 0.003 MHz. In either unregulated or constant-current

	No Regulation	Constant Current	Constant Output Power
Beam Power	Varies as $V_0^{5/2}$ Part of available power unused	Varies as $V_0$ All available power used	Constant, but power is wasted at voltages above design minimum
Focusing and Efficiency	Experimental tests required	Experimental tests required	Beam Transmission falls with solenoid power. Efficiency is greatest at minimum voltage; least at maximum voltage.
Construction	Simplest: no modifications needed to constant-power tube	Requires a gridded gun	Requires a complex and heavy collector
Phase Change at Output	About 22° for each percent voltage change	About 22° for each percent voltage change	None
Stability	Most stable	Focusing may be unstable at low voltage	Collector may be unstable at low voltage

Figure 4-29. Klystron Voltage Control

operation, a drop of beam voltage reduces the beam speed, increasing the phase delay between input and output signals. Using design values for the PPM tube, the total phase delay between input- and output-gap voltages is about 4400 degrees; a one percent drop in voltage increases this by one-half percent or 22 degrees. In the high-power tube the corresponding estimate is 19 degrees for a total phase delay of 3800 degrees.

#### 4.2.6 NOISE, GAIN AND HARMONIC CHARACTERISTICS

The separate cavities of the klystron give it an inherently narrow bandwidth, and hence advantages as a low-noise amplifier. Thermal noise originates in the low-level microwave oscillator and is amplified in the initial stages that precede the klystron. The combined noise and drive signals then modulate the beam, and the klystron acts as a filter by reducing spurious signals. This is in contrast to the amplatron, which itself generates noise and requires an additional output filter.

The noise output of a klystron under saturated drive is calculated as follows. The gain-frequency characteristic is first obtained:

a. A large-signal computation and the circuit theory for the input cavity give the ratio (output power/RF drive power) as the gain at the center frequency  $f_0$  (see Appendix A).

b. Small-signal space-charge-wave theory gives the gain at frequencies near the center frequency.

c. When the power transfer characteristic is treated as linear for small modulations of the drive level, the gain of a noise signal at frequency  $f$  is approximately (saturation gain at  $f_0$ ) + (small-signal gain at  $f$ ) - (small-signal gain at  $f_0$ ).

d. Outside the band of cavity resonances the decrease of gain in a klystron with "n" cavities is given by:

$$\text{gain} \approx -10 \log_{10} \frac{\delta^2}{\delta_0^2}$$

for

$$\delta \gg \frac{1}{\text{loaded } Q \text{ of input cavity}}$$

$$\delta = \frac{\text{drive frequency} - f_o}{f_o}$$

and  $\delta_o$  is a constant depending on the midband gain. This is the characteristic of an ideal "n-pole filter" with the gain falling by  $6.02n$  dB as  $\delta$  doubles.

At temperature  $T^\circ\text{K}$ , the initial noise power is  $kT$  W/Hz, <sup>(23)</sup> where  $k = 1.38 \times 10^{-23}$  J/K. For  $T = 450^\circ\text{K}$  this is  $-112.1$  dBm/MHz. Assume an oscillator output power of 1 mW at the drive frequency, and a noise figure of 10 dB for the preamplifier. Noise originating in the klystron itself is then negligible in comparison, so that the klystron amplifies both drive and noise signals equally to give a noise power of 102.1 dB below output power at drive frequency. The relative gain then gives the noise power at other frequencies.

The gain figures of Figure 4-30 are calculated for the PPM tube using a small-signal klystron program developed by Shared Applications, Inc. The cavity resonances are chosen to give the correct gap impedances to match the large-signal results for this tube. Appendix E explains the procedure. Figure 4-31 shows the noise power. It is less than  $-102$  dB relative to output power in the frequency band containing the cavity resonances, and decreases by 24 dB per octave of frequency difference outside this band. A confined-flow tube can be made even better. A second-harmonic bunching cavity (see below) should further reduce the noise power by as much as 72 dB:

At saturation the bunched beam contains harmonic currents of amplitude  $I_o$  or greater at the output gap (whether or not the bunching section contains second-harmonic cavities). Harmonic output power depends on the coupled harmonic impedance of the output cavity, which is tuned to drive frequency and must have no spurious harmonic resonances. The impedance decreases with frequency shift  $f_o \delta$  at least as fast as  $(1/Q_L \delta)$ , and output power as  $(1/Q_L^2 \delta^2)$ , where  $Q_L$  is the loaded Q of the output cavity, so that when  $\delta = 1$  and  $Q_L = 140$  the second-harmonic output power is at most 43 dB below fundamental. Similarly, a second-harmonic bunching cavity, while improving bunching at drive frequency under saturated drive, reduces the gain of noise signals at nearby frequencies by about  $(1/4Q_L^2)$ , where  $Q_L$  is now about 2000, so that noise power is reduced by  $-72$  dB near drive frequency. Input noise at the second harmonic is, of course, filtered by the fundamental-frequency cavities.

Gain at Saturation: 32.7 dB (derived in Appendix E)

Frequency (GHz)	Frequency Minus Center Frequency (MHz)	Small-Signal Gain (dB)	Noise Gain at Saturation (dB)	Noise Level Relative to Output Power (dB)
2.437	-13	-3.9	-5.7	-140.5
Cavities 1 and 4, Drive Frequency: 2.45	0	34.5	32.7	-102.1
2.463	13	-0.3	-2.1	-136.9
2.476	26	-7.8	-9.6	-144.4
Cavity 2: 2.489	39	12.3	10.5	-124.3
2.502	52	-25.7	-27.5	-162.3
Cavity 3: 2.515	65	-17.8	-19.6	-154.4
2.528	78	-45.0	-46.8	-181.6
2.541	91	-61.6	-63.4	-198.2

Figure 4-30. Gain and Noise in PPM-Focused Klystron

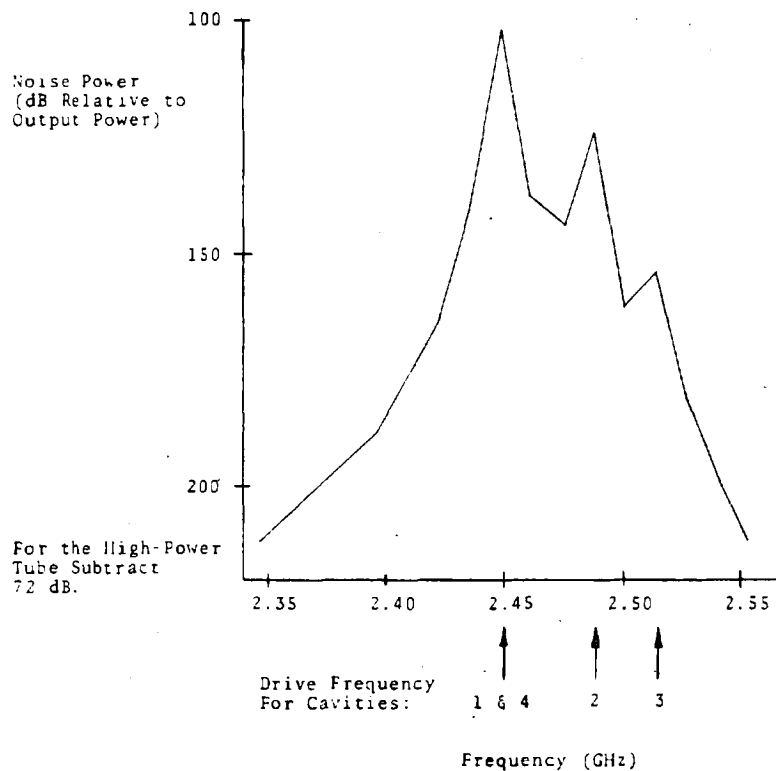


Figure 4-31. Computed Noise Characteristic of the PPM Klystron

#### 4.2.7 TUBE DESIGNS

The tube layouts have been developed sufficiently here to provide realistic weight and cost estimates. The cross-section outlines of Figures 4-28(a) and 4-28(b), respectively, show the 5.57 kW PPM-focused klystron and the 43.18 kW (48 kW) solenoid-focused tube. Figure 4-32 summarizes the principal design parameters, and these data should serve as a basis for a more detailed mechanical design. The dimensions of the drift tunnel scale in proportion to the speed of the beam, or to (beam power)<sup>0.2</sup> at constant perveance, so that the present outlines can readily be adapted for higher or lower power levels.

An advantage of the low perveance and high voltage is the long tube, which separates the cavities well and leaves ample space for heat pipes or cooling channels. At the output cavity the heat pipes and the output waveguide must be brought out without disturbing the magnetic focusing circuit. This section forms a critical part of the mechanical design and should incorporate the best features of existing klystrons adapted for minimum weight, while being straightforward to mass-produce. The full size of waveguide is 11 cm (transverse) by 5 cm (parallel

	PPM Tube	Confined-Flow Tube with Solenoid	References in Section 4.2.7
Frequency (GHz)	2.45	2.45	
Beam Power (kW)	10.0	60.0	
Beam Voltage (kV)	25.1	39.0	
Beam Current (A)	0.4	1.54	
Electronic Efficiency	0.83 (with depressed collector)	0.75 (0.84)	
Circuit Efficiency	0.87	0.96	
Net Conversion Efficiency	0.72	0.71 (0.80)	
Output Power (kW)	5.57	43.18 (48)	
Drive Power (W)	3.0	about 300	
Gain at Saturation (dB)	32.7	about 21 dB	
Perveance ( $\times 10^6$ )	0.1	0.2	
Number of Cavities	4	5 or 6	a
Drift Lengths (cm)	17.5, 17.5, 9.8	28.1, 9.4, 9.4, 9.4 (with 5 cavities)	b
Reduced Plasma Drift Angles (deg.)	47, 47, 27	90, 30, 30, 30 (nominal)	a
Magnetic Focusing Field/ Brillouin Field	$2\sqrt{2}$ (peak)	2.5 to 3	b
Focusing Field (G)	577 (peak)	775 to 930	
Field at Cathode (G)	20	15	
Cathode Diameter (cm)	1.6	3.13	
Maximum Current Density at Cathode (edge) ( $A/cm^2$ )	0.24	0.24	c
Beam Area Convergence	15:1	45:1	c
Tunnel Radius (a), (cm)	0.29	0.36	
(Beam Radius)/(Tunnel Radius)	0.7	0.65	d
$B_0$ (Normalized Radius)	0.5	0.5	e
$Q_u$ for All Cavities	4200	4200	f
External Q for Input Cavity	2865	2024	f
External Q for Output Cavity	628	175	f
R/Q (NOMINAL)	130 (buncher), 120 (output)	120	f
Cavity Outer Radius (cm)	6	3	f
Cavity Height (cm)	2	4	f
Cavity Tuning (MHz above drive)	0, 39, 65, 0	Not calculated. At least one near second harmonic.	g

Figure 4-32. Summary of Design Parameters.



to the tube axis), so that a "stepped-height" transition is necessary from the iris in the output cavity. <sup>(21)</sup>

The following design note numbers refer to column 4 of Figure 4-32:

a. The cavities represent only a small fraction of the weight (see paragraph 4.2.9), so that the tube can use as many as are needed for high efficiency; an existing Varian design (VKS-7773) <sup>(4, 11)</sup> used eight, of which two are tuned to the second harmonic of the drive frequency. The drift lengths can be optimized using existing designs and further large-signal calculations.

b. Relativistic effects reduce the focusing field required by about 4 percent in the high-power tube (see Appendix H). The field used must be large enough to give 98 percent beam transmission or better at saturation in the solenoid tube; in the PPM tube the peak field is restricted by beam stability. The cathode field is chosen to give balanced flow. <sup>(7)</sup> (See also Reference 8, Appendices G and H.)

c. Cathode current density is highest at the edge, but is restricted to  $0.24 \text{ A/cm}^2$  or less in a tube of long life. The gun convergence of 45 to 1 is, however, well within current technology <sup>(2)</sup>. The gun outline drawn follows Branch and Mihran, allowing a length of 30 beam radii for convergence and a gun diameter three times the cathode diameter.

d. For maximum gap coupling the beam should be as large as transmission allows.

e. The normalized tube radius,  $\beta a$ , equals  $2\pi \times \text{frequency} \times \text{tube radius}/\text{beam speed}$ . A low value has advantages:

1. The output-gap interaction is efficient <sup>(12)</sup>.
2. The buncher gaps have almost uniform fields and thus produce low radial rf velocities.

f. At this stage an outline is sufficient for the cavities; further design should use the values from existing tubes at this frequency, while field computations may be useful to increase  $R/Q$  and  $Q_u$ . The short cylindrical cavity in the PPM tube enables the magnetic period also to be short. In the confined-flow tube toroidal cavities may give higher efficiency. <sup>(21)</sup> At the output a gap length of 1.3 tube radii

is near optimum;<sup>(12)</sup> the input gap should be longer in order to raise R/Q and the beam-loading conductance, and thus increase the coupling and the tube gain.

g. The input and output cavities resonate at the drive frequency  $f_0$  (in the presence of the beam), while intermediate cavities of fundamental frequency are unloaded and tuned above drive frequency to give nearly  $\pi/2$  phase lead of voltage from current for high efficiency. Second-harmonic cavities are tuned slightly below  $2f_0$ .<sup>(4)</sup> Appendix E gives the calculation of the required resonant frequency from the bunched current and the gap voltage.

#### 4.2.8 TUBE LIFETIME

The goal of the satellite power system is to produce near-maximum design power with minimum maintenance over 25 to 30 years. For existing tubes this is optimistic. For example, field tests of high-power klystrons by Varian Associates<sup>(3)</sup> showed an average life of about 16,700 hours (2 years). Of 22 klystrons reported, seven failed with unknown cause, while cathode failure was reported in eight, collector burnout in five, and output cavity arcs in two. In the vacuum of space (less than  $10^{-12}$  Torr) an output gap of 4.5 mm should safely withstand an rf voltage of 100 kV or more; for ground-based tubes at about  $10^{-7}$  Torr, 60 kV/cm is about the maximum safe field. A 200 microsecond "pulse-off" period would extinguish occasional arcs. The space environment has the further advantage of making vacuum sealing unnecessary on both the output waveguide and the collector. The tube must be protected, however, against loss of rf drive to avoid overheating the radiating collector. Heat pipes and the cathode remain as the most likely parts to fail. Reported lifetimes for heat pipes have attained only 41,000 hours, but the technology is relatively new. A conventional "nickel matrix oxide" cathode<sup>(5)</sup> is still the most promising, with a current density of up to  $0.24 \text{ A/cm}^2$ , whereas cold field-emitting cathodes are as yet unproven on linear-beam tubes. The high vacuum has the advantage of virtually eliminating ion bombardment in the tube.

#### 4.2.9 WEIGHT AND COST

The weights and costs of three proposed klystrons are shown in Figures 4-33 to 4-35. Figure 4-36 summarizes the results.

Material	Base Cost \$/KG	Weight (GR)	Cost \$
Samarium Cobalt	48.07(M) 39.68(F)	2000	175.50
Pyrolytic Graphite	23.34	6915	161.40
Base Metals	4.84(M) 121.00(F)	1316	95.62
Platinum	700.00	N/A	-
Solder	-	-	-
Motor and Control	-	N/A	-
Heat Pipes	110.00	2208	242.88
Gun Assembly	-	50	10.00
Solenoid	10.00	N/A	-
Molybdenum	30.00	7	0.21
Tungsten	30.00	-	-
Totals		12,496	685.61
Specific Weight		2243.45 GR/kW	
Specific Cost		123.09 \$/kW	

M = Materials  
F = Fabrication

Figure 4-33. Weight and Cost Analysis of the PPM Klystron with 5.57 kW Output

Material	Base Cost \$/KG	Weight (GR)	Cost \$
Samarium Cobalt	48.07(M) 39.68(F)	N/A	N/A
Pyrolytic Graphite	23.34	13,705	319.87
Base Metals	4.84(M) 121.00(F)	3,303	415.65
Platinum	-	N/A	N/A
Motor and Control	-	N/A	N/A
Heat Pipes	110.00	4917	540.87
Gun Assembly	-	50	10
Solenoid	10.00	13,376	133.76
Molybdenum	30.00	495	14.85
Tungsten	30.00	0	
Totals	-	35,846	1425.00
Specific Weight		2240 GR/kW	
Specific Cost		89.06 \$/kW	

M = Materials  
F = Fabrication

Figure 4.34. Weight and Cost Analysis of an EM Klystron with 16 kW Output

Material	Base Cost \$/KG	WG (GR)	Cost \$
Samarium Cobalt	48.07(M) 39.68(F)	N/A	N/A
Pyrolytic Graphite	23.34	23,835	556.31
Base Metals	4.84(M) 121.00(F)	3,313	416.91
Platinum		N/A	N/A
Motor and Control		N/A	N/A
Heat Pipes	110	6,282	691.02
Gun Assembly	-	50	10
Solenoid	10.00	16,300	163.00
Molybdenum	30.00	844	25.32
Tungsten	30.00	0	-
Specific Weight		1055 GR/KW	
Specific Cost		38.70 \$/KW	

M = Materials  
F = Fabrication

Figure 4-35. Weight and Cost Analysis of an EM Klystron with 48 kW Output

Focusing magnets, body radiators and heat pipes account for about 90 percent of the total weight. The cost and weight advantages of the highest power klystron are clear, but the klystron does not yet effectively compete with the amplifier.

#### 4.2.10 CONCLUSIONS

The conceptual designs and layouts presented here for both periodic-permanent-magnet and solenoid-type klystrons permit a clear comparison of the two. Despite the lower weight and cost of the PPM structure, the higher power capability of the confined-flow tube gives significant advantages to a tube with an output of 16 kW or higher. Figure 4-36 summarizes these results. Electrostatic focusing, while not studied in detail here, gives rf transmission similar to that with PPM focusing,

	Klystron with PPM Focusing	Klystron with Solenoid
Output power	5.5 kW	16 kW or more
Efficiency before collector depression	55 percent	70 percent or more
Heat dissipation	Severe problems at output gap (1000W heating)	16 kW tube presents less difficulty than 5.5 kW PPM tube (950W at output gap)
Output noise level	100 dB below output power or less	170 dB below output power or less, using a second-harmonic bunching cavity
Collector depression	4-stage reflex collector necessary to raise efficiency to 72 percent	Requires further study. 80 percent efficiency may be practicable
Total weight/kW output	2243 g/kW	2240 g/kW (16 kW tube) 1055 g/kW (48 kW tube)

Figure 4-36. Comparison of Tube Types

i. e., at least 5 percent interception and typically 50 percent efficiency (Reference 3, Appendix F). For low-power applications, such as satellite traveling-wave tubes, periodic focusing regains its value, but for the present application further development should concentrate on the electromagnetically focused klystron.

For minimum weight per kilowatt of useful power, the tube power must be a maximum. The available cathode current sets an upper limit of about 175 kW output; however, the capacity of a heat-pipe cooling system requires the most urgent study. The quantities and distribution of heat are derived here, and the next stage should be to develop a thermal model of the output cavity, with heat pipes as an integral part of the design. A toroidal shape should yield the highest circuit efficiency.<sup>(21)</sup> It may be possible to use thin cavity walls of dispersion-hardened copper, lined outside the cavity with copper mesh as a wick for a heat-pipe evaporator.

The radiator area required to cool the tube body is too large for conduction alone; a panel of heat pipes is necessary to distribute the heat and maintain a nearly uniform surface temperature.

### 4.3 SYSTEM CONSIDERATIONS

There are certain properties of the amplitron and the klystron important to their application in a complex, multiple installation such as the MPTS transmitting antenna. The thermal interface is covered in the transmitting antenna section. Topics described here concern efficiency, noise, phase error, failure modes and waveguide losses.

#### 4.3.1 AMPLITRON GAIN AND EFFICIENCY

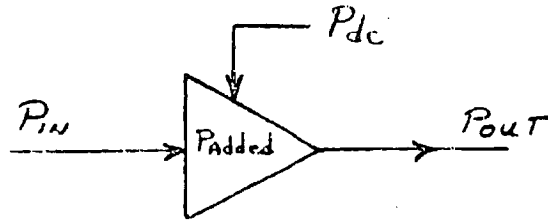
The amplitron is basically a saturated amplifier, i. e., an amplifier in which the rf output is essentially independent of the rf input. In addition, it is also a low gain device, so that the rf input can be a significant part of the output power. Because of this, the concepts of gain and efficiency, when applied to the amplitron, are subject to a slightly different formulation than is generally considered to be standard.

With the provision that the rf input is sufficient to achieve device operating stability, the power generated is independent of the rf power input. In this context, the amplitron can be viewed as a power adder, and when this concept is related to gain, it always exhibits minimum gain of one.

From Figure 4-37 we see that the rf drive power,  $P_{in}$ , is a component in both the input and output of the tube. This is true even when the  $P_{added}$  term of Equation (1) is equal to zero. Thus, the amplitron has a minimum gain of one, and is frequently used in this manner, generally referred to as the feed through mode.

In the second term of Equation (1),  $P_{added}$  and  $P_{in}$  are independent terms (once  $P_{in}$  is greater than a threshold necessary to lock operation) and either term can be varied independently of the other. Therefore, a given amplitron is not a fixed gain device, but will operate at different gains, depending upon the ratio of power added to  $P_{in}$ . The output power is determined principally by the dc power input to the tube.

When considering the efficiency of the amplitron, it is customary to refer to the dc-rf conversion efficiency of the tube. This efficiency relates the power added to the dc input power and is slightly different than the standard definition of efficiency, which relates total power output to total input power.



$$P_{out} = P_{in} + P_{added}$$

$$(1) \text{ Gain} = \frac{P_{out}}{P_{in}} = \frac{P_{in} + P_{added}}{P_{in}} = 1 + \frac{P_{added}}{P_{in}}$$

$$(2) \text{ Power Out} = P_{in} + P_{added}$$

$$(2) \text{ Conversion Efficiency} = \frac{P_{added}}{P_{dc}}$$

$$(3) \text{ Conventional Efficiency} = \frac{\text{Total Power Out}}{\text{Total Input Power}} = \frac{P_{in} + P_{added}}{P_{in} + P_{dc}}$$

Figure 4-37. Amplitron Gain and Efficiency

When these relationships are examined, it is seen that the conventional efficiency is higher than the conversion efficiency. This results from the rf input drive power being a higher percentage of the rf output power than it is of the dc input power. Following is a numerical example:

$$P_{in} = 1.25 \text{ kW}$$

$$P_{out} = 6.25 \text{ kW}$$

$$\text{Gain} = 7 \text{ dB}$$

$$P_{added} = 5.0 \text{ kW}$$

$$P_{dc} = 5882 \text{ kW}$$

$$\text{Conventional Eff} = \frac{P_{out}}{P_{added}} = \frac{6250}{1250 + 5882} = \frac{6250}{7132} = 87.6\%$$

$$\text{Conversion Eff} = n_c = \frac{P_{added}}{P_{dc}} = \frac{5000}{5882} = 85\%$$



#### 4.3.2 CASCADED VS. PARALLEL CONFIGURATIONS

The amplatron and klystron have quite different characteristics in a number of important respects. Of particular interest is the capability of feed through for the amplatron, i. e., if prime power is removed, the RF drive power feeds through and provides a significant output power. This is not true of a klystron. With no dc power the klystron is not a 0 dB gain amplifier but is an attenuator of significance (typically 90 dB).

The second characteristic of interest is the phase sensitivity for changes in source power supply voltage. Phase sensitivity for the amplatron, using constant current regulation, is  $0.1^\circ/\% \Delta V$ . Without this regulation it would be  $0.5^\circ/\% \Delta I$ , resulting in  $3300^\circ/\% \Delta V$ . Also of interest in the case of the amplatron is the phase change from the feed through to the amplifying mode; i. e., the phase change in output rf with and without dc power applied. This is typically  $12^\circ$ . Phase shift across the klystron for the MPTS is nominally  $5000^\circ$ . Change in phase with source voltage is approximately  $24^\circ/\% \Delta V$ . For the klystron it is proposed to operate unregulated, and this effect must be compensated by an offsetting change in phase command at the input. Major voltage changes at the power source can be prevented in the case of a solar photovoltaic source by varying sun angle and/or by switching parallel-series combinations of cell arrays (needed for amplatron startup).

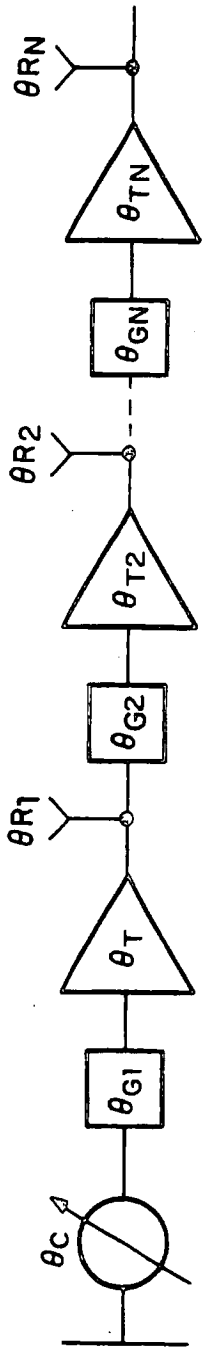
A third feature to be considered is the effect of loss of rf drive power on the amplifier. A totally different effect occurs in each case. An operating amplatron from which rf drive is removed inherently generates a noisy oscillation, which because of the uncontrolled rf voltages will result in rf arcing, and resulting dc arcing. In the MPTS the dc arc will initiate a crowbar (circuitbreaker) cycle, which removes the dc voltage for 100 microseconds. When dc is reapplied, there is no rf voltage available to initiate conduction, and conditions will remain stable. Thus the amplatron, in conjunction with the crowbar circuitry, is inherently self protecting for loss of rf drive. In an operating klystron, however, no instability occurs when rf is removed, there is simply no rf output and the total beam power is dissipated in the collector. The effect of the large increase in collector dissipation was not evaluated but must be considered in detailed design either by thermal overdesign or by protective circuitry incorporation. The latter would likely be the better approach.

Finally, the effect on mismatches on the tube must be considered. This is of particular concern in the case of the amplatron because of the lack of attenuation of reverse power. Experience with amplitrons has generally indicated that a 2.0/1 voltage standing wave ratio (VSWR) on the output is a practical high limit to maintain stability. This may not be true if the source VSWR is also as high as 2.0/1, i. e., from the preceding amplatron. The klystron on the other hand presents excellent isolation between the output and input. As such its operation is relatively insensitive to mismatches at either the output or input. Since the input and output of the klystron are tuned circuits, the VSWR of the tube itself may be quite high.

Figures 4-38 and 4-39 examine the effects of passive phase shift per tube on the cascaded and parallel feed amplifier configurations, respectively. For both configurations the requirement is that the RF phase at each radiating element be similar. Limits of  $2^{\circ}$  rms at any element are appropriate for MPTS as discussed in the transmitting antenna section.

A tabulation of the behavior for both types of amplifier configurations is given by Figures 4-40 and 4-41 for amplifier failures. Figure 4-40 is a sketch of the probable configuration with cascaded operation and Figure 4-41 is a sketch of probable configuration using the parallel feed configurations. The following points are noted:

- a. In the cascade arrangement using klystrons, either removal of dc power or opening of a heater can stop a significant number of tubes from providing useful output.
- b. Because of source voltage variations, to operate either converter in a cascade arrangement requires regulation of the tube in a manner to control the phase shift for source voltage variations.
- c. In the parallel feed configuration, recognizing that equal changes in source voltages are seen by all converters in the subarray, correction for phase shifts can be made by the existing phase shifter. Sensitivity of amplifiers to voltage changes must be controlled in the design to within a specified tolerance so that all are similar.



$\theta_C$  = SUBARRAY PHASE CONTROL

$\theta_G$  = INTERCONNECTING LINE PHASE SHIFT

$\theta_T$  = AMPLIFIER TUBE PHASE SHIFT

$\theta_R$  = RADIATED PHASE

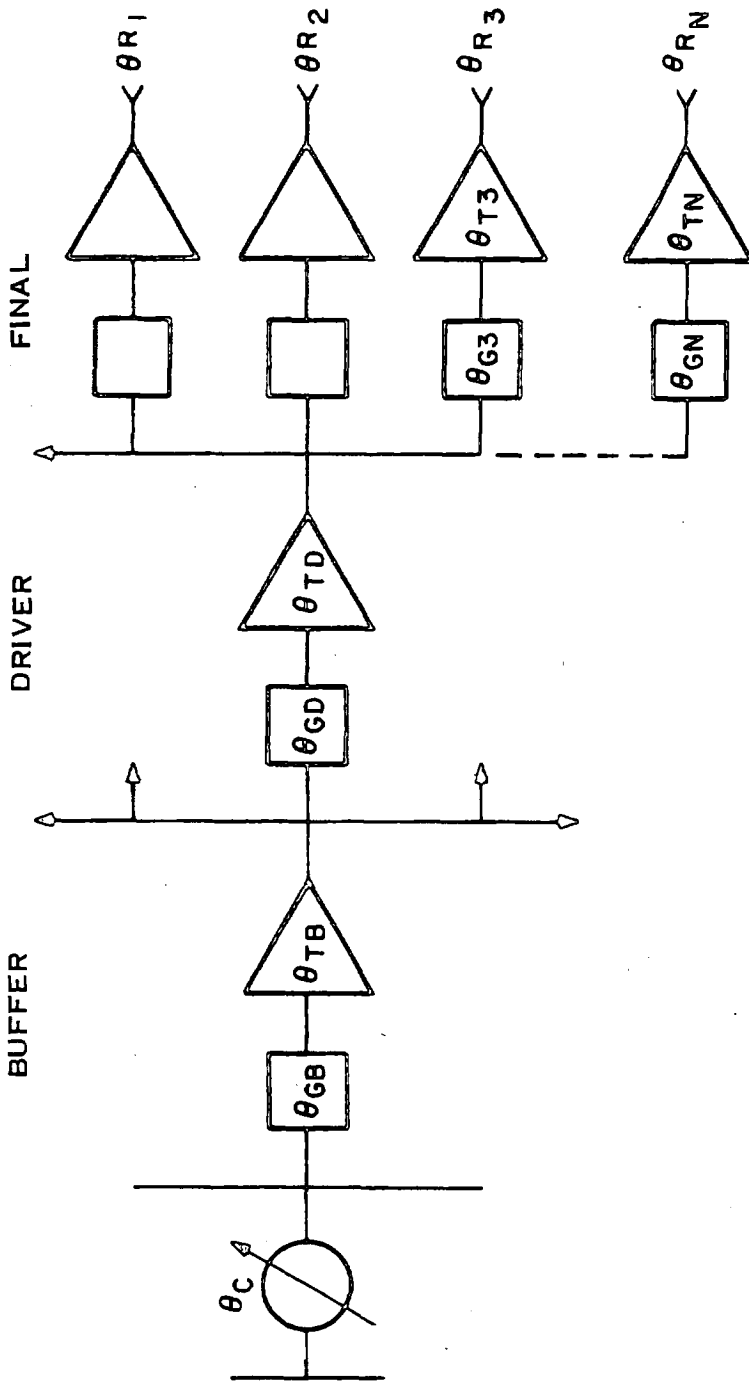
REQUIREMENT ( $\leq 6^\circ$  RMS):  $\theta_{R1} = \theta_{R2} = \dots = \theta_{RN}$

IN AMPLIFIER ABOVE:  $\theta_{RN} = \theta_C + N(\theta_G + \theta_T)$

FOR  $\theta_{RN} = K$ :  $N(\theta_G + \theta_T) = K$

AND  $(\theta_G + \theta_T) = 0^\circ$  RELATIVE

Figure 4-38. Cascaded Amplifier Configuration Phase Characteristics



$\theta_C$  = SUBARRAY PHASE CONTROL

$\theta_{G-}$  = TRANSMISSION LINE PHASE SHIFT FOR BUFFER, DRIVER OR FINAL

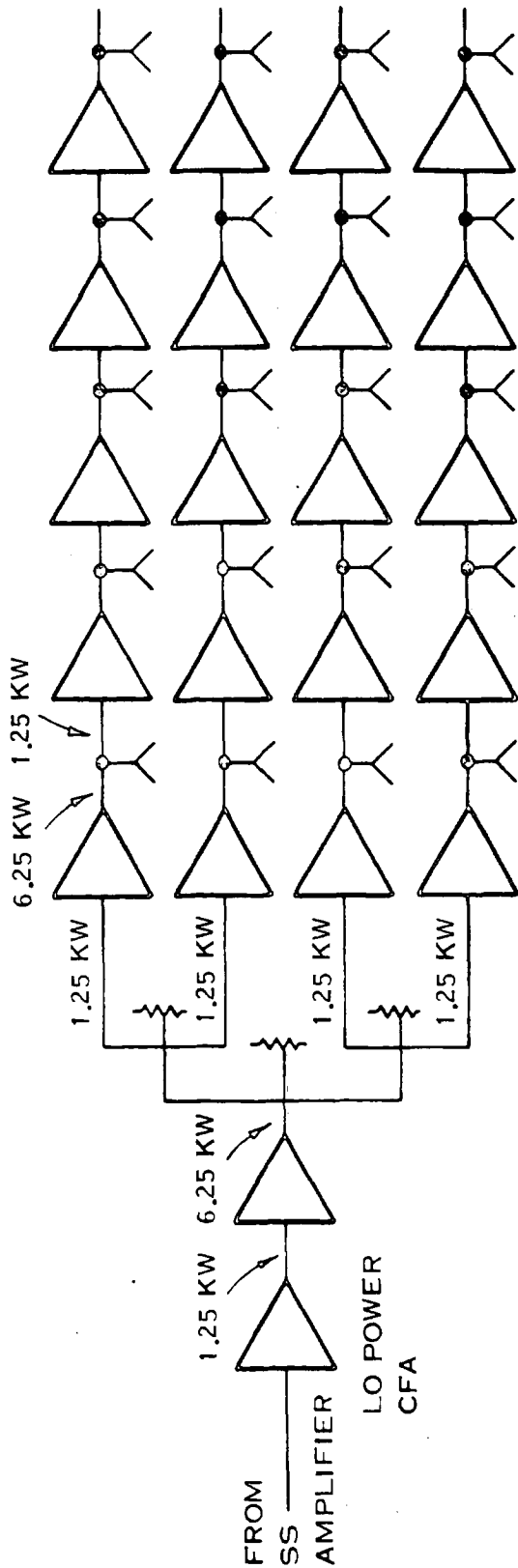
$\theta_{T-}$  = TUBE PHASE SHIFT FOR BUFFER, DRIVER OR FINAL

$\theta_{R_N}$  = RADIATED PHASE SHIFT FOR  $N^{TH}$  ELEMENT

REQUIREMENT:  $\theta_{R_1} = \theta_{R_2} = \theta_{R_3} = \dots = \theta_{R_N}$

FROM DIAGRAM:  $\theta_{R_N} = \theta_C + \theta_{GB} + \theta_{TB} + \theta_{GD} + \theta_{TD} + \theta_{GN} + \theta_{TN}$   
 $= (\theta_C + \text{CONSTANT})$

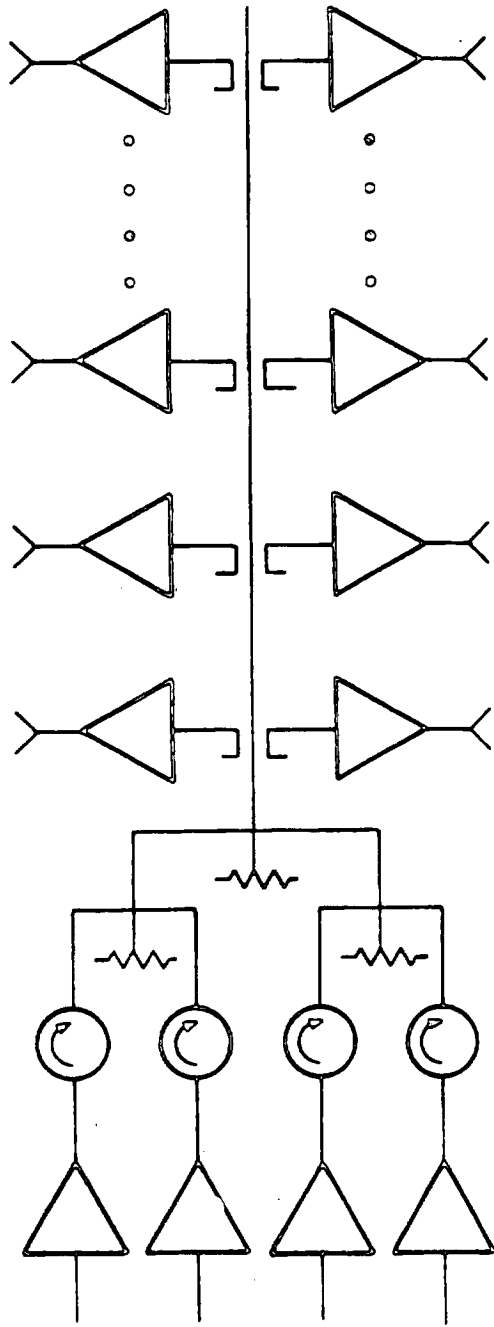
Figure 4-39. Parallel Feed Amplifier Considerations Phase Characteristics



FAILURES IN CASCADED AMPLIFIERS

	<u>AMPLITRON</u>	<u>KLYSTRON</u>
LOSS OF DC POWER TO NTH TUBE	≈ 12 DEGREES PHASE CHANGE BEYOND NTH TUBE	NO RF OUT BEYOND NTH TUBE
LOSS OF RF DRIVE	NO RF OUTPUT	COLLECTOR BURNOUT
OPEN HEATER	N/A	NO RF OUT BEYOND NTH TUBE. TUBES BEYOND 'N'TH - TUBE TUBE OVERHEAT

Figure 4-40. Cascaded Amplifier Chain



FAILURES IN PARALLEL FEED AMPLIFIERS

	<u>AMPLITRON</u>	<u>KLYSTRON</u>
LOSS OF DC POWER TO NTH TUBE	12 DEGREES PHASE CHANGE, -5 DB POWER OUT NTH OUTPUT TUBE	NO OUTPUT FROM 1 TUBE
LOSS OF RF DRIVE	NO RF OUTPUT	COLLECTOR BURNOUT
LOSS OF HEATER POWER OR OPEN HEATER	N/A	NO OUTPUT FROM 1 TUBE

Figure 4-41. Parallel Amplifier Chain

It is concluded that the loss of performance from a large number of output converters resulting from the failure of a single klystron when used in the cascaded amplifier arrangement makes this an unsatisfactory operating mode. It is recommended that klystrons only be considered for operation in a parallel fed configuration. Although the amplitron could operate in either arrangement, its relatively low gain per tube (and therefore the higher number of driver stages required) makes it more suitable for the cascade arrangement than for the parallel feed arrangement.

#### 4.3.3 CASCADED AMPLITRON GAIN

The amplitron efficiency of concern for the MPTS is the dc to rf conversion efficiency, or the power added divided by the high voltage dc input power. The MPTS would have cascaded amplitrons in large quantities as shown in Figure 4-42.

By inspection of the cascaded amplifier diagram it is apparent that the total power output of each tube is effectively divided into two parts, the radiated power per tube and the power input to the following stage. By design the power input to the following stage is equal to the  $P_{in}$  of the first stage. Thus, the only RF power available for radiation is the power added, and the array dc to RF conversion efficiency is the ratio of  $P_{added}$  per tube to power input per tube.

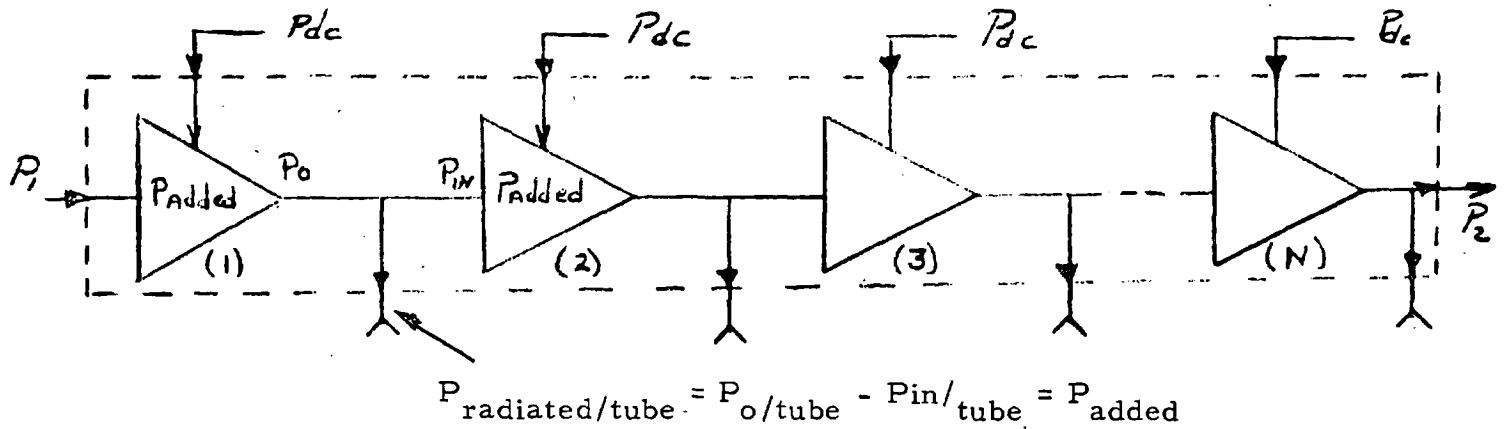
#### 4.3.4 AMPLIFIER NOISE

Figure 4-43 schematically represents the concepts for determining the output noise of a cascaded amplifier chain. The total noise can be divided into two components, the component appearing at the input  $n_i$  and the component due to self generation within the tube,  $n_t$ . The magnitude for input noise  $n_i$  is obtained by assuming that it is generated from an amplifier with 10 dB noise figure and an input power level of 0.1 mW. This is indicated by Figure 4-44.

From Figure 4-43 the noise output from the  $n^{th}$  tube in amplifier chain is given by:

$$\text{Noise} = n_i G + n_t NG$$

Representative parameters for a ten tube amplifier chain are as follows:



$$P_{\text{radiated}} = P_1 + N P_{\text{added}} - P_2$$

$$P_1 = P_2 \text{ by design}$$

$$\therefore P_{\text{radiated}} = N P_{\text{added}}$$

$$= N P_{dc} \times n_C$$

$n_C$  = Conversion Efficiency

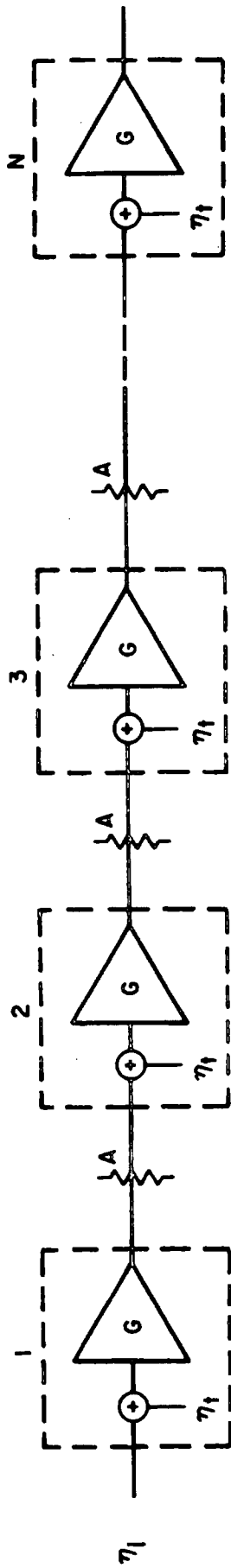
$N$  = Number of tubes in chain

Figure 4-42. Amplitrons in Cascade

	<u>Amplitron</u>	<u>Klystron</u>
(1) $n_i$	$0.01 \times 10^{-4}$ W/MHz	$0.5 \times 10^{-7}$ W/MHz
(2) $n_t$	$0.122 \times 10^{-4}$ W/MHz	$0.025 \times 10^{-9}$ W/MHz
(3) $n_i G$	$0.5 \times 10^{-4}$ W/MHz	$0.5 \times 10^{-5}$ W/MHz
(4) $n_t N G$	$6.1 \times 10^{-4}$ W/MHz	$0.25 \times 10^{-7}$ W/MHz
(5) S/N/Output	70.1 dB/MHz	90.8 dB/MHz

From lines (3) and (4) above we can see that for the amplitron the chain noise output is primarily related to the noise generated per tube (line 4) and that for the klystron the noise is primarily determined by the input noise (line 3). Figure 4-45 is a tabulation of S/N levels at the output of each tube for a cascaded amplifier chain up to 100 tubes. In the case of the klystron, where the tube





FOR MPTS  $G \cdot A = 1$

NOISE OUTPUT N<sup>TH</sup> TUBE  $\eta_i G + \eta_t NG$

$\eta_i$  = INPUT NOISE

$\eta_t$  = NOISE PER TUBE RELATIVE TO INPUT

$N$  = NUMBER OF TUBES

FOR KLYSTRON -  $\eta_i G \gg \eta_t NG$

NOISE TYPICALLY - 90 DB/MHZ BELOW  $P_0$

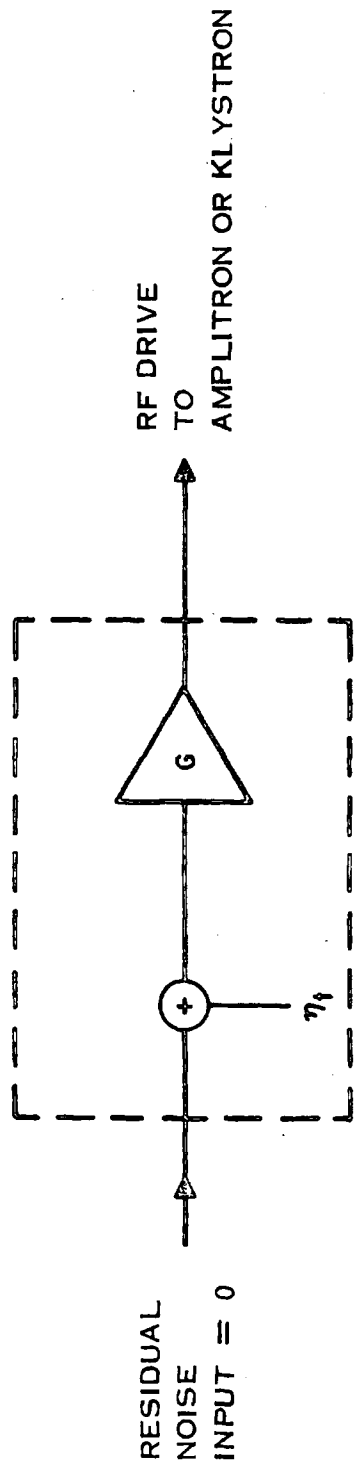
FOR  $N = 10$

FOR AMPLITRON -  $\eta_t NG \gg \eta_i G$

NOISE TYPICALLY - 70 DB/MHZ BELOW  $P_0$

FOR  $N = 10$

Figure 4-43. Amplifier Noise



	AMPLITRON	KLYSTRON
PREAMP OUTPUT	1.25 KW	60W
GAIN (RF IN = 0.1 MW)	71.0 DB	57.8 DB
PREAMP N.F.	10 DB	10 DB
KTB (300 °C)	-111 DBM/MHZ	-111 DBM/MHZ
PREAMP OUTPUT NOISE		
DB	-30 DBM/MHZ	-46.2 DBM/MHZ
WATTS	$0.1 \times 10^5$ WATTS/MHZ	$0.5 \times 10^{-7}$ WATTS/MHZ

Figure 4-44. Noise Output of Preamplifier Stages

Number of Stages	KLYSTRON		AMPLITRON			
	Power Watts/ MHz	S/N per Nth Tube dB/MHz	Power Watts/ MHz	S/N per Tube db/MHz		
1	$0.5 \times 10^{-5}$	90.78	$0.61 \times 10^{-4}$	80.1		
2	↑ ↓	↑ ↓	$1.22 \times 10^{-4}$	77.04		
3			$1.83 \times 10^{-4}$	75.3		
4			$2.44 \times 10^{-4}$	74.03		
5			$3.05 \times 10^{-4}$	73.06		
6			$3.66 \times 10^{-4}$	72.27		
7			$4.27 \times 10^{-4}$	71.6		
8			$4.88 \times 10^{-4}$	71.1		
9			$5.49 \times 10^{-4}$	70.5		
10			$6.1 \times 10^{-4}$	70.05		
20			$12.2 \times 10^{-4}$	67.04		
30			$18.3 \times 10^{-4}$	65.28		
40			$24.4 \times 10^{-4}$	64.03		
50			$30.5 \times 10^{-4}$	63.06		
60			$36.6 \times 10^{-4}$	62.27		
70			$42.7 \times 10^{-4}$	61.6		
80			$48.8 \times 10^{-4}$	61.1		
90			$54.9 \times 10^{-4}$	60.6		
100			$0.5 \times 10^{-5}$	90.78	$61.0 \times 10^{-4}$	60.05

Figure 4-45. Amplifier - Noise Power Output

generated noise is not a significant contributor to the output noise, the output S/N ratio per tube remains constant. If the klystrons are operated in parallel instead of cascade, the same noise level per tube would occur.

#### 4.3.5 KLYSTRON POWER LEVEL

The converters will have outputs feeding into a waveguide array as described in the transmitting antenna section. Since the waveguide losses vary directly with the rf power output, this should be considered in determining an optimum power output level.

The basis for this analysis is the high power klystron described earlier, using a beam conversion efficiency of 75 percent. For final analysis this efficiency was raised to 84 percent. Dr. Kosmahl at Lewis Research Center has predicted this efficiency as being attainable. Figure 4-46 tabulates the resulting tube parameters for the 84 percent beam efficient klystron versus the 75 percent tube.

Waveguide losses versus rf power output per tube are indicated in Figure 4-47 for two waveguide configurations. The first configuration has the full rf output power connected directly to the waveguide system using approximately a one meter length of interconnecting waveguide. In the second configuration, the rf output per tube is divided into six, using the configuration of Figure 4-48. The tube output is divided into two by a power splitter and then subdivided into three parts by using sidewall directional couplers. Losses are estimated based upon a waveguide attenuation of 0.015 dB/meter. Only  $I^2R$  losses are considered. In estimating the losses for the direct connection of the klystron to the antenna, a one meter length of guide was allowed as a connecting link between the klystron and antenna.

Klystron parameters obtained by extrapolation of previous data is tabulated in Figure 4-49. Figures 4-50 and 4-51 give the waveguide losses and net efficiency of the two cases studied: the klystron to antenna direct feed and the klystron to antenna connection being made through a 6/1 power divider.

The results of this analysis indicate that to a direct connected waveguide the optimum power per tube is at approximately 36 kilowatts. Below 36 kilowatts the solenoid and filament power dominate over the klystron beam efficiency.

Parameter	75% Beam Eff	84% Beam Eff
Total Beam Power	60,000W	60,000W
Collector Dissipation	13,680	8,755.2
Body Interception	1,320	844.8
RF Generated	45,000	56,400
I <sup>2</sup> R Losses	1,820	2,038.4
RF Output	43,180	48,361.6
Sol Power	1,000	1,000
Heater	60	60
Total Input Power	61,060	61,060
Net Eff	70.7%	79.2%

Figure 4-46. Klystron Parameters for 60 kW Beam

Above 36 kilowatts the increasing large waveguide losses dominate over the basic klystron efficiency. Maximum efficiency when the klystrons are directly connected to the waveguide is approximately 76.7 percent.

When the klystron output power is divided, the waveguide losses become proportionally less. It is therefore possible to go to a much higher value of peak power per tube before the waveguide losses dominate and result in decreased efficiency. For the 6/1 divider studied, peak efficiency of 78.8 percent occurs at approximately 100 kW per tube. If higher power divider ratios are used the power per tube and maximum efficiency can be expected to increase further.

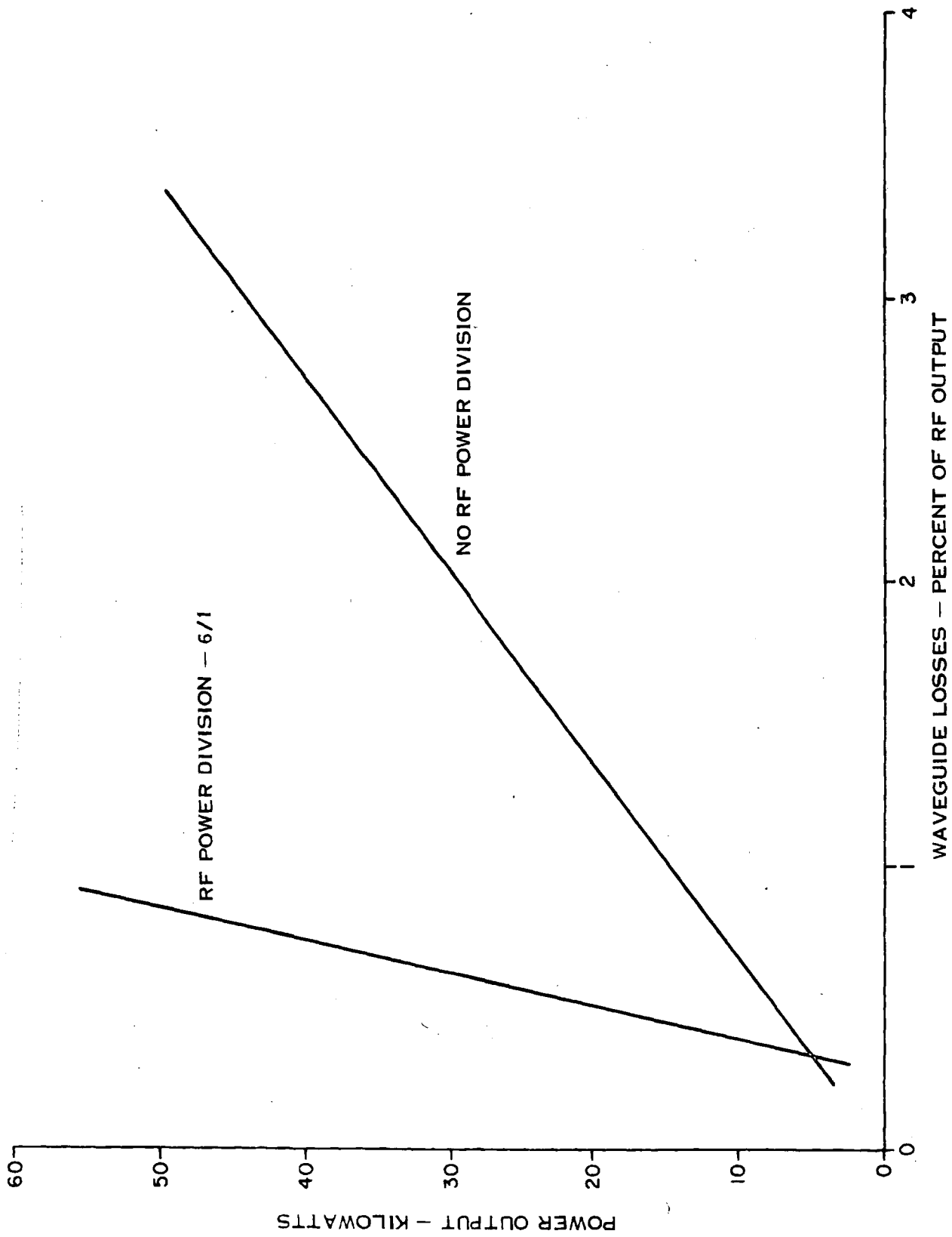


Figure 4-47. Waveguide Losses vs. RF Power Per Tube

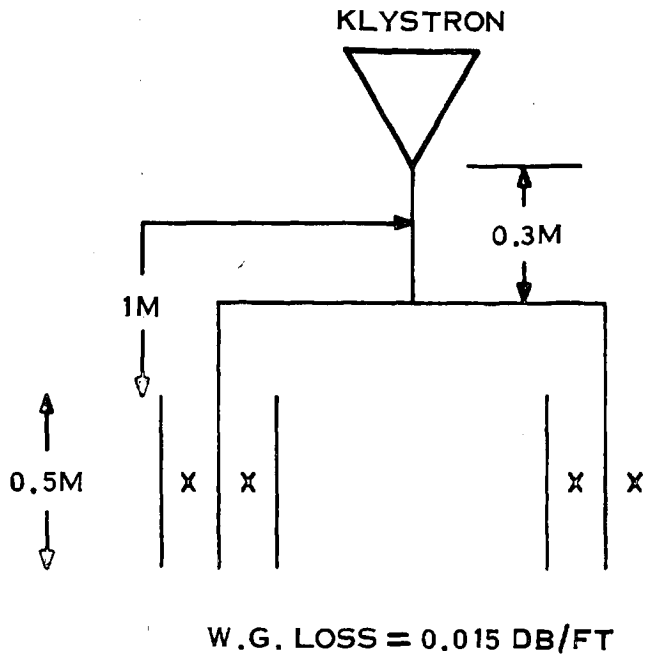


Figure 4-48. Power Divider

#### 4.3.6 CONVERTER FILTER REQUIREMENTS

The section on radio frequency allocation and interference covers the importance of reducing noise in the MPTS to preserve a maximum of the spectrum for other users. The klystron has a built-in bandpass filter effect due to its basic construction and needs no further addition except possibly for a harmonic filter as noted later. Its characteristics are shown in Figure 4-52. The five cavity tube case is selected for the recommended design. The amplatron on the other hand according to current estimates will need an output filter to reduce both random noise and harmonics.

In the amplatron circuit designed for MPTS the phase shift versus frequency characteristics are such as to locate the  $180^\circ$  mode (eight re-entrant spokes) at 2450 MHz. The network consists of 17 equally spaced vanes with a drift space of 1.0 pitch. Because of the MPTS narrow band requirements, the  $180^\circ$  mode operation is preferred which is close to the lower frequency cutoff of the amplatron network. The lower frequency cutoff of the network will occur at 2437.5 MHz.

RF Output Watts	Beam Interception	RF Losses	Solenoid Power	Heater Power	Tube Efficiency
1. 161,212.8	32,000	6787.2	1000	60	80.2%
2. 120,909.6	24,000	5096.4			80.0%
3. 100,757.6	20,000	4242.4			79.9%
4. 80,606.6	16,000	3393.6			79.5%
5. 56,424.48	11,200	2375.52			79.4%
6. 48,361.6	9,600	2038.4			79.2%
7. 44,333.52	8,800	1866.48			79.06%
8. 40,303.2	8,000	1696.8			78.9%
9. 36,272.9	7,200	1527.1			78.7%
10. 30,630.42	6,080	1289.6			78.4%
11. 24,088.0	4,897.9	1014.1			77.5%
12. 16,121.3	3,200	678.72			76.5%
13. 9,676.8	1,920	403.2	1000	60	74.1%

Figure 4-49. Klystron Parameters (Electronic Efficiency = 84%)



Tube RF Out	Antenna Waveguide Losses 1/1 6/1	Net Efficiency 1/1 6/1
161,212.8W	6196.75	77.1%
120,909.6	1945.0	78.7%
100,757.6	4455.21	78.82%
80,606.6	942.62	78.83%
56,424.48	2211.84	78.69%
48,361.6	1637.26	78.4%
44,333.52	339.71	78.48%
40,303.2	279.0	78.38%
36,272.9	936.84	78.22%
30,630.42	427.12	77.9%
24,088.0	130.19	77.13%
16,121.3	200.52	76.2%
9,676.8	37.15	73.8%

Figure 4-50. Total Efficiency with Waveguide Losses

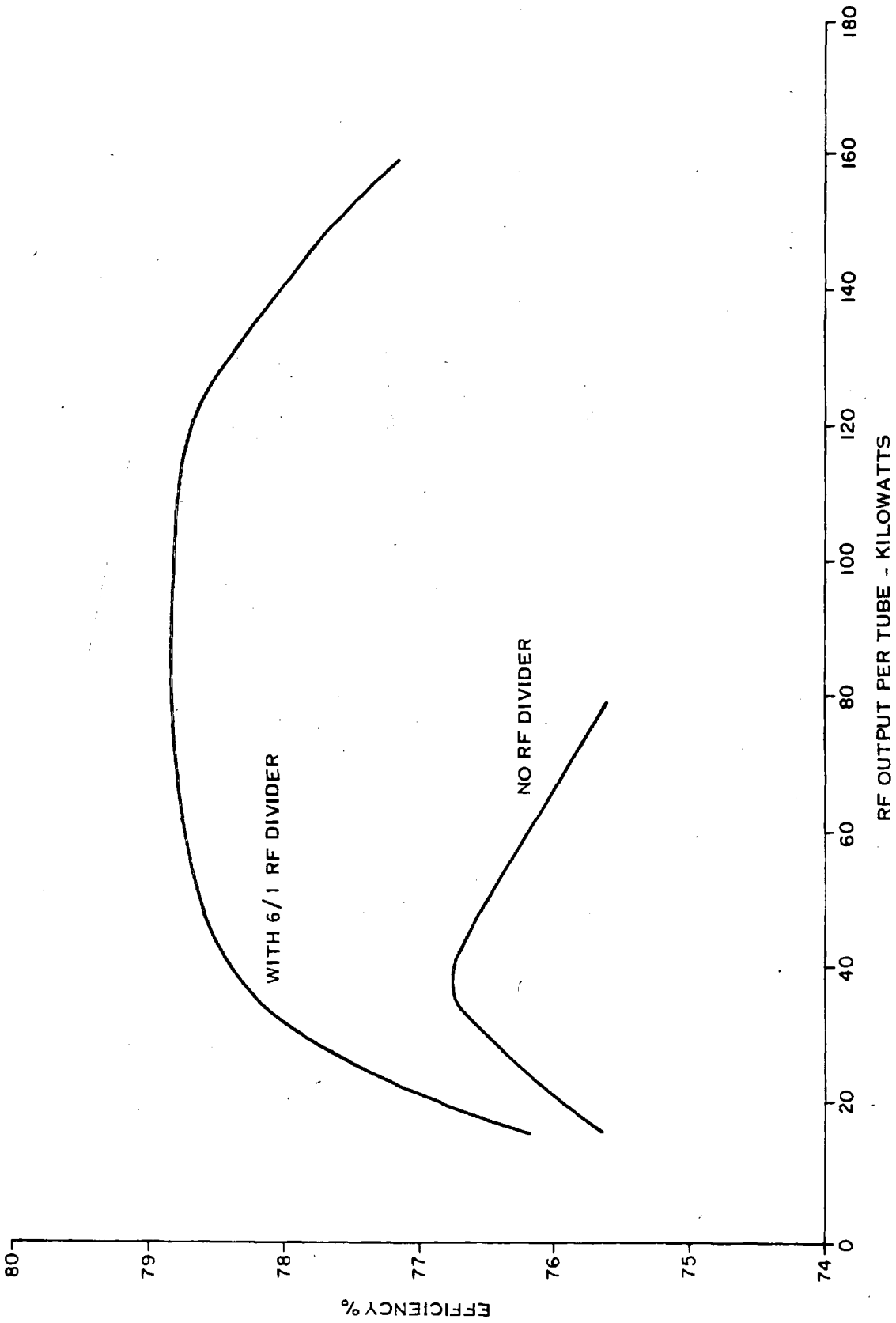


Figure 4-51. Lystron System Efficiency Including Waveguide Losses

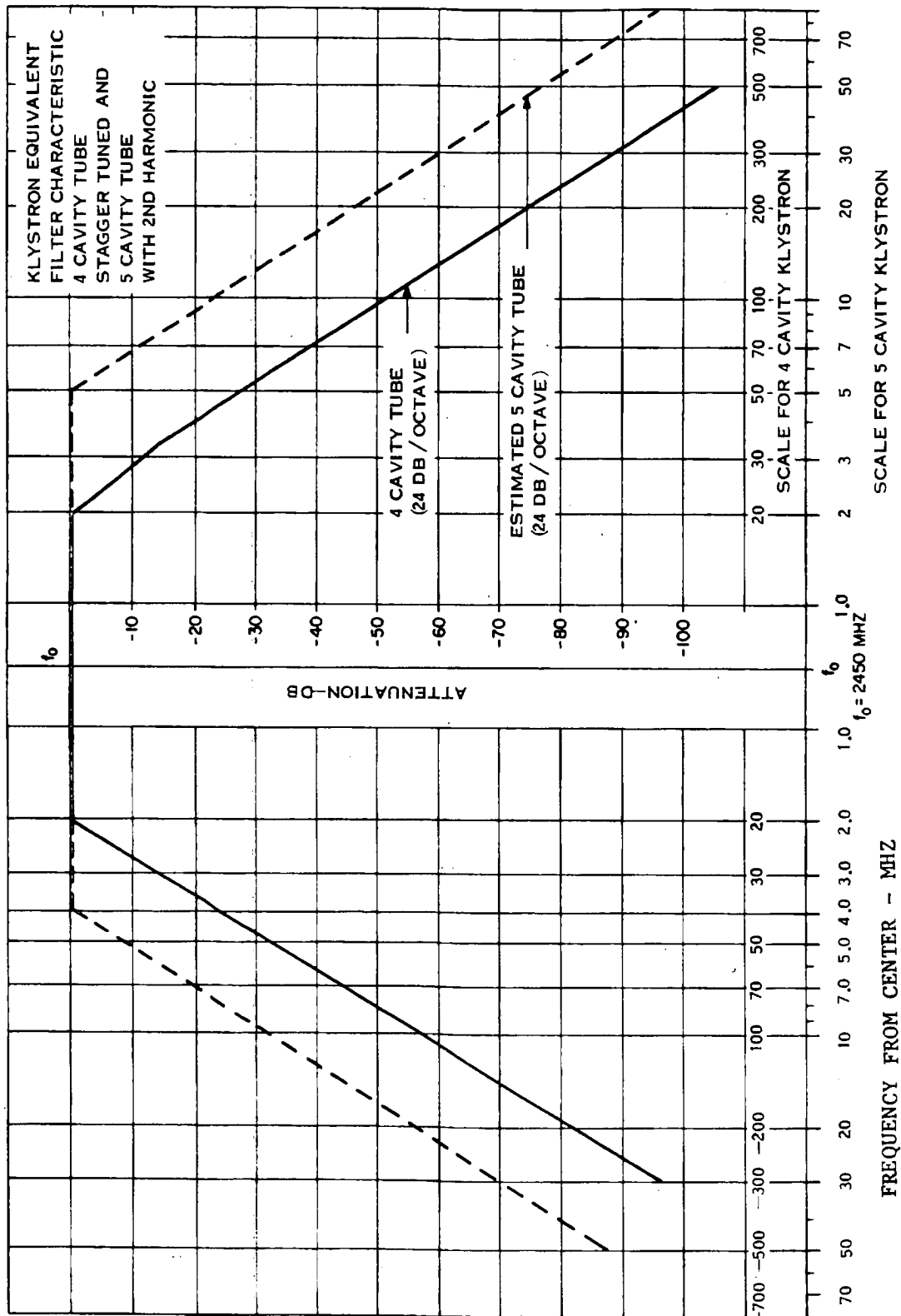


Figure 4-52. Klystron Equivalent Filter Characteristic

At this frequency the phase shift across the circuit is  $0^\circ$ . In the cutoff region the network will provide an attenuation of -18 dB/octave. Insertion loss is only 0.2 dB.

The low frequency attenuation together with characteristics for two possible designs for an output filter are shown in Figure 4-53. The filter center frequencies are offset from the MPTS operating frequency of 2.45 MHz in such a way as to minimize attenuation or insertion loss at that frequency while still providing a significant attenuation at higher frequencies. The parameters in Figure 4-2 include provision for the output filter.

#### 4.4 CONCLUSIONS AND RECOMMENDATIONS

For the amplatron:

- a. Cold pure metal cathode (platinum) for long life.
- b. Pyrolytic graphite radiator for cathode and anode for light, efficient waste heat radiation.
- c. Samarium cobalt permanent magnet for light weight and low cost.
- d. Operating frequency 1.5 GHz to 3.0 GHz; 2.45 GHz preferred.
- e. Power added 5 kW to 10 kW per tube; 5 kW preferred.
- f. Efficiency with rf noise and harmonic filters is conservative 85 percent; improvement to 90 percent is a realistic goal.
- g. Cascade configuration because of low gain characteristic.
- h. Regulation of constant current or constant phase by movable pole piece or impulse magnet technique for high efficiency.
- i. Open tube construction, possibly with contaminant baffle, for higher reliability, simple thermal control, and lower weight.

For the klystron:

- a. Hot cathode design used in study, but a cold cathode development desirable for a longer life.
- b. Pyrolytic graphite radiators for efficient heat radiation.

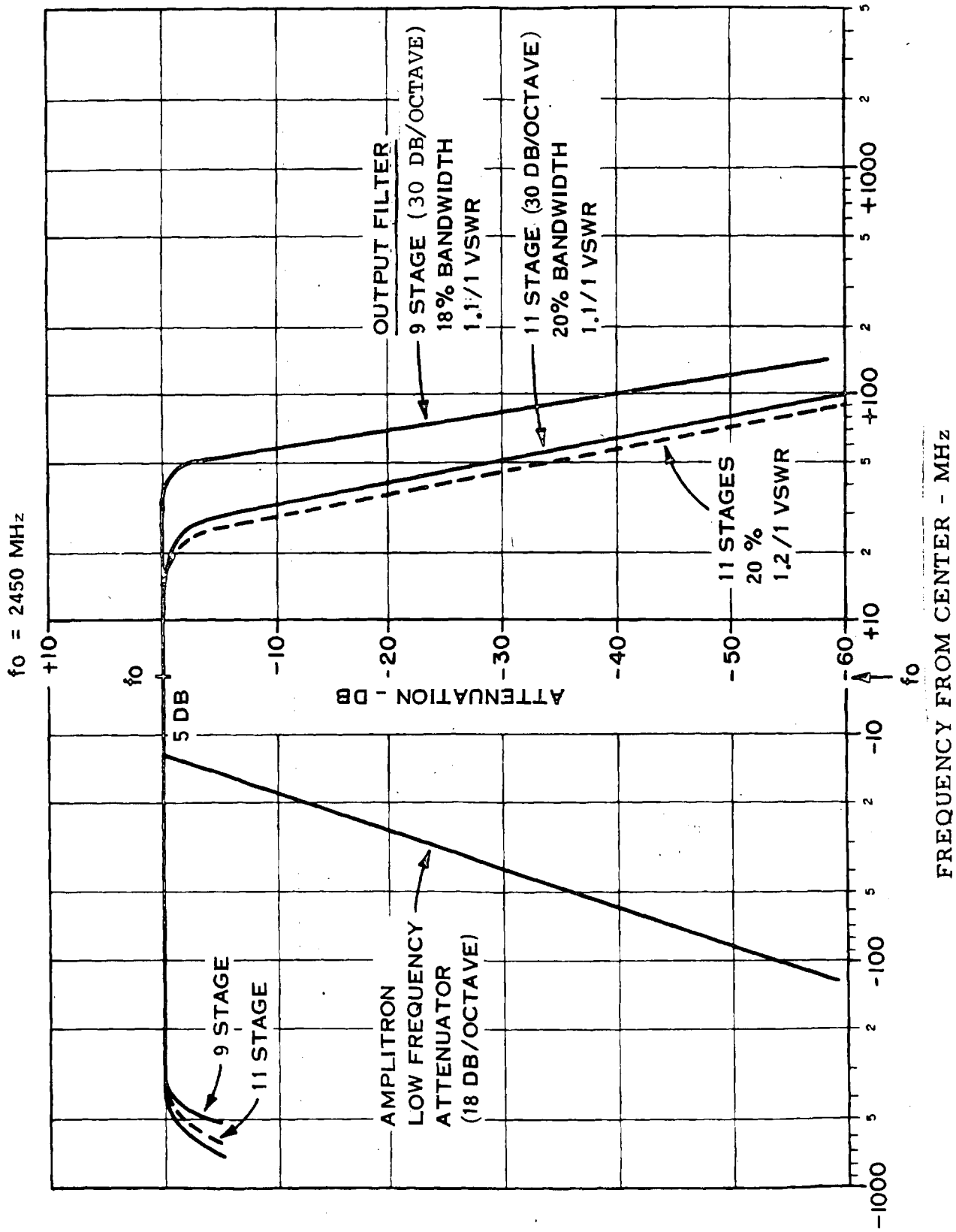


Figure 4-53. Amplitron Equivalent Filter Characteristics ( $f_o = 2450 \text{ MHz}$ )

- c. Heat pipes needed for transfer of heat to the radiator surface; study and development required.
- d. Operating frequency can be 1 GHz - 30 GHz; 2.45 GHz is good.
- e. Solenoid focusing and power outputs of 48 kW or greater, with output power dividers to the waveguide.
- f. Collector depression needed for highest efficiency; requires further study to determine practicality of reaching 80 percent.
- g. Five-stage design including a second harmonic bunching cavity to reduce noise bandwidth.
- h. Open tube construction, possibly with contaminant baffle, for higher reliability, simple thermal control, and lower weight.
- i. Parallel operation to minimize failure effects and simplify compensation for phase shift variations with voltage changes.

#### REFERENCES (SECTION 4)

- (1) Skowron, J. F., "The Continuous-Cathode (Emitting Sole) Crossed-Field Amplifier", Proc. IEEE, Vol. 61, No. 3, pp. 330-356, March 1973.
- (2) Branch, G.M. and Mihran, T.G., "Analytical Designs of a Space-Borne Magnetically-Focused Klystron Amplifier", NASA Contractor Report CR-72461, General Electric Co., Tube Department, Schenectady, New York; October 1968.
- (3) Nelson, R.B., Abraham, W.G., Lien, E., et al., "Research and Experimental Study for the Development of a 1000-Watt CW Space Environment S-Band Power Amplifier", NASA Contractor Report CR-66648, Varian Associates, Palo Alto, California; September 1968.
- (4) Lien, E. L., "Advances in Klystron Amplifiers", Microwave J., Vol. 16, No. 12, pp. 33-39; December 1973.
- (5) TWT's, Tech. Brochure, Hughes Aircraft Co., Electron Dynamics Div., Torrance, California; 1972.
- (6) McCune, E. and Misuhara, A., "X-Band PPM-Focused Wide-Band Klystron", Paper presented at the Electron Devices Meeting, Washington, D. C.; December 1972.
- (7) Mendel, J. T., "Magnetic Focusing of Electron Beams", Proc. IRE, Vol. 43, No. 3, pp. 327-331; March 1955.
- (8) Detweiler, H.K., "Characteristics of Magnetically Focused Large-Signal Traveling-Wave Amplifiers", Tech. Report No. RADC-TR-68-433, University of Michigan, Electron Physics Lab., Ann Arbor, Michigan; October 1968.
- (9) Detweiler, H.K. and Rowe, J.E., "Electron Dynamics and Energy Conversion in O-Type Linear Beam Devices", Advances in Microwaves, Vol. 6, p. 29, Academic Press, New York; 1971.
- (10) Slater, J.C., Microwave Electronics, Van Nostrand, New York; 1950.

- (11) Lien, E. L., "High Efficiency Klystron Amplifiers", Eighth Int. Conf. on Microwave and Optical Generation and Amplification, pp. 11-21 to 11-27; September 1970.
- (12) Kosmahl, H.G. and Albers, L.V., "Three-Dimensional Evaluation of Energy Extraction in Output Cavities of Klystron Amplifiers", IEEE Trans. on Electron Devices, Vol. ED-20, No. 10, 11. 883-890; October 1973.
- (13) Walder, J. and McIsaac, P.R., "Experimental Analysis of the Biased-Gap Klystron", IEEE Trans. on Electron Devices, Vol. ED-13, No. 12, 11. 950-955; December 1966.
- (14) Kosmahl, H.G., McNary, B.D. and Sauseng, O., "High-Efficiency, 200-Watt, 12-Gigahertz Traveling Wave Tube", NASA Tech. Note D-7709, Lewis Research Center, Cleveland, Ohio; June 1974.
- (15) Neugebauer, W. and Mihran, T.G., "A Ten-Stage Electrostatic Depressed Collector for Improving Klystron Efficiency," IEEE Trans. on Electron Devices, Vol. ED-19, No. 1, pp. 111-121; January 1972. Kosmahl, H., "A Novel Axisymmetric Collector for Linear Beam Microwave Tubes," NASA Tech. Note D-6093, 1971.
- (16) Stankiewicz, N., "Evaluation of Magnetic Refocusing in Linear-Beam Microwave Tubes", NASA Tech. Note D-7660, Lewis Research Center, Cleveland, Ohio; May 1974.
- (17) Feldman, Jr., K.T. and Whiting, G.H., "The Heat Pipe", Mechanical Engineering, pp. 30-33; February 1967.
- (18) Dutcher, C.H. and Burke, M.R., "Heat Pipes -- A Cool Way to Cool Circuitry", Electronics, pp. 94-100; February 16, 1970.
- (19) Anand, D.K., ed., Report on Heat Pipe Symposium/Workshop, The University of Maryland, College Park, Maryland; November 5-6, 1973.
- (20) Nishida, J.M. and Broderson, L.K., "Design, Construction and Evaluation of a 12.2 GHz 4.0 kW-CW High Efficiency Klystron Amplifier", NASA Contractor Report CR-134659, Varian Associates, Palo Alto, California; August 1974.
- (21) Branch, G.M., "Circuit Efficiency Enhancement Studies at 12 GHz", NASA Contractor Report CR-72696, General Electric Co., Tube Department, Schenectady, New York; May 1970.



- (22) Lien, E.L., "Linear Beam Tube Having a Beam Collector Cooled by Radiation through an Infrared Window", U.S. Patent No. 3448325; 1969.
- (23) Freeman, J. J., Principles of Noise, John Wiley and Sons, Inc., New York, Chs. 5 and 6; 1958.
- (24) Ginzton, E. L., Microwave Measurements, McGraw Hill, New York, pp-397, 399; 1957.
- (25) Gittins, J. F., Power Traveling-Wave Tubes, American Elsevier Publishing Co., New York, p. 144; 1965.
- (26) Tallerico, P. J. and Rowe, J. E., "Relativistic Effects in the Traveling-Wave Amplifier", IEEE Trans. on Electron Devices, Vol. 17, No. 7, pp. 549-561; July 1970.
- (27) Letter to AGED, 17 September 1975, "Results of Life Tests on Cathode Operated in Actual Microwave Guns at Two Amps/cm<sup>2</sup>", published in AGED/ Working Group A. Second Additions to Agenda for Meeting on 8 and 9 October 1975.

## SECTION 5

### POWER SOURCE INTERFACE AND DISTRIBUTION

The power interface and distribution part of the study relates to the design of the equipment bringing the high voltage and high current power from the orbital power source, beginning at the brushes of the rotary joint of a solar oriented source, throughout the transmitting array to the dc-rf converters. It must provide switching capability, regulation of the power as required by the converters, and it must protect the MPTS against individual and localized failure modes. A solar photovoltaic power source was taken as the power source model because it is a leading candidate, is relatively well defined and presents a relatively difficult problem in regulation.

The amplatron is to be operated in a constant current or constant phase regulation mode and the klystron is to be operated unregulated. A particular problem with the amplatron and solar cell power source combination is the high voltage as the system is started (such as following an eclipse), and it is recommended that this be solved by switches within the solar array that would bring up voltage in a programmed sequence.

#### 5.1 POWER SOURCE CHARACTERISTICS

Information on the solar cell characteristics has been obtained from a preliminary report<sup>(1)</sup> in the solar photovoltaic array prepared by Spectro Lab, Inc. for the earlier SSPS Feasibility Study. Figure 5-1 presents the probable characteristics of a 1985 type solar photovoltaic array with no concentrators. This condition has been chosen as representing the most severe interface problems. Although the use of concentrators increases the current available from a given area of solar cells, there is no significant change in solar cell load characteristics. The following characteristics are evident:

- a. At the normal operating temperature of  $300^{\circ}\text{K}$ , the open circuit voltage is approximately 22 percent greater than the operating voltage.
- b. At colder solar cell temperature, the available voltage from the cell increases as the maximum current decreases. This characteristic presents a turn-on problem, particularly when the solar array emerges from an earth eclipse.

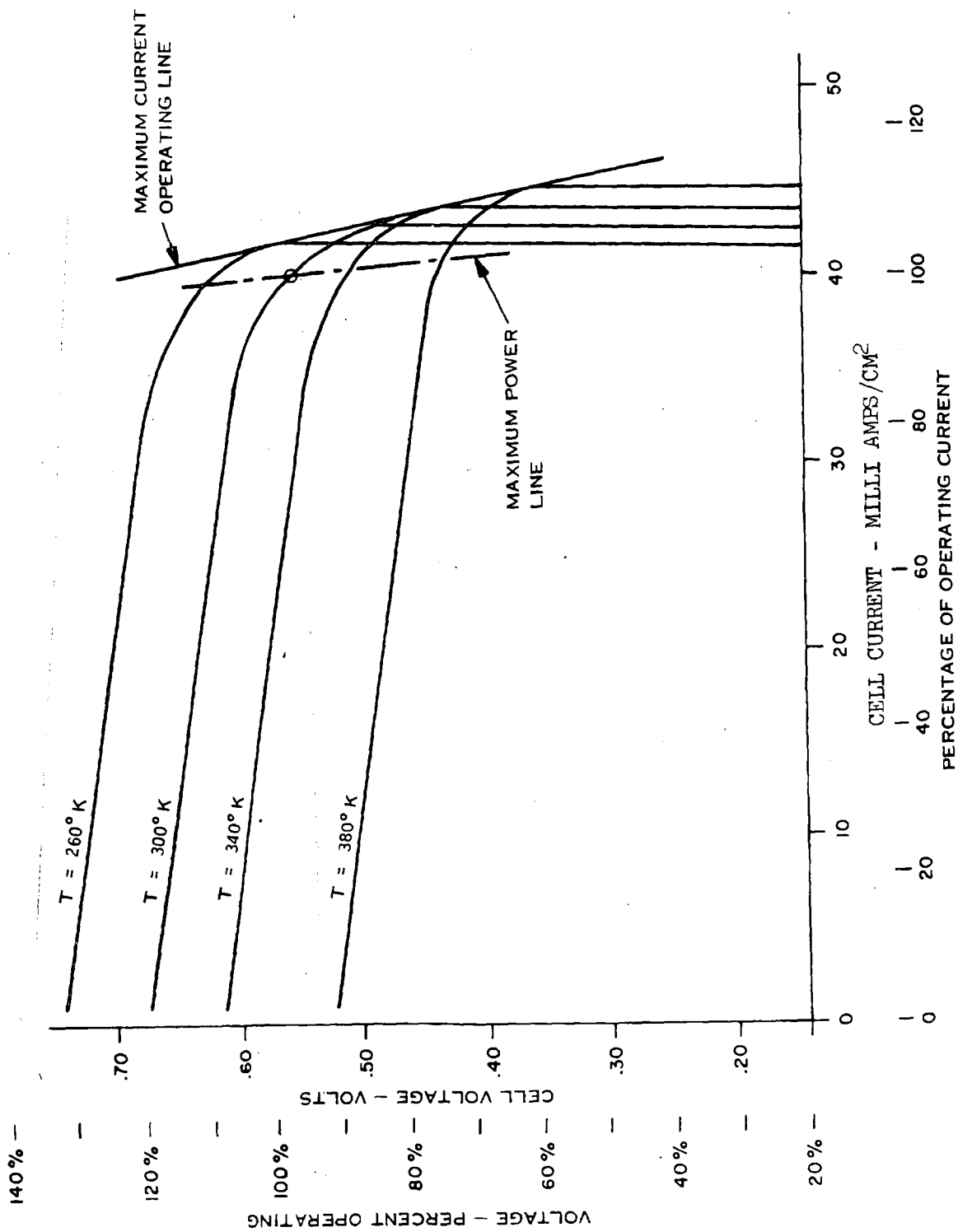


Figure 5-1. Typical Solar Cell Characteristics Based on 1985 Cell With No Concentrators

In addition to the inherent regulation of the solar cells, there are other characteristics which must be considered, such as the IR drop on conductors and protective equipment, variation in the photovoltaic cell output with solar intensity and the long term degradation of the cells' output. These various losses can all add and present a minimum voltage to the load. Figure 5-2 summarizes these losses. The impact of these losses on the solar cell source characteristics is indicated by Figure 5-3.

## 5.2 POWER SOURCE-CONVERTER INTERFACE

The interface requirements for the solar array and converters was originally examined from the standpoint of obtaining a minimum output power variation over the 30 year operating life of the MPTS. A better criteria used here is to obtain maximum available power, which depends on the maximum current line. It must be remembered, however, that this maximum current line is a limitation of the solar cells when they are all involved as a group with all of the converters operating as a group. Current for an individual converter is not limited by the maximum current line.

Figure 5-4 is a diagram depicting the volt-ampere characteristics of the klystron and the volt-ampere characteristics of the solar cells superimposed. The use of available power is given in Figure 5-5, where available power usage refers to the percentage of source power converted to rf compared to the maximum available for conversion at the particular operating voltage. Except for the case of constant current operation, where a 5 percent additional loss in efficiency occurs at minimum voltage, klystron efficiency is assumed to be constant. These results show little difference between constant current operation and no regulation. The implementation of the no-regulation technique is simpler and less complex. It is the recommended method of operating the klystron assuming accurate phase correction can be made in this mode as described in Section 4 (DC-RF Conversion).

● NO-LOAD-FULL LOAD VARIATION	-	18%
● DECREASE WITH LIFE	-	6.6%
● VARIATION WITH SUN INTENSITY	-	5.3%
● SOLAR ARRAY VOLTAGE DROP	-	3.0%
● MICROWAVE ARRAY VOLTAGE DROP	-	3.0%
<b>TOTAL VARIATION</b>		<b>35.9%</b>

Figure 5-2. Source Voltage Characteristics Solar Cell

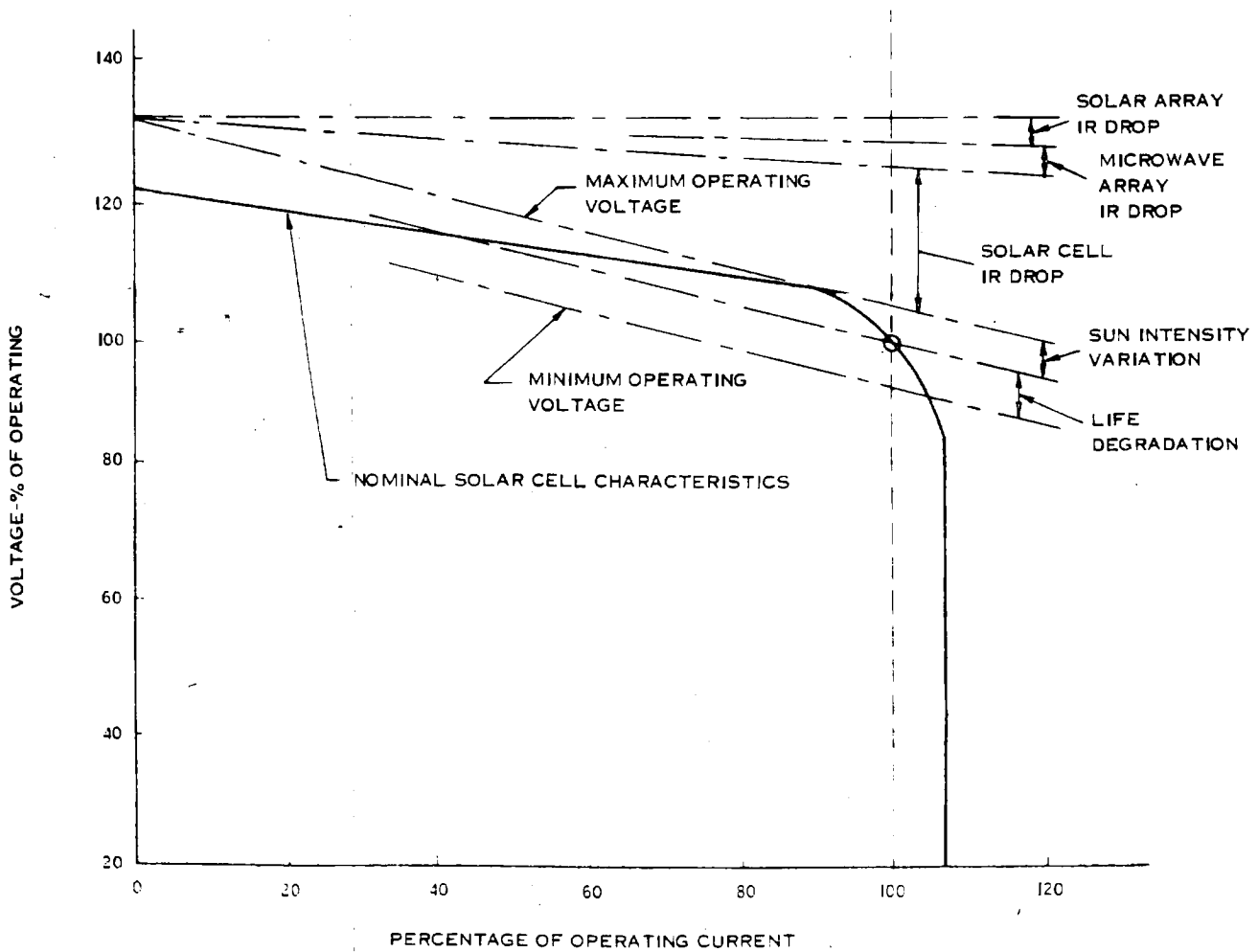


Figure 5-3. Total Source Characteristics

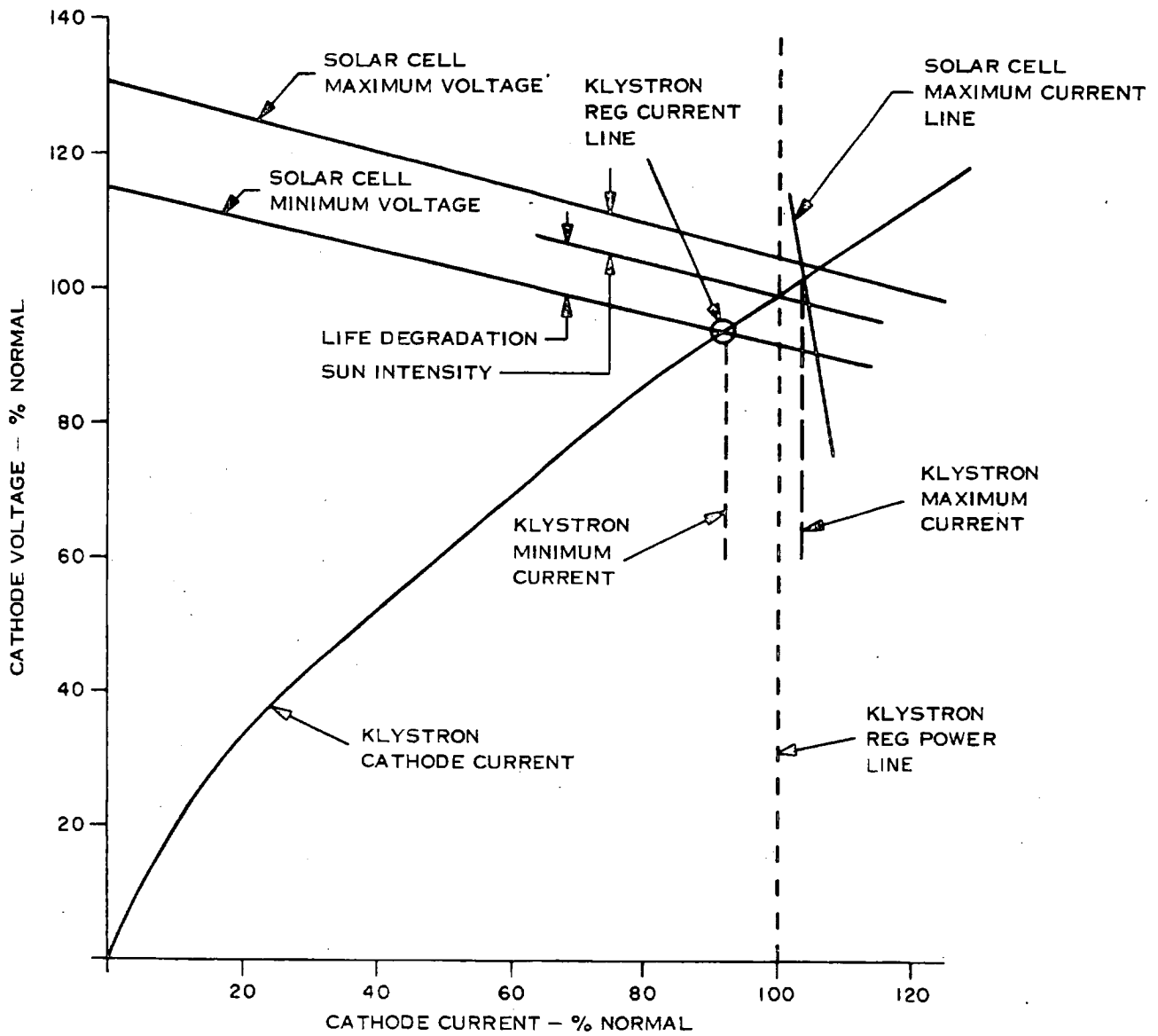


Figure 5-4. Klystron-Solar Cell Interface

	Minimum Voltage	Maximum Voltage
Unregulated	90 %	98.6%
Constant Current	90.5%	98.1%
Constant Power	98 %	86.9%

Figure 5-5. Klystron Operation Available Power Usage

In the amplatron case, the same modes of operation are analyzed as for the klystron. Figure 5-6 shows the superposition of the amplatron characteristics with the solar cell characteristics. For these potential operating modes the percentage usage of available power is given as follows:

AMPLITRON OPERATION - AVAILABLE POWER USAGE

	Minimum Voltage	Maximum Voltage
Unregulated	79 %	97.2%
Constant Current	92.4%	97 %
Constant Power	98.7%	89.8%

We see that there is a significant disadvantage in operating the amplatron unregulated. The constant current mode of operation is recommended because it has both good phase stability (see Section 4) and power usage. Regulation for constant phase may be superior overall because of higher beam efficiency or possibly easier implementation. It is therefore recommended to be investigated as an option.

### 5.3 POWER DISTRIBUTION FLOW PATHS

Three alternate flow paths for the dc power in the microwave array can be projected as possible options: lateral power flow, circular power flow and radial power flow. To enable analysis of the distribution system, the microwave transmitting array was subdivided into an arbitrary network of equal power areas. This is indicated by Figure 5-7, with a distribution grid superimposed for the lateral and circular flow paths as indicated by Figure 5-8 and 5-9.

Analysis of the system consisted of subdividing the distribution into four categories, identified as primary feeders, secondary feeder, testing feeders and subarray distribution. These are identified for the lateral flow case in Figure 5-9. Methodology involved in comparing the flow systems is as follows:

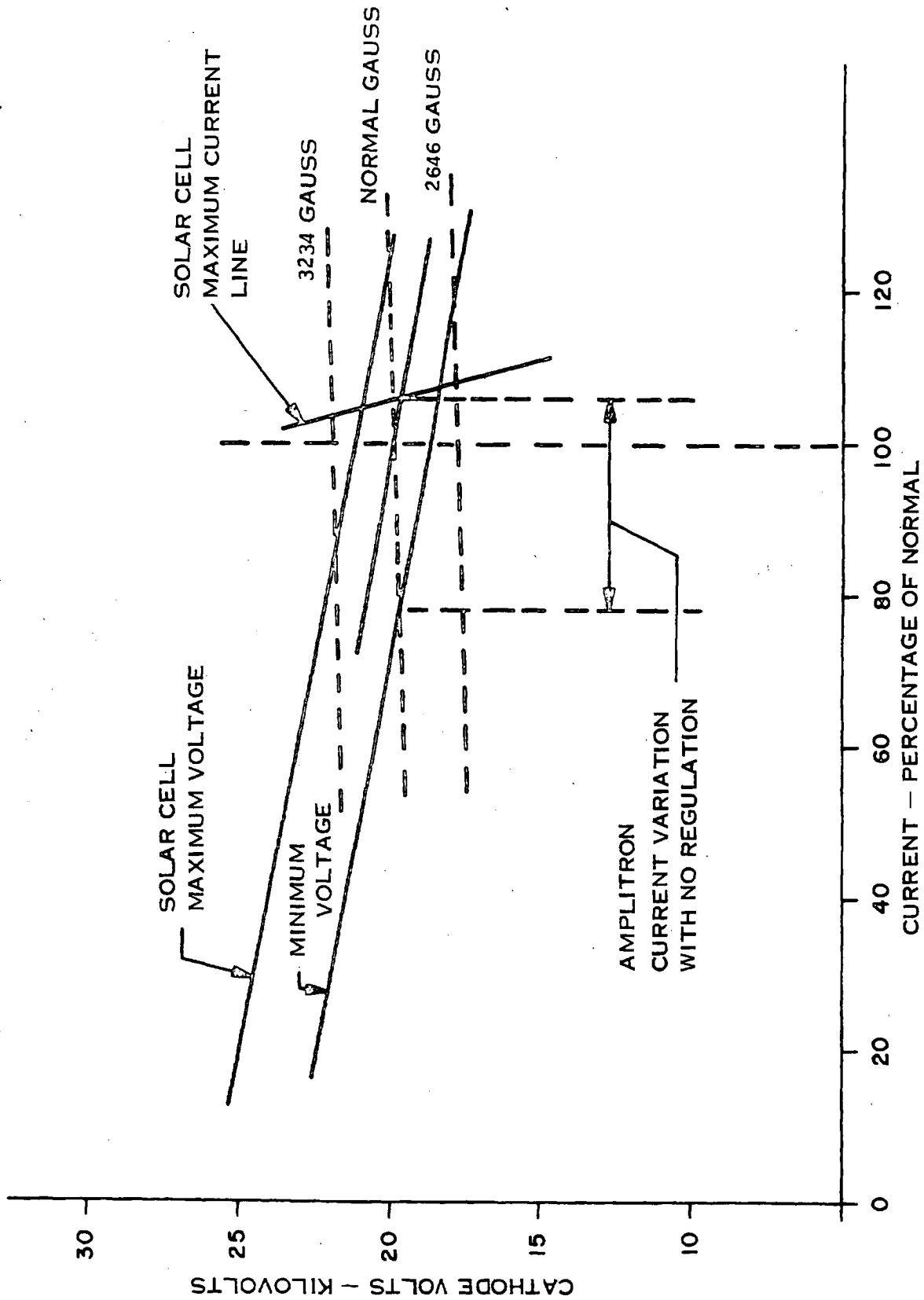


Figure 5-6. Amplitron-Solar Cell Interface



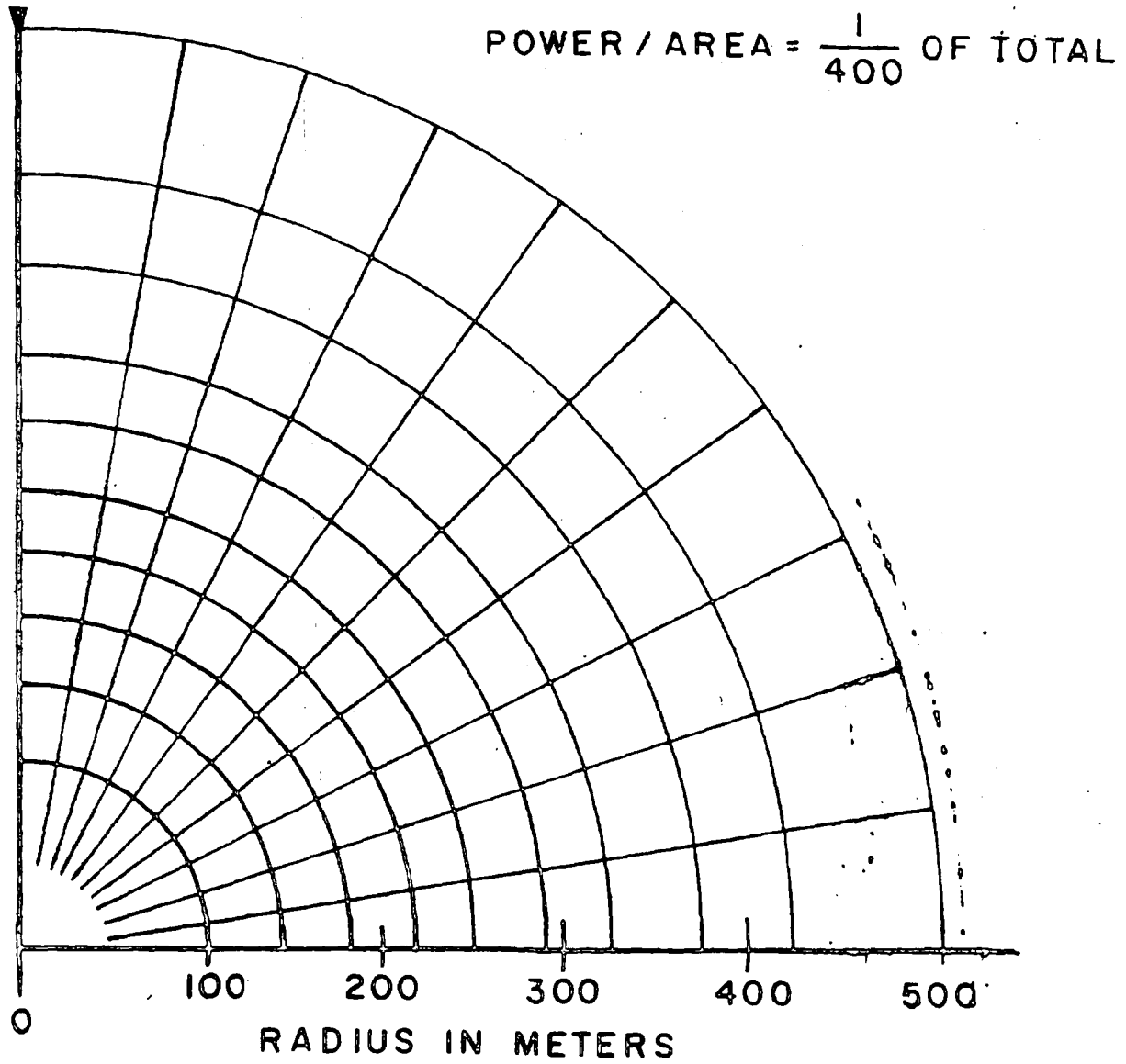


Figure 5-7. Quadrant of Microwave Platform Divided into Areas of Equal Power

CIRCULAR FEED NO.	UNIT AREAS PER FEED
----------------------	------------------------

1	30
2	40
3	30

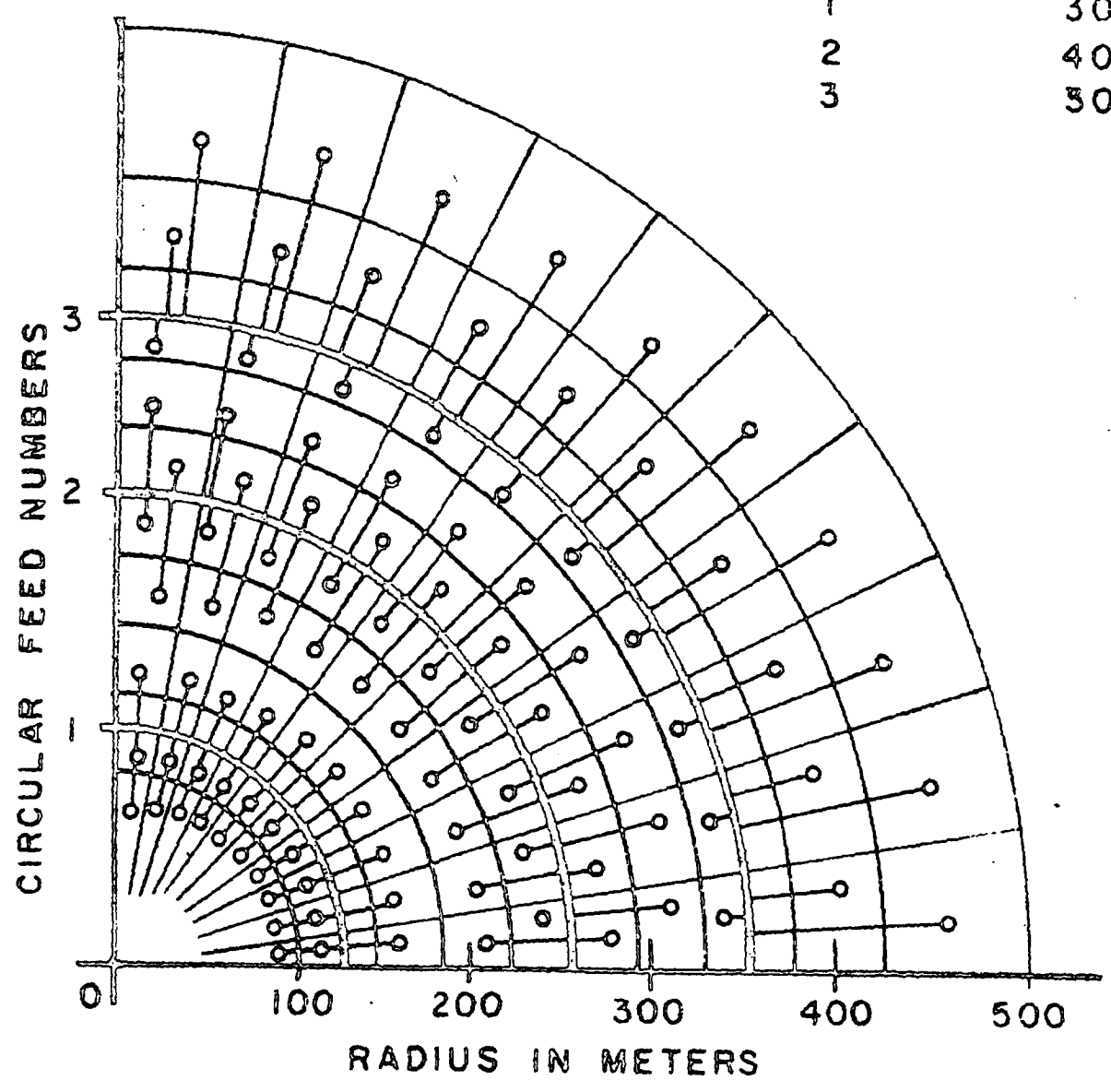


Figure 5-8. Circular Power Flow

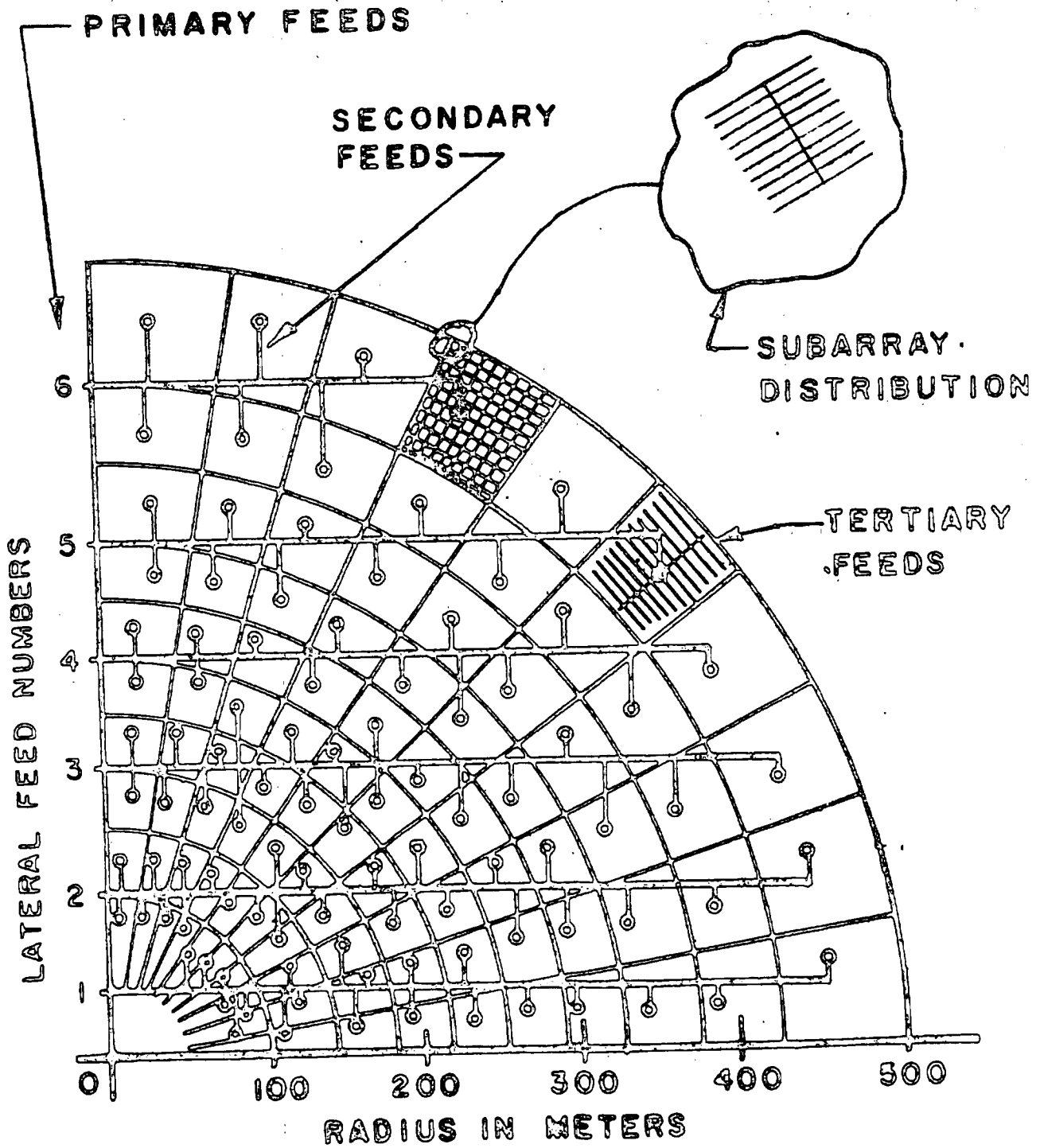


Figure 5-9. Power Distribution Lateral Power Flow

a. A total source power requirement of 15 GW (10 GW Ground Power) was used for the base parameters in preliminary analysis.

b. Voltage drop per feeder buss was chosen, buss area was calculated from the relationship

$$A = \frac{\rho}{E} \frac{IL}{2}$$

where:

$\rho$  = specific resistivity (= 2.83 ohmmeters at room temperature)

$I$  = total current

$L$  = buss length

$E$  = voltage drop (max drop at end of buss assuming uniform loading along length)

c. For secondary feeders area was calculated using average length of feeder.

d. For tertiary feeders it was assumed that each unit area of equal power was divided into 64 subarrays.

e. Subarray distribution assumes 100 tubes/subarray - with 20 busses feeding five tubes each.

Results of this analysis are given in Figure 5-10, for the lateral, circular and radial flow patterns. Data shown in these figures are for an operating temperature of 293°K (20°C).

Preliminary estimates of operating temperature indicated that temperatures could be between 400°K - 500°K (127°C - 227°C). Resistance versus temperature is given by:

$$R_{T_2} = R_{T_1} [1 + \alpha (T_2 - T_1)]$$

where

$\alpha$  = thermal coefficient of resistivity

= 0.0039 ohm - °C for aluminum

CONDUCTOR WGT'S KG'S

	CIRCULAR	RADIAL	LATERAL
<b>PRIMARY FEED</b>	$62.6 \times 10^3$	$44.2 \times 10^3$	$47.7 \times 10^3$
<b>SECONDARY FEED</b>	$6.1 \times 10^3$	$13.9 \times 10^3$	$1.6 \times 10^3$
<b>TERTIARY DIST.</b>	$.7 \times 10^3$	$.7 \times 10^3$	$.7 \times 10^3$
<b>SUBARRAY DIST.</b>	<u><math>.1 \times 10^3</math></u>	<u><math>.1 \times 10^3</math></u>	<u><math>.1 \times 10^3</math></u>
<b>TOTAL</b>	$70.4 \times 10^3$	$58.9 \times 10^3$	$50.4 \times 10^3$
	$(134.8 \times 10^3 \text{ LBS})$	$(129.6 \times 10^3 \text{ LBS})$	$(110.9 \times 10^3 \text{ LBS})$

Figure 5-10. Distribution System Weight Estimate (15 GW Input Power)

For purposes of the present parametric study, a multiplying factor of two was assumed for resistance of the conductor at operating temperatures. Thus to maintain the design values of voltage drop requires doubling both the area of the conductors and the weight of the conductors from that given in Figure 5-10.

#### 5.4 MAGNETIC INTERACTION

The direct current distribution of the transmitting antenna produces magnetic dipoles, which will react with the Earth's magnetic field and produce rotational torques. The power flow paths used in the array must be such as to minimize this torque. Figures 5-11 and 5-12 indicate the basic torque relations for the cases of lateral power flow and radial power flow. Providing reasonable symmetry is maintained in all quadrants of the circular array, both of these distribution patterns exhibit a natural cancelling effect, and the net torque will be near zero.

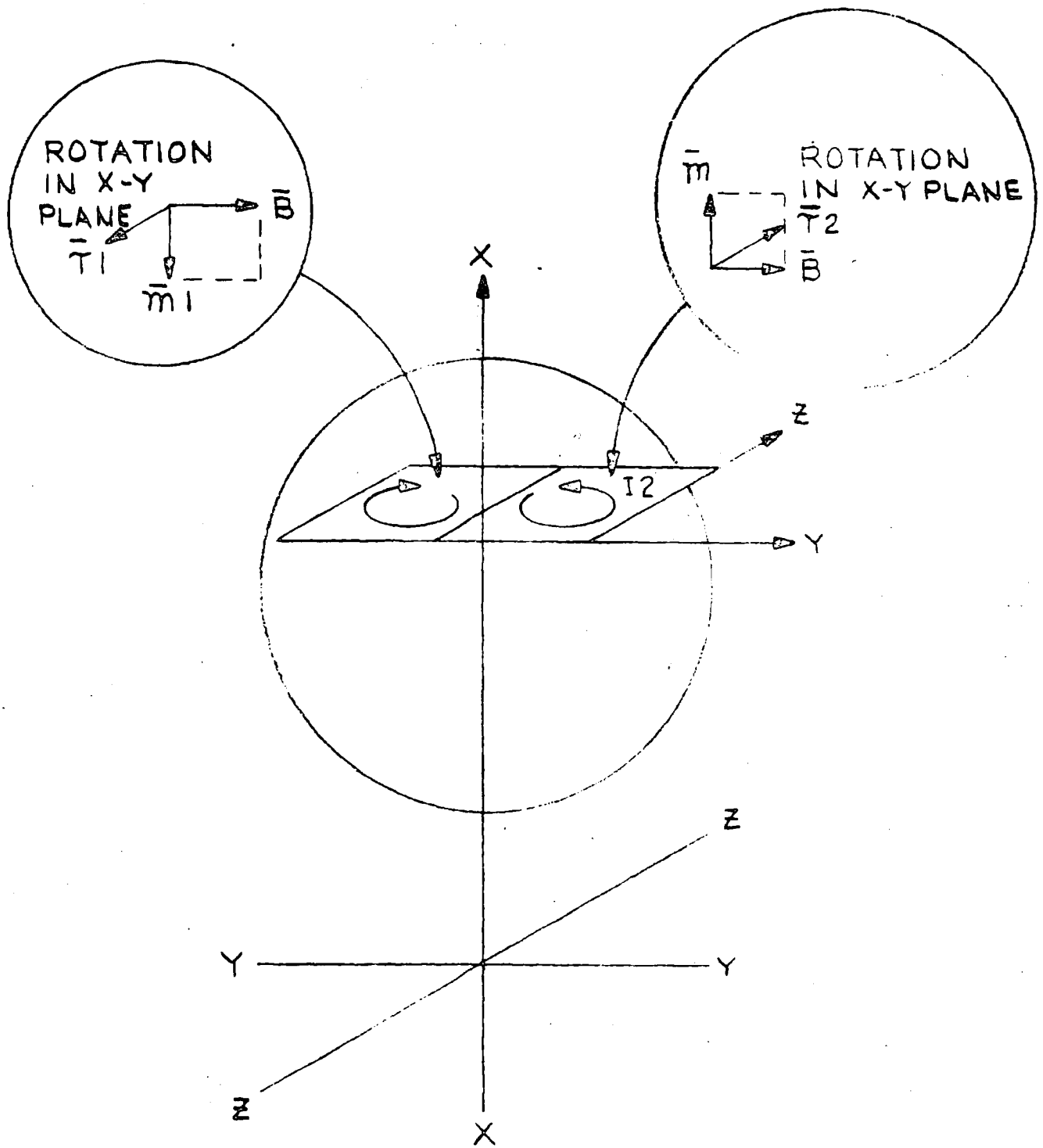
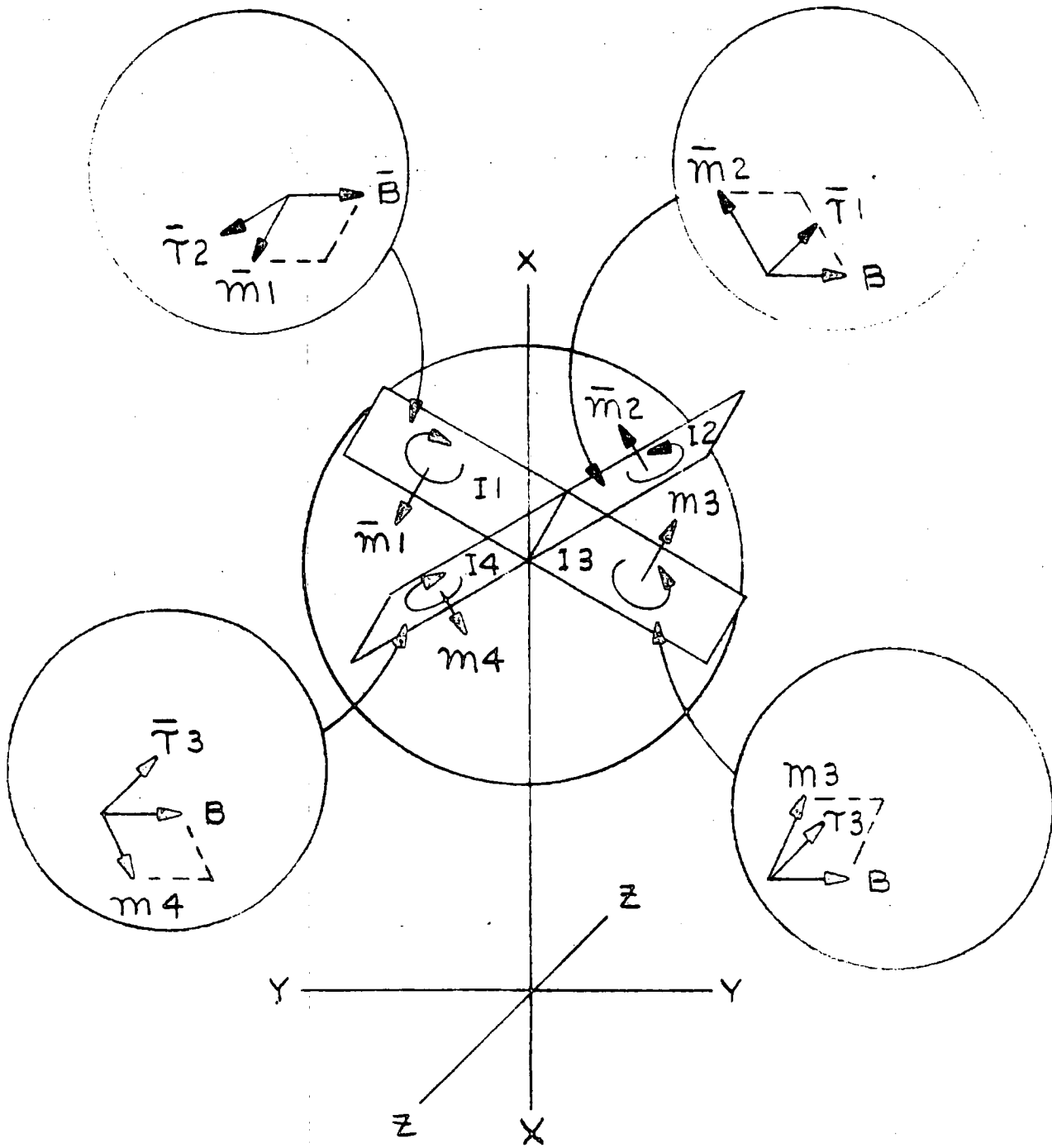


Figure 5-11. Microwave Array - Magnetic Torque - Lateral Power Flow



$$\begin{aligned} \bar{T}_1 &= \bar{m}_2 \times \bar{B} = |m \cdot B| \sin 120^\circ = -.866 mB \\ \bar{T}_2 &= \bar{m}_2 \times \bar{B} = |m B| \sin 240^\circ = .866 mB \\ \bar{T}_3 &= \bar{m}_3 \times B = |m B| \sin 60^\circ = .866 mB \\ \bar{T}_4 &= \bar{m}_3 \times B = |m B| \sin (-60^\circ) = -.866 mB \\ \Sigma T'S &= \bar{T}_1 + \bar{T}_2 + \bar{T}_3 + \bar{T}_4 = 0 \end{aligned}$$

Figure 5-12. Microwave Array - Magnetic Torque - Radial Power Flow

However, there does exist the probability of a power failure on one of the feeds, resulting in the opening of a circuit interrupter and an unbalance in the magnetic torques acting on the array. To establish an order of magnitude of this unbalance, the effect of opening a secondary and a primary feeder on the lateral flow arrangement was examined. It was found that the effect of opening a secondary feeder results in an unbalance torque of between one and two newton - meters (0.75 - 1.5 ft. lbs.), while the effect of opening a primary feed is a torque of 1.45 n-m (1.07 ft. lbs.). These torques are negligible compared with other disturbances (see Section 8).

### 5.5 DC TO RF CONVERTER PROTECTION

In microwave radar and communications applications considerable effort is devoted to protecting the individual rf tube from damage. Typical protection sensing device parameters are given below.

#### Typical RF Tube Protective Sensing Device Parameters

- a. High gas pressure
- b. High cathode voltage
- c. Excessive body current
- d. High average beam current
- e. High VSWR in output waveguide
- f. Arcing in output waveguide
- g. Overtemperature sensing
- h. Excessive rf drive
- i. rf drive interlock

Protection is generally necessary and justified because the rf output device typically represents the largest cost item and one of the most sensitive elements for catastrophic failure resulting as a secondary failure from faults in other parts of the system. The same strategy of tube protection should not be applied in MPTS. First, the large number of tubes has resulted in a relatively low tube cost, such that it is not economical to provide protection on a one to one basis. Secondly, the long life and the goal of minimal maintenance requires a system



that will allow maximum performance from each tube but, in the event of a tube failure, will remove the faulty tube from service, while maintaining the maximum capability from the remainder of the system.

A detail analysis of probable failure modes will have to be made by the tube design engineer in later design efforts. However, some first order failure modes are examined here. Figures 5-13 and 5-14 tabulate faults for the klystron and amplitrons with a preliminary estimate of their effect on system performance. A review of these indicates that only dc and rf arcing need to be of concern over the expected life of the tube. With Samarium-cobalt accidental degaussing is not very likely. RF arcing is not expected to occur unless there is pollution that will allow the arcing to start. Once started it can be expected to clean up with time.

The fault mode of significant concern is that of a dc arc. Periodic dc arcing is common in many high power microwave tubes and because the dc arc represents a short circuit directly across the power source, a tremendous amount of energy is available to sustain the arc. Not only can this energy cause irreparable damage to the rf amplifier, but severe overloading and damage in the lower portion of the distribution system can occur.

Failure	Result
DC Arcing	<ul style="list-style-type: none"> <li>o Loss of rf output</li> <li>o dc short circuit</li> </ul>
RF Arcing	<ul style="list-style-type: none"> <li>o Intermittent/erratic drive to tubes further down chain</li> <li>o Noisy output</li> <li>o Generation of gas</li> </ul>
Decrease of Magnetic Field	<ul style="list-style-type: none"> <li>o Compensated within regulation range</li> <li>o Low power output</li> </ul>

Figure 5-13. Amplitron Failure Modes and Probable Results

Failure	Result
DC Arcing	<ul style="list-style-type: none"> <li>● Loss of rf output</li> <li>● dc short circuit</li> </ul>
RF Arcing	<ul style="list-style-type: none"> <li>● Intermittent/erratic drive to tubes further down chain</li> <li>● Generation of gas</li> <li>● Noise</li> </ul>
Decrease in Magnetic Field	<ul style="list-style-type: none"> <li>● Poor beam transmission</li> <li>● High body interception</li> <li>● Low power output</li> </ul>
Low Emission	<ul style="list-style-type: none"> <li>● Loss of power output</li> </ul>

Figure 5-14. Klystron Failures and Probable Results

Normal protection for rf tube dc arcing is generally provided by an electronic crowbar circuit. This circuit effectively diverts energy from the load within a few microseconds of an arc. As usually employed, an electronic crowbar requires manual resetting for resumption of normal operation. In systems such as MPTS employing a large number of tubes, this is an unacceptable procedure. Raytheon has performed experimental testing on a recycling crowbar (Reference 5-2) intended to provide automatic resetting of crowbar faults.

A concept for the dc-rf conversion device and the crowbar unit is given by Figure 5-15. An increase in current above a preset reference is detected by the voltage increase across the energy diverting resistors. The logic and trigger generator circuits then trigger a vacuum spark gap TVG-1. TVG-1 fires and effectively short circuits the load, removing voltage from the faulted tube and allowing for the arc to recover. The short circuit of TVG1 allows L1 and C1 to form a resonant loop, conducting on one-half cycle through TVG-1 and on the alternate half cycle through CR-1. TVG-1 recovers during the conduction of CR-1. Full voltage is reapplied to the load after one resonant cycle of L1 and C1. L2 provides isolation from the power source during this time.

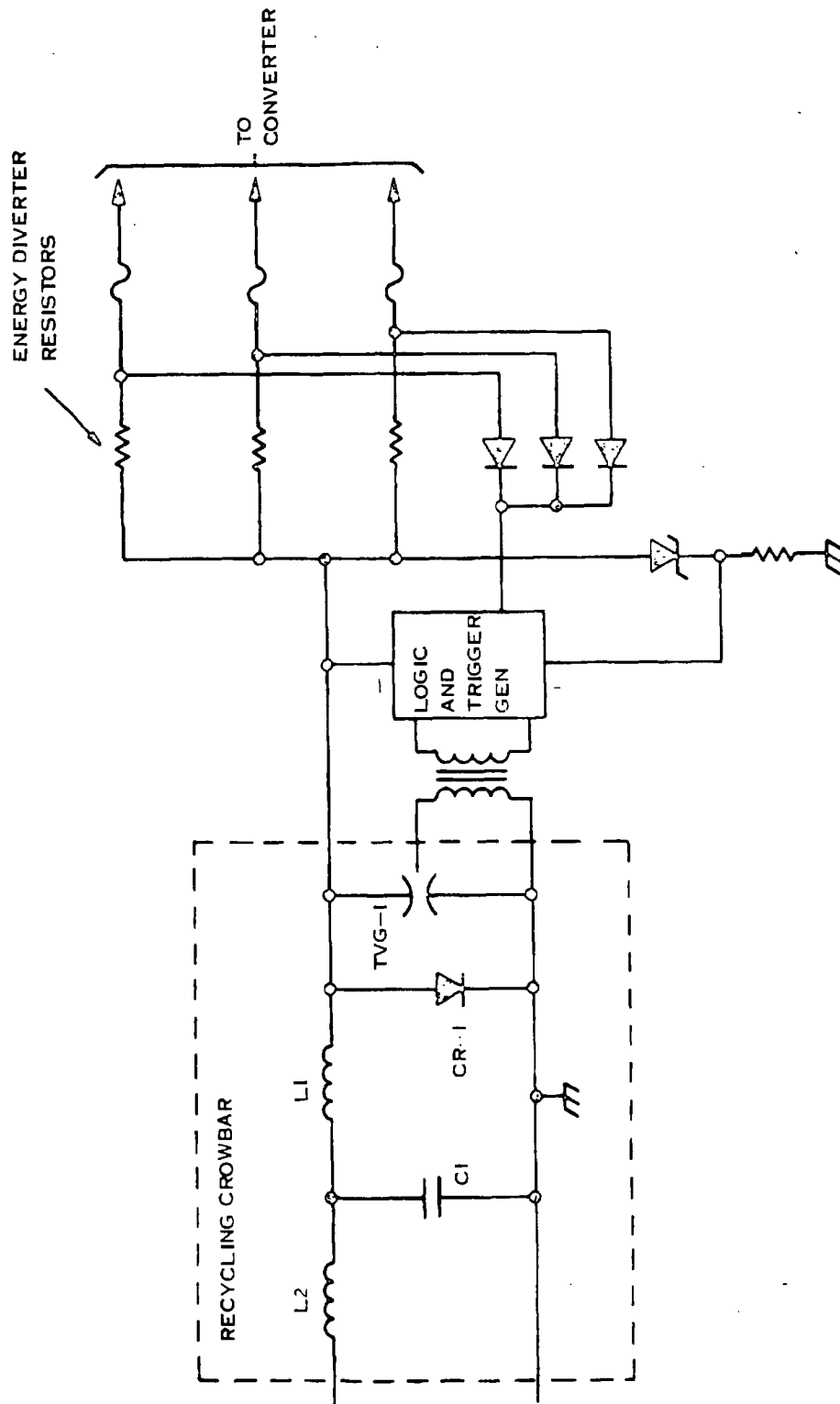


Figure 5-15. Concept for Converter/Crowbar Interface

Recovery of the faulted tube is expected to occur during the one crowbar cycle described (approximately 100 microseconds). In the event that it does not, the logic circuit will recycle the crowbar over several cycles. If, after several cycles, the fault continues to exist, the fuse in series with the shorted load will open, effectively removing the faulted tube from the supply. The remainder of the tubes will continue to operate.

## 5.6 POWER DISTRIBUTION SYSTEM

In applications of crowbar type devices the major design criteria generally is the arc energy dissipated in the rf tube before the stored energy of the power supply is diverted by the crowbar unit. Typical values of energy allowed per arc varies from 4.0 to 40 joules. A value of 4.0 joules per arc will be used. In the proposed distribution layout the maximum length of a feeder from the crowbar unit to the tube is 77.5 meters. Estimating capacity and inductance based upon Number 19 wire one meter from the ground plane gives a conductor inductance and capacitance of:

$$\begin{aligned} L &= 130.9 \text{ uhy} \\ C &= 488.5 \text{ pfd} \\ \text{Stray cap/tube} &= 90 \text{ pfd} \end{aligned}$$

The total energy stored is then given by:

$$\text{Total Energy Stored} = 1/2 L_C (nI)^2 + 1/2 (C_C + nC_T) V^2$$

where

$$\begin{aligned} n &= \text{number of tubes} \\ L_C &= \text{conductor inductance} \\ I &= \text{current per tube} \\ C_C &= \text{conductor conductance} \\ C_t &= \text{tube capacitance} \\ V &= \text{operating voltage} \end{aligned}$$

Solving for n with an operating voltage of 20,000 volts results in a maximum number of tubes per crowbar of 1126 tubes.

A second limitation on the number of tubes per crowbar is related to the performance degradation that occurs each time a crowbar fires. For a first order approximation we assume the following characteristics:

- o RF devices will have an arc rate of one every 3,000 hours
- o The maximum arc current per spark gap is 100,000 amperes
- o The maximum design life for a spark gap is 100,000 operations

For 30 year life the spark gap must hold off voltage and trigger upon command for this period. If the triggered spark gap has a life of 100,000 arc firings, then the number of allowable crowbar firings (over the 30 year life) would be:

$$\frac{262,000 \text{ hours}}{100,000} = 2.62 \text{ hours per crowbar operation}$$

The number of tubes per spark gap is found to be:

$$\begin{aligned} \text{No. Tubes} &= 3,000 \frac{\text{hours}}{\text{arc}} \times \frac{1 \text{ arc}}{\text{crowbar}} \times \frac{1 \times \text{BAR}}{2.62 \text{ hours}} = 1145. \\ &= 1150 \text{ tubes/crowbar} \end{aligned}$$

At 0.3 amperes per tube this would result in a maximum current of 345 amperes per crowbar.

A third consideration in the number and location of the crowbar units is their relationship to a subarray, a basic antenna building block as described in the section on Transmitting Antenna. The crowbar unit, in addition to being a protective element also incorporates the features of a low level switch gear. Since the lowest subintegral of tube groups is a subarray, it is desirable that a relationship exist between the number of crowbar units and the number of subarrays.

To relate the number of subarrays with the number of crowbar units, the five step approximation to a 10 dB taper (covered in Transmitting Antenna section) has been chosen. Figure 5-16 indicates the relationship between the number of crowbars and the subarrays. As can be seen, this results in a maximum current of 259.2 amperes per crowbar unit, conservatively within the postulated maximum of 345 amperes per crowbar.

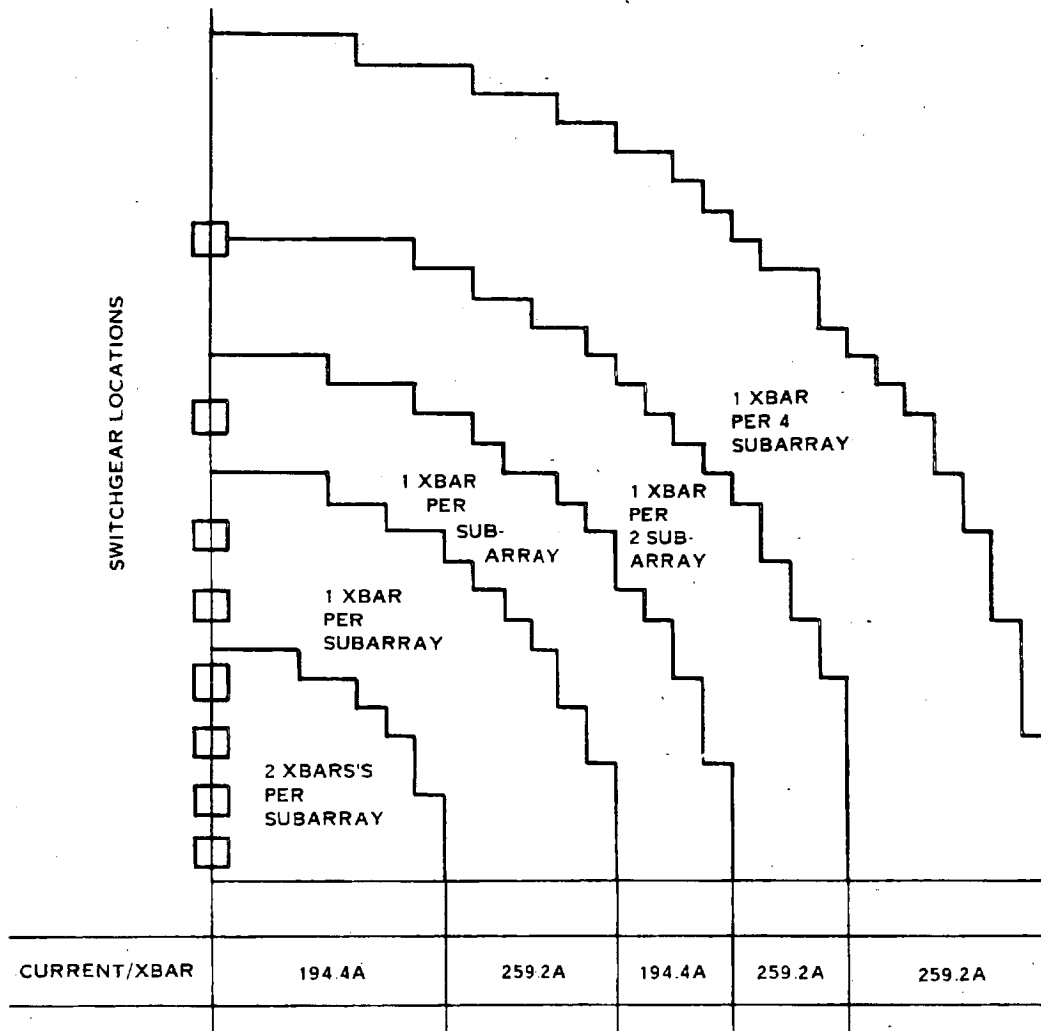


Figure 5-16. Crowbar and Switchgear Distribution

The design of the crowbar and circuit interrupter units are dependent upon the fault current existing at the time of contact interruption. For this purpose the projected fault currents that exist at different places in the power distribution system have been examined.

Figure 5-17 indicates the short circuit current under two conditions: circuit conduction limited and solar cell maximum current limited, a more realistic case.

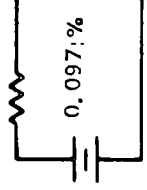
	SOLAR ARRAY	PRIMARY FEEDERS	SWITCH-GEAR	LATERAL FEEDERS	CROWBAR UNIT	SUBARRAY FEEDERS
						
	0.097%	0.93%	0.33%	46.7%	9.8%	208.3%
PERCENTAGE IMPEDANCE NORMALIZED TO $250 \times 10^6$ W						
CKT LIMITED SHORT CIRCUIT CURRENT	12,571,000	1,186,000	898,000	25,365	21,097	4,364
SOLAR CELL LIMITED SHORT CIRCUIT CURRENT	438,000	438,000	438,000	35,365	21,097	4,634

Figure 5-17. Power Distribution System Short Circuit Currents

The magnitude of the short circuit currents occurring in the event of a short at the output of the switch gear (438,000 amperes for a 5 GW ground output MPTS) is of particular concern, primarily because it is a dc circuit. In circuit breaker applications the actual interruption of current occurs at close to current zero's. In ac circuits, the current zero occurs naturally.

For a dc circuit therefore, the zero current condition must be artificially induced. One technique (Reference 5-3), indicated schematically by Figure 5-18, uses a triggered resonant circuit to provide an alternating bucking current to the dc. Units using this technique have been constructed for voltages of 20,000 volts and interrupting currents of 20,000 amperes (Reference 5-4). Units of this approximate size are suitable for the crowbar unit, but are for a much lower current than needed for the switch gear unit. To reduce the current level at the switch gear, it is recommended that the solar array be sectored into a minimum of eight units and that the interface use a minimum of eight sets of independent conductors and slip rings. The effect on the switch gear design would be to limit the individual maximum short circuit current to approximately 55,000 amperes, a value that should be attainable in a switch gear development program.

#### 5.7 POWER DISTRIBUTION COST AND WEIGHT

A cost and weight estimate for a 9 GW power input which approximates a 5 GW ground power output system requirement, is given in Figures 5-19 and 5-20. Cost estimates assume:

- a. 85 percent learning curve
- b. Labor costs equal to materials cost
- c. 1975 dollars

The auxiliary power portion is relatively expensive and represents the equipment needed to provide the lower level voltages for operating the electronic equipment.

To convert to a parametric cost basis, the overall cost can be assumed to vary as the square root of the total power. The cost of the conductors will vary directly as the power, but because the conductors represent a small proportion of the total cost, it is well within the accuracy of the estimate to vary this cost as the square root of the total power.



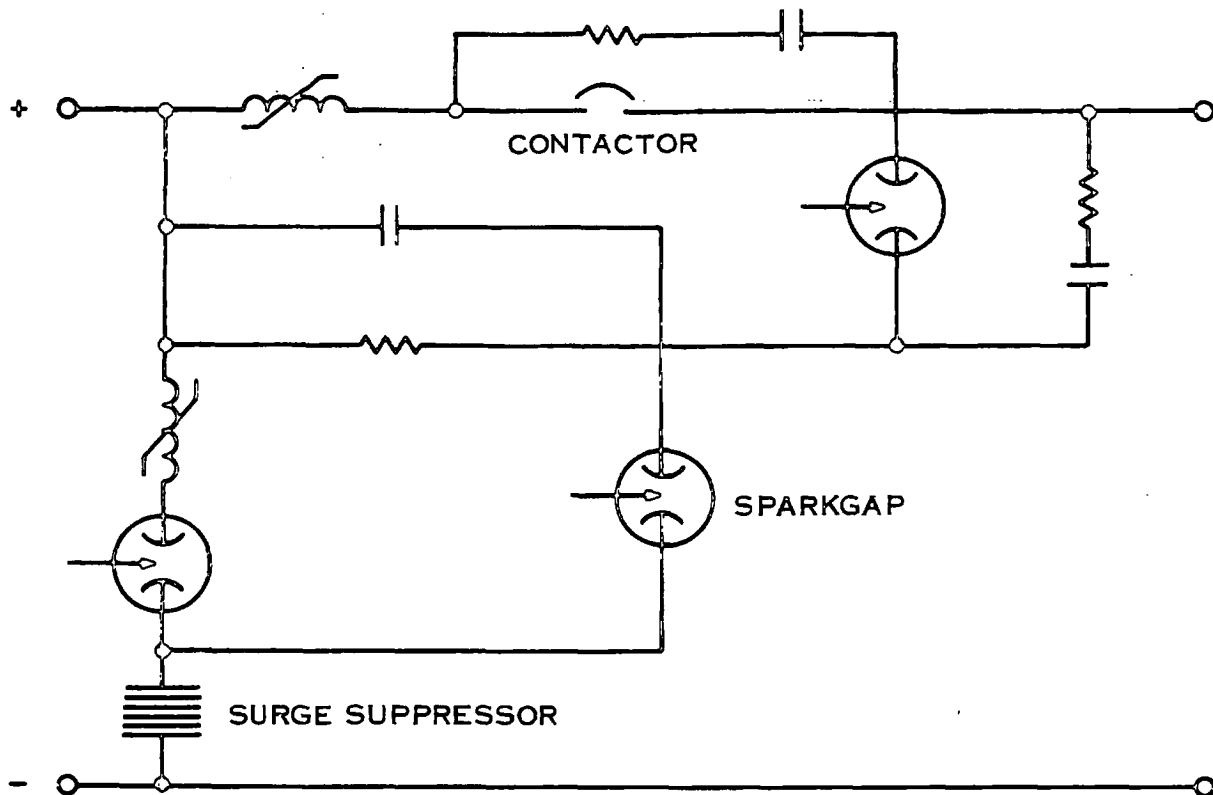


Figure 5-18. Simplified Diagram - HVDC Interrupter

### 5.8 POWER BUDGET

A power budget chart estimating the percentage losses for each element of the microwave array is given in Figure 5-21. In calculating the waveguide losses it was assumed that the full rf power output from each tube was tied directly to the waveguide. Waveguide losses vary directly as the power flowing into the guide. For the higher power Klystron, an increase in overall efficiency can be obtained by dividing the power prior to feeding the actual antenna waveguide sections, as described in the section on dc-rf conversion.

### 5.9 CONCLUSIONS AND RECOMMENDATIONS

The following conclusions and recommendations are made (see Section 11 for risk assessment).

- a. Lateral power flow for minimum weight.
- b. Recycling switchgear (crowbar) needed for protection against tube arcing.

- c. Power source and slip rings to be sectored into a minimum of eight independent units to permit a practical switchgear design by limiting maximum short circuit current.
- d. Cost and weight can be scaled by the square root of input power for system tradeoff studies.
- e. Magnetic interaction effects are negligible in attitude control system design.

For the amplitron:

- f. Constant current regulation at the converter to maximize power output and minimize phase shift variations with voltage changes.
- g. Cascade configuration because of low gain characteristic.
- h. Power source voltage should be  $\approx 20$  kVdc.

For the klystron:

- i. Unregulated operation to maximize power output.
- j. Parallel operation to minimize failure effects and simplify compensation for phase shift variations with voltage changes.
- k. Power source voltage should be  $\approx 40$  kVdc.

#### SECTION 5 - REFERENCES

- (1) "The Solar Photovoltaic Array, Preliminary Technical Report," Spectro Lab, Division of Textron Inc., Sylmar, California.
- (2) "Rapid Recycle Crowbar Circuits," G.R. Lyuta and T.A. Weil, Paper presented at Annual Modulator Symposium, 1973.
- (3) "Theory and Application of the Commutation Principle for HVDC Circuit Breakers," A.N. Greenwood and T.H. Lee.
- (4) "HVDC Circuit Breakers," A.N. Greenwood, P. Barkham, and W.C. Kracht.

Item	Description	Quantity Required	Unit Cost (\$ x 10 <sup>3</sup> )	Total Cost (\$ x 10 <sup>6</sup> )
1	Recycling Crowbar	1769	28	49.5
2	Switch Gear	32	178	5.7
3	Conductors	60 x 10 <sup>3</sup> Kg	2.2 \$/Kg	0.1
4	Auxiliary Power	1769	29.5	52.2
				107.5 Total

Figure 5-19. Power Distribution Cost Summary (9 GW Power Source)

Item	Description	Quantity	Unit Weight (Kg)	Total Weight (10 <sup>3</sup> Kg)
1	Recycling Crowbar	1769	170	300.7
2	Switch Gear	32	1726	55.2
3	Conductors	-	60 x 10 <sup>3</sup>	60.0
4	Auxiliary Power	1769	50	88.4
				504.3 Total

Figure 5-20. Power Distribution Weight Summary (9 GW Power Source)

	Amplitron (85% Eff)	PPM Klystron - % (75% Beam Eff)	High Power Solenoid Klystron - % (75% Beam Eff)	High Power Solenoid Klystron - % (84% Beam Eff)
Radiated Power	80.07	67.38	68.12	75.87
Waveguide Losses	0.32	0.24	2.12	2.64
Filter Losses	1.61	-	-	-
Amplifier Losses	14.47	29.93	27.31	19.02
Preamplifier Losses	1.26	0.18	0.19	0.20
Subarray Feeders	0.09	0.09	0.09	0.09
XBAR Unit	0.21	0.20	0.20	0.20
Auxiliary Power	0.11	0.11	0.10	0.11
Lateral Feeders	0.91	0.91	0.91	0.91
Switch Gear	0.16	0.17	0.17	0.17
Primary Feeder	0.79	0.79	0.79	0.79
Source Power	100	100	100	100

Figure 5-21. Typical Microwave Array, Power Usage

## SECTION 6

### TRANSMITTING ANTENNA

#### 6.1 APERTURE ILLUMINATION AND SIZE

The optimum transmitter aperture distribution is one that places the most power within the angle subtended by the receiving antenna. Beam efficiency is defined as the fraction of power radiated into a cone with half angle  $\theta$ , for  $c = 2\pi a/\lambda \sin \theta_0$ , where  $a/\lambda$  is the normalized transmitting antenna radius,  $\lambda$  is the wavelength, and  $\theta_0$  is the angle through which the power is radiated. The beam efficiency is given by

$$\eta_s = \frac{\int_0^{2\pi} \int_0^c \left[ \int_0^{2\pi} \int_0^1 f(\rho, \psi) e^{j t \cos(\psi - \phi)} d\psi d\rho \right]^2 t dt d\phi}{\int_0^{2\pi} \int_0^1 \left[ f(\rho, \psi) \right]^2 \rho d\rho d\psi}$$

where  $t = 2\pi a/\lambda \sin \theta$ ,  $f(\rho, \psi)$  is the aperture illumination over a circular aperture of radius  $a$ , and  $\rho$  and  $\psi$  are circular coordinates. The optimum illumination is the  $f(\rho, \psi)$  that maximizes  $\eta_s$ . This function  $S_{00}$  is known as a hyperspheroidal or generalized prolate wave function and satisfies the integral equation

$$\alpha_{\max} S_{00}(c, \rho) = \int_0^1 S_{00}(c, s) J_0(cps) s ds.$$

The maximum value of  $\eta_s$  is  $\eta_{s \max} = \alpha_{\max}^2 c^2$ , where  $\alpha_{\max}$  is the associated equation. Figure 6-1 is a plot of beam efficiency. Figure 6-2 is a plot of beamwidth and first sidelobe level.

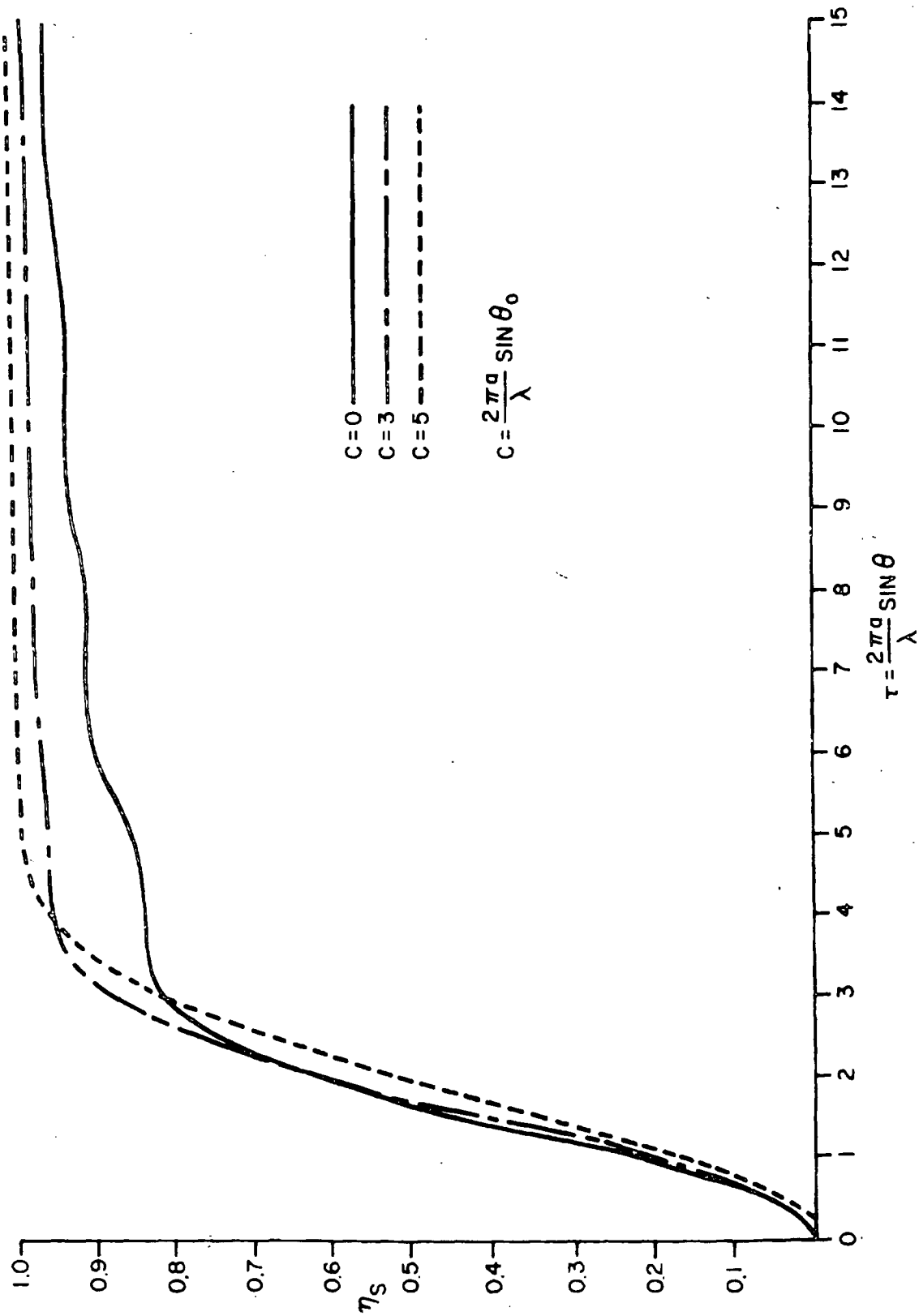


Figure 6-1. Fraction of Total Power in Sectors of Prescribed Radii

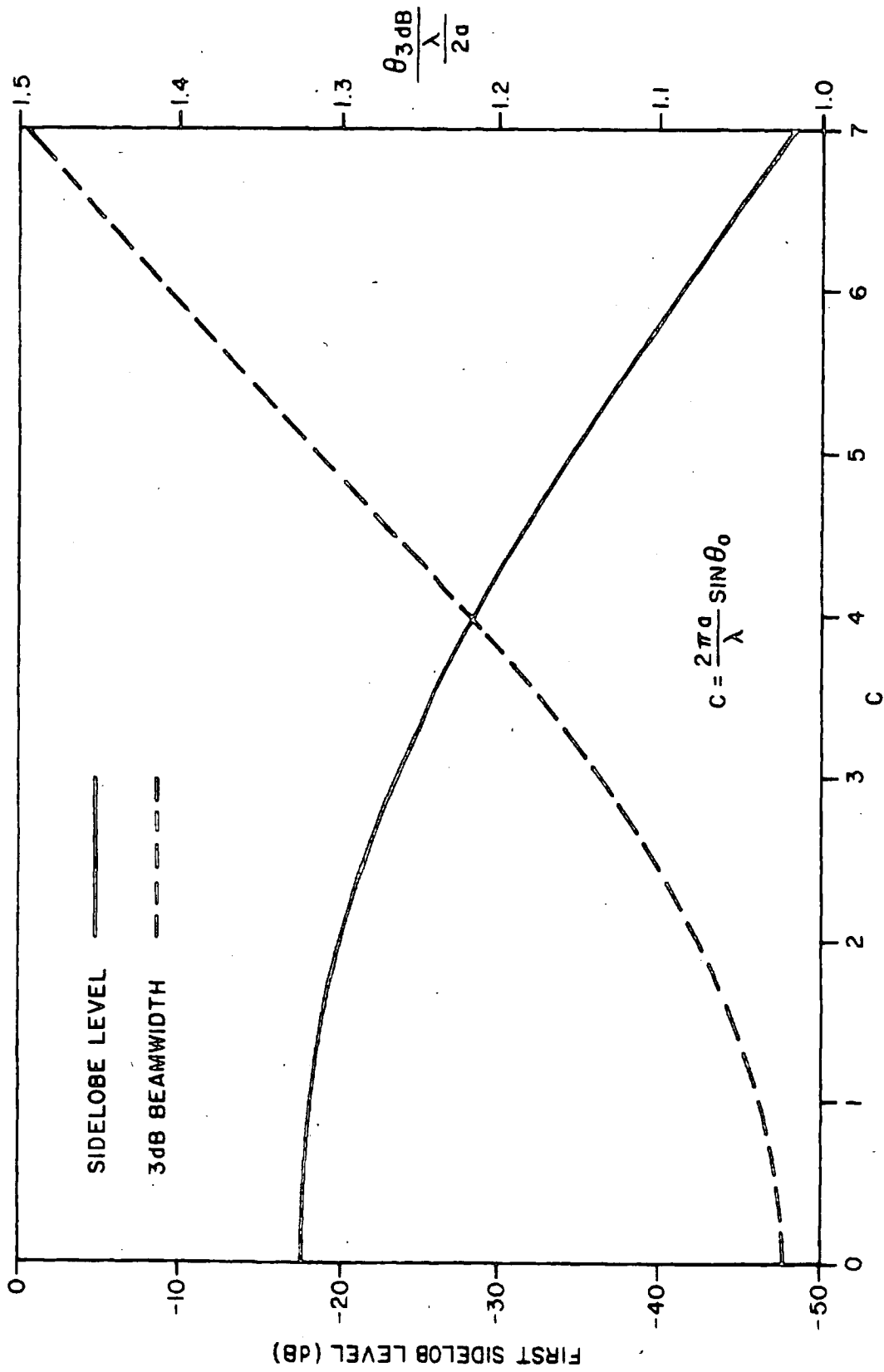


Figure 6-2. Sidelobe Level and Beamwidths

A truncated Gaussian amplitude distribution with uniform phase distribution is a satisfactory approximation to the ideal prolate wave functions. Figures 6-3 through 6-6 show the pattern and sidelobe characteristics for various amplitude tapers. These are obtained from the following relations:

$$E(\theta) = \int_0^a f(p) J_0\left(\frac{2\pi}{\lambda} p \sin \theta\right) p dp$$

where

$E(\theta)$  = electric field strength

$$f(p) = e^{-K\left(\frac{p}{a}\right)^2}$$

$$K = \frac{dB/n10}{20}$$

dB = amplitude taper, center to edge

$$\text{Efficiency} = \frac{\int_0^{\pi/2} E^2(\theta) \sin \theta d\theta}{\int_0^{\pi/2} E^2(\theta) \sin \theta d\theta}$$

Results are now plotted against the parameter

$$\frac{\sqrt{A_T A_R}}{\lambda D} = C/2$$

where

$A_T$  = transmitting antenna area

$A_R$  = receiving antenna area

$D$  = distance between antennas

A comparison of characteristics for an assumed 1 km diameter transmitting antenna in synchronous orbit is given in Figure 6-7, where it can be seen that the greater taper provides greater efficiency for a given receiving antenna diameter. It also is evident that the scale of the MPTS will be on the order of 1 km for the transmitting antenna and 10 km for the receiving antenna for acceptable efficiencies.



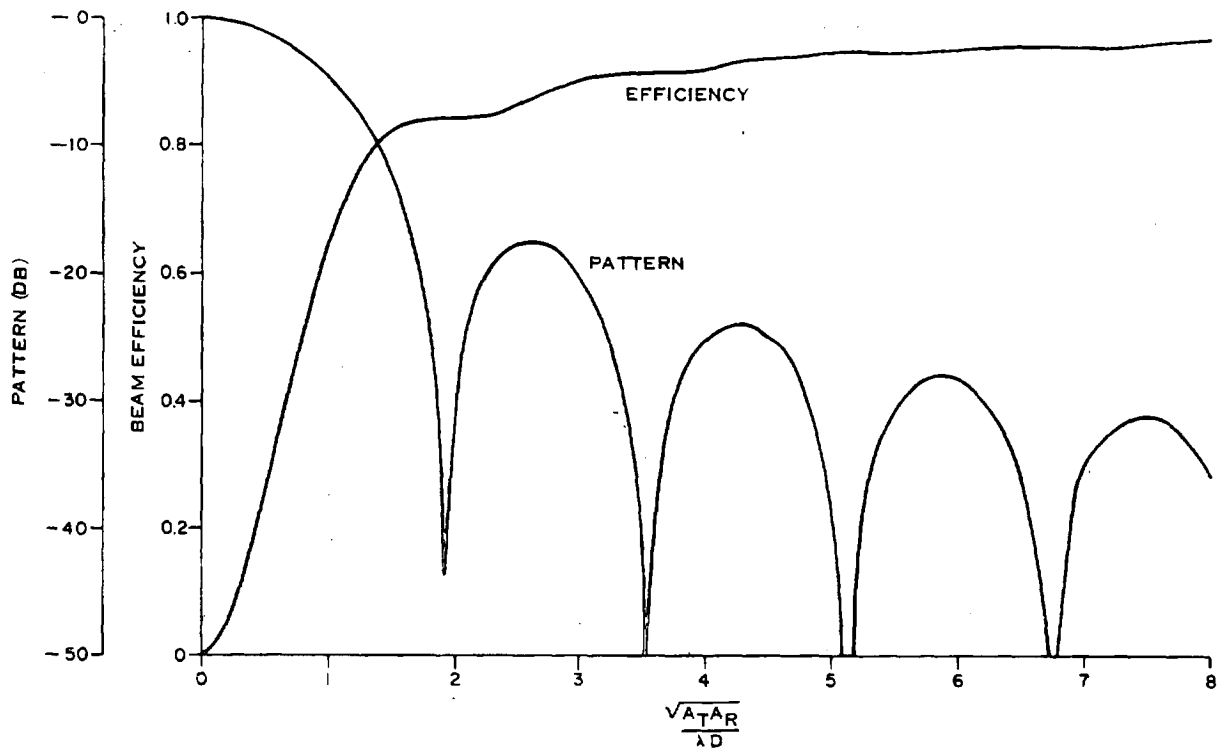


Figure 6-3. Pattern Efficiency for Uniform Illumination (0 dB Taper)

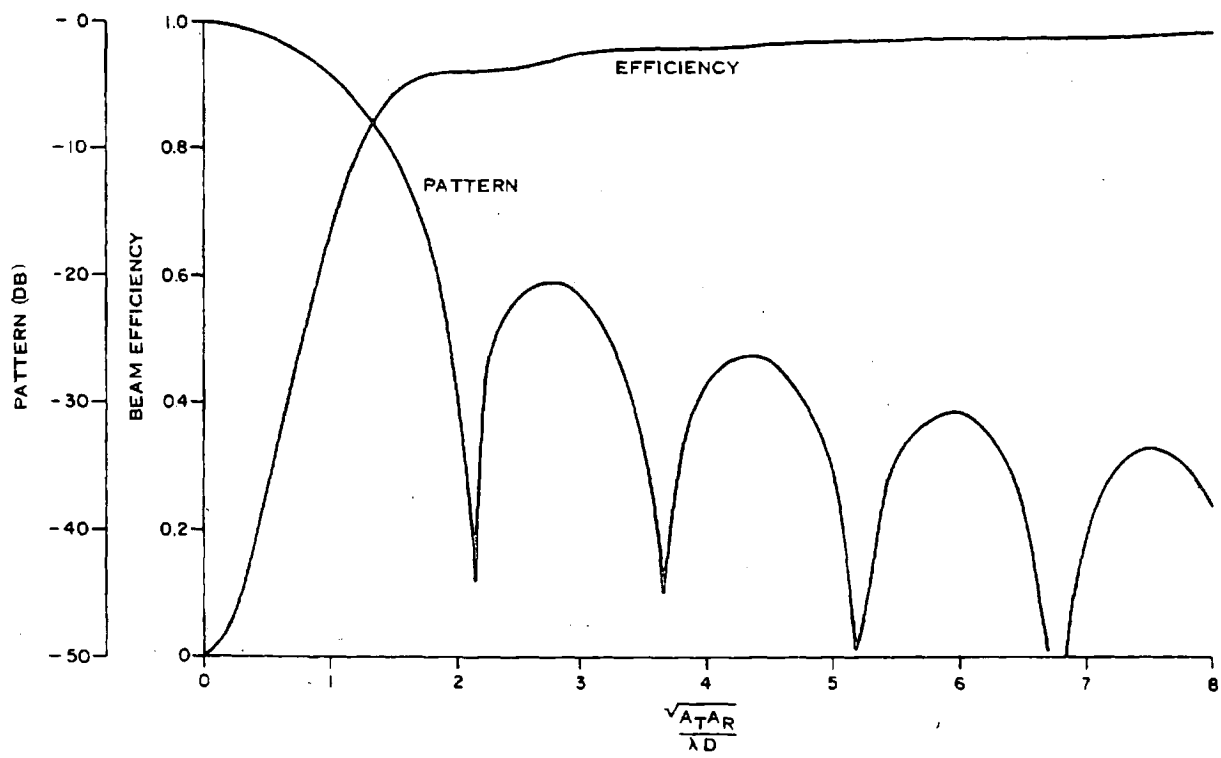


Figure 6-4. Pattern Efficiency for Uniform Illumination (5 dB Taper)

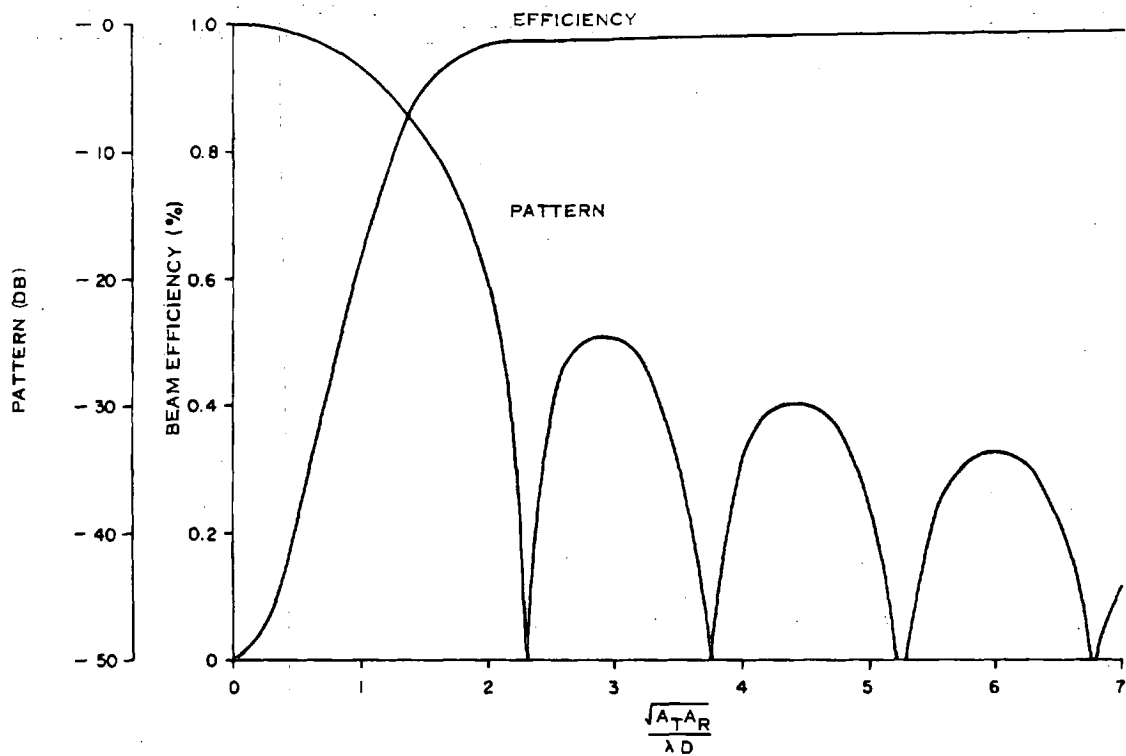


Figure 6-5. Pattern Efficiency for Uniform Illumination (10 dB Taper)

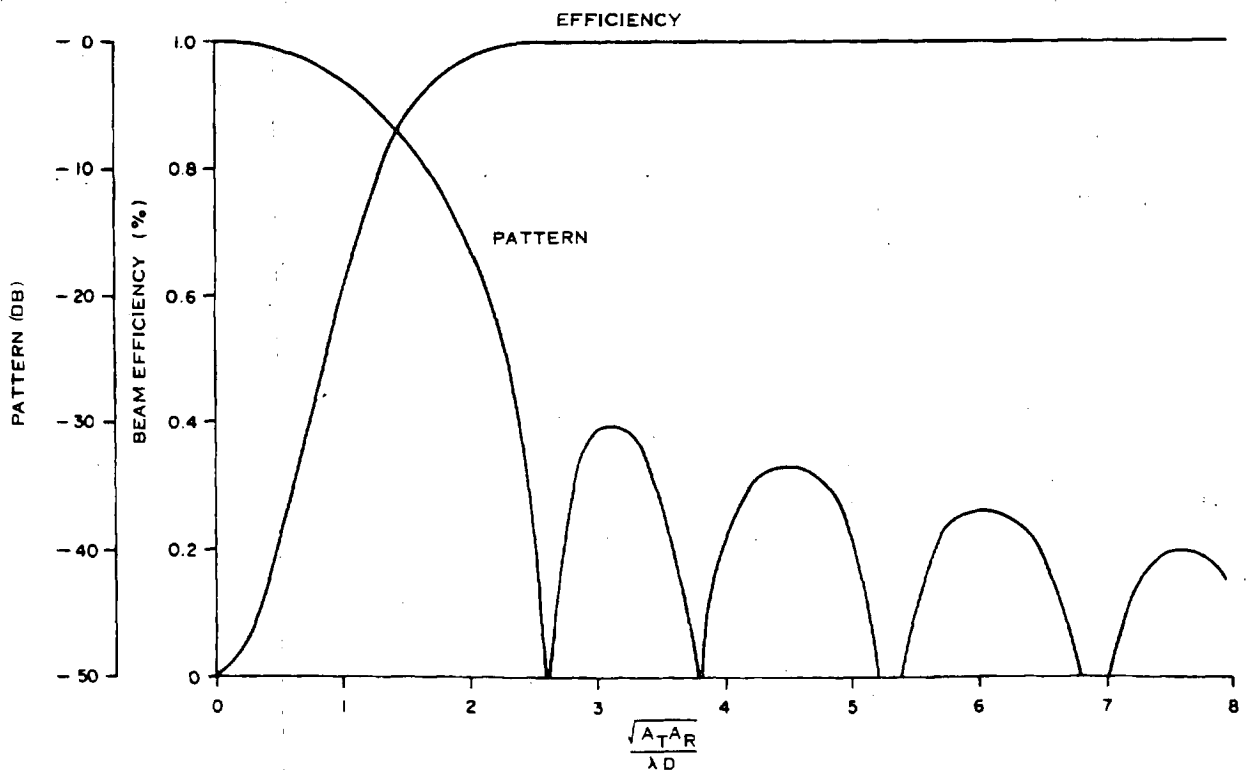


Figure 6-6. Pattern Efficiency for Uniform Illumination (15 dB)

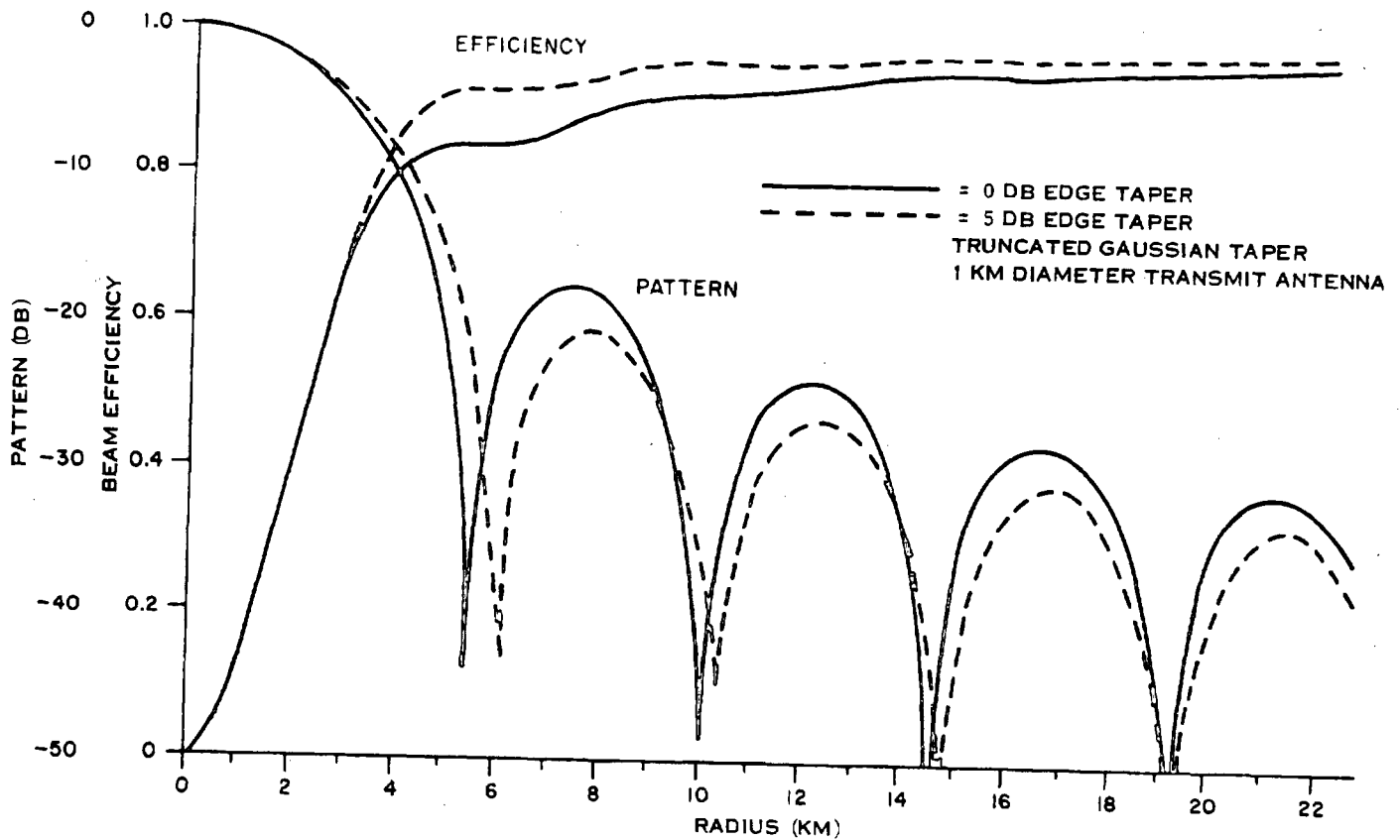


Figure 6-7. Taper Effect on Pattern and Efficiency

The total area  $A_T$  must be obtained in a single antenna of continuous elements, and not made up of a set of spaced antennas whose total area equals  $A_T$ . Widely spaced ( $\gg \lambda/2$ ) segments result in very low efficiency because power is diverted into grating lobes that are not directed at the ground antenna. This is true even if the space between active elements is filled with passive elements tuned to the proper frequency.

Figure 6-8 shows the reduction in first sidelobe level as taper is increased with more power placed in the main beam. Figure 6-9 shows that higher beam efficiencies call for higher tapers and that there will be near optimum combinations of taper and efficiency to limit receiving antenna size.

The large size of the transmitting antenna dictates that it be sectored into many subarrays, or sections, so that errors due to mechanical distortion can be corrected. (This phase front control problem is covered in the next section.) An example of this sectored arrangement is given in Figure 6-10 for a circular

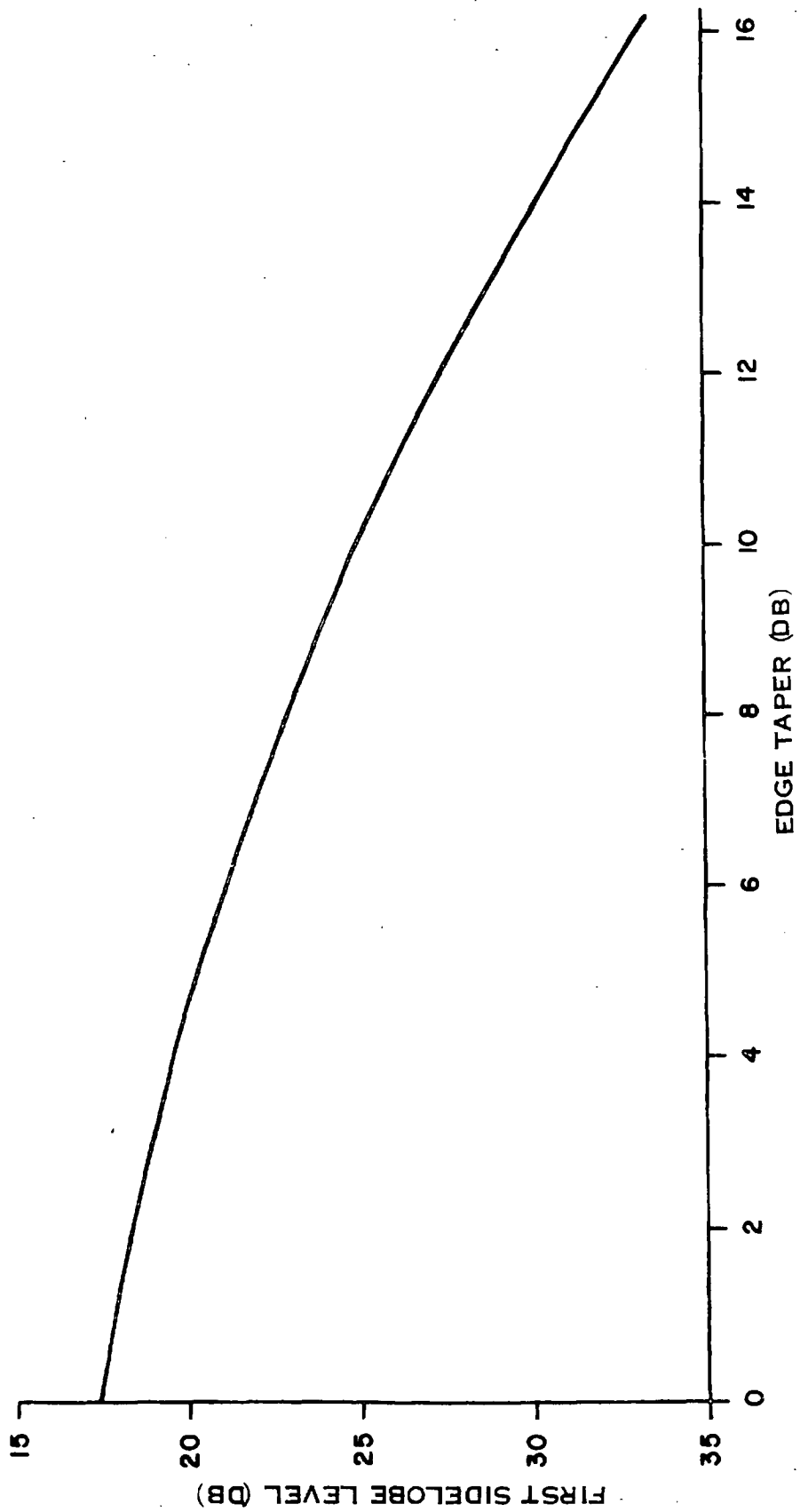


Figure 6-8. First Sidelobe Level vs. Truncated Gaussian Taper

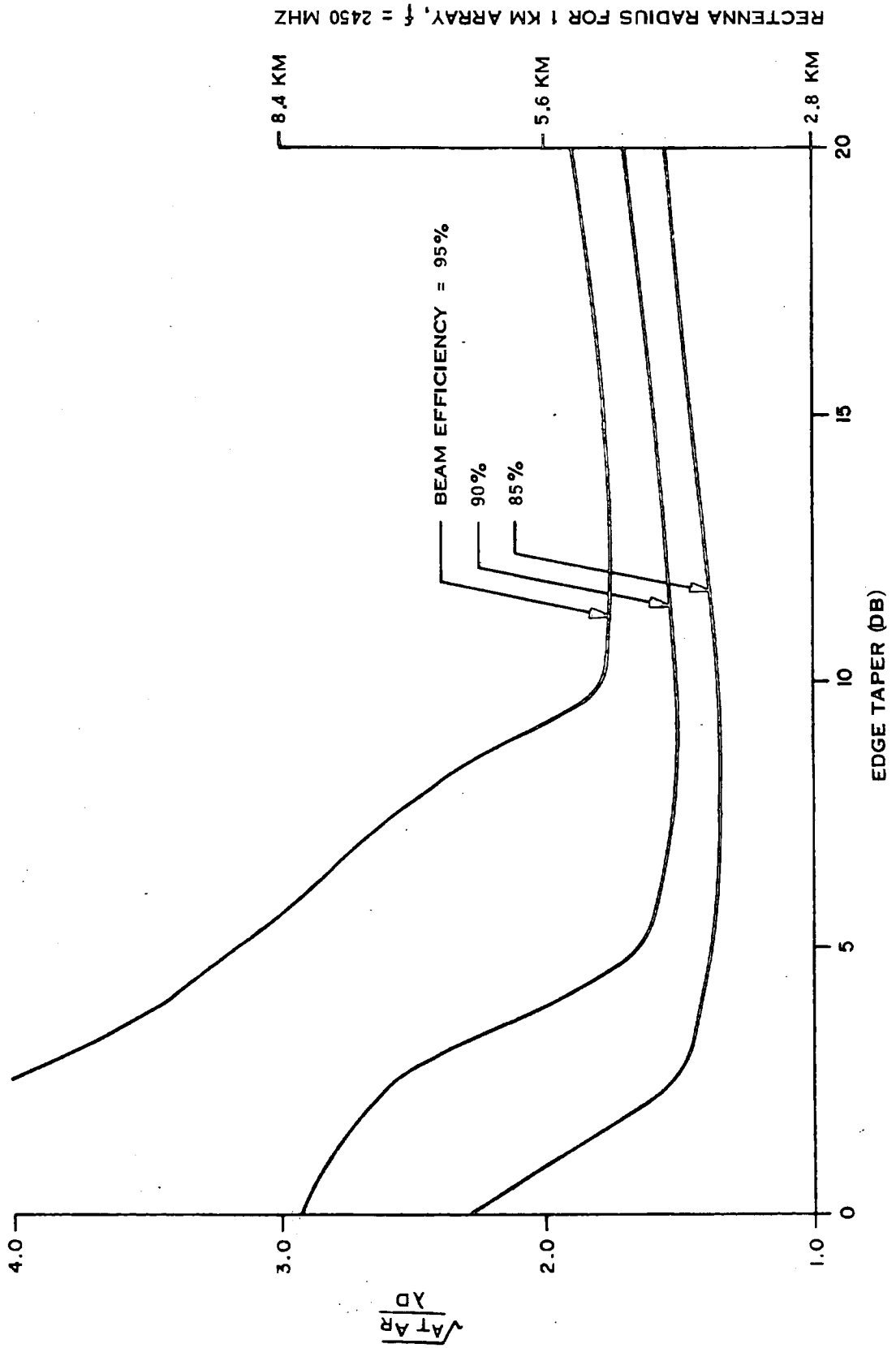


Figure 6-9. Antenna Sizes for Truncated Gaussian Tapers

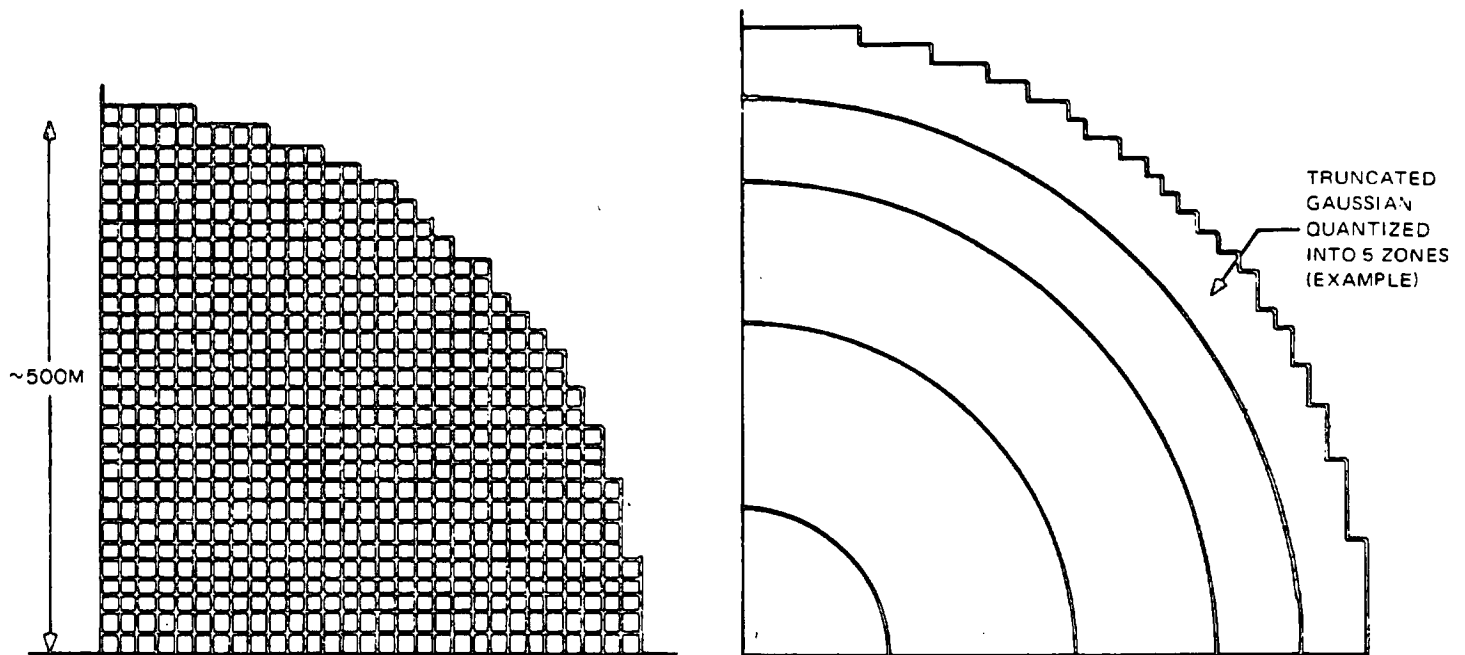


Figure 6-10. Array-Subarray Organization

planar array antenna, and also shown is a quantized approximation to the Gaussian amplitude distribution, as may be the case for a practical implementation of an active array. Figures 6-11 and 6-12 indicate that five steps or more are needed to maintain efficiency, whereas Figures 6-13 and 6-14 show that only three steps are needed to hold down sidelobes. Effect of failure of a dc power feeder (described in a previous section) is shown in Figure 6-15 to have a large but probably not an environmentally significant effect on sidelobes if the sidelobe levels are initially well below biological or environmental standards.

## 6.2 ARRAY TYPES

The prime candidate for transmitting antenna implementation has been a circular, active, planar phased array, as illustrated in Figure 6-16. The reasons have been:

- a. High beam formation efficiency (95 percent)
- b. Passive dc-rf converter heat transfer to space
- c. Convenient phase control implementation
- d. Short rf distribution paths with low losses

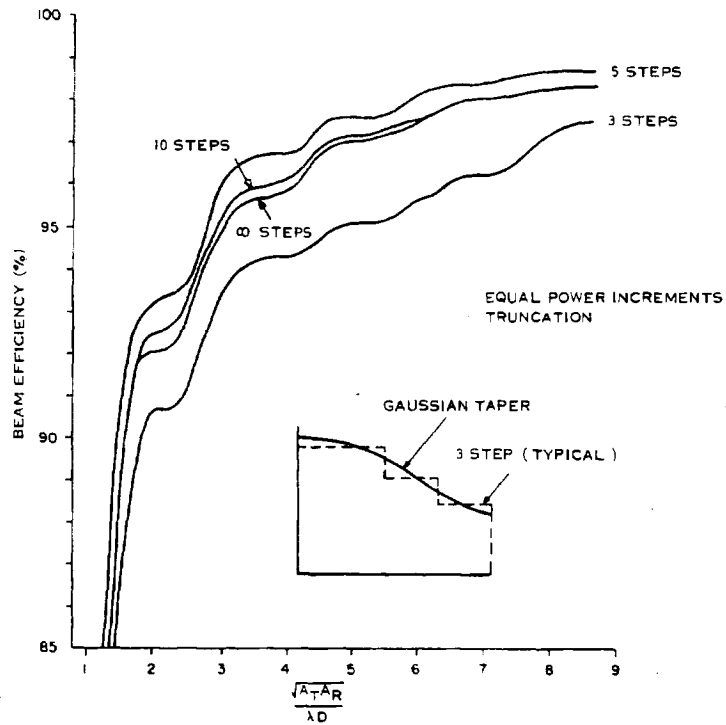


Figure 6-11. Beam Efficiency - Truncated Gaussian Distribution (5 dB Edge Taper)

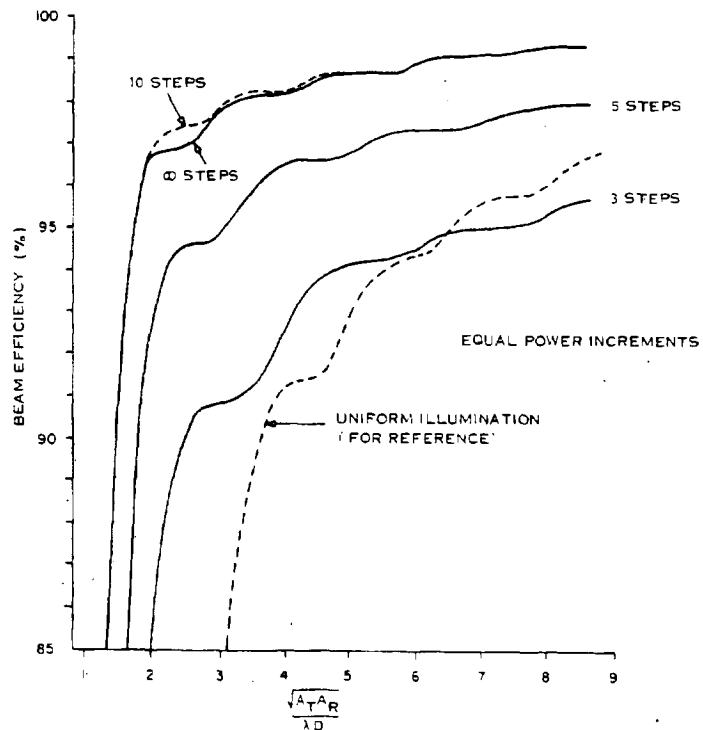


Figure 6-12. Beam Efficiency - Truncated Gaussian Distribution (10 dB Edge Taper)

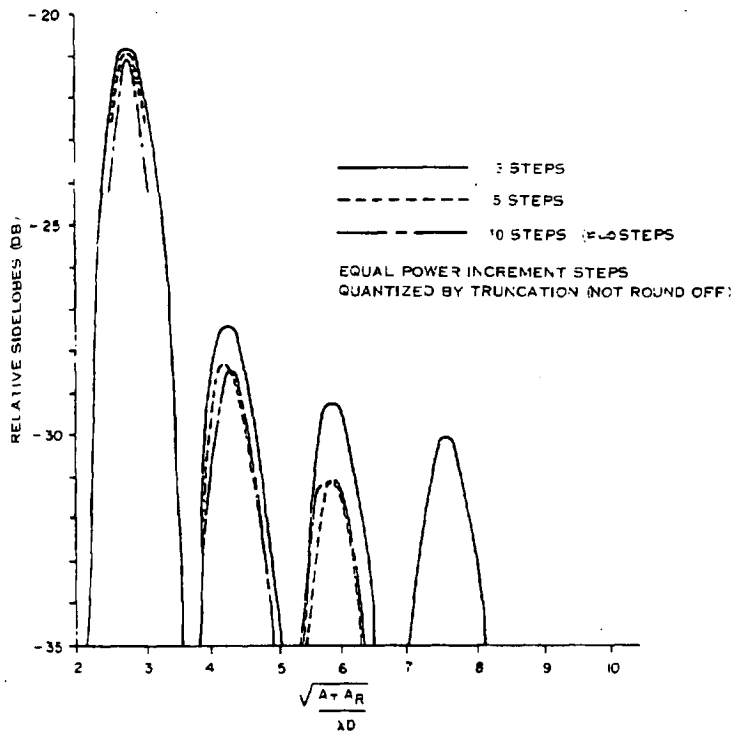


Figure 6-13. Relative Sidelobes - Truncated Gaussian Distribution (5 dB Edge Taper)

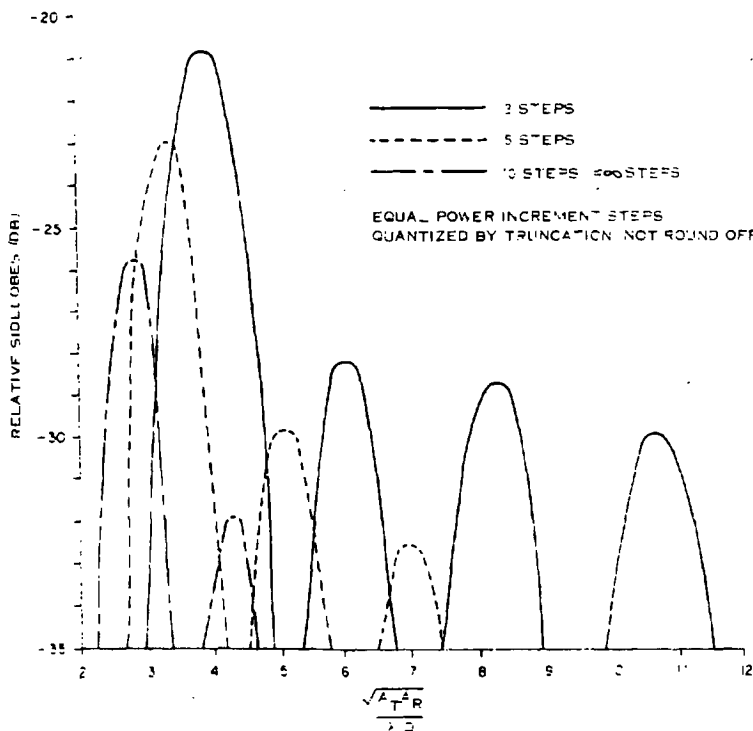


Figure 6-14. Relative Sidelobes - Truncated Gaussian Distribution (10 dB Edge Taper)



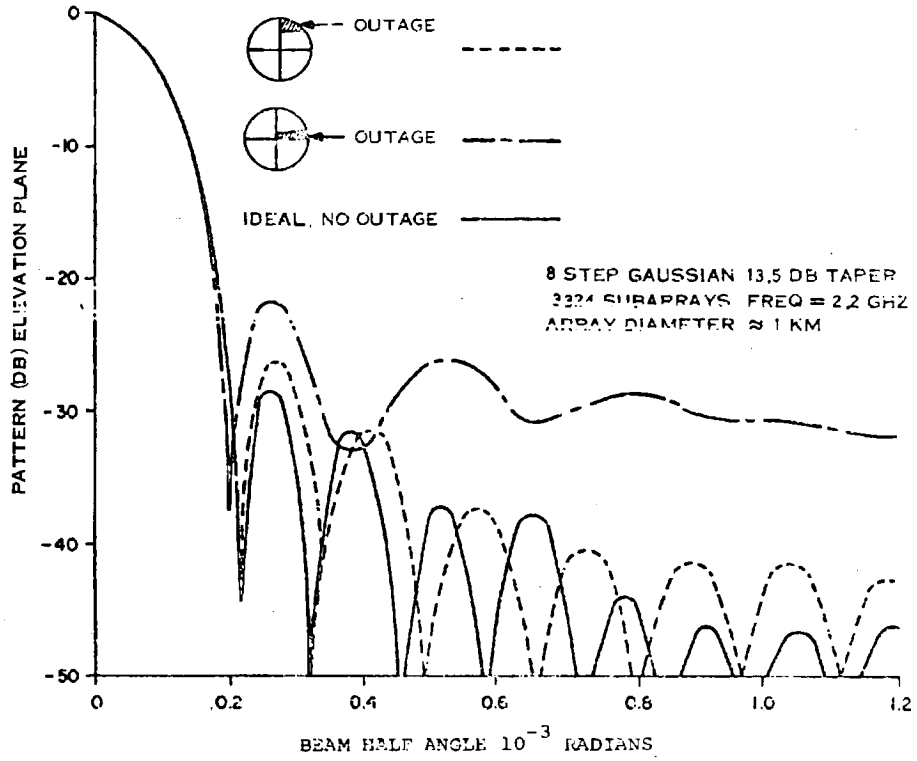


Figure 6-15. Outage of a Single DC Filter

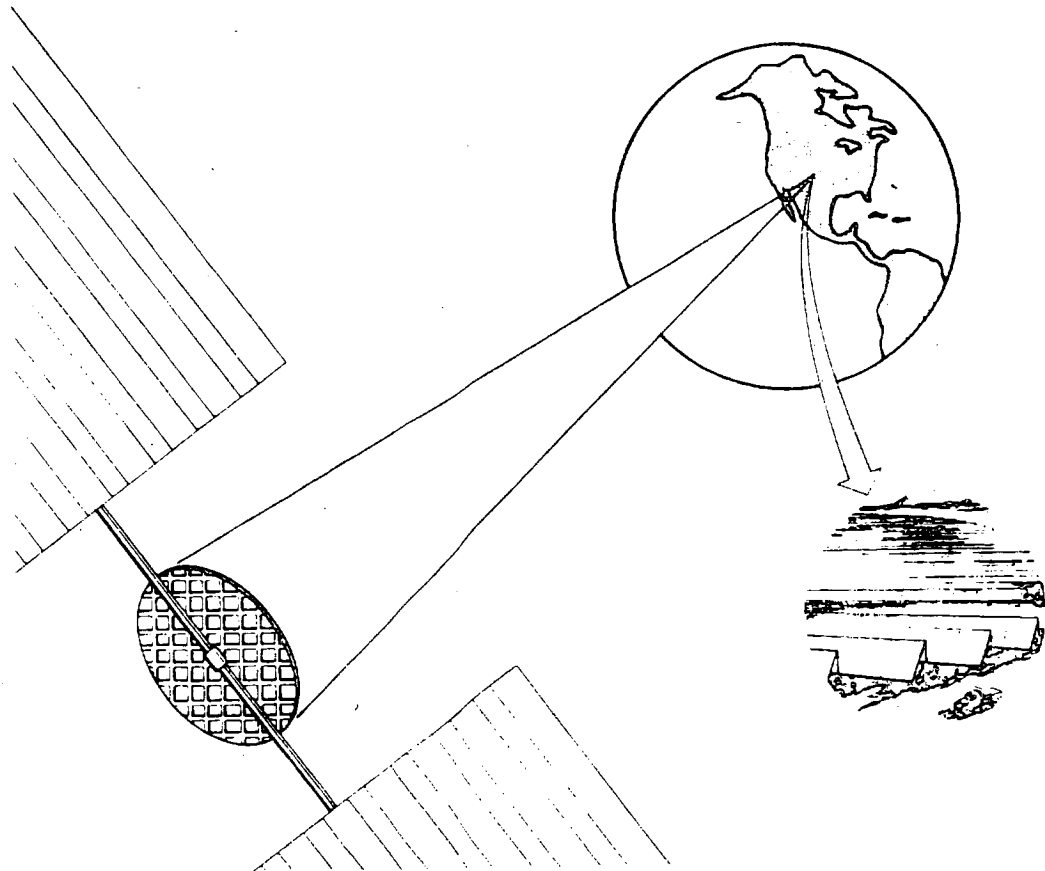


Figure 6-16. MPTS Concept

Two alternative approaches as shown in Figure 6-17 were considered. One is a spaced array in which large power converters, e.g., 100 kW klystrons, would be centrally located to facilitate maintenance; the other is a cylindrical, active array using electrical switching to eliminate a rotary joint to a solar oriented power source.

The spaced array approach would use radiators near the converters to illuminate the larger aperture needed to launch the beam to earth as shown in Figure 6-18. The disadvantages are the need for mechanical alignment of the active elements, mechanical adjustment of the array for phase control (electrical means are too inefficient), need for an active cooling scheme to get the converter waste heat to a radiating surface, and finally, the very high microwave power density at the feed which increases in direct proportion to the reduction in area at the feed relative to the array and therefore would be on the order of  $\lambda$  in dimension. For an F/D of about unity as shown in Figure 6-19, all elements must be in a dimension of about  $3\lambda$ . Intermediate feed concepts can be devised, but they approach the dimensions of the primary array and have lowered efficiency as they become physically realizable.

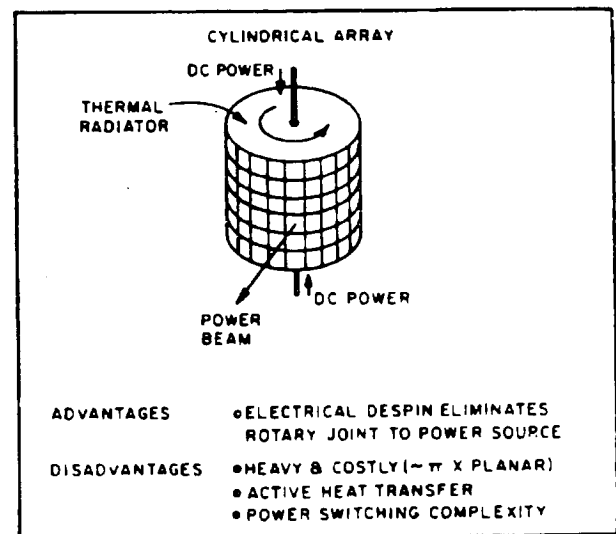
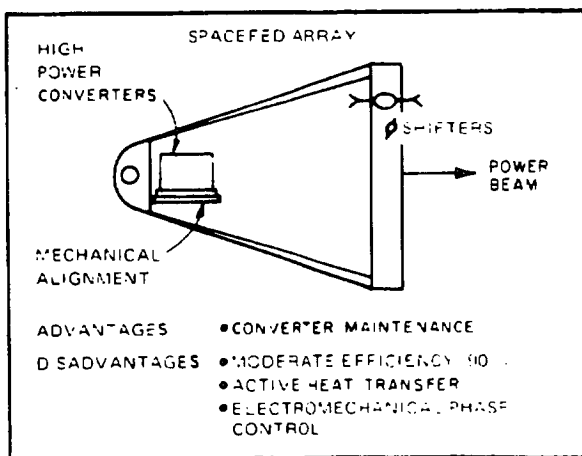


Figure 6-17. Alternative Array Types

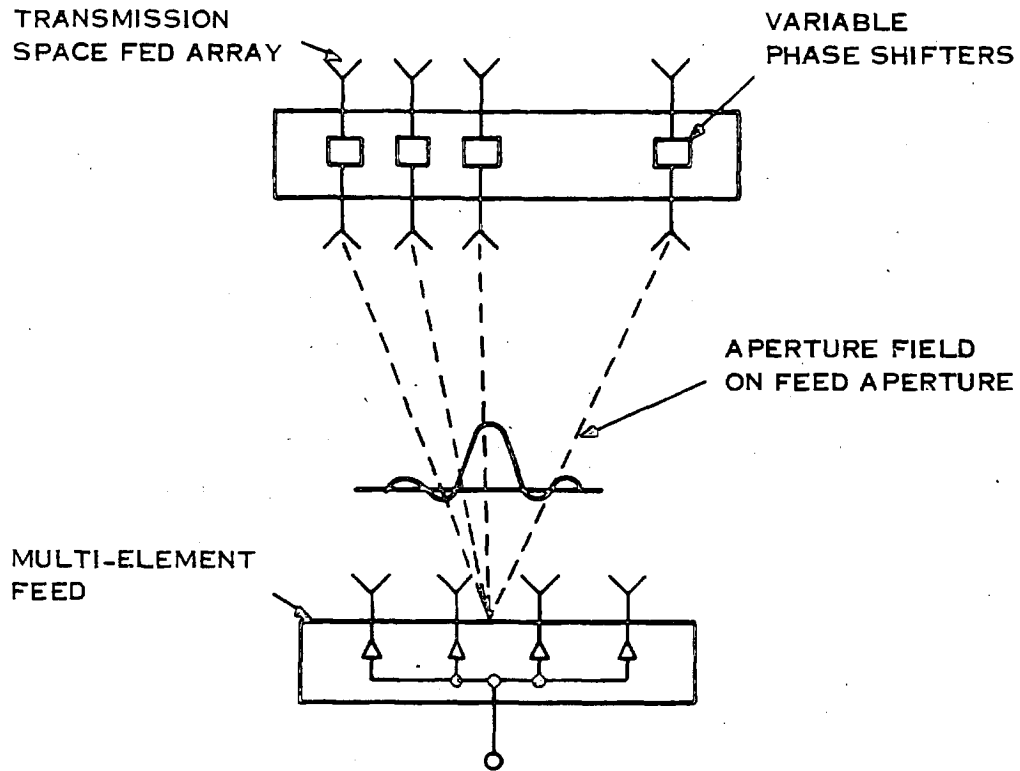


Figure 6-18. Space Fed Array

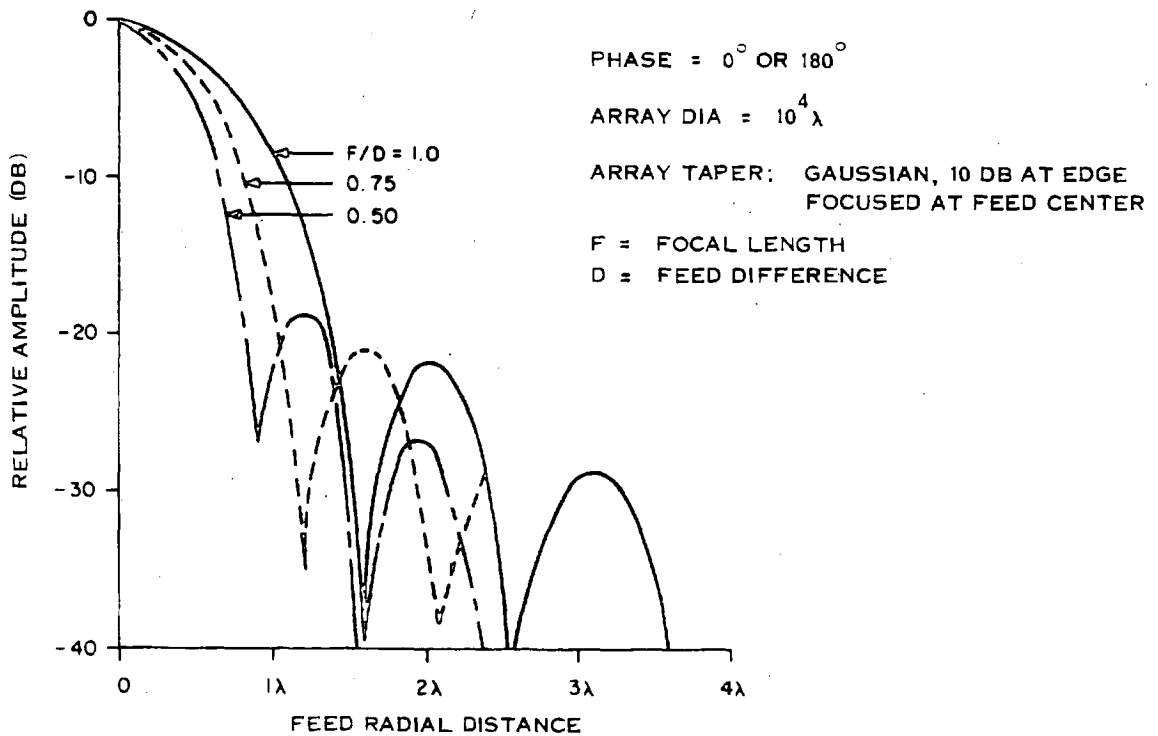


Figure 6-19. Feed Illumination (Array Focused at Feed)

The cylindrical array must develop the same aperture area as the planar array in the direction of the ground antenna to maintain equivalent efficiency. Therefore it must have at least  $\pi$  as much total area. It must also have  $\pi$  as many dc-rf converters with some form of active heat transfer to radiating surfaces at the top and bottom of the cylinder, or it must locate the converters at the cylinder ends and suffer the power loss in distributing the microwave power to the cylinder walls. There also is the complexity of switching power on and off to the converters as the cylinder rotates. The weight and cost penalty for a rotary joint (see Section 8) is sufficiently small that the planar array is a clear choice.

### 6.3 SUBARRAY TYPES

The options in subarray types are shown in Figure 6-20. In Figure 6-21 they are shown individually together with a listing of advantages and disadvantages. The indicated efficiencies are due to  $I^2R$  losses, spillover and aperture taper for the individual subarrays. Additional losses at the array level would be associated with the pyramidal horn and paraboloid types due to the higher array side lobes. Only the slotted waveguide and the helix configuration have adequately high aperture efficiency, and the helix has two drawbacks: (1) the beam would be circularly polarized which would necessitate a dual polarized receiving antenna at added cost and complexity, and (2) there would still be a need for microwave power distribution hardware, i. e., waveguide, from the converters to the helices, and from converter to converter in the case of the amplatron.

### 6.4 SUBARRAY DIMENSIONS

The size of a subarray is determined by the amount of power loss that is budgeted for the effects of mechanical distortion, misalignment and effects of attitude control errors. These effects are illustrated in Figure 6-22 where the high gain (narrow beam pattern) associated with the larger dimension exhibits greater power loss than the smaller dimension with relatively wide beam patterns. The trend to smaller subarrays must be traded off against (1) the added cost of the supporting electronics and control hardware that must be associated with subarrays of any size, and (2) the power lost due to poorer area utilization.

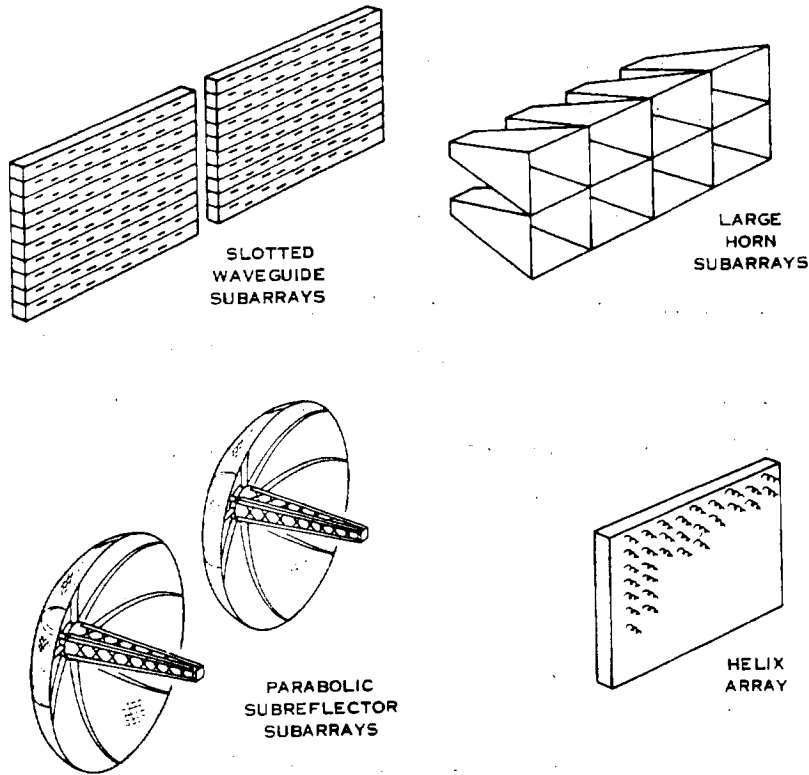


Figure 6-20. Subarray Types

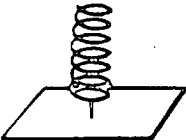
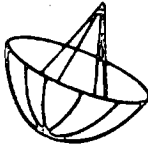
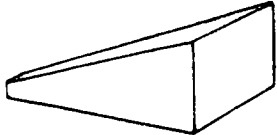
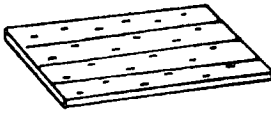
 <p><b>HELICAL RADIATORS</b></p> <p><b>ADVANTAGES</b></p> <ul style="list-style-type: none"> <li>• HIGH EFFICIENCY (98%)</li> </ul> <p><b>DISADVANTAGES</b></p> <ul style="list-style-type: none"> <li>• DUAL POLARIZATION AT RXCV</li> <li>• REQUIRES RF DISTRIBUTION FROM CONVERTER</li> </ul>	 <p><b>UNFURLABLE GORE-TYPE PARABOLOIDS (MESH AND FLEX RINGS)</b></p> <p><b>ADVANTAGES</b></p> <ul style="list-style-type: none"> <li>• EXTREMELY LIGHTWEIGHT</li> <li>• DEPLOYABLE</li> </ul> <p><b>DISADVANTAGES</b></p> <ul style="list-style-type: none"> <li>• SPILLOVER LOSSES:</li> <li>• LOW EFFICIENCY (65%)</li> <li>• HIGHER ARRAY SIDELOBES</li> <li>• FABRIC IS HIGH POWER LIMITED</li> </ul>
 <p><b>PYRAMIDAL HORNS (MESH OR THIN METAL SIDES)</b></p> <p><b>ADVANTAGES</b></p> <ul style="list-style-type: none"> <li>• LIGHTWEIGHT</li> </ul> <p><b>DISADVANTAGES</b></p> <ul style="list-style-type: none"> <li>• SUSCEPTIBLE TO MODING</li> <li>• HIGHER ARRAY SIDELOBES</li> <li>• MODERATE EFFICIENCY (90%)</li> </ul>	<p><b>SLOTTED WAVEGUIDE (RECOMMENDED APPROACH)</b></p>  <p><b>ADVANTAGES</b></p> <ul style="list-style-type: none"> <li>• HIGH EFFICIENCY (99%)</li> <li>• COMBINES RF DISTRIBUTION AND ANTENNA</li> <li>• LOW FREQUENCY CUTOFF REDUCES RFL</li> </ul>

Figure 6-21. Subarray Types

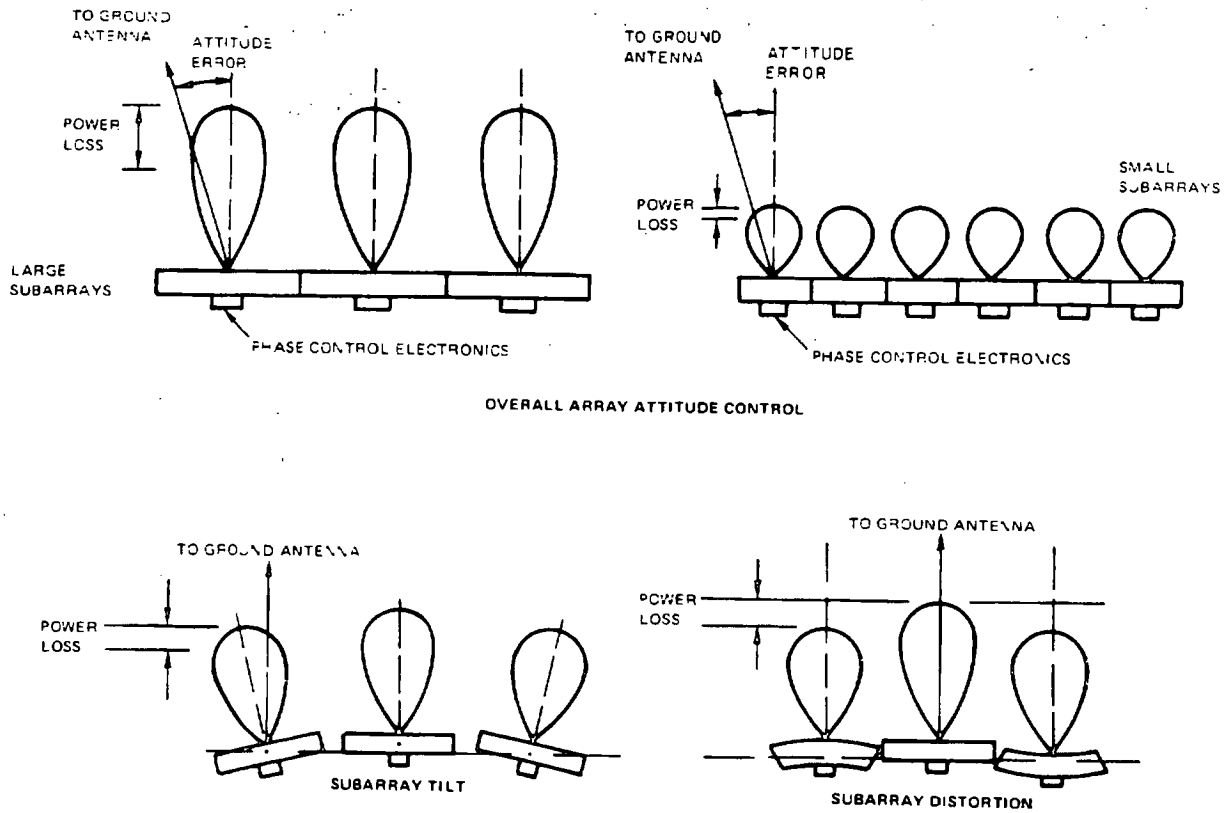


Figure 6-22. Subarray Size Considerations

The relations for the factors favoring a smaller subarray are:

Attitude Error

$$\text{Power Loss (dB)} = 3 \left[ \frac{\Delta\theta D_S}{0.44\lambda} \right]^2$$

where

- $\Delta\theta$  = attitude error
- $D_S$  = subarray dimension
- $\lambda$  = wavelength

### Flatness (Manufacturing Tolerance)

$$\text{Fractional Power Loss} = \sigma_{\phi}^2$$

where

$$\sigma_{\phi}^2 = \left[ \frac{2\pi \times 10^{-4} D_S}{\lambda} \right]^2$$

$$\sigma_{\phi} = \text{rms phase error}$$

### Thermal Distortion

$$\sigma_{\phi}^2 = \left[ \frac{2\pi \Delta d}{3 \lambda} \right]^2$$

where

$$\Delta d = \text{maximum deflection} \sim D_S$$

### DC-RF Converter Phase Error

$$\sigma_{\phi}^2 \sim D_S \Delta \phi^2$$

where

$$\Delta d = \text{individual converter phase error}$$

$$\sigma_{\phi}^2 = 0.613 D_S^2 \Delta \phi^2 \text{ (amplitron)}$$

$$(D_S \text{ in meters, } \Delta \phi \text{ in degrees)}$$

The factors favoring a larger subarray are area utilization, estimated at a fractional power loss =  $1.9/D_S^2$ , and cost of subarray electronics and mechanical actuators, including both manufacturing and orbital transportation costs. These are discussed in later sections, but the net result for an appropriate range of factors is given in Figure 6-23. A nominal value of 18m was chosen as an acceptable figure that also is the maximum that can be accommodated by the Shuttle Orbiter without folding in more than one dimension. The Shuttle is expected to play a role in MPTS development. The rationale for selecting the operating

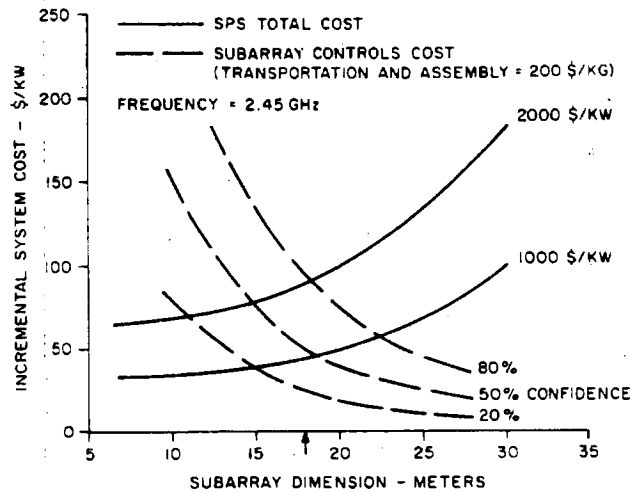


Figure 6-23. SPS Incremental Cost vs. Subarray Size

frequency of 2.45 GHz is given in Section 2, supported by material in Sections 3, 4 and 10.

### 6.5 SUBARRAY LAYOUT

Locating the tubes and the radiating waveguides within a subarray presents a topology problem in that the "natural" flow of rf power is unidirectional in a straight line whereas the subarray boundary constraint requires that the rf power be confined to a somewhat rectangular area. Dimensions of various components must be properly related. For example, the waveguide width must be a multiple of the thermal radiator diameter in order that the input to each waveguide be located close to its tube. The subarray width is also related to the thermal radiator width and the method of terminating the waveguide rows.

Figure 6-24 demonstrates three subarray layout concepts. In general, a good subarray layout approach should have the minimum amount of transmission lines, maximum aperture utilization, near rectangular boundaries for mechanical reasons, and minimum use of active lossy components such as high power phase



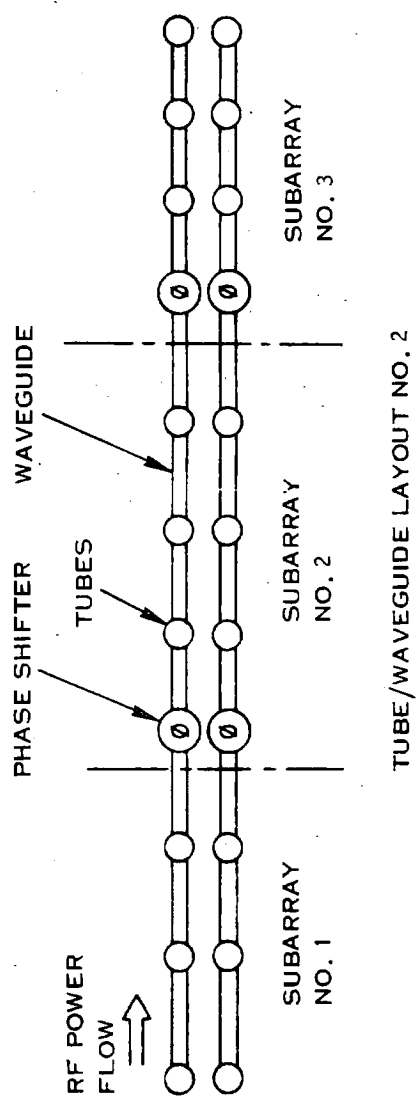
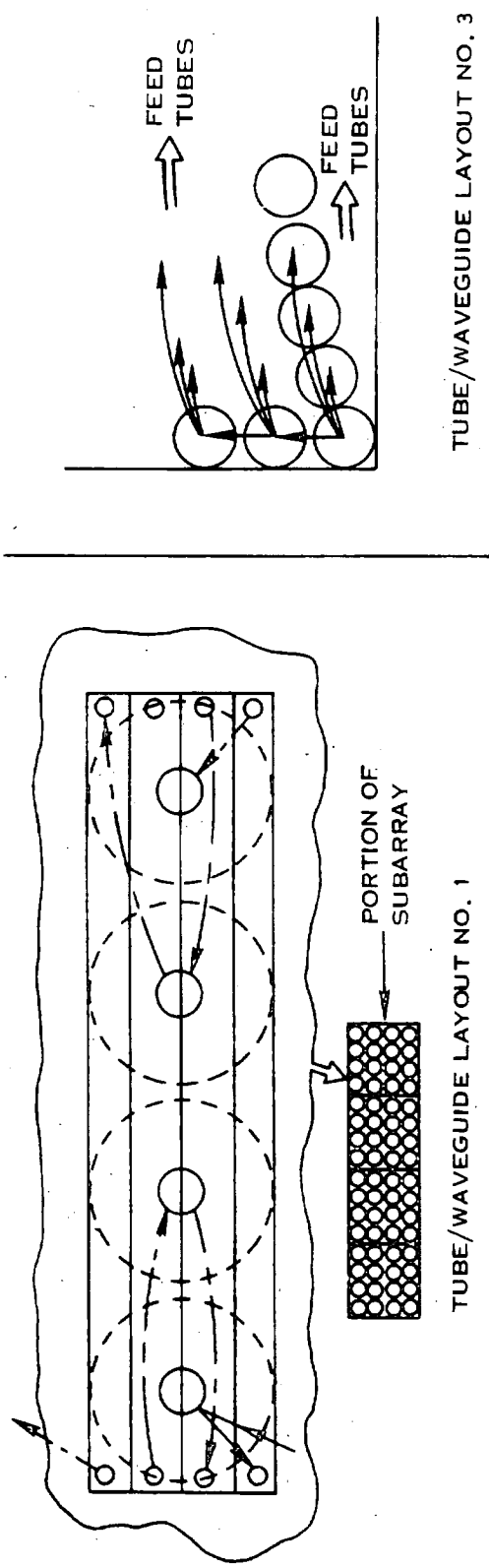
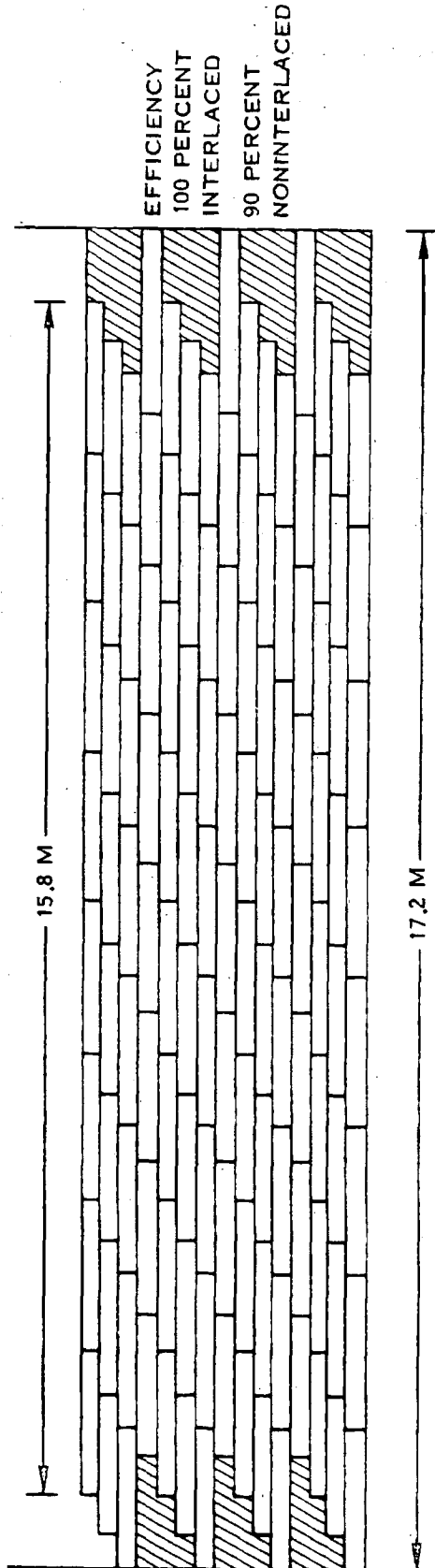


Figure 6-24. Three Subarray Layout Approaches

shifters. These requirements will insure a light weight-high efficiency array. In layout No. 1, the tubes are arranged on a square grid to yield a square subarray that utilizes approximately 100 percent of the available aperture. A square grid, however, does not allow a tube to be located at the input of each slotted waveguide and, hence, additional transmission lines are required. Transmission lines are also required to reverse the direction of rf power flow at the subarray edges. This approach is undesirable because of the complexity and greatly increased weight.

Layout No. 2 shows an approach whereby rf power flows continuously across a large portion of the array. This approach yields a very simple rf power distribution system but greatly complicates the subarray phasing approach. Since the rf flows across several subarrays, it will accumulate the phase error of each subarray. Consequently, the phase of each row must be compensated as it enters into each subarray. This requires a large number ( $\approx 150/\text{subarray}$ ) of high power lossy ( $\approx 1.25 \text{ kW cw}$ ;  $\approx 1 \text{ dB loss}$ ) phase shifters. These phase shifters would greatly increase the weight, losses, and cost of the array.

Layout No. 3 does not have the disadvantages of the previous layouts (i. e., large number of transmission lines or high power phase shifters). A small corporate feed structure is required to start each row. Staggering the tubes allows a tube to be located at the input to each slotted waveguide. At the input (i. e., left) side of the subarray, the tube staggering yields a staggered aperture edge and, hence, some of the available rectangular subarray aperture is not used. If the right edge of the subarray was also staggered, the subarrays could be interlaced with approximately 100 percent aperture utilization. The staggered left edge yields a loss in aperture. There are two approaches for the right edge that must be compared. Figure 6-25 demonstrates the two approaches. In the first approach, all rows are identical and the right edge is staggered similar to the left edge. In the second approach, the end waveguide of each row is extended to yield a straight edge. The power density across the end waveguides are not identical and the subarray aperture is no longer uniformly illuminated. The efficiency and sidelobes associated with these two right edge approaches are compared below. The power coupled out of the end of a waveguide is used as input to the next tube in the row. The last waveguide in a row does not excite another



NOTE:  
1) CROSS-HATCHED REGIONS NOT USED.  
2) RF POWER FLOW FROM LEFT TO RIGHT.

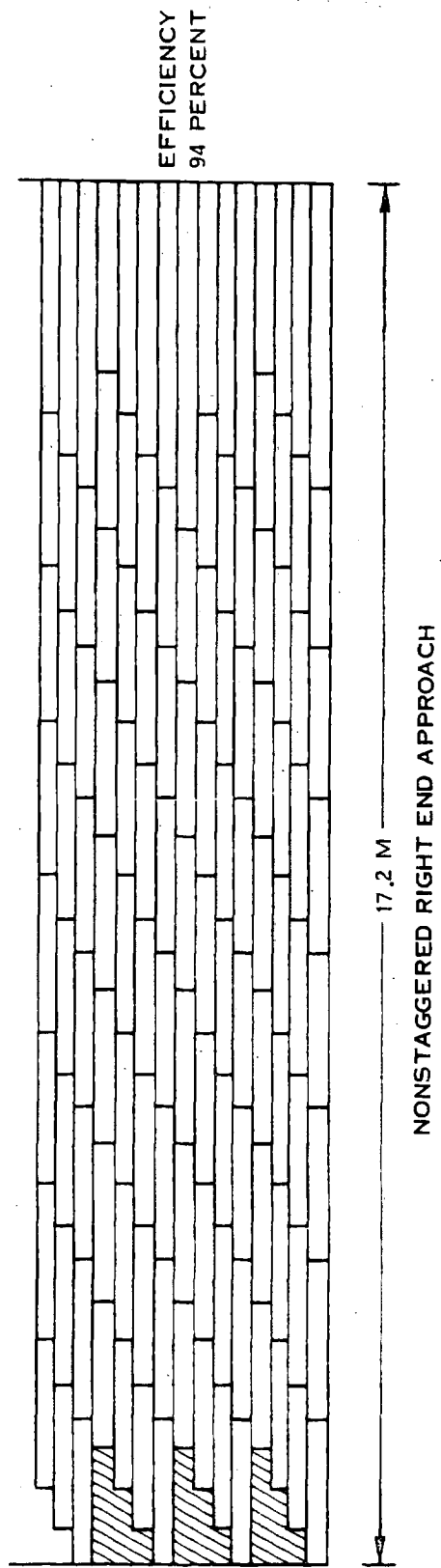


Figure 6-25. Subarray Right End Termination Approaches

tube. Instead it radiates approximately all of its power. A small percentage ( $\approx 10\%$ ) of its power must be dumped in a load to yield realizable slot coupling.

Figure 6-25 shows two row terminating approaches using Layout No. 3 of Figure 6-24. The staggered end approach has identical waveguide rows. The rows are staggered horizontally by 0.48m in a periodic fashion. Each row contains seven waveguides having 0.12m x 1.92m dimensions and one waveguide having 0.12m x 2.35m dimensions. The subarray width is 17.2m, a multiple of the radiator diameter of 48 cm for the amplatron. Each row is only 15.8m long and, hence, the subarray aperture efficiency is

$$N_a = \frac{15.8}{17.2} = 91\%$$

In order to make the 2.35m long waveguide uniformly distributed, ten percent of its power must be dumped in a load. The efficiency associated with the dumped power is:

$$N_L = \frac{7.9}{8.0} = 98.75\%$$

The total aperture efficiency for the staggered edge approach is:

$$N = N_a N_L = 89.9\%$$

The aperture efficiency for the non-staggered edge approach was computed to be 94 percent, which includes the effect of loss of aperture at the left edge, aperture taper at the right edge and ten percent dumped power in the right edge waveguides.

Peak grating lobes were found to be -21.1 dB for the staggered approach and below -22 dB for the non-staggered approach. Figure 6-26 shows two of the slotted waveguide designs required.

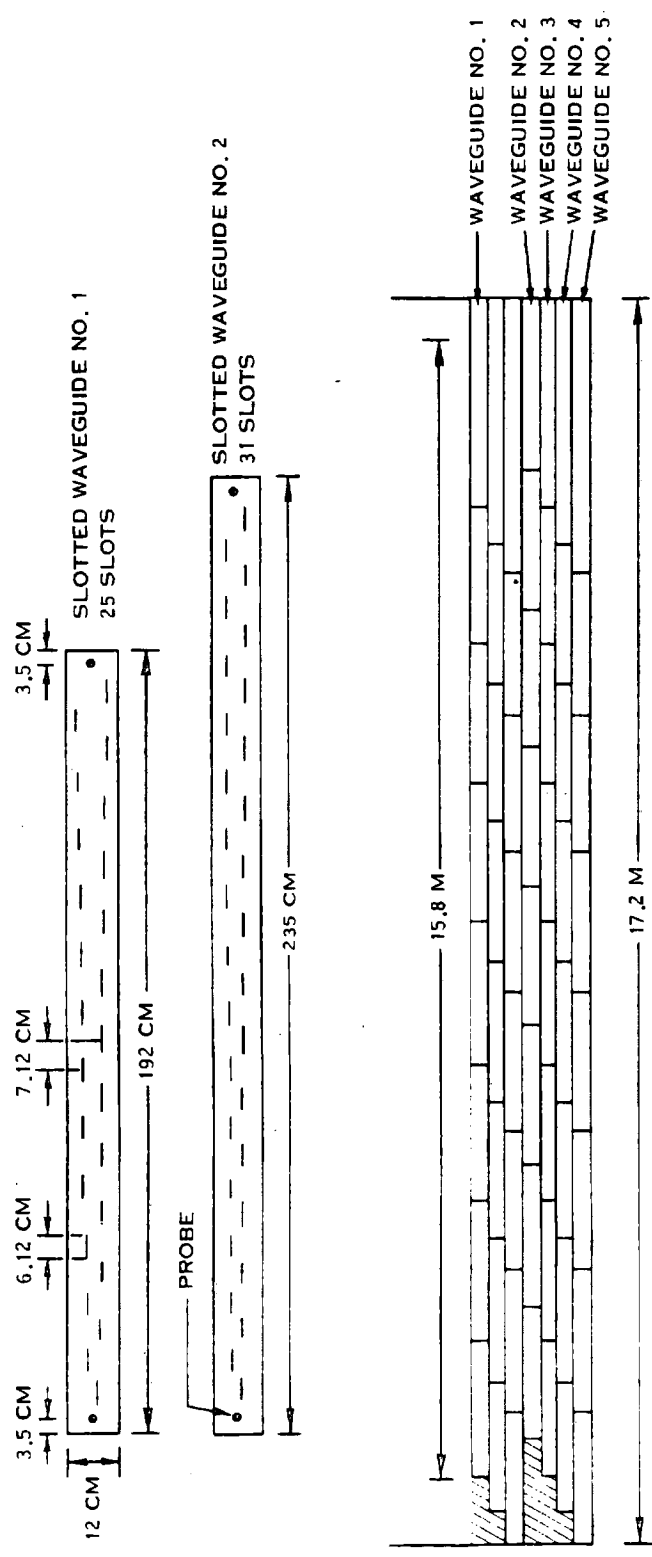


Figure 6-26. Two Slotted Waveguide Designs

## 6.6 TOLERANCE AND ATTENUATION

### 6.6.1 FREQUENCY TOLERANCE

Near the center of the transmit array, the slotted waveguide length between amplitrons is 1.92 meters as determined by fully packing with radiators 48 cm in diameter. A change in frequency or a change in waveguide width will cause the subarray to frequency scan if the direction of rf power flow is unilateral. If this occurs slowly, it can be compensated periodically by the jack screws near the corners of the subarray. If the amount of frequency scan is different for each subarray, a change in frequency will not fully compensate.

To maintain subarray beam squints within one arc minute (same as mechanical attitude control requirement) requires that the phase error over 1.92 meters (including the amplitron) be less than:

$$\Delta\phi = \frac{360d}{\lambda} \sin \theta = \frac{360(1.92)}{0.122} \left( \frac{1}{60 \times 57.296} \right) = 1.64^\circ.$$

The frequency stability can be found as follows. The phase shift down the guide is given by:

$$\phi = \frac{360d}{\lambda_g} = \frac{360d \sqrt{1 - \left(\frac{\lambda}{\lambda_c}\right)^2}}{\lambda}$$
$$\frac{2\phi}{2f} = \frac{2\phi}{2\lambda} \frac{2\lambda}{2f} = -360d \left[ \frac{1}{\lambda\lambda_g} + \frac{\lambda_g}{\lambda\lambda_c^2} \right] \left[ -\frac{c}{f^2} \right]$$
$$\therefore \Delta\phi = -360d \cdot \left[ \frac{1}{\lambda_g} + \frac{\lambda_g}{\lambda_c^2} \right] \left( \frac{\Delta f}{f} \right)$$

Using  $f = 2.45$  GHz,  $\lambda_g = 0.1424$ m,  $\lambda_c = 0.24$ m,  $d = 1.92$ m, and  $\Delta\phi = 1.64^\circ$  yields:

$$\frac{\Delta f}{f} = 0.00025 \text{ or } 0.025\%$$

Consequently,  $\Delta f \leq 612$  Hz.

$\lambda_c$  = fundamental mode cutoff wavelength

$\lambda_g$  = wavelength in waveguide.

### 6.6.2 WAVEGUIDE DIMENSIONAL TOLERANCES

The tolerable change in waveguide width to maintain beam pointing to one arc minute can be found as follows. The beam pointing angle is given by:

$$\frac{2\pi d}{\lambda} \times \sin \theta - \left( \frac{2\pi dx}{\lambda g} - \pi \right) = 0$$

or

$$\sin \theta = \frac{\lambda}{dx} \left( \frac{dx}{\lambda g} - \frac{1}{2} \right)$$

where  $\theta$  is measured as a negative angle toward the feed end.  $dx$  is the spacing between a pair of slots.

$$\frac{\partial \sin \theta}{\partial a} = 2 \frac{\partial \sin \theta}{\partial \lambda c} = 2 \frac{\partial}{\partial \lambda c} \left( \frac{\lambda}{\lambda g} \right) = \frac{2\lambda \lambda g}{\lambda c^3}$$

or

$$\Delta a \leq \Delta \sin \theta \left[ \frac{\lambda c^3}{2\lambda g \lambda} \right] = 0.012 \text{ cm} = 0.005 \text{ in.}$$

Errors in properly locating the slots will produce random phase errors. The rms phase error due to rms location errors is given by:

$$\sigma_{\phi} = \frac{2\pi \sigma_d}{\lambda g}$$

$\sigma_{\phi} = 0.5^{\circ}$  implies that  $\sigma_d = 0.0014\lambda g = 0.0197 \text{ cm} = 0.008''$ . The slot conductance is relatively insensitive to slot width. The resonance changes, however, with length.

The effect of temperature variation and waveguide length and width causes beam scanning in the manner of a frequency change. The maximum temperature variation due to the diurnal rotation of the antenna relative to the sun was estimated from the data of Figure 3.3-23 of Section 8, on the assumption that waveguide

and structural temperatures gradient variations will be comparable. If waveguide lengths are adjusted to the average temperature, the residual changes as a function of radius would be:

<u>Radius-M</u>	<u>± Temp Difference Variation C°</u>
0	25
100	33
200	35
300	41
400	48
500	60

If uncompensated, this variation would result in a relatively large (~8%) peak loss of efficiency for aluminum waveguide construction (negligible for composites). A frequency change can partially compensate by changing the effective electrical length of the waveguide. For a 5 dB taper and selecting 35C° as the nominal correction value, the peak efficiency loss is reduced to 0.5 percent. At 10 dB taper it is 0.4 percent. The required shift in wavelengths is only  $1/10^4$ , representing 245.0 kHz at a 2.45 GHz nominal operating frequency. Since the average loss over the diurnal cycle is  $2/\pi$  of the peak value, the net impact on the system efficiency budget is negligible.

### 6.6.3 WAVEGUIDE ATTENUATION

The attenuation in a waveguide is given by:

$$\alpha = \frac{C}{\sqrt{\sigma}} \left[ \frac{1}{\sqrt{1 - \left(\frac{\lambda}{2a}\right)^2}} + \frac{\frac{2b}{a} \left(\frac{\lambda}{2a}\right)^2}{\sqrt{1 - \left(\frac{\lambda}{2a}\right)^2}} + \frac{K_p \left(\frac{\lambda_c}{\lambda_g}\right)^2 \left(\frac{2b}{a}\right) \frac{\lambda}{2a}}{\sqrt{1 - \left(\frac{\lambda}{2a}\right)^2}} \right]$$

↑

side walls

↑

top and bottom walls

↑

surface roughness

The MPTS guide has  $a = 12$  cm,  $b = 6$  cm,  $\lambda_g = 14.23$  cm,  $\lambda = 12.24$  cm, and  $\lambda_c = 24$  cm. The top and bottom walls account for 0.0019 dB/m and the side-walls account for 0.0072 dB/m.  $K_p \approx 1$  in practice. The 0.0091 dB/m is a theoretical value based on  $K_p = 0$ . Consequently, the surface roughness contribution is 2.84 times greater than the broad wall attenuation. The total attenuation



including surface roughness is 0.0145 dB/m. These calculations are based on a dc conductivity of  $3.43 \times 10^7$  mhos/m at 20°C temperature. The temperature variation of conductivity for aluminum is given by:

$$\sigma_T = \frac{\sigma_{20^\circ}}{1 + 0.0039 (T - 20^\circ)}$$

where

T = temperature in °C

If the broad wall under the thermal radiator (no insulation) is 220°C, the conductivity of that wall decreases to  $1.93 \times 10^7$  mhos/m. The top wall attenuation of 0.00095 dB/m increases to 0.00127 dB/m and the total attenuation is 0.0148 dB/m (0.451 dB/100').

In the past, waveguide attenuation calculations have been based on dc conductivity due to the lack of rf conductivity measurements at the frequencies of interest. The rf conductivity at 2.45 GHz may be slightly lower than the value used here. For example, rf conductivity of aluminum waveguide at 24 GHz is much lower, i. e.,  $1.97 \times 10^7$  mhos/m. A value of 0.451 dB/100' is probably typical for MPTS aluminum waveguide at 2.45 GHz. If the side walls are also at an elevated temperature, the attenuation would be greater.

## 6.7 MECHANICAL DESIGN AND ANALYSIS

### 6.7.1 THERMAL ANALYSIS AND CONFIGURATION

Preliminary thermal analyses were conducted on the amplatron and klystron converter candidates mounted on the waveguide in the maximum packing configuration as appropriate for the central arrays of a high power system. These were done to establish radiator sizes for the converters and to determine thermal deflection characteristics and maximum temperatures of the waveguide.

To obtain a reasonable temperature gradient along the waveguides, three different waveguide thicknesses were evaluated initially. These thicknesses were 0.01 inch (0.0254 cm), 0.02 inch (0.0508 cm) and 0.03 inch (0.0762 cm). Gradients and deflection decrease as wall thickness increases. Based upon considerations of temperature, weight and structural strength, the 0.02 inch

(0.0508 cm) thickness was chosen for extended analysis, and the temperature data presented here are based upon a uniform waveguide thickness of that value.

The efficiency of the microwave beam is directly proportional to the flatness of the waveguide antenna. Distortion due to temperature gradient between upper and lower surfaces of the waveguides degrades this efficiency. In determining the magnitude of the thermal gradient, three candidate waveguide materials were evaluated. These materials were Aluminum, Epoxy/Graphite Laminate and Graphite/Polyimide Laminate. For the amplitron model of Figure 6-27 the analysis results are presented in Figure 6-28.

Due to the temperature limitations of the magnet on the amplitron, the constraints in sizing the radiators were:

- a. Cathode temperature not to exceed  $640^{\circ}\text{C}$  (Point A).
- b. The temperature at the root of the anode radiator (Point D) not to exceed  $350^{\circ}\text{C}$ .

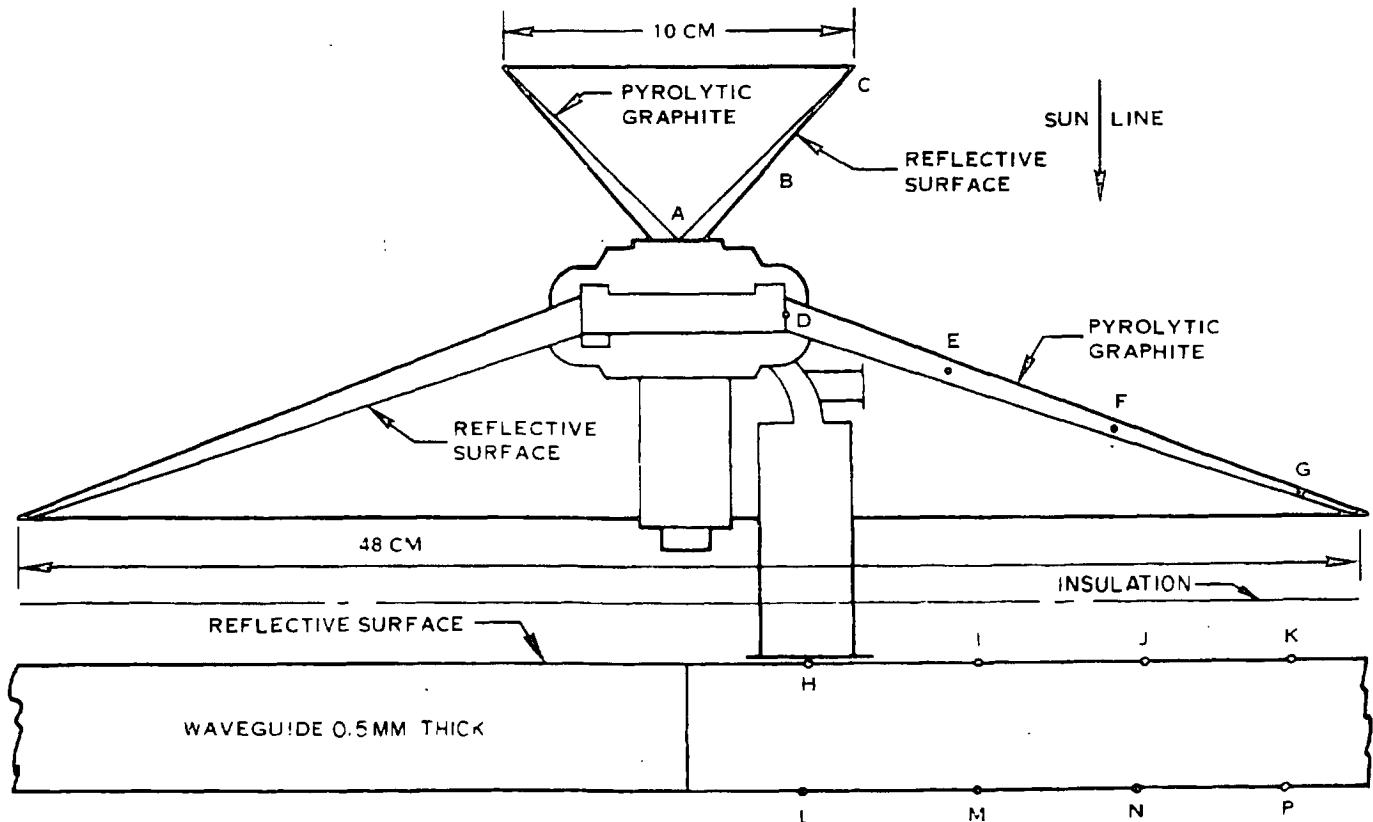


Figure 6-27. Amplitron Thermal Model

ALUMINUM WAVEGUIDE TEMP. ~ °C

LOCATION	A	B	C	D	E	F	G	H	I	J	K	L	M	N	P
NO INSULATION	635	591	570	349	305	282	265	52	49	48	46	39	40	41	41
WITH INSULATION	635	591	570	350	306	282	265	51	47	46	44	39	40	40	40

GRAPHITE/EPOXY WAVEGUIDE TEMP. ~ °C

LOCATION	A	B	C	D	E	F	G	H	I	J	K	L	M	N	P
NO INSULATION	635	591	570	350	305	282	265	148	126	115	97	38	40	40	40
WITH INSULATION	635	591	570	350	306	282	265	141	111	100	87	38	39	40	40

GRAPHITE/POLYIMIDE WAVEGUIDE TEMP. ~ °C

LOCATION	A	B	C	D	E	F	G	H	I	J	K	L	M	N	P
NO INSULATION	635	591	570	349	305	282	265	107	91	84	74	39	40	40	41
WITH INSULATION	635	591	570	350	306	282	266	101	81	74	66	38	40	40	40

Figure 6-28. Amplitron Thermal Analysis

- c. The power dissipation at the cathode was 235 watts.
- d. The power dissipation at the anode was 647 watts.
- e. The sun line is normal to the radiator as shown.

Applying these parameters, the cathode radiator was calculated to be a truncated 85 degree cone with a 10 cm (3.9 inches) base while the anode radiator is a truncated 140 degree cone with a 48 cm (18.9 inches) base. The radiator material used was Pyrolytic Graphite. This material was selected because of its high temperature strength and its unique thermal conductivity characteristics.

In an effort to reduce the radiated heat flux on the waveguides from the anode radiator, analyses were conducted with a sheet of metallized (both sides) Kapton insulation inserted between them. Results of these analyses are itemized for comparison.

The klystron tube design was not as well defined as that of the amplatron throughout the study and its power level and focusing technique were altered as new data were generated. The PPM design at 6 kW output changed to solenoid focused designs at higher powers culminating in the 48 kW design. The material in Figures 6-29 and 6-30 relates to the 6 kW version which was later scaled to the larger power level for the aluminum insulated case. As shown in Figure 6-30, temperatures are much lower for the 48 kW tube due to a lower radiator temperature.

The inherent lower efficiency and the configuration of the klystron results in excessive temperature when cooled by a passive approach to heat transfer. Body temperature reached 615°C. In order to provide some comparison with the amplatron, it was assumed that a heat pipe jacket could be designed to surround the klystron and keep the magnets to a maximum temperature of 350°C (Point D). This heat pipe is connected to a radiator as illustrated in Figure 6-29. In order to maintain the heat pipe temperature at no higher than 350°C, this radiator was calculated to be a truncated 140 degree cone with a 64 cm (25.2 inches) base.

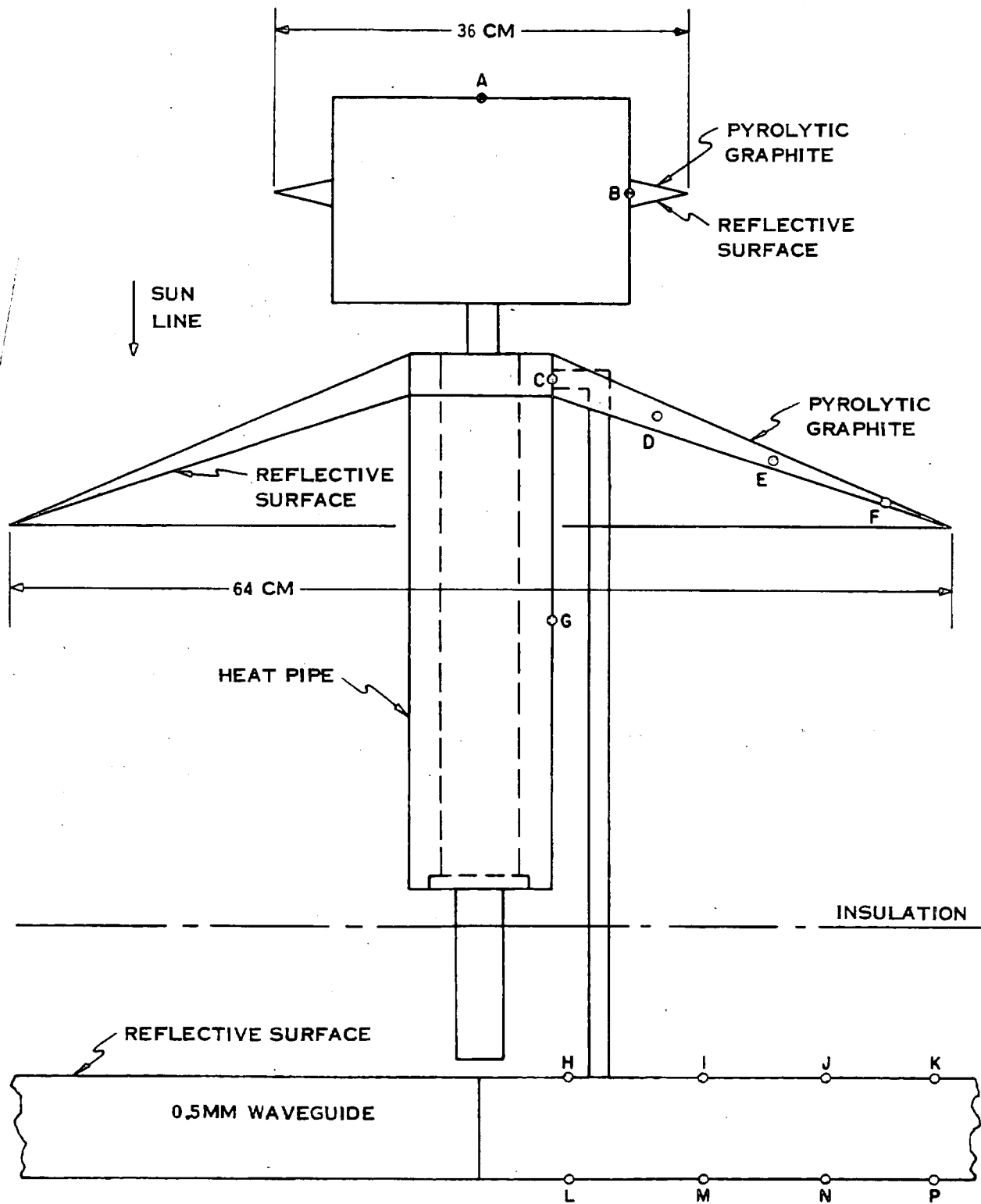


Figure 6-29. 6 kW Klystron Configuration

0.02" Thick Aluminum Waveguide - Temperature ~ °C															
Location	A	B	C	D	E	F	G	H	I	J	K	L	M	N	P
No Insulation	253	622	346	308	282	260	346	101	113	108	106	95	96	97	97
With Insulation	253	622	347	309	283	261	347	99	106	104	103	95	95	96	96
								(55)	(59)	(58)	(57)	(53)	(53)	(54)	(54)
0.02" Thick Graphite/Polyimide Waveguide - Temperature ~ °C															
Location	A	B	C	D	E	F	G	H	I	J	K	L	M	N	P
No Insulation	253	622	346	309	282	261	346	122	177	148	140	95	96	96	97
With Insulation	253	622	347	310	283	262	347	118	151	135	130	94	95	96	96
0.2" Thick Graphite/Epoxy Waveguide - Temperature ~ °C															
Location	A	B	C	D	E	F	G	H	I	J	K	L	M	N	P
No Insulation	253	622	347	309	283	261	347	138	212	171	160	94	96	96	96
With Insulation	253	622	347	310	284	262	347	134	182	156	148	94	95	95	96

Note: 6 kW tube except ( ) for 48 kW tube.  
Heat pipe body conduction assumed.

Figure 6-30. Klystron Configuration Temperature Distribution

With the above assumptions, analyses similar to those for the amplitron were performed for three waveguide materials. The klystron power dissipation employed for these analyses is as follows:

Collector	998.5 watts
Circuit Loss	900.0 watts
Beam Inter- ception	155.0 watts
Heater	60.0 watts

Results of these analyses are shown in Figure 6-30.

A total of 22 configurations differing in waveguide material, waveguide design, converter type, converter conductivity and waveguide surface treatment were studied using the 18m subarray size. As the study progressed it became apparent that a waveguide thickness of 0.020 in (0.5 mm) was a good compromise considering subarray size, structural stability, and weight. This dimension also is the thinnest known to have been fabricated to date. Figure 6-31 shows the results for a selection of candidates for the amplitron, and Figure 6-32 compares amplitron and 6 kW klystron results for an unshielded waveguide design.

We see that deflections for the aluminum result in a power loss above one percent as the dimension exceeds 5m for the amplitron and near 15m for the polyimide material. There is a modest improvement for a shielded waveguide case. The klystron, due to its higher waste heat, produces greater deflection than the amplitron even though a large portion (at the collector) can be radiated at elevated temperature. The difficulty with the aluminum requirement for an extremely small subarray dimension of 5m (order of magnitude increase in control electronics cost relative to 15m) was circumvented by devising a segmented subarray concept in which 5m sections are suspended from the supporting structure as shown in Figure 6-33. There is a weight penalty for this elaboration that would not be needed for the composite materials, and there may be a temperature problem on the stringers that was not evaluated, tungsten, for example, may have to be used.

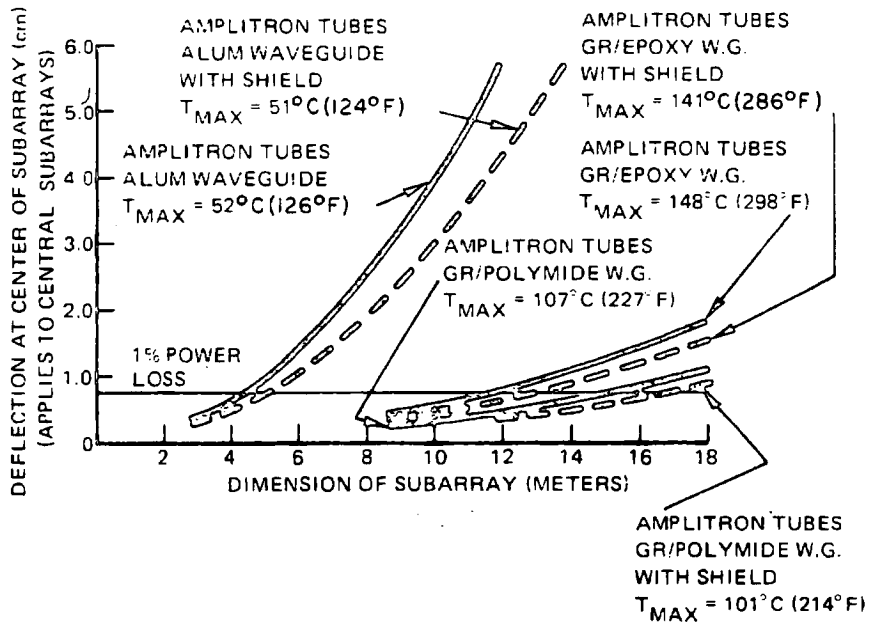


Figure 6-31. Subarray Deflection vs. Size

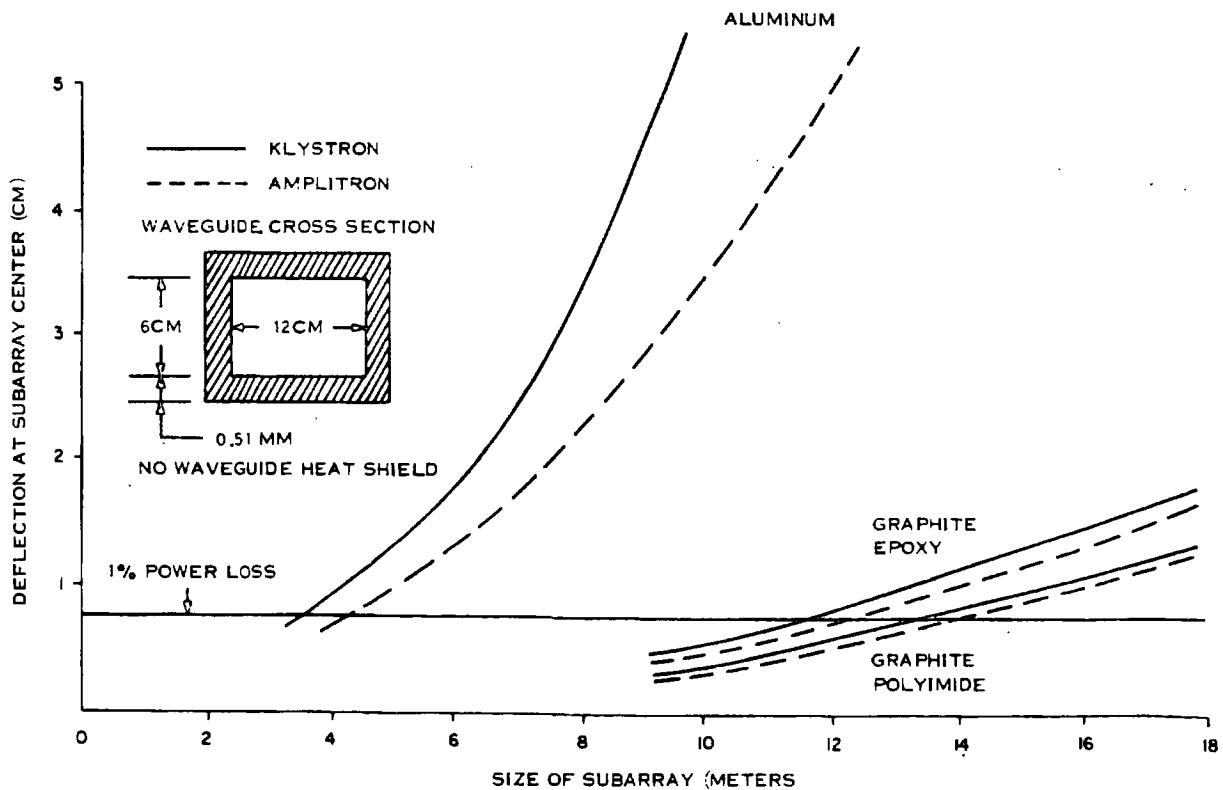


Figure 6-32. Subarray Deflection vs. Size



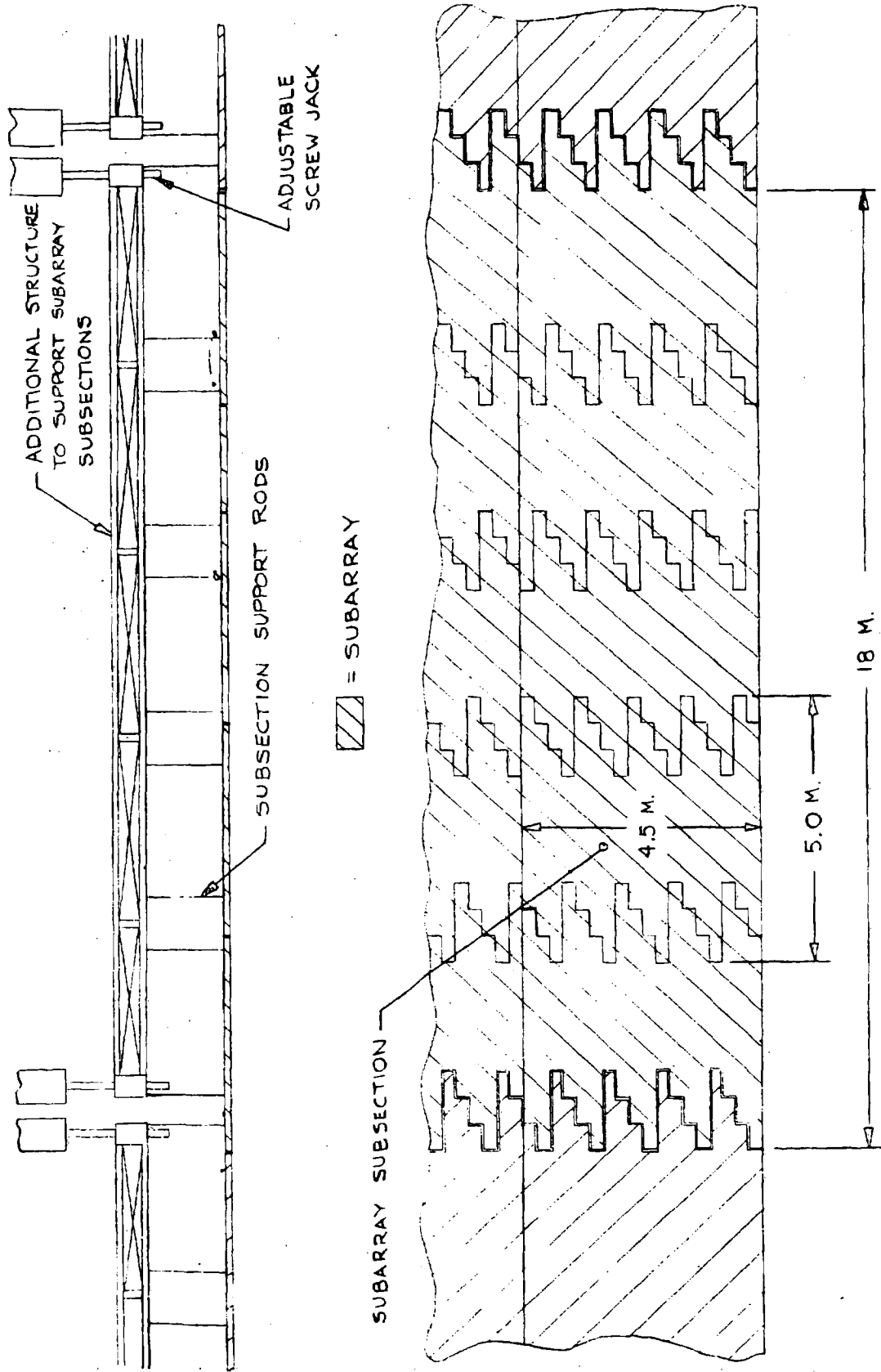


Figure 6-33. Subarray Configuration (Using 6061-T6 Al. Waveguide)

In the case of the Amplitron detailed thermal design considering such approaches as biasing the thermal flow path in the region of H&L (Figure 6-27) to conduct more heat to the L side of the waveguide should be undertaken. The goal would be to minimize the average temperature gradient along the length of the waveguide which in turn would lead to smaller thermal distortions. This as well as detailed considerations of thermal coatings, blankets and shields should be the subject of in-depth thermal materials and structural technology development. Such a development program may lead to lighter waveguides than the 0.0508 cm assumed here and the goal in this regard should be to develop the waveguide with its interfaces to the tube, neighbor's waveguides and the supporting structure to make it producible and functional with high efficiency, low weight and low system cost.

A preliminary layout of a complete subarray for fully packed amplitrons and composite material is given in Figure 6-34. The screwjacks shown (three) provide for attitude and translation adjustments at installation and at periodic intervals as may be required. The primary means of beam control is electronic, as described in the next section.

### 6.7.2 MATERIALS

A search for information on graphite epoxy and graphite polyimide composites showed considerable data had been generated but for very specific conditions and for short time periods relative to the 30-year life needed by MPTS. Some data are shown in Figures 6-35 through 6-37 as reported by R. Poloti of American Cyanamide Co. The composites offer high specific stiffness (modulus of elasticity/density) and have very low thermal expansion coefficients, and the graphite polyimides offer the additional advantage of high temperature stability, as indicated by the figures.

There is no question of the ability to manufacture composites with the required dimensional tolerances, and surface finishes ( $500\mu$  in and  $50\mu$  in have been achieved) and to obtain good adhesion of a silver conductive liner for the waveguide [References 6-1, 6-2]. Graphite epoxy reflectors have been made for spacecraft microwave application, and a number of structural components for the Space Shuttle will be of graphite epoxy. However, composites are relatively costly, and the long term stability in the space environment and

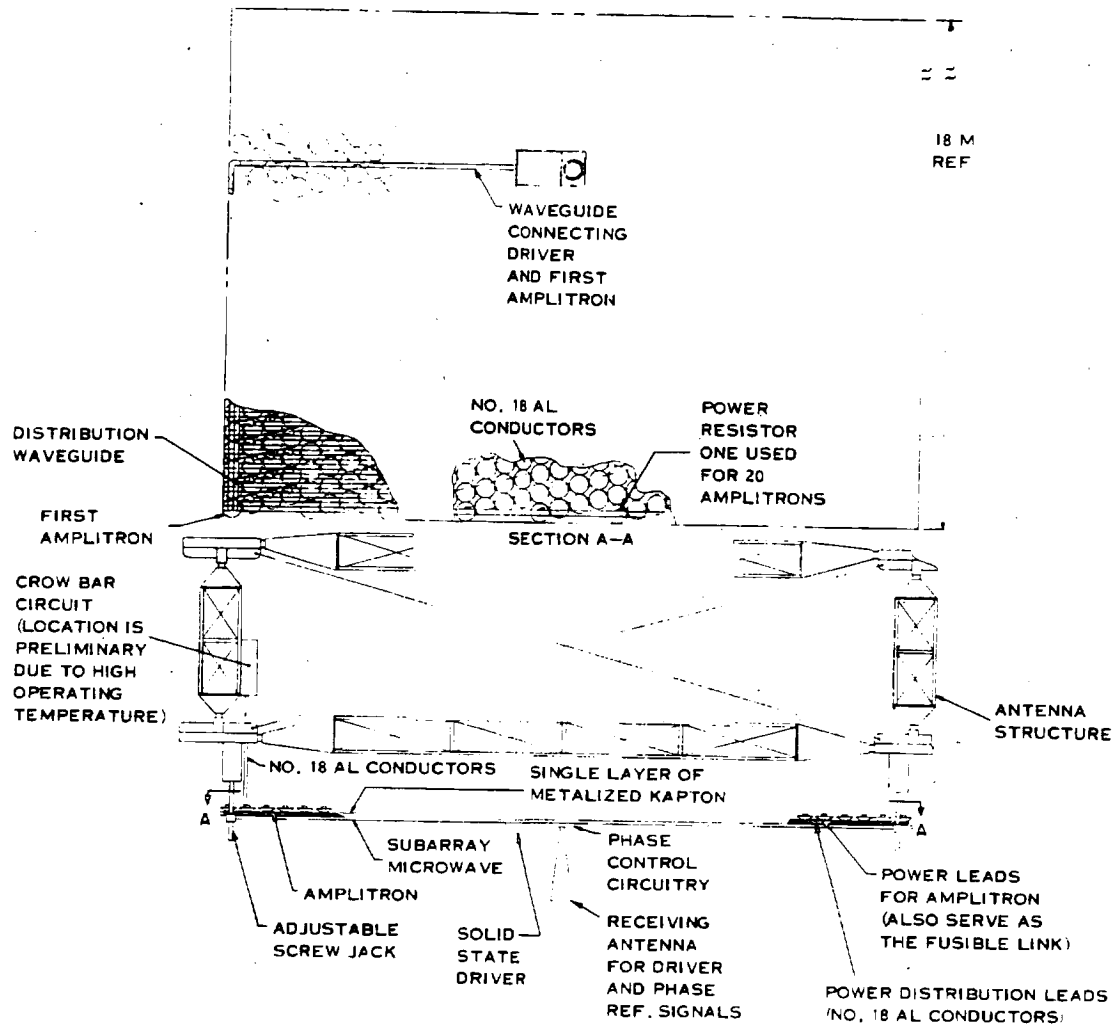


Figure 6-34. Subarray Layout

degree of outgassing are questions to be answered for MPTS. The outgassing concern stems from the potential arcing problem for open-tube amplitron or klystron design if contaminants are prevalent. The use of sealed jackets adds weight, but more importantly degrades reliability at least in earth-based applications. It may be that a baffle or molecular barrier would suffice to prevent arcing without reliability degradation; nevertheless the open tube construction would be a highly desirable goal, if not mandatory.

ORIGINAL PAGE IS  
OF POOR QUALITY

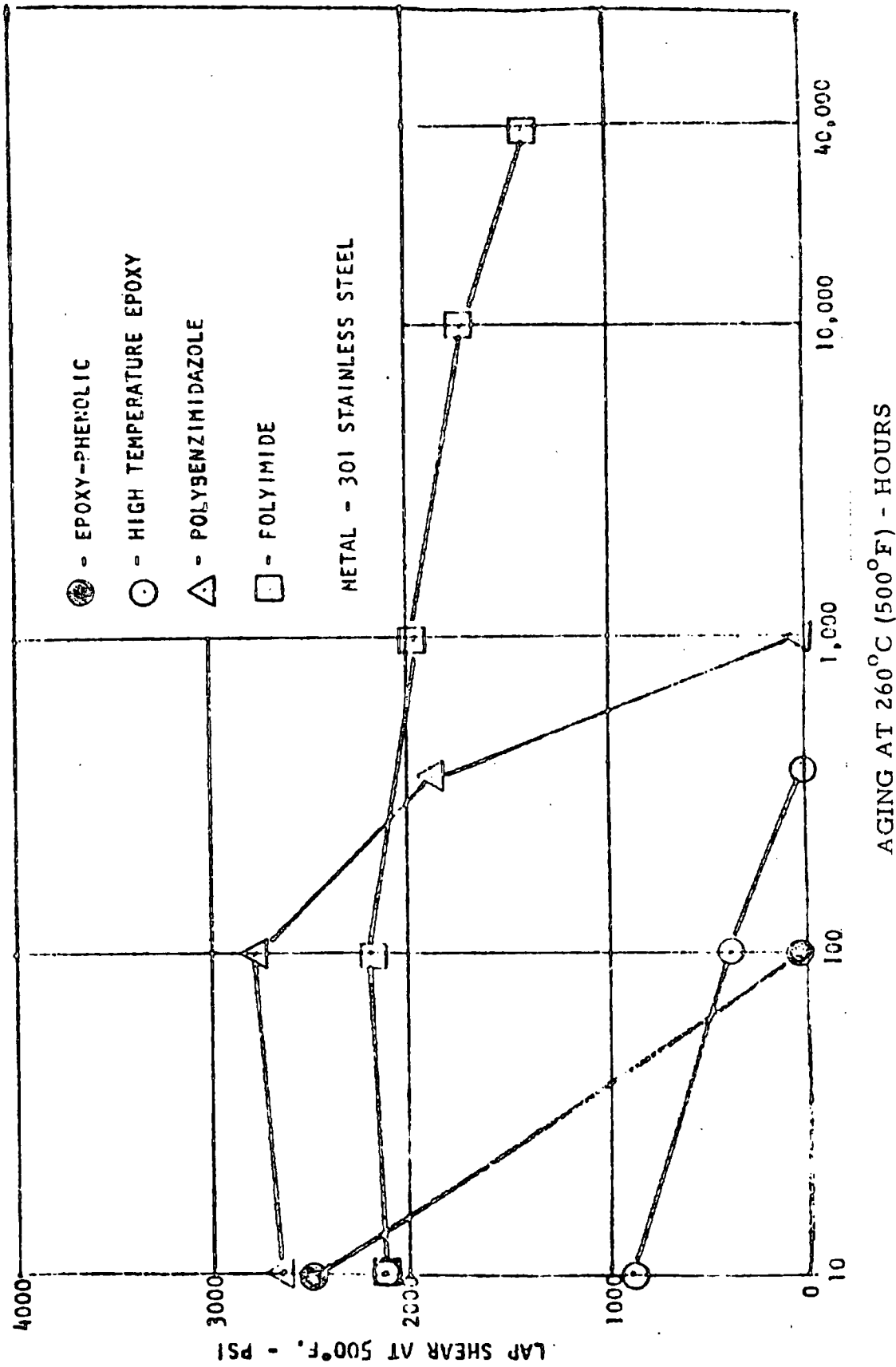


Figure 6-35. Thermal Stability at 260°C of Various Adhesives

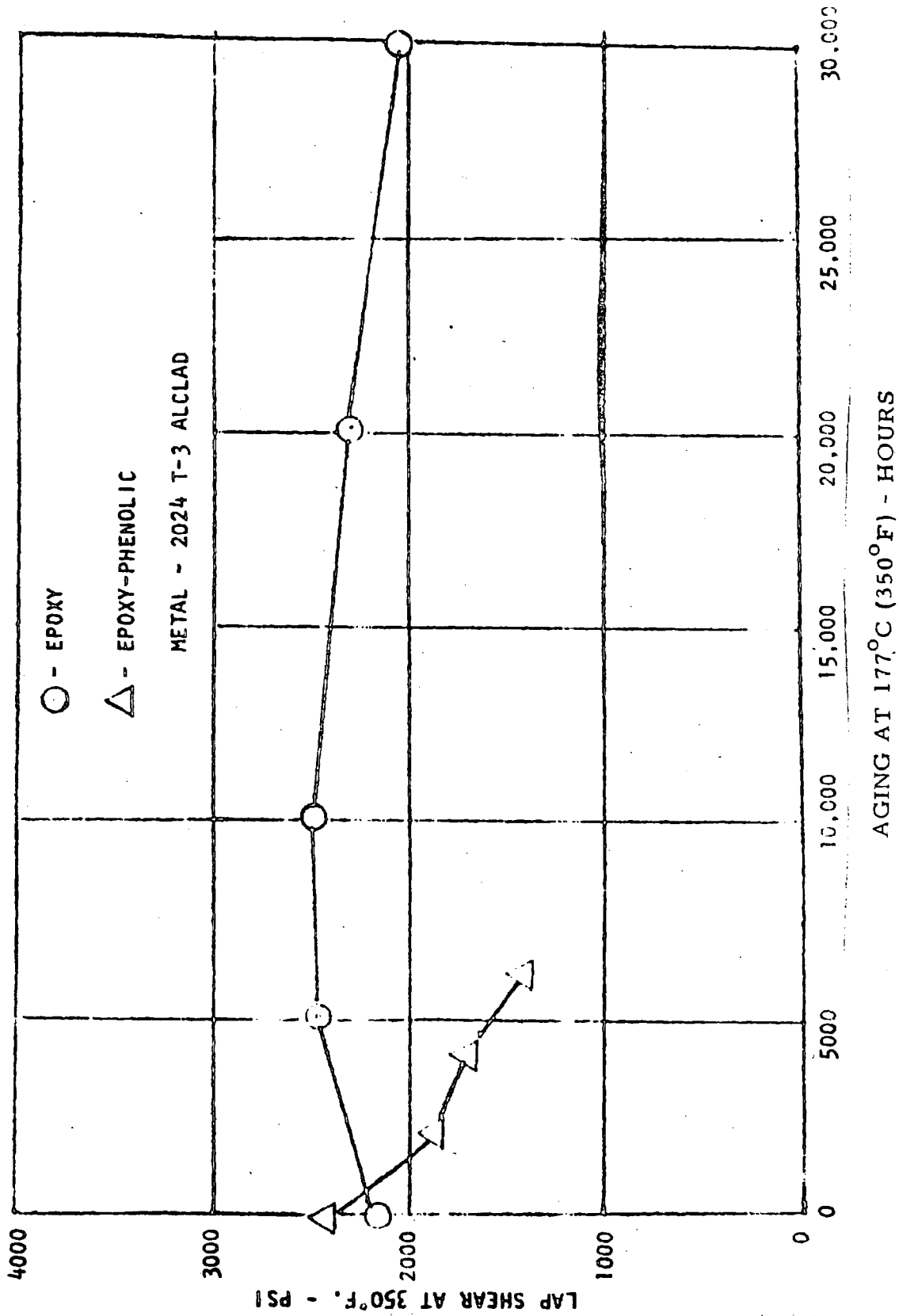


Figure 6-36. Thermal Stability at 177°C of Epoxy and Epoxy-Phenolic Adhesives

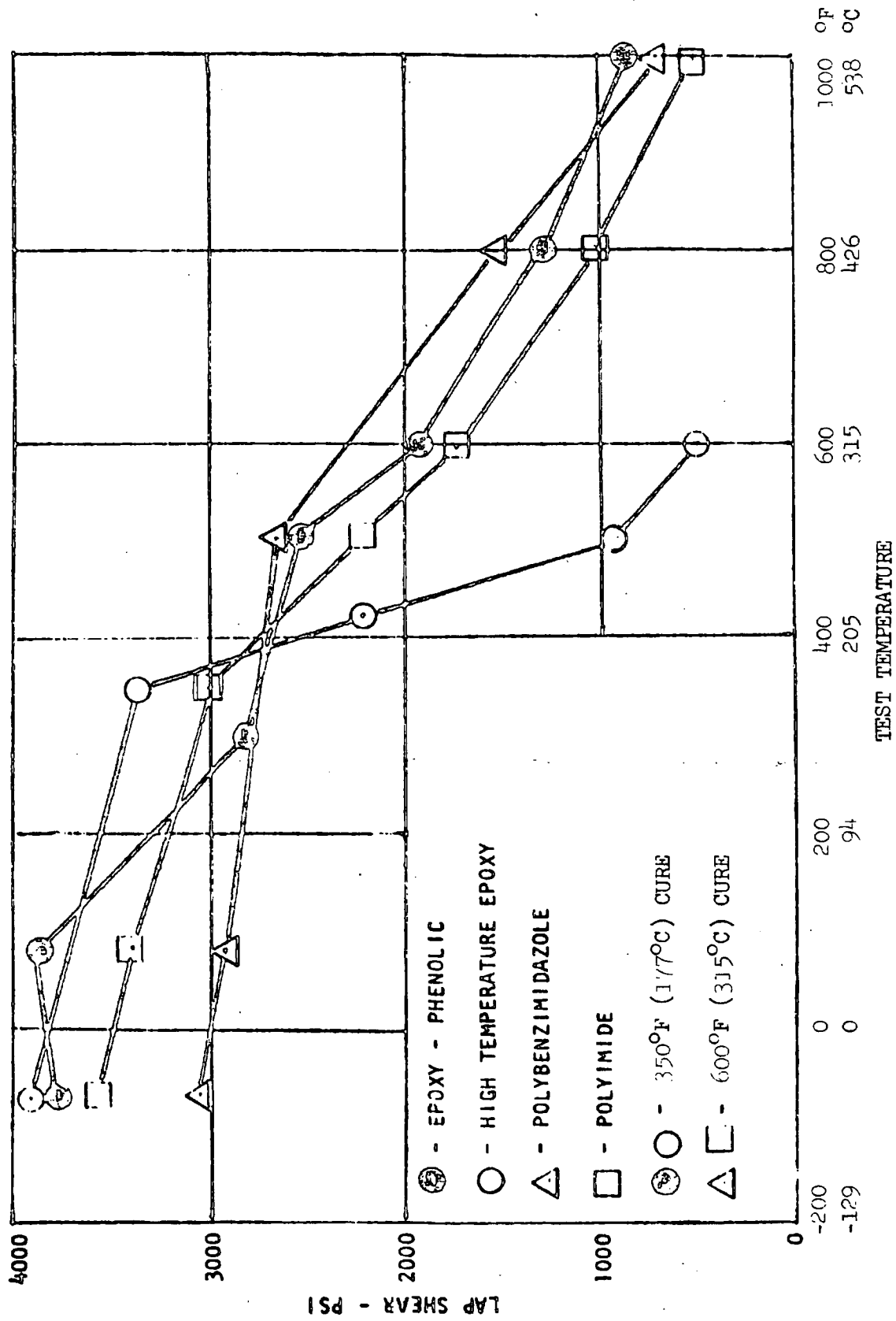


Figure 6-37. Comparison of High Temperature Strength of Various Types of Adhesives

### 6.7.3 TRANSPORTATION, ASSEMBLY AND PACKAGING

Three transportation, assembly and packaging alternatives exist for the subarray, which is the basic building block of the transmitting antenna. These are:

- a. Build the waveguide, converters, etc. on the ground, and assemble the parts into subarray sections which can be fitted into the launch vehicle.
- b. Build the waveguide, converters, etc. on the ground and transport the parts in the launch vehicle; assemble into subarrays in orbit.
- c. Produce the waveguide material, converters, etc. on the ground and transport the material and parts in the launch vehicle; manufacture the waveguide and assemble the subarrays in orbit. A manufacturing module would be required.

These options are illustrated in Figures 6-38 through 6-40 using the Space Shuttle as the launch vehicle. A variation for alternative B is shown in Figure 6-41 where the implications of waveguide wall thickness also are illustrated for the Space Shuttle, and it can be seen that even for that relatively sophisticated packing concept that the Shuttle remains volume limited. The threshold for weight limit should be reached for lowest cost transportation. The implications of alternatives A, B, and C above are:

<u>Alternative</u>	<u>Packing Density - lb/ft<sup>3</sup></u>		<u>Shuttle Limitation</u>
	<u>Aluminum</u>	<u>Composite</u>	
A	1.0	0.8	Volume
B	5.2	4.1	Volume
C	6.1	6.1	Mass

We see that Alternative C is the desired approach if space manufacturing of waveguide is feasible. The question of transportation and assembly is addressed further for the structures and entire MPTS in the later section on Mechanical Systems and Flight Operations.

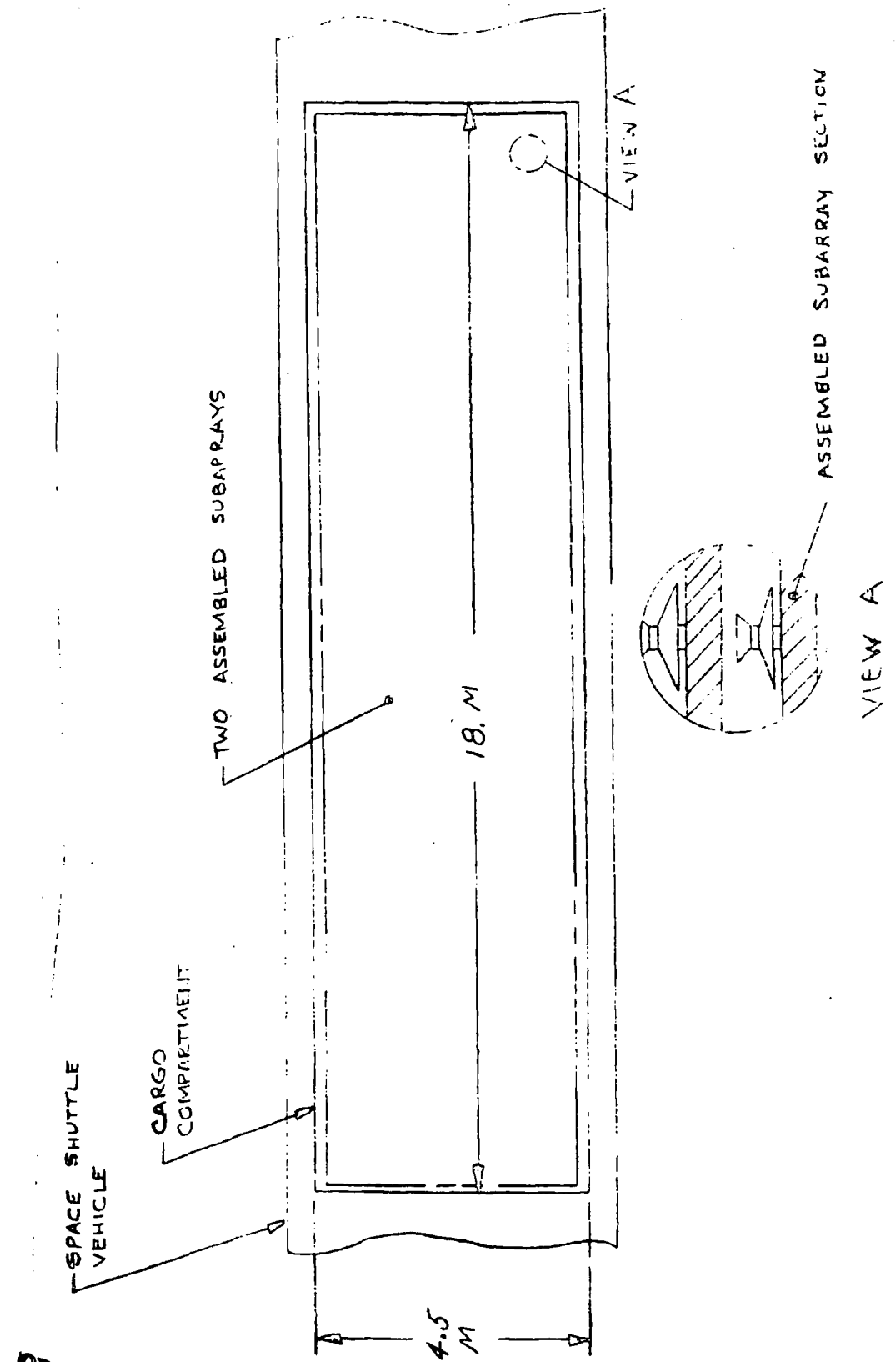
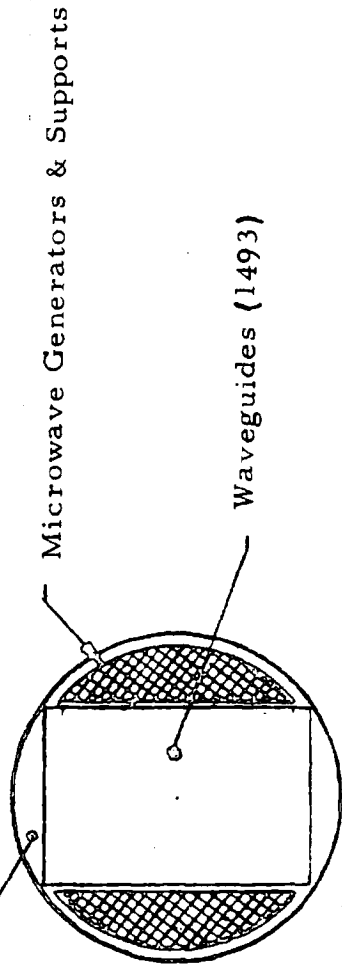


Figure 6-38. Transportation Alternative A

ORIGINAL PAGE IS  
OF POOR QUALITY



Power Dist. Equip. & Driver/Phase Control Unit



Microwave Generators & Supports

Waveguides (1493)

Space Shuttle Vehicle

SECTION A-A

Microwave Generators & Supports, Power Dist. Equip., & Driver/Phase Control Units

Cargo Compartment

Cargo Supports

Waveguide

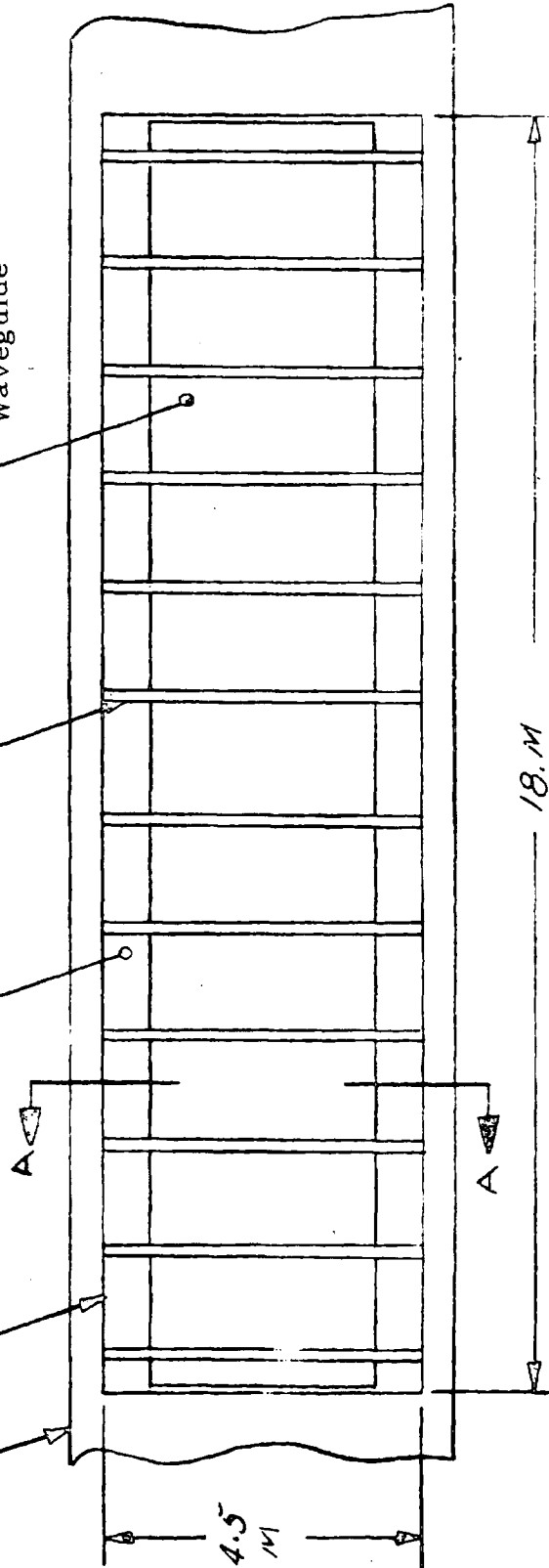


Figure 6-39. Transportation Alternative B

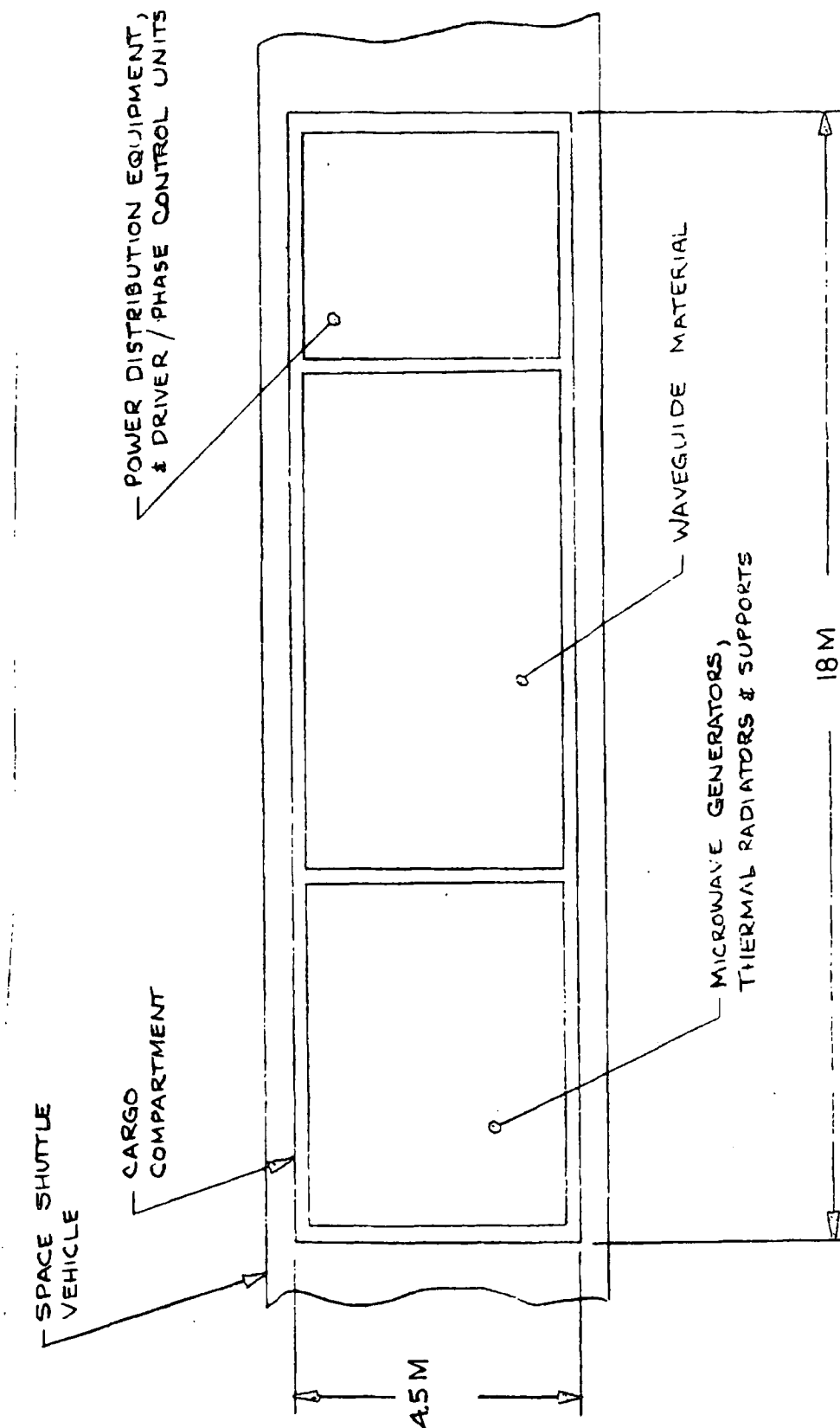


Figure 6-40. Transportation Alternative C

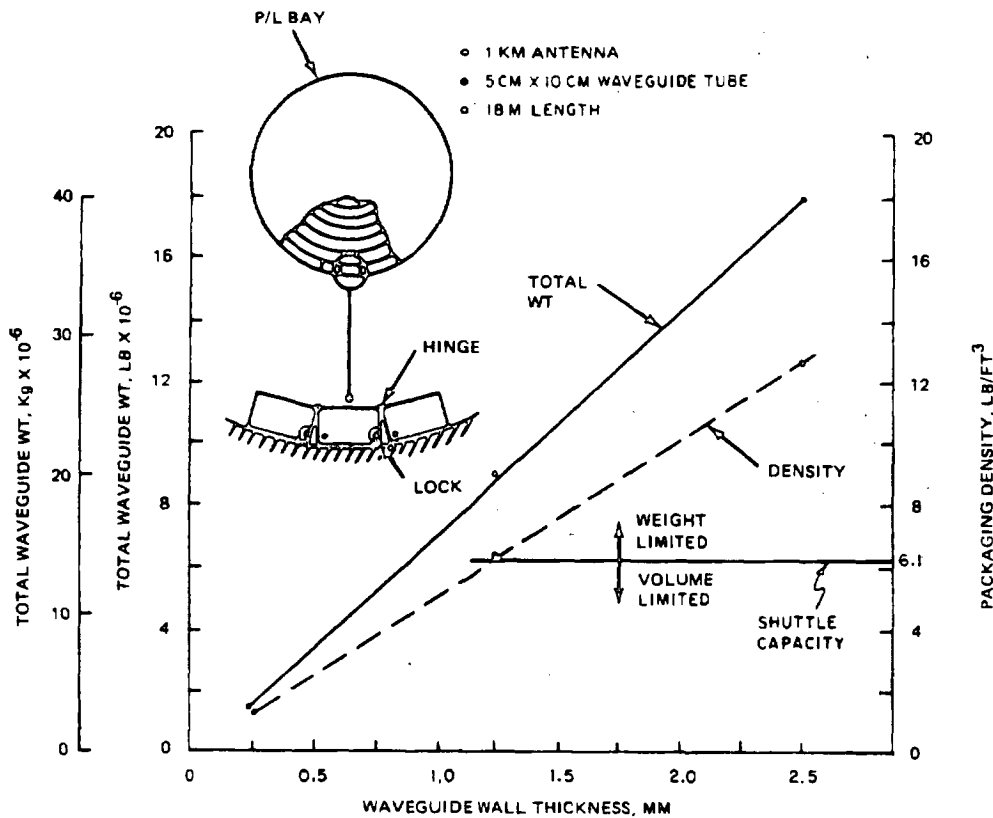


Figure 6-41. Waveguide Weight and Packaging Density

## 6.8 ATTITUDE CONTROL AND ALIGNMENT

The subarrays must be aligned to a nominal, ideal surface within about one arc minute to maintain efficiency. It is proposed that the reference alignment plane be established at the center subarray by means of interferometers that determine the angle of arrival of the pilot beam. This primary sensor with triple redundancy would be backed up by other instruments: star sensors, earth sensors, inertial sensors. A best estimate of line-of-sight to the ground would be determined by redundant processors in the central subarray, which becomes the command-control center not only for MPTS, but for an entire SPS as well.

Alignment of each subarray at installation and at intervals throughout the system lifetime (perhaps following eclipse periods) requires a similar reference. It is recommended this also be based on interferometers and that the necessary adjustments be made using the screwjacks noted above and described in detail in Section 8. Alternate sensing approaches would be (1) to employ the

bit wiggle scheme to examine the ground pattern of each subarray while all are operating and (2) to power up one subarray at a time for comparison with a standard ground pattern.

The weight breakdowns for the command - control central section and for the subarray phase and attitude control subsystems are:

Central Command Control Section (Triple Redundancy)

<u>Communication Subsystem</u>	<u>kg</u>
rf, Network (up-down link)	70
Digital, Network	45
rf, Subarray	70
Digital Subarray	<u>45</u>
	230

<u>Computer Subsystem</u>	<u>kg</u>
CPU and Memory	80

<u>Attitude Sensors</u>	
Interferometer	60
Star Sensors	30
Earth Sensors	15
Inertial Reference	<u>360</u>
Total Central Sections	465

Subarray Control (Dual Redundancy)

Phase Control Subsystem	17
Converter Driver	23
Command Control Subsystem	5
Digital Subsystem	10
Interferometer	<u>20</u>
	<u>75</u>
Screwjack Actuators (3)	60

## 6.9 CONCLUSIONS AND RECOMMENDATIONS

- a. The transmitting antenna will be a circular, planar, active phased array on the order of 1 km in diameter.
- b. Antenna illumination will be truncated Gaussian with tapers of 5 dB to 10 dB, which can be quantized into about five regions of uniform power.
- c. The antenna will be sectored into subarrays of nominal dimensions 18m x 18m.
- d. Subarrays consist of slotted waveguide radiators providing a high overall beam formation and interception efficiency of at least 95 percent for a contiguous rectenna within the main lobe.
- e. Waveguide wall thickness nominally is 0.5 mm, but additional investigation may show this can be reduced; width is 12 cm and depth is 6 cm. Cross-sections other than rectangular should be included in future detailed investigations.
- f. Aluminum, graphite epoxy and graphite polyimide are candidate materials for the slotted array waveguides.
- g. Aluminum configurations require structural segmenting of the subarrays and variation of operating frequency to compensate for longitudinal thermal distortions.
- h. Graphite Polyimide configurations offer the highest temperature margin with minimal distortion, but all composites must be evaluated for stability and outgassing properties.
- i. Waveguide manufacture and subarray assembly on orbit is recommended to achieve favorable launch vehicle packaging density.
- j. Microwave interferometers are recommended for MPTS and SPS attitude control, and for initial and periodic alignment of subarrays using screwjack actuators on each subarray.

#### REFERENCES (SECTION 6)

- 6-1 "Developments of a Unique Graphite/Epoxy Antenna Subreflector," E. Y. Robinson, R. A. Stonier, C. L. Lofgren, Composite Materials (Third Conference, 1973), ASTM, pp. 632-650.
- 6-2 "Manufacturing Methods for Dimensionally Stable Composite Microwave Composites," L. B. Keller and H. Raech, Hughes Aircraft Report, May 1974.

## SECTION 7

### PHASE FRONT CONTROL

The MPTS subarray phase front control subsystem must provide high accuracy beam pointing and focusing of a high power microwave beam in the presence of a non-homogeneous, time varying atmosphere and ionosphere, thermal deformation of the array waveguide and structure, and phase variation of transmission lines, converters, and phase shifters. Safety considerations, to limit high power densities to acceptable values outside the receiving antenna area, require positive control over beam focusing and pointing during steady state and transient conditions. High overall efficiency requires both accurate beam pointing and proper focus. The effect of efficiency degradation with phase error is shown in Figure 7-1.

Figure 7-2 illustrates two basic approaches to phase control: command and adaptive. The former relies upon measurements made at the receiving site to make connections via a telecommunications link to the transmitting array. The latter uses a reference beam sent from the receiving antenna site to enable measurements and corrections to be made at each subarray. The command scheme could be implemented in two ways: phase estimation and "bit wiggle." Phase estimation relies upon measurements made over a matrix of sensors covering the entire receiving site. These are processed by algorithms which interpret the errors in beam center location and power density distribution on the ground as distortion of the phase front at the transmitting antenna from the ideal. Corrections are then sent over the command link to a central distribution point at the transmitting antenna and/or directly to a subarray. The "bit wiggle" approach sequentially examines each subarray's performance by commanding a distinctive (phase) modulation on its output. Corrections are then sent via the command link. The approaches are illustrated schematically in Figure 7-3 and a summary comparison is given in Figure 7-4.

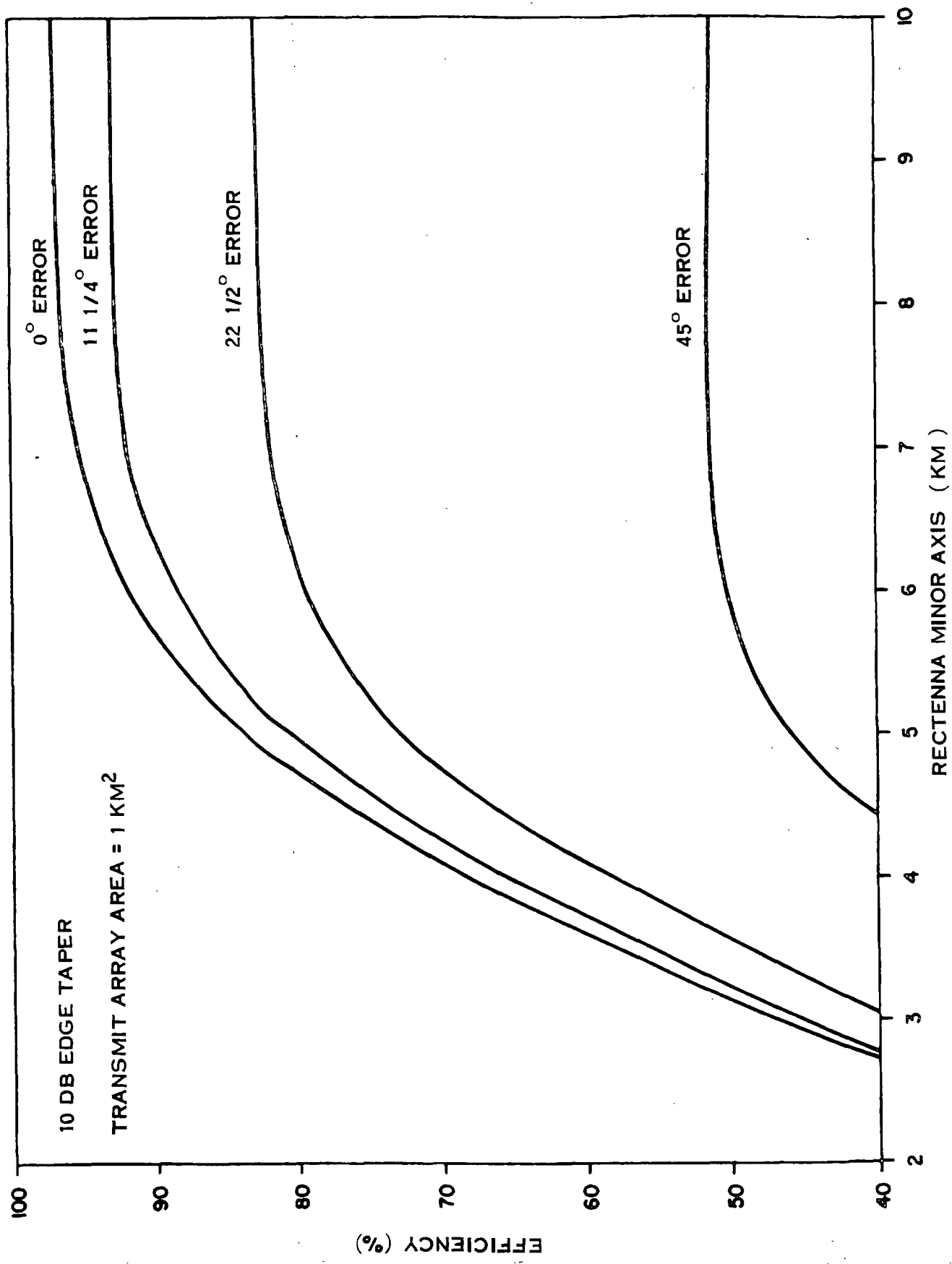


Figure 7-1. Effect of rms Phase Errors on Beam Efficiency



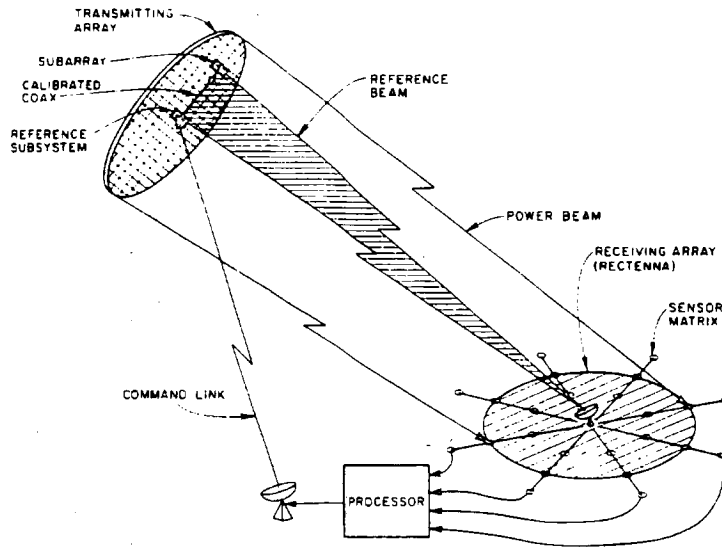
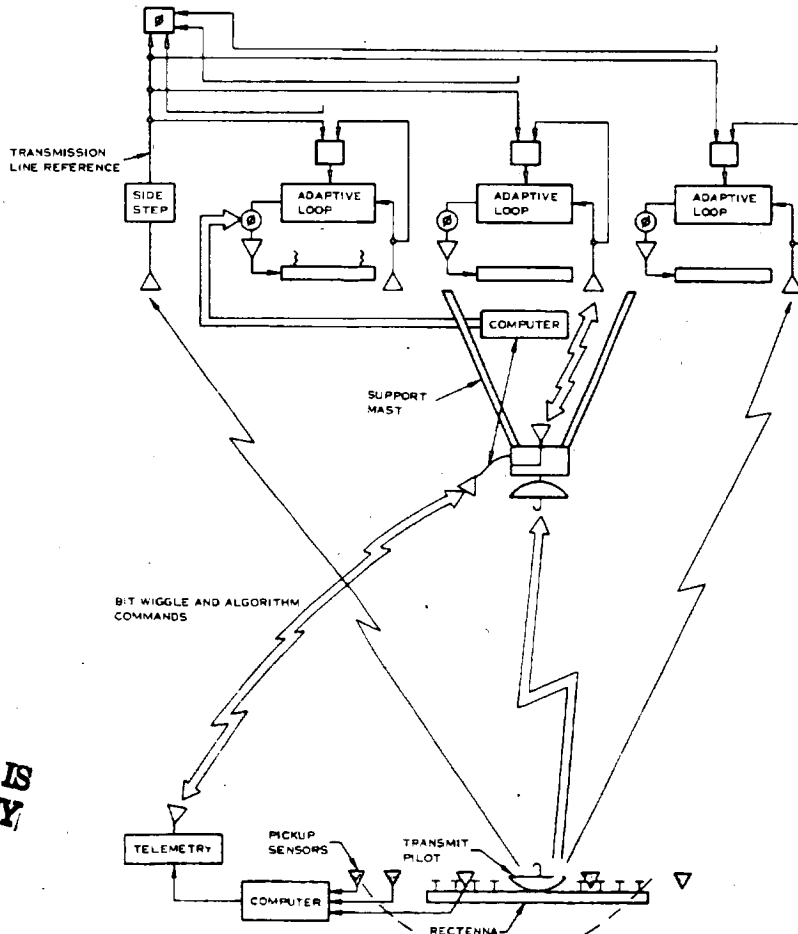


Figure 7-2. Command and Adaptive Phase Front Control Concepts



ORIGINAL PAGE IS  
OF POOR QUALITY

Figure 7-3. MPTS Phase Front Control Approaches

	Adaptive	Command
Primary Use	Routine Operation	Safety
Corrects for Structure Deflections and Media Errors	Yes	Low Order Corrections Only
Phase Shift Device	Mixers	Phase Shifters
Control Signal	Pilot Signal	Telemetry Commands
Electronics Complexity on Orbit	High	Low
Electronics Complexity on Ground	Low	High
Response to Transients	0.25 sec/max	Time Required to Process Algorithm + 0.25 sec

Figure 7-4. Phase Front Control Approach Comparison

### 7.1 ADAPTIVE PHASE FRONT CONTROL

The variations in the propagation conditions through the ionosphere and atmosphere have negligible effects on the efficiency of power transmission or location for reception because (1) the path length from the media to earth is short, and (2) the rectenna (described in Section 9) is insensitive to phase variations. However, the media introduces variations of phase across the transmitting antenna that in principle could interfere with an adaptive scheme if the variations were significantly large across the array and occurred in a time interval comparable with the propagation transit time from earth to the satellite in geosynchronous orbit. These effects are estimated, in Section 3, to have correlation lengths long with respect to the transmitting antenna and to have correlation times long with respect to the propagation time, so that the adaptive approach should be feasible for correcting distortions at the transmitter. It potentially is the most accurate of the techniques examined in that it can resolve errors down to a single subarray and has rapid response.

The adaptive scheme requires that a reference phase be distributed to all of the subarrays as a standard against which the incoming signal from the ground pilot transmitter can be compared. Any errors in the reference will induce equal errors in the phasing of the outgoing power phase front so that it must be accurate and must penalize the antenna as little as possible as regards weight and reliability. Four all-rf schemes for achieving this are listed and compared in Figure 7-5, and a description of the front side space distribution scheme and transmission line approach are given in Figure 7-6.

The spaced frontside, spaced rearside, transmission line, and subarray-to-subarray transfer schemes are leading candidates. The latter was proposed by Jet Propulsion Laboratory as a technique to eliminate cable weight and potential cable errors; an error buildup will be developed as the reference signal propagates from the center to the edges of the antenna. On the other hand the transmission line approach requires that the cable be calibrated against thermal path length changes using a two-way path measurement technique. The spaced frontside approach does not appear to offer a weight advantage while it does produce rf blockage and adds complexity in the antenna mechanical design. The spaced rearside approach has multipath problems due to structure geometry.

Approaches	Advantages	Disadvantages
Spaced (Frontside)	Signal path through space rather than hot coax. No reflections off array structure.	Mast blockage; must predict phase through mast; mast added weight.
Spaced (Rearside)	May use existing horn support on elevation gimbal rather than mast.	Multipath scattering from support structure. (Pulse and phase-lock may reduce problem.)
Transmission Line (Reference Line)	No multipath scattering. Series-parallel layout.	Cable calibration required.
Subarray-to-Subarray Transfer (JPL)	No multipath.	Extra mixers for reference phase conjugation error buildup.

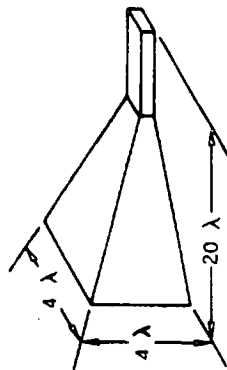
Figure 7-5. Reference Distribution Systems

GROUND PILOT CHARACTERISTICS

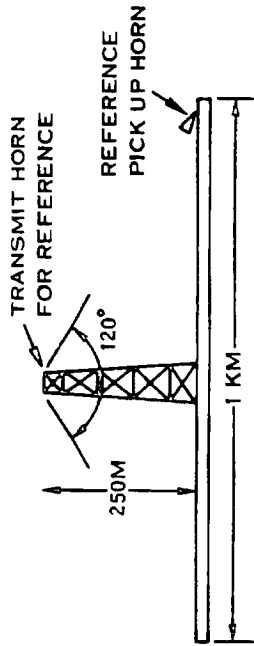
PILOT ANTENNA = 30 FEET DIAMETER PARABOLOID (60%  $\eta$  ,  $F/D = 0.4$ , GAIN = 63.4 DB  
 RECEIVED HORN GAIN = 20 DB  
 RECEIVED PILOT SIGNAL = -57 DBM  
 TRANSMIT PILOT LEVEL = 132 WATTS CW

SPACE FED APPROACH (FRONT SIDE)

ON ORBIT REFERENCE



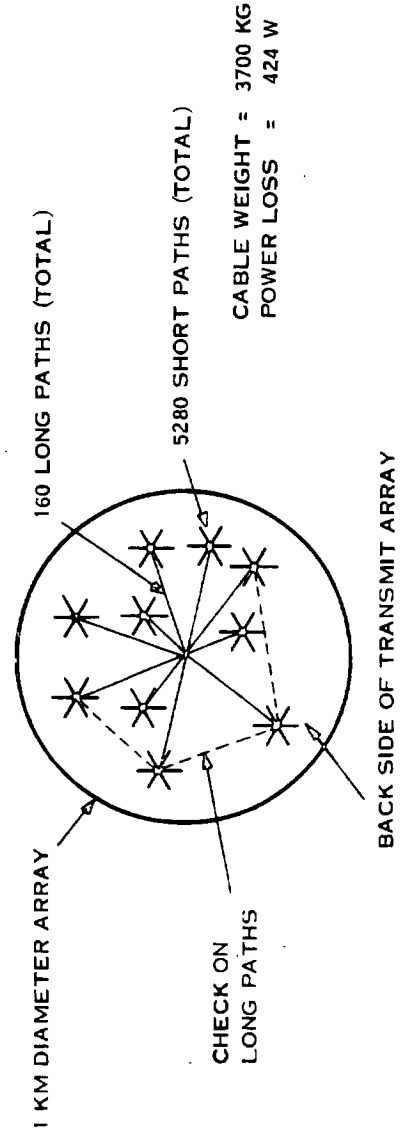
REFERENCE RECEIVE HORN  
 PYRAMIDAL OR CONICAL  
 (CORRUGATED OR DUAL MODE)



120 DEGREES 10 DB BEAMWIDTH FOR TRANSMIT  
 HORN  $\Rightarrow$   $1\lambda \times 1\lambda$  APERTURE AND  $\approx$  10 DB GAIN

RECEIVE HORN GAIN  $\approx$  20 DB  
 TRANSMIT HORN GAIN AT ARRAY EDGE  $\approx$  0 DB  
 TRANSMIT HORN TO ARRAY EDGE DISTANCE = 559 M  
 REQUIRED REFERENCE POWER = 3.3 KW

TRANSMISSION LINE APPROACH



CABLE WEIGHT = 3700 KG  
 POWER LOSS = 424 W

Figure 7-6. Ground Pilot and Phase Distribution

The best solution may be the transmission line combined with the subarray-to-subarray transfer approach to exploit the advantages of each; i. e., use subarray-to-subarray transfer approach locally and use the transmission (reference) line approach to reach out to the edges of the antenna.

Other approaches that have been discussed for phase reference distribution or direct mechanical antenna distortion measurement involve laser techniques. These approaches are thought to produce added complexity and questionable reliability, especially in the light of a 30-year goal. The direct measurement of subarray physical displacement from a reference line, such as relative to a matrix of taut cables across the antenna, or comparison of the overall surface with a stored hologram pattern lack the mechanical simplicity of a direct rf measurement translated into an rf phase-adjusted power beam output. The latter seems best suited at this time to an active phased array and has the ability to correct both electrically and mechanically produced errors in the phase front, which the former does not.

Figure 7-7 shows a detailed block diagram for implementing the adaptive approach. Feedthrough nulling is shown as a means of preventing high power coupling into the receiver to reduce receiver saturation problems. The ground based pilot beam would have the following characteristics:

Ground System:	30 ft paraboloid (60% eff., F/D = 0.4, Gain = 63.4 dB) 132 watts cw
Spaceborne Systems:	20 dB receive horn 57 dBm signal level

The error budget for the adaptive control system is given in Figure 7-8 where it is seen to produce a two percent power loss relative to a perfect implementation. The effect of this error on beam pointing accuracy is of great interest from control and safety standpoint, and this can be evaluated from the following relation:

$$\sigma_{\theta} = \frac{0.5 \theta_{3 \text{ dB}} \sigma_{\phi}}{\sqrt{N}}$$

PILOT FREQUENCY = 2.44 GHZ  
 REFERENCE FREQUENCY = 2.42, 2.47 GHZ  
 FEEDBACK REFERENCE = 4.84 GHZ  
 TRANSMIT FREQUENCY = 2.45 GHZ

PYRAMIDAL HORN  
 GAIN = 20 DB  
 DIMENSIONS =

--- SPACE-FED APPROACH

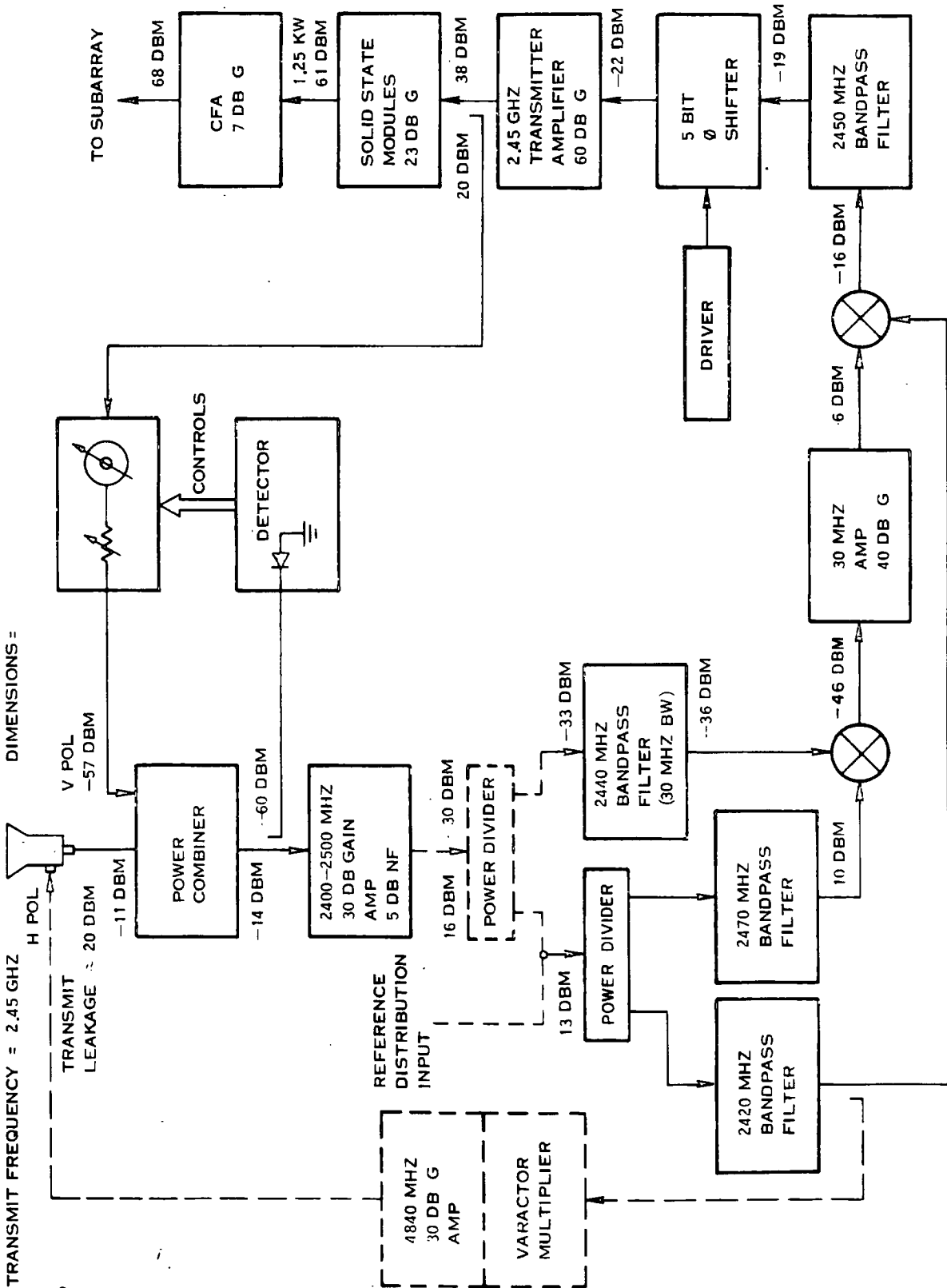


Figure 7-7. Subarray Phase Control Block Diagram

ORIGINAL PAGE IS  
 OF POOR QUALITY

One Sigma - Degrees

Reference Subsystem

Ref. Initial Alignment	2
Feedback Initial Alignment	2
Feedback Phase Measurement	2

Subarrays

Phase Shift in Converters*	6
Insertion Phase of Phase Shifter (Six Bits)	3
Total Path Lengths Through Circuit	2
Mixer Insertion Phase Variations	3
Media Effects	<u>1</u>
RMS Total	8.4

Associated Scatter Loss                      ~2%

\* Equivalent for 18M Subarray

Figure 7-8. Adaptive Phase Front Control Error Budget

where

$\sigma_{\theta}$  = rms pointing angle

$\theta_{3 \text{ dB}}$  = 3 dB power angle  $\approx \lambda / D$

$\sigma_{\phi}$  = rms error per subarray

N = number of subarrays

D = diameter of transmitting array.

For a 0.83 km antenna with 1670 subarrays, the rms error is about 10 meters, a value which is well within control requirements.

## 7.2 COMMAND PHASE FRONT CONTROL

### 7.2.1 PHASE ESTIMATION

Sensing antenna elements are distributed within and around the receiving antenna site. The signal-to-noise ratio will be high at the sensors. Ground measurements can be used to estimate the transmit aperture phase distribution. For example, if the amplitude and phase of the beam were measured all over the earth, an inverse Fourier transform would yield the transmit aperture distribution. Since this approach is quite impractical, a reduced set of measurements in the vicinity of the main beam and possibly at the sidelobes is used. The main beam can be approximated by curve fitting the amplitude measurements. The peak of the beam reveals any linear phase gradients across the array. The beamwidth reflects any defocusing. The location of the peak and the beamwidth could be used to determine the appropriate linear and quadratic phase front corrections. An optimum system of this kind would be a Kalman filter which included all a priori information (e.g., measured or calculated array surface distortion) and estimated the required subarray phase compensation based on pattern measurements on the ground. Array temperature and other data measured on board would be telemetered down so that the appropriate phase corrections could be telemetered up. The computer model should rapidly improve as time goes on and data are accumulated.

As an example of this technique, consider a uniformly illuminated array that is 1 km in diameter and has 20m wide subarrays. The wavelength is 0.10 meters. The rectenna array subtends an angle of  $\pm 0.075$  milliradians at the array. The edge rectenna elements are at the -11.1 dB part of the beam for a properly aligned and focused system.

$$E(\theta) = \sum_{n=-25}^{25} e^{-K_1(\theta-B)^2} e^{j[K_2 X^2 + \frac{2r}{\lambda} (K_3 - \theta)X]}$$

where

$X = 20.0n =$  distance of nth subarray from array center

$$B = \frac{2 y_{\max} X}{(0.5 D_1)^2} = \text{squint of subarray pattern caused by quadratic bowing}$$



of the array structure.  $y_{\max}$  is the maximum deviation at the ends of the array.  $D_1$  is the array diameter (i. e., 1000m).

$$K_1 = 0.3467 \left( \frac{D_2}{0.44\lambda} \right)^2 \text{ for the proper 3 dB beamwidth of a } D_2 = 20\text{m}$$

diameter subarray.

$$K_2 = \frac{\phi_{\max} / 57.296}{(0.5 D_1)^2}$$

where

$\phi_{\max}$  is the maximum quadratic phase error (in degrees) at the array ends.

$K_3$  provides beam squint.  $K_3 = 0$  yields no pointing error.

Figure 7-8 shows the rectified dc power and the 10 dB beamwidth on the ground vs.  $\phi_{\max}$  with  $y_{\max} = K_3 = 0$ . This case corresponds to a flat array having quadratic subarray phase errors. Figure 7-9 shows similar results as a function of  $y_{\max}$  with  $\phi_{\max} = K_3 = 0$ . This case corresponds to a curved array having a focused aperture.

The rectified dc power on the ground can be approximated by

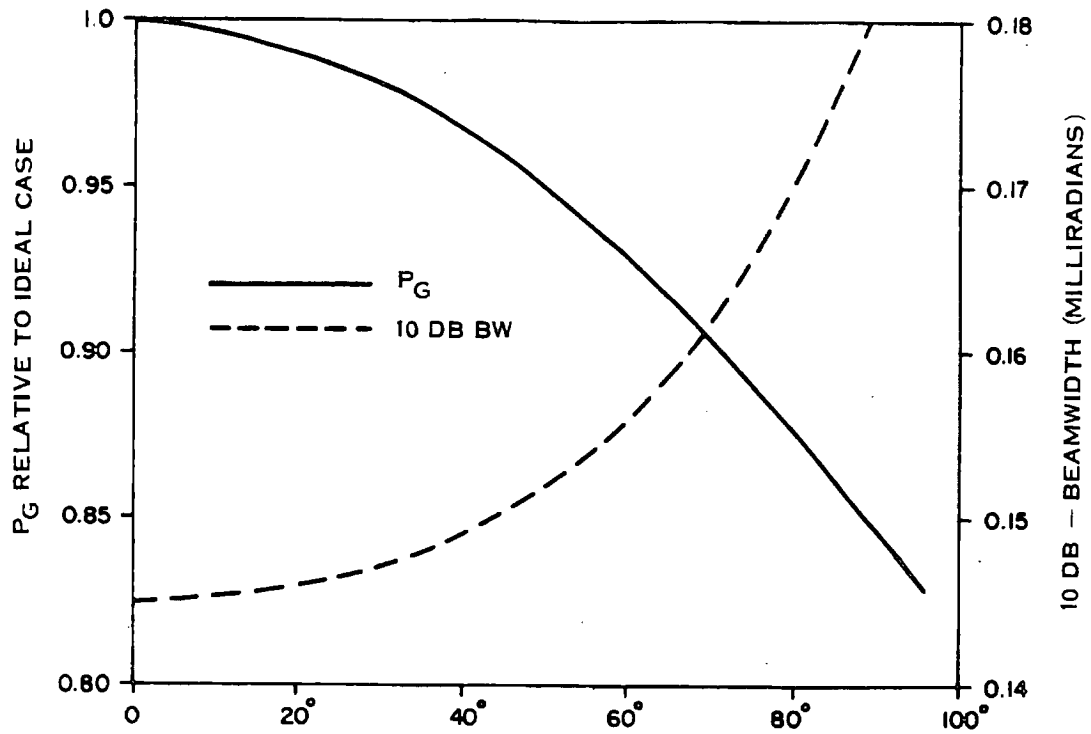
$$P = P_o (1 - a\phi^2) (1 - by_{\max}^2) \approx P_o [1 - a\phi^2 - by_{\max}^2]$$

where  $P_o$  is the rectified power for an ideal focused system.  $a = 1.929 \times 10^{-5}$  and  $b = 0.611$  were determined from Figures 7-8 and 7-9.

The beamwidth can be approximated by

$$B = B_o (1 + c\phi^2) (1 + dy_{\max}^2) \approx B_o [1 + c\phi^2 + dy_{\max}^2]$$

where  $B_o = 1.45 \times 10^{-4}$  is the ideal 10 dB beamwidth.  $c = 1.589 \times 10^{-5}$  and  $d = 0.19155$  were determined from Figures 7-8 and 7-9.



QUADRATIC PHASE ERROR EXAMPLE

Figure 7-8. Quadratic Phase Error Example

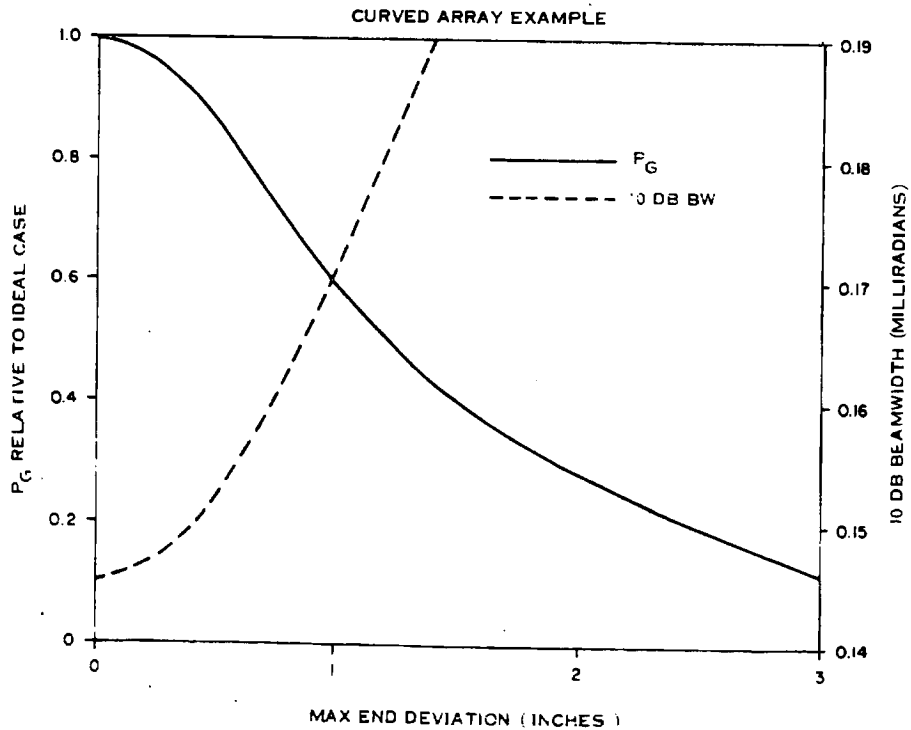


Figure 7-9. Curved Array Example

Solving these two equations yields the following estimates of  $\phi$  and  $y_{\max}$ :

$$\phi = \sqrt{\frac{\hat{P}d - b\hat{B}}{ad - bc}}$$

$$y_{\max} = \sqrt{\frac{a\hat{B} - \hat{P}c}{ad - bc}}$$

where

$$\hat{P} = 1 - P/P_0 \text{ and } \hat{B} = B/B_0 - 1.$$

The accuracies of several estimates compared with the actual errors assumed are listed in Figure 7-10.

<u>Assumed Actual Values</u>		<u>Values Estimated by Algorithm</u>	
<u><math>y_{\max}</math></u>	<u><math>\phi</math></u>	<u><math>y_{\max}</math></u>	<u><math>\phi</math></u>
0.2	18°	0.19	20.4°
0.3	50°	0.23	59.9°
0.2	30°	0.17	35.3°
0.15	20°	0.13	28.8°
0.1	15°	0.08	19.4°
0.25	25°	0.23	30.2°
0.5	45°	0.42	57.3°

Figure 7-10. Phase Estimation Example

This rather simple example has demonstrated the feasibility of inferring simple surface distortion and phase errors from amplitude measurements within the main beam. Sensors far from the main beam could be used to sense the level of random phase errors. A loss of rectified power with little change in beamwidth would imply tube or subarray outages.

### 7.2.2 BIT WIGGLE

Figure 7-11 demonstrates the bit wiggle approach. The phase shifter in one subarray is phase modulated by switching between  $\phi$  and  $\phi + 180^\circ$  at a given rate. The signal received on the ground has a large carrier (all subarrays) and a weak sideband (subarray under test). The sideband is filtered and phase compared with the modulating reference. Providing the same modulating reference at both the transmit array and the ground introduces the reference distribution problem. The modulating reference could be transmitted periodically and a local oscillator could be phase locked to the received signal. Good filtering of the sideband is required so that the carrier does not introduce an error in the measurement.

### 7.3 CONCLUSIONS AND RECOMMENDATIONS

Both adaptive and command approaches will be needed. The adaptive has the accuracy and rapid response potential needed for maximum efficiency; the command has the safety and backup features of a ground based monitoring system that is essential to an acceptable control scheme. The command scheme favored is the phase estimation technique which appears less complex and more likely to succeed than the bit wiggle approach. The bit wiggle technique may find a role as a diagnostic tool in assessing the status of individual subarrays on a periodic basis. These may be more briefly stated as follows:

- a. Adaptive (retrodirective) approach needed for maximum efficiency.
- b. Command approach needed for safety and back-up.
- c. Calibrated transmission line and/or subarray-to-subarray transfer of reference phase data for adaptive phase control mechanization.
- d. Phase estimation for command mechanization.
- e. Investigate bit wiggle technique as diagnostic tool.
- f. Detailed investigations should be conducted to minimize phase control electronics costs, weight, and blockage for each subarray.

BIT WIGGLE PHASING APPROACH  
TRANSMITTING ARRAY

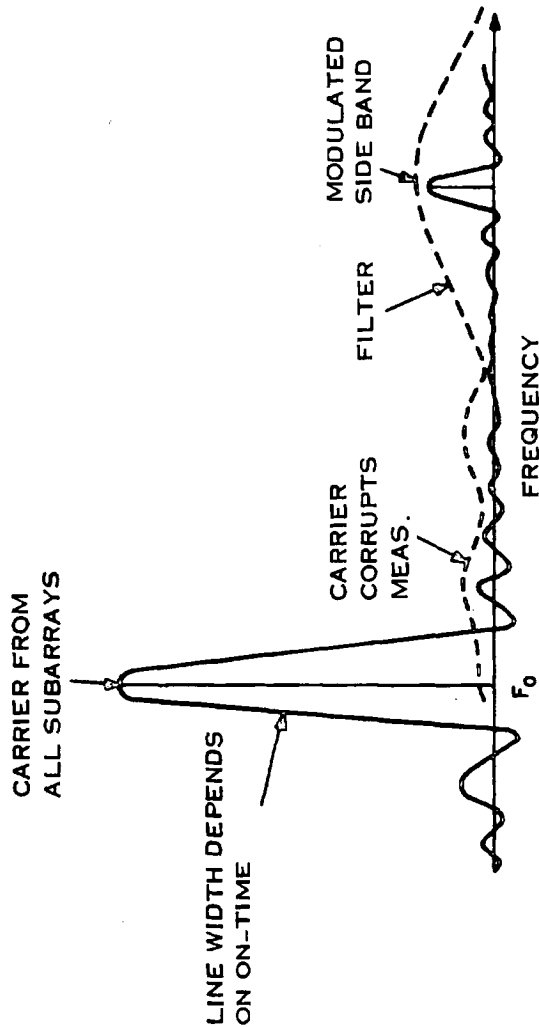
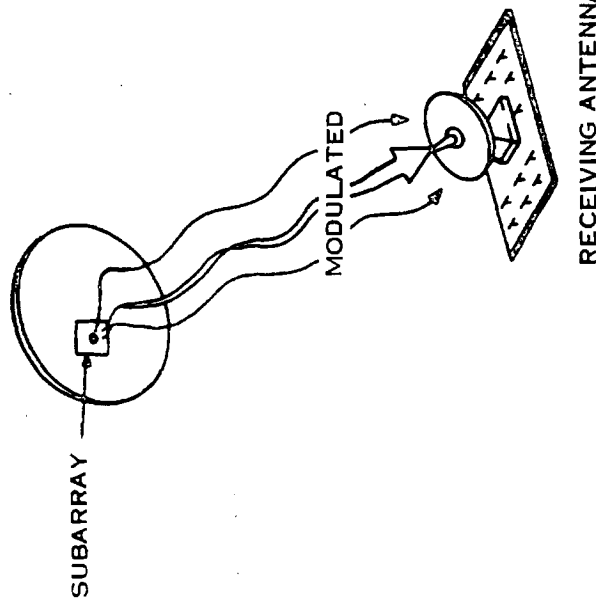


Figure 7-11. Bit Wiggle Approach

## APPENDIX A

### RADIO WAVE DIFFRACTION BY RANDOM IONOSPHERIC IRREGULARITIES

#### A.1 INTRODUCTION

The occurrence of small scale irregularities in the electron density is known to be a normal feature of the ionosphere. One of the main effects of an irregular ionosphere on a radio wave passing through the medium is to impose fluctuations in the wave field. These fluctuations, referred to as scintillations, are present in the amplitude, phase and angle-of-arrival of the signals received from distant sources such as radio stars and satellites. The magnitude of the scintillations, however, are dependent upon the operating frequency, angle of incidence of the wave and the characteristics of the electron density irregularities. The irregularities responsible for the radio wave scintillation are believed to be confined to the F-region ( $\approx 150$  to  $340.0$  km) of the ionosphere and are aligned along the direction of the earth's magnetic field. When the radio wave source is at large angles from zenith, approaching the horizon, it is possible that irregularities in the E-region ( $\approx 90$  to  $150$  km) at the heights near  $100$  km, become important. Observations of the radio wave diffraction pattern produced on the ground can be used to deduce the characteristics of the ionosphere irregularities or conversely, the wave field can be described provided the source location and the medium properties are specified. The electron density irregularities and likewise the diffraction pattern are both described usually in terms of their statistical properties. The diffraction pattern, for instance, is described in terms of the rms fluctuations in amplitude and phase and their spatial and temporal correlation functions.

The problem of describing the fluctuations imposed on a radio wave traversing an irregular medium may be treated theoretically using two different approaches, namely the diffraction method and the scattering method. In the diffraction method, the medium is considered to be equivalent to a certain thin diffracting screen. Because the absorption in the ionosphere is negligible for the frequencies normally used for the scintillation observations, the diffracting screen will produce variations only in phase but not in amplitude across the emerging wavefront. The

diffracting screen for this reason is referred to as the phase changing screen. The amplitude fluctuations will develop as the wave propagates away from the screen. The diffraction method employs Rayleigh-Sommerfeld diffraction theory to calculate the behavior of the amplitude and phase of the wave as a function of distance from the phase screen. Analytic solutions have been obtained to the diffraction problem usually under the assumption that the rms phase deviation imposed on the incident wavefront by the screen does not exceed one radian. This is the shallow-screen (weak-scatter) approximation. Under this approximation, the amplitude and phase fluctuations correspond respectively to the in-phase and quadrature-phase fluctuating components (relative to the mean undeviated component) of the wave field. The two components become approximately equal when the observations are made in the far-field of the diffracting screen. In the scattering approach, the wave at the observing point is considered to be the sum of the unscattered wave and the waves scattered by the irregularities in the medium. This method can also be successfully applied in treating a case of weak scattering where the effects of multiple scattering may be neglected. It was shown that both the diffraction and the scattering methods are equally valid and provide identical results. The model computations for the statistical description of the wave field presented in Section 3 are based upon the diffraction method. In the following, the discussion will therefore be limited to this method.

## A.2 MODEL FOR ELECTRON DENSITY IRREGULARITIES

It is necessary to specify a model for the electron density irregularities in the ionosphere in order that the fluctuations in the radio wave field can be derived using the diffraction theory. A simple model which is often used considers the irregularities to be field aligned, axially symmetric and randomly distributed. They are described in terms of a Gaussian spatial correlation function defined such that

$$\begin{aligned}
 \langle \Delta N(r, s) \Delta N(r+R, s+S) \rangle &= \langle \Delta N^2 \rangle P_N(R, S) \\
 &= \langle \Delta N^2 \rangle \exp \left\{ -\frac{R^2}{r_0^2} - \frac{S^2}{\alpha^2 r_0^2} \right\}
 \end{aligned}
 \tag{A-1}$$

where  $\Delta N$  is the deviation in electron density from the mean  $N$ , and the brackets  $\langle \rangle$  denote an ensemble average,  $r$  and  $s$  are a pair of cylindrical coordinates such that  $s$  is measured along the magnetic field and  $r$  is perpendicular to the field;  $r_0$  is the transverse Gaussian scale size of the irregularities and  $\alpha$  is the axial ratio. The electron density in each of the randomly distributed irregularities is given as:

$$\Delta N(r, s) = \Delta N_0 \exp \left\{ \frac{-r^2}{(r_0^2/2)} - \frac{-s^2}{(\alpha r_0)^2/2} \right\} \quad (\text{A-2})$$

where  $\Delta N_0$  is the excess electron density at the center of the irregularity. The density and the correlation scale sizes differ by a factor of  $\sqrt{2}$  as may be noted from Equations (A-1) and (A-2). The simple model of Gaussian irregularities is amenable to analytic treatment. This mathematical convenience seems to be part of the reason for its wide application. There is some evidence that this model is favored observationally in describing the irregularities induced by high power radio wave modification of the ionosphere.<sup>1</sup> The irregularities, while being Gaussian, may nevertheless exist in more than a single scale size. The observations made during the times of radio wave modification of the ionosphere indicate the presence of two dominant scale sizes and to allow for this, the model is extended accordingly. The results given in Section 3 represent a two scale size model.

### A. 3 PHASE FLUCTUATIONS AND THEIR SPATIAL CORRELATION AT THE DIFFRACTING SCREEN

Radio wave scintillation observations are most often made at very high frequencies for which the refractive index deviates only slightly from unity. Using the high frequency approximation and a model of Gaussian irregularities, Briggs and Parkin<sup>2</sup> have derived an expression for the spatial correlation function of phase in the emerging wavefront for a plane wave incident on the ionosphere. It is given as:

$$P_\phi = \exp \left\{ -\frac{\xi^2}{\beta^2 r_0^2} - \frac{z^2}{r_0^2} \right\} \quad (\text{A-3})$$

where

$$\beta = (\alpha^2 \sin^2 \psi + \cos^2 \psi)^{1/2} \quad (\text{A-4})$$



$\xi$  and  $\eta$  are measured along x and y axes which are normal to the propagation direction with the x axis in the plane containing the propagation direction and the magnetic field line (Figure A-1);  $\psi$  is the angle between the propagation direction and the field line. The phase correlation function has an anisotropic Gaussian form similar to the correlation function of the electron density except the axial ratio of the ellipses of equal correlation is now  $\beta$  rather than  $\alpha$ . The rms phase fluctuation  $\phi_0$  for an extended irregular medium is given by:

$$\phi_0 = \frac{\pi^{1/4} r_e \lambda [\langle \Delta N^2 \rangle \Delta h \alpha r_0 \sec i]}{\beta^{1/2}} \quad (\text{A-5})$$

where  $\lambda$  is the radio wavelength,  $r_e$  is classical electron radius,  $i$  is the angle from zenith at the irregularities, and  $\Delta h$  is the thickness of the irregularity layer.

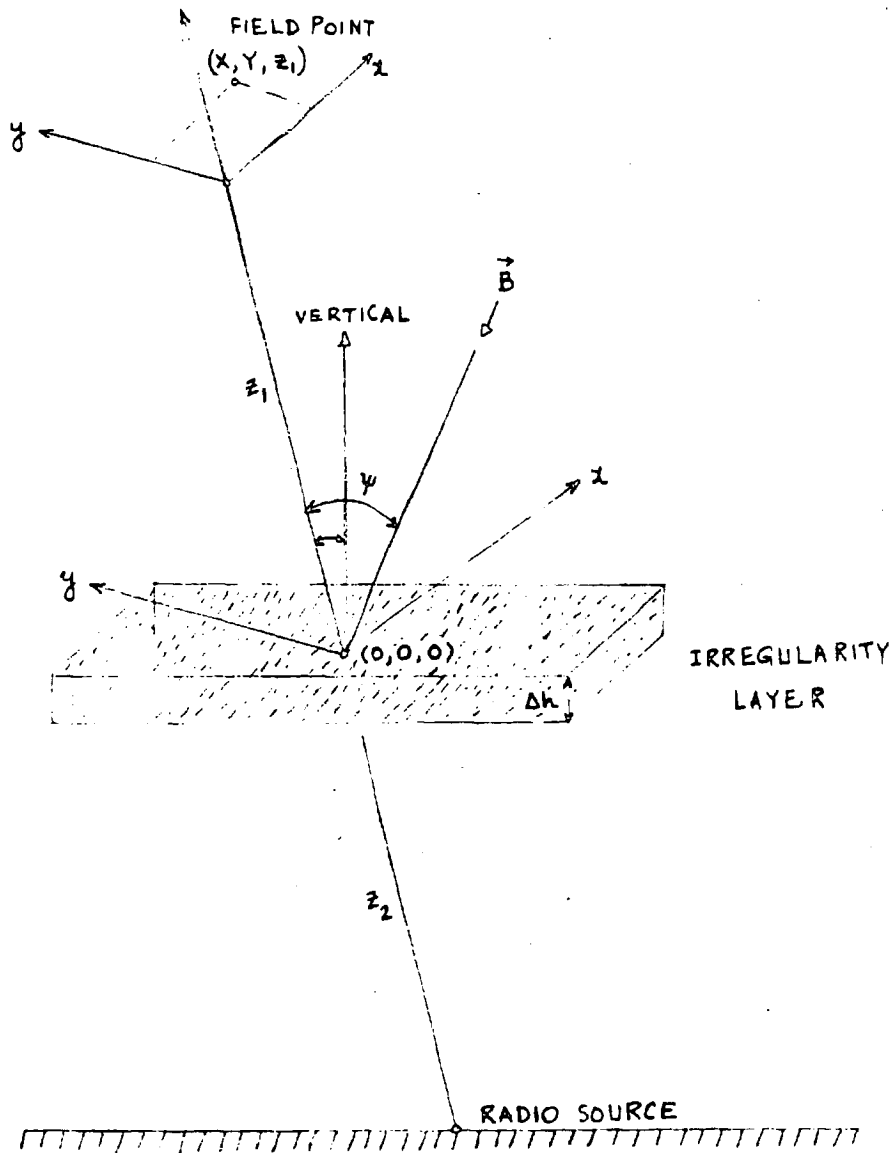
#### A. 4 PHASE AND AMPLITUDE FLUCTUATIONS AND THEIR SPATIAL AND TEMPORAL CORRELATION FUNCTIONS ON AN OBSERVATIONAL PLANE

The phase deviations of the wavefront emerging from the irregular medium described above will lead also to amplitude fluctuations as the wave propagates away from the screen. Using diffraction theory Bowhill<sup>3</sup> has derived expressions to describe the statistical properties of the wave field at a distant point for the general case where the source and the observational point are located at finite distance from the diffracting screen. The results are summarized in a convenient form in a recent report by Evans.<sup>4</sup> The spatial correlation functions of amplitude and phase ( $P_A$ ,  $P_\phi$ ) and the rms fluctuations in amplitude (divided by mean amplitude) and phase ( $\sigma_A$ ,  $\sigma_\phi$ ) are defined by:

$$C_A(x, Y) = \sigma_A^2 P_A(x, Y) = \frac{\langle A(x, y) A(x+x, y+Y) \rangle - \langle A(x, y) \rangle^2}{\langle A(x, y) \rangle^2} \quad (\text{A-6})$$

$$C_\phi(x, Y) = \sigma_\phi^2 P_\phi(x, Y) = \frac{\langle \phi(x, y) \phi(x+x, y+Y) \rangle - \langle \phi(x, y) \rangle^2}{\langle \phi(x, y) \rangle^2} \quad (\text{A-7})$$

The covariance functions  $C_A(X, Y)$  and  $C_\phi(X, Y)$  are derived as:



ORIGINAL PAGE IS  
OF POOR QUALITY

Figure A-1. The Geometry used in the Diffraction Calculations

$$\begin{aligned}
\left. \begin{array}{l} C_A(X, Y) \\ C_\phi(X, Y) \end{array} \right\} &= \frac{\phi_0^2}{2} \left[ \exp \left\{ -\frac{X'^2}{\beta^2 r_0^2} - \frac{Y'^2}{r_0^2} \right\} \mp (1+W_1)^{-1/4} (1+W_2)^{-1/4} \right. \\
&\quad \left. \exp \left\{ -\frac{X'^2}{\beta^2 r_0^2 (1+W_1^2)} - \frac{Y'^2}{r_0^2 (1+W_2^2)} \right\} \right. \\
&\quad \left. \cos \left\{ \frac{X'^2 W_1}{\beta^2 r_0^2 (1+W_1^2)} + \frac{Y'^2 W_2}{r_0^2 (1+W_2^2)} - \frac{1}{2} (\tan^{-1} W_1 + \tan^{-1} W_2) \right\} \right]
\end{aligned}
\tag{A-8}$$

The negative sign in Equation (A-8) refers to  $C_A$  and the positive sign to  $C_\phi$ . The symbols in the above equation are given as:

$$\begin{aligned}
W_1 &= 2 \lambda z_1 / \pi r_0^2 \beta^2 \\
W_2 &= 2 \lambda z_1 / \pi r_0^2 \\
X' &= X z_2 / (z_1 + z_2) \\
Y' &= Y z_2 / (z_1 + z_2)
\end{aligned}$$

where  $z_1$  and  $z_2$  are the distances to the observation point and the source from the diffracting screen and  $(X, Y)$  are the coordinates of the field point on the observational plane as illustrated in Figure A-1. The rms fluctuations in amplitude (normalized by mean amplitude) and phase  $\sigma_A$  and  $\sigma_\phi$  are given as:

$$\sigma_A = [C_A(0,0)]^{1/2} = \frac{\phi_0}{\sqrt{2}} \left[ 1 - (\cos U_1 \cos U_2)^{1/2} \cos \frac{1}{2} (U_1 + U_2) \right]^{1/2} \tag{A-9}$$

$$\sigma_\phi = [C_\phi(0,0)]^{1/2} = \frac{\phi_0}{\sqrt{2}} \left[ 1 + (\cos U_1 \cos U_2)^{1/2} \cos \frac{1}{2} (U_1 + U_2) \right]^{1/2} \tag{A-10}$$

where

$$U_1 = \tan^{-1} \left[ 2 \lambda Z / \pi \beta^2 r_0^2 \right]$$

$$U_2 = \tan^{-1} \left[ 2 \lambda Z / \pi r_0^2 \right]$$

and

$$Z = z_1 z_2 / (z_1 + z_2)$$

The Equations (A-8), (A-9) and (A-10) are basic to the description of the radio wave field on any observational plane. It is a simple matter to extend these equations to consider multiple scale sizes present in the irregular medium. Specifically, for a two scale-size model used in obtaining the results given in Section 3, the equations for  $\phi_o^2$ ,  $C_A$ ,  $C_\phi$ ,  $\sigma_A^2$  and  $\sigma_\phi^2$  take the form

$$F = a F_1 + (1-a)F_2 \quad (A-11)$$

where  $a$  is the weighting factor that determines the relative importance of the two scale sizes and  $F_1$  and  $F_2$  have the same functional form as that given for the single scale size.

In addition to the spatial correlations described above, it is often necessary to determine the temporal correlations of the wave field. It is straightforward to transform the spatial correlation to the temporal correlation for the case where the irregularities are drifting with a constant velocity and not changing in form. Let  $V$  be the horizontal velocity of the irregularities in the plane containing the  $x$  axis and the propagation direction. Now if  $z_1$  and  $z_2$  are the distances to the field point and the source from the irregularities and  $i$  is the angle of incidence, then the diffraction pattern at the observation point moves along the  $x$  axis with the velocity given by:

$$V_d = V \cos i (z_1 + z_2) / z_2 \quad (A-12)$$

using the assumption of drifting pattern with no changes in its structure, the spatial correlation can be related to the temporal correlation as:

$$P(\Delta x) = P(\Delta t) \quad (A-13)$$

where

$$\Delta t = \Delta x / V_d = \frac{\Delta x z_2}{V \cos i (z_1 + z_2)} \quad (A-14)$$

using the above equation, the time constant  $\tau$  for which the correlation falls to  $1/e$  can be obtained from the corresponding spatial correlation scale size  $D$ . A computer program has been developed to compute the rms phase and amplitude

fluctuations and their spatial and temporal correlation functions using both single as well as double Gaussian scale size models of the irregularities. The results of the model calculations are presented in Table 3-3 and Figure 3-9 of Section 3.

## REFERENCES (APPENDIX A)

1. Bowhill, S. A., E. K. Walton and D. R. Ward, "Geostationary and Orbital Satellite Measurements of Artificial Spread-F Produced by Ionospheric Heating", presented at 1974 URSI Meeting, October 14-17, Boulder, Colorado.
2. Briggs, B. H., and I. A. Parkin, "On the Variation of Radio Star and Satellite Scintillations with Zenith Angle", J. Atmos. Terr. Phys., 25, 339, 1963.
3. Bowhill, S. A., "Statistics of a Radio Wave Diffracted by a Random Ionosphere", Jour. Res. NBS - D. Radio Propagation, 65D, 275, 1961.
4. Evans, J. V., "Millstone Hill Radar Propagation Study: Scientific Results - Part II", ESD-TR-73-260, Lincoln Laboratory, MIT, Lexington, Massachusetts, November 1973.

## APPENDIX B

### SELF-FOCUSING PLASMA INSTABILITIES

Many instabilities are known to be excited in the ionospheric plasma by HF waves with intensities on the order of  $50 \mu\text{W}/\text{m}^2$ . Although the threshold for these instabilities increases rapidly with frequency, the much larger intensities planned for the MPTS require careful examination of the possible effects of such instabilities. In this appendix we will consider the possibility of self-focusing instabilities. The theory of this instability has been given by Perkins and Valeo<sup>1</sup>, and the self-focusing instability has been observed at HF frequencies as discussed by Thome and Perkins<sup>2</sup>.

The basis of the instability can be understood from the diagram in Figure B-1 which shows an rf wave propagating in the x-direction and moving across a density perturbation wave in the ionosphere. At the points of greatest plasma density (denoted by the + signs), the index of refraction has a minimum, and therefore the rf wave is focused so it has its greatest intensity in the troughs of the plasma wave. These troughs are therefore heated more intensely than the wave crests so that the plasma tends to be pushed towards the crest of the perturbation and the instability grows.

Our description up to this point has been overly simplified because it neglects the effect of the magnetic field. The magnetic field causes charged particles to travel mainly along the electric field. We can neglect the motion of electrons across the field unless the plasma gradient (in the Y-direction) satisfies  $(k_{\parallel}/k_{\perp})^2 < m v_e v_c / M \Omega_i^2$  which means that the Y-direction must make an angle larger than  $1/3$  degree with the  $\perp$  to the field. Here we take  $k$  to be the wave vector in the Y-direction and  $k_{\parallel}$  and  $k_{\perp}$  are its components which are parallel and perpendicular to the magnetic field. Also  $m$  is the electron mass,  $M$  is the ion mass,  $\nu_i$  and  $\nu_e$  are the ion and electron collision frequencies and  $\Omega_i$  is the ion cyclotron frequency.

The instability is driven by the ohmic heating but this would be smoothed out if the thermal conductivity, which is carried by the electrons, has a large component in the Y-direction. The electrons are such efficient carriers of heat that the instability tends to be eliminated unless  $\theta$ , the angle between the Y-direction and

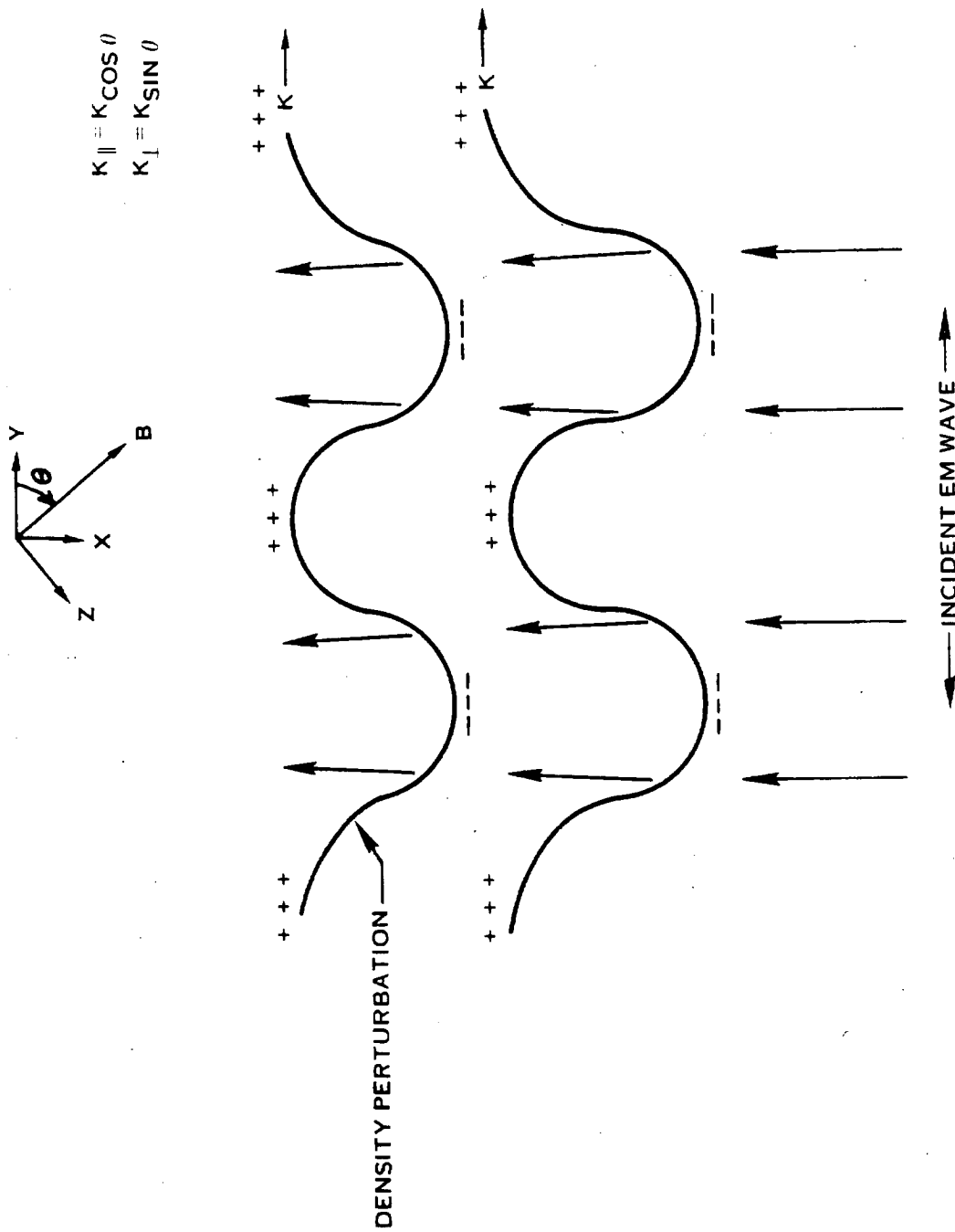


Figure B-1. Self-Focusing Instability



the field, is close to 90 degrees. Thus the instability will be most likely when the wave vector is close to perpendicularity. However, it is important to remember that our derivation does not hold if the wave vector is exactly perpendicular to the field, although we can go as close as 1/3 of a degree from perpendicularity.

Following Perkins and Valeo<sup>1</sup>, the rf field vector can be written as:

$$\vec{E} = \frac{1}{2} \hat{z} [\epsilon_0 + \epsilon_1(x) \cos kY] \exp(i \int_0^x k_0 dx + i\omega t) + \text{complex conjugate} \quad (\text{B-1})$$

where we assume that  $\omega \gg \omega_p$ , the plasma frequency. Note that reference 1 used  $k_{\perp}$  where we use  $k$  since our  $k_{\perp}$  is the component of the wave vector perpendicular to the magnetic field while their  $k_{\perp}$  was the entire wave vector in the Y-direction (so that it is perpendicular to the rf propagation direction and not perpendicular to the magnetic field).

Substituting Equation (B-1) into Maxwell's equations, we find that  $\epsilon_1$  satisfies the parabolic equation:

$$\frac{\partial \epsilon_1}{\partial x} + i(k^2/2k_0)\epsilon_1 = -i\epsilon_0 k_0^2 \tilde{n}(x) (2k_0 n_c)^{-1} \quad (\text{B-2})$$

where  $k_0 = 2\pi c/f$  and  $n_c$  is the critical electron density at which  $\omega_p = \omega$ . Equation (B-2) is solved for  $\epsilon_1$ .

$$\epsilon_1 = \frac{i\epsilon_0 k_0}{2n_c} e^{-iDx/L} \int_x^L e^{iDx'/L} \tilde{n}(x') dx' \quad (\text{B-3})$$

and the increase in ohmic heating is

$$\tilde{Q} = -\nu \epsilon_0^2 n k_0 L \cos(kx) I / 8\pi n_c^2 \quad (\text{B-4})$$

where

$$D = k^2 L / 2k_0 \text{ and}$$

$$I = \int_x^L \sin [D(x'-x)/L] \tilde{n}(x') L^{-1} dx' \quad (\text{B-5})$$

The ohmic heating given by Equation (B-4) is higher by a factor of two than the result given by Perkins and Valeo.

The ohmic heating term given by Equation (B-4) must now be substituted into the hydrodynamic equations for the plasma. This is generally a complicated problem but it is simplified by several assumptions. In particular, it is assumed that not only the electrons but also the ions move parallel to the field. This requires that  $k_{\parallel}/k_{\perp} > v_i/\Omega_i$  or, using values appropriate to the F-region,  $\theta$  must be less than 87 degrees. With these assumptions we find that the wave is spatially amplified in traveling through the ionosphere by the amount

$$\exp(\sqrt{\lambda-1} Dx/L) \exp \gamma t$$

where

$$\lambda = \frac{\nu_e \epsilon_0^2 k_0 L (n/n_c)^2}{4k M \nu_{Ln} [\gamma + 2T(k \cos \theta)^2 / M \nu_{Ln}]} \quad (\text{B-6})$$

where  $n$  is the actual plasma density,  $k$  is the thermal conductivity, and  $n_c$  the critical plasma density. Again this has an additional factor of two compared with Equation (18) of reference 1. The threshold field is found by setting  $\lambda = 1$  and  $\gamma = 0$  while the growth rate  $\gamma$  is found by setting  $\lambda = 1$ .

On the basis of Equation (B-6), it is stated in reference 1 that, with

$$D = 5 \quad (\text{B-7})$$

and

$$k \cos \theta = D/L \quad (\text{B-8})$$

the perturbation will grow with a rate  $\gamma = 0.1$  which will cause the ionospheric temperature to increase in a few seconds. We find, however, that, if we take  $L = 100$  km and the rf frequency equal to 2.2 GHz\*, Equations (B-7) and (B-8) can

only be satisfied when  $\theta = 89.96$  degrees which is beyond the region of validity of the theory.

The threshold power is shown as a function of wavelength for three values of  $\theta$  in Figure B-2. Here we assume that  $n = 5 \times 10^5 \text{ cm}^{-3}$  and  $T_e = 1000^\circ\text{C}$ . (The plasma becomes more stable as  $n$  decreases and  $T$  increases.) We note that for  $\theta = 89$  degrees, a design power of  $30 \text{ mW/cm}^2$  will excite only plasma wavelengths greater than 130 m. (This angle, we note, is greater than the 87 degree maximum angle for which ion diffusion perpendicular to the field can be safely ignored.) For  $\theta = 85$  degrees only wavelengths greater than 320 m can be excited. For 2.2 GHz\* and  $L = 100 \text{ km}$ ,  $D = 4.1 \times 10^4 / \lambda_{\perp}^2$ , so there will only be a small amount of spatial amplification for  $\lambda_{\perp} > 100 \text{ m}$ . (The spatial amplification is  $\exp(\sqrt{\lambda_{\perp} - 1}D)$  for a thickness of slant length  $L$ .) Even a power flux of  $240 \text{ mW/cm}^2$  with  $\theta = 89$  degrees will only excite wavelengths greater than 70 m.

Figure B-3 shows the growth rate  $\gamma$  in  $\text{sec}^{-1}$  as a function of the perturbation wavelength for 5 values of  $\theta$ . This has been carried to angles as close to perpendicular as 89.9 degrees for the same electron density and temperature as Figure B-2 with a power flux of  $50 \text{ mW/cm}^2$ . At 89.9 degrees, wavelengths greater than 30 m have positive growth rates while at 85 degrees only wavelengths greater than 300 m are unstable. Similar curves are shown in Figure B-4 for the case where the plasma density in the ionosphere is  $10^6 \text{ electrons/cm}^3$ .

It is clear that only wave vectors in a narrow cone about the direction perpendicular to both the magnetic field and the propagation direction have short wavelength instabilities. For directions with  $\theta$  between 87 and 89.7 degrees, a simplified theory is possible in which we assume that electrons move parallel to the magnetic field but ions move only perpendicular to the field. This approximation is valid for:

$$\frac{m v_e v_e}{M \Omega_i^2} < \left( \frac{k_{\parallel}}{k_{\perp}} \right)^2 < \left( \frac{v_e}{\Omega_i} \right)^2 \quad (\text{B-9})$$

corresponding in the F-region to angles between 87 and 89.7 degrees.

---

\* Results are nearly the same for the design frequency of 2.45 GHz.

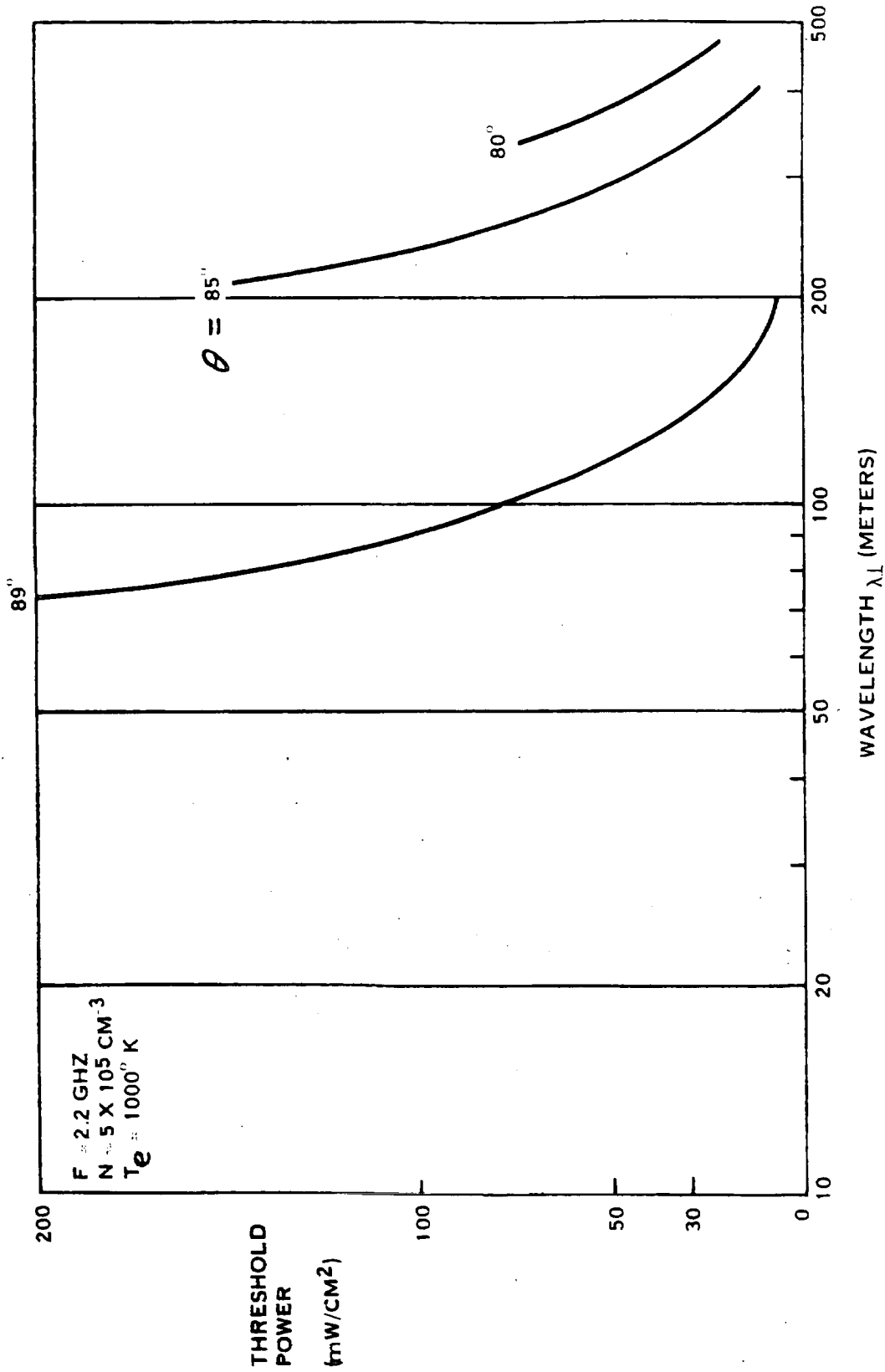


Figure B-2. Self-Focusing Instability Threshold Power Density

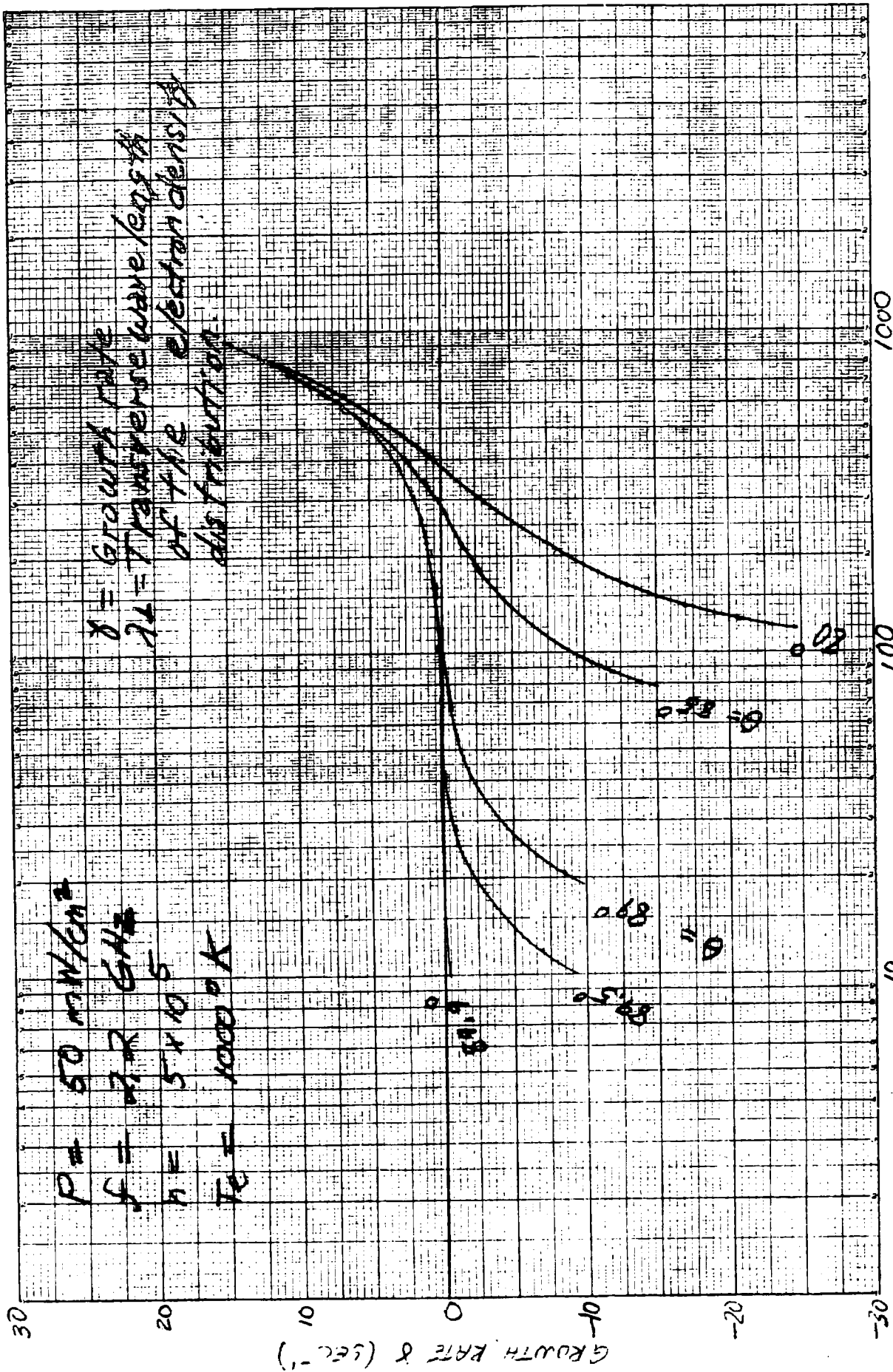


Figure B-3. Growth Rate versus Transverse Wavelength (Night Time Conditions)

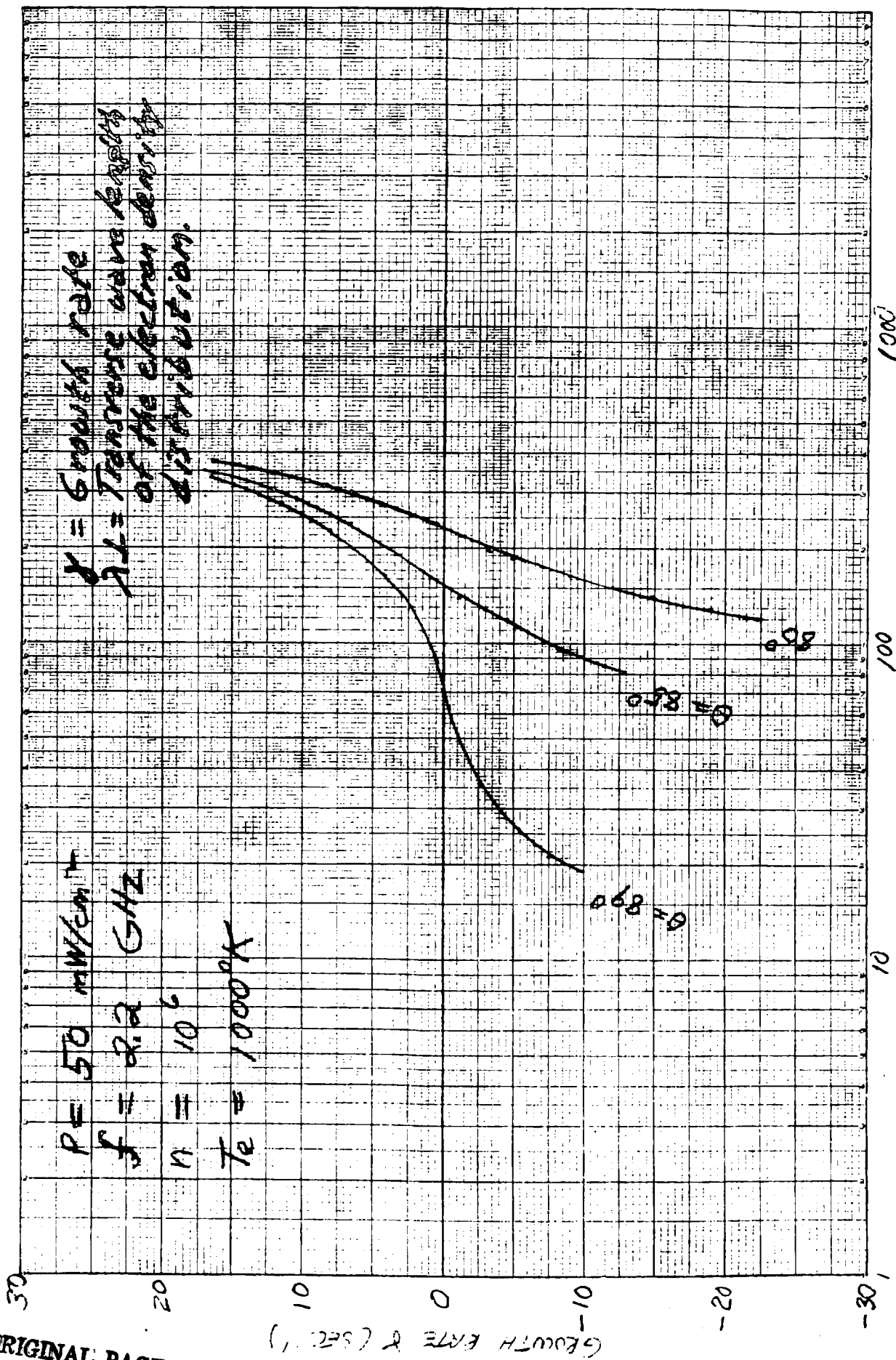


Figure B-4. Growth Rate versus Transverse Wavelength (Daytime Conditions)

ORIGINAL PAGE IS  
OF POOR QUALITY

In this approximation, the electron and ion continuity and momentum equation and the electron energy equation are used to obtain a relation between  $\tilde{n}$  and  $\tilde{Q}$ . The previous expression for  $\tilde{Q}$  is used to obtain

$$\lambda = \left( \frac{k_0^2}{k^4} \right) \left( \frac{\nu_e \epsilon_0^2 n}{4\pi n_c^2} \right) \left( \frac{k_{||}^2 M \Omega_i^2}{m \nu_e \nu_i} \right) \left( \frac{1}{3.16 T_e} \right) \cdot \left( \gamma + k^2 \nu_i (T_e + T_i) / M \Omega_i^2 \right)^{-1} \quad (\text{B-10})$$

The threshold field is found by setting  $\lambda = 1$  and  $\gamma = 0$ . In the range of angles for which the approximation is valid, we have

$$F_{\text{critical}} = 3.8 \times 10^{14} \lambda_{\perp}^{-4} (k_{||} / k)^2 \quad (\text{B-11})$$

which has its maximum value near 89.7 degrees where

$$F_{\text{critical}} = 94 \times 10^8 \lambda_{\perp}^{-4} \quad (\text{B-12})$$

Here  $\lambda_{\perp}$  is in meters and  $F$  in  $\text{W/m}^2$ . Thus  $F = 94 \text{ W/m}^2$  for a wavelength of 100 m. If the MPTS is designed for a flux of  $300 \text{ W/m}^2$ , then the instability may be excited for wavelengths greater than about 70 m.

Although the theory as developed is not valid for angles between 89.7 and 90 degrees, the threshold field can be expected to remain constant within this cone of angles since the conductivity along the Y-direction will be nearly constant with the small value characteristic of thermal conduction across the magnetic field.

We conclude that field-aligned striations are likely to develop with rf energy fluxes on the order of those planned for the MPTS.

Some further study will be required to determine the in depth effect of these instabilities. Since the wavelength of the perturbation is greater than 70 m, the effects on the upward link of the control loop is expected to be small. The most likely effect is that field-aligned structure will develop in a similar fashion to the

field-aligned structure which developed in the ionospheric modification experiment<sup>2,3</sup>. Since these instabilities are basically convective instabilities, their growth must occur over the finite path length through the ionosphere so that the perturbation would not be expected to grow to the extent that it could effect the downward heating beam significantly.



## REFERENCES (APPENDIX B)

1. F.W. Perkins and E.J. Valeo, Phys. Rev. Lett. 32, 1234 (1974).
2. G.D. Thome and F.W. Perkins, Phys. Rev. Lett. 32, 1238 (1974).
3. For example, see the special issue of Radio Science on Ionospheric Modification (November 1974).

## APPENDIX C

### OHMIC HEATING OF THE D-REGION

High power radio waves can cause the electron temperature in the lower D-region ( $\cong$  60 to 90 km) to increase to many times its ambient value, whenever the flux exceeds a critical value:<sup>1, 2, 3</sup>  $S_c = 25f_e^2$  where  $f_e$  is in MHz and  $S_c$  is in  $\mu\text{W}/\text{m}^2$ .

For  $f_e = 2.45 \text{ GHz} = 2,450 \text{ MHz}$

$S_c$  becomes  $15 \text{ mW}/\text{cm}^2$ . Thus, where the MPTS produces a flux of  $20 \text{ mW}/\text{cm}^2$  it will be an increase of  $1.3 \times$  the critical value. Calculations such as those in reference 3 indicate that a flux of this magnitude will raise the electron temperature to a value on the order of  $1000^\circ\text{K}$ . For  $70 \text{ mW}/\text{cm}^2$  it would be an increase of  $4.7 \times$  the critical value and the associated electron temperature would be raised to a value on the order of  $2000^\circ\text{K}$ .

In assessing the effects of the temperature rise, it must be remembered that the electrons are a minor constituent of the D-region since there are  $10^{10}$  neutral molecules for each electron. Since the neutral molecules remain at the same temperature, the energy per unit volume of the D-region is not significantly changed.

The two most important effects of the increase in electron temperature are: (1) a change in the chemistry of the ionosphere which reduces the rate of recombination of electrons and ions and thus increases the electron density; and (2) an increase in the electron collision frequency. The increase in electron-collision frequency will increase the absorption of radio waves with  $w > v_{en}$  and decrease the absorption in the opposite limit. This effect will be localized to signals which pass through the heated cylinder whose diameter is on the order of five km. This effect might interfere with specific receivers but it would not effect any geographically-widespread communication systems. It might effect individual receivers of LORAN if they were located close to the heated region since the electron temperature rise would extend all the way down to low altitudes where the rf radar frequency equals the electron-collision frequency, and the electron density is much less than the LORAN critical density.

Thus the MPTS will definitely increase the electron temperature in a small region of the ionosphere directly above the receiver. By changing the average electron energy, the chemistry of this localized region which involves electron reactions will be changed. The absorption of radio signals which pass through this region will also be altered substantially. However, the power flux in the MPTS beam will be reduced only negligibly. No deleterious environmental effects from the localized electron temperature rise have been identified.

#### REFERENCES (APPENDIX C)

1. L.H. Holway, Jr., and G. Meltz, J. Geophysical Research 78, 8402 (1973).
2. G. Meltz, L.H. Holway, Jr., and N. Tomjlanovich, Radio Science, November 1974 (to be published).
3. L.H. Holway, Jr., and G. Meltz, "Modification of the Lower Ionosphere by High-Power HF Transmissions", Raytheon Research Division Report T-989 (1974).

APPENDIX D  
CAVITY CIRCUIT CALCULATIONS

D.1 INPUT IMPEDANCE

The input cavity of the klystron amplifier presents a complex impedance given by the following as seen from a waveguide of impedance  $Z_0$  at the plane of the detuned short (reference 24 of Section 4):

$$\frac{Z}{Z_0} = \frac{Q_0}{Q_{\text{ext}}} \frac{1}{1 + 2iQ_0\delta} \quad (\text{D-1})$$

The terms  $\delta$  and  $Q_0$  account both for wall and beam-loading effects and are given by:

$$\frac{1}{Q_0} = \frac{1}{Q_u} + \frac{R}{Q} G_B \quad (\text{D-2})$$

and

$$\delta = \delta_u + \frac{1R}{2Q} B_B = \frac{f_{\text{drive}} - f_{\text{resonant}}}{f_{\text{resonant}}} \quad (\text{D-3})$$

where  $Q_u$  and  $\delta_u$  refer to the cavity in the absence of the beam. The voltage standing-wave ratio at the input of a synchronously tuned cavity is  $Q_0/Q_{\text{ext}}$  or  $Q_{\text{ext}}/Q_0$  accordingly as  $Q_0 > Q_{\text{ext}}$  or  $Q_{\text{ext}} > Q_0$ . With a drive power of  $P_{\text{input}}$ , the power absorbed by the cavity is:

$$\frac{4Q_0Q_{\text{ext}}}{(Q_0 + Q_{\text{ext}})^2} P_{\text{input}} \quad (\text{D-4})$$

This power is dissipated in an equivalent shunt resistance  $(R/Q) Q_0$  to produce the gap voltage  $V_1$ , so that

$$V_1^2 = 8 \frac{R}{Q} \frac{Q_0^2 Q_{\text{ext}}}{(Q_0 + Q_{\text{ext}})^2} P_{\text{input}} \quad (\text{D-5})$$

The cavity presents a perfect match to the drive when

$$Q_o = Q_{ext} \quad (D-6)$$

then it can be seen that

$$V_1^2 = 2 \frac{R}{Q} Q_o P_{input} \quad (D-7)$$

## D.2 INPUT POWER AND GAIN AT SATURATION

If the beam voltage  $V_o$  is used as the normalization factor, then the gain is given by:

$$\frac{\text{Output power}}{\text{Input power}}$$

or

$$\frac{\eta I_o 2 \frac{R}{Q} Q_o}{(V_1/V_o)^2 V_o} \quad (D-8)$$

using Equation (D-5), where  $\eta$  is the net efficiency. In a large-signal calculation,  $V_1/V_o$  is chosen at the input gap and  $\eta$  is derived. For the PPM klystron, it is seen that

$$R/Q = 130 \text{ ohms}$$

$$Q_u = 4200$$

$$G_o = 1.58 \times 10^{-5} \text{ mho and}$$

$$V_o = 25.1 \text{ kV}$$

On the basis of values computed for an ungridded gap of transit angle 0.77 radian, small-signal theory gives

$$G_B/G_o = 0.054$$

$$B_B/G_o = \frac{G_B}{G_o} / \tan (0.77/2)$$

$$= 0.133$$

Then from Equations (D-2) and (D-3) it is found that  $Q_o = 2865$  and  $\delta = \delta_o + 1.37 \times 10^{-4}$  which represents a total detuning of 0.34 MHz due to beam loading. These equations also give the effects of beam-voltage variation.

In the large-signal simulation, it was found that

$$V_1/V_o = 0.06 \text{ at the input gap,}$$

$$P_{\text{input}} = 3.04 \text{ watts,}$$

from Equation (D-7) assuming perfect coupling and also that the cavity was synchronously tuned when the beam was present. The output power is 5574 watts using large-signal results, so that the saturation gain is  $10 \log_{10} (5574/3.04)$  or 32.7 dB. The EM-focused tube may be treated similarly.

### D.3 INTERMEDIATE- AND OUTPUT-GAP VOLTAGES

These gaps are driven by the beam; the gap voltage is given by:

$$V_1/V_o = G_o M^2 \frac{R}{Q} \left( \frac{I_1}{I_o} \right) \frac{1}{\sqrt{1 + 4Q_L^2 \delta^2}} \quad (\text{D-9})$$

where  $M^2$  is the (radially averaged) squared gap-coupling factor, about 0.88. The intermediate bunching cavities are detuned above the drive frequency for highest efficiency:

$$\delta^2 \gg \frac{1}{4Q_L^2}$$

so that

$$V_1/V_o = \frac{G_o M^2 R}{2|\delta| Q} \frac{I_1}{I_o} \quad (\text{D-10})$$

### D.4 CAVITY TUNINGS

In the PPM klystron, with

$$R/Q = 130$$

and

$$G_o = 1.58 \times 10^{-5} \text{ mho,}$$

the values of  $V_1/V_0$  and  $I_1/I_0$  from large-signal simulation yield the following:

	$I_1/I_0$	$V_1/V_0$	Detuning Above Drive Frequency (MHz)
Gap 2	0.7	0.04	39
Gap 3	1.2	0.04	65

The small-signal gain program then uses these values to obtain the gain and noise characteristics given in Section 7.

#### D.5 OUTPUT CAVITY AND CIRCUIT EFFICIENCY

The cavity losses dissipate power as heat:

$$V_1^2/2R \quad (D-11)$$

where R is the shunt resistance,  $(R/Q)Q_u$ , due to wall and output-coupling losses only. When the normalized rf voltage  $V_1/V_0$  is used, the heat is expressed as.

$$\text{power lost} = \left(\frac{V_1}{V_0}\right)^2 \frac{1}{2(R/Q)Q_u} \frac{(\text{beam power})^{0.8}}{(\text{beam perveance})^{0.8}} \quad (D-12)$$

This equation was used to calculate the heating of the cavities of the two types of tubes. The circuit efficiency is then 1 - (heat dissipated)/(power supplied by electron beam) or

$$\eta_{cct} = 1 - \frac{\frac{1}{2} \left(\frac{V_1}{V_0}\right)^2}{(R/Q)Q_u \eta_e (\text{perveance})^{0.8} (\text{beam power})^{0.2}} \quad (D-13)$$

or

$$1 - \frac{Q_L}{Q_u} \quad (D-14)$$

where  $Q_L$  is the loaded "Q" accounting for total power dissipation and  $\eta_e$  is the electronic efficiency before collector depression. Thus the circuit efficiency is maximized by making R/Q,  $Q_u$ , the electronic efficiency, the beam power and the perveance as large as possible. Accounting for collector depression one finds the net efficiency to be:



$$(\eta_e \eta_{cct}) / (\text{total power input} - \text{power recovered at collector}) \quad (\text{D-15})$$

With the following data, circuit efficiency was plotted using Equation (D-13).

	<u>PPM-Focused Tube</u>	<u>EM-Focused Tube</u>
Beam power	10 kW	60 kW
Perveance	$0.1 \times 10^{-6}$	$0.2 \times 10^{-6}$
R/Q	120	120
$Q_u$ at 20°C	6115	6115
$Q_u$ at 300°C	4200	4200
$\eta_e$	0.64 (computed)	0.75 (assumed)

and

$$Q_u \text{ at } T^\circ\text{C} = \frac{Q_u \text{ at } 20^\circ\text{C}}{\sqrt{[1 + \alpha(T - 20)]}} \quad (\text{D-16})$$

where for copper  $\alpha = 0.004$ . Table D-1 shows that 0.2 microperveance is near optimum for the solenoid-focused klystron. Equation (D-13) gives the circuit efficiency; the electronic efficiencies were read from Figure 9 of the paper by Kosmahl and Albers (reference 12 of Section 4).

TABLE D-1  
OPTIMUM PERVEANCE OF A 60 kW KLYSTRON BEAM

<u>Microperveance</u> ( $\mu\text{A}/\text{V}^{3/2}$ )	<u>Electronic Efficiency</u> $\eta_e$	<u>Circuit Efficiency</u> $\eta_{cct}$	<u>Net Efficiency</u> $\eta = \eta_e \times \eta_{cct}$
0.1	0.84	0.937	0.787
0.2	0.83	0.963	0.800
0.3	0.82	0.973	0.798
0.5	0.81	0.982	0.795
0.75	0.77	0.986	0.759
1.0	0.72	0.988	0.712

## APPENDIX E

### OUTPUT POWER OF THE SOLENOID-FOCUSED KLYSTRON

The following assumptions have been made:

Solenoid power	=	1 kW
Cathode heater power	=	60 W
Beam perveance at the output cavity	=	0.2 microperveance
R/Q	=	120
$Q_u$	=	4200
RF voltage, $V_1$	=	$1.1 V_0$

The output cavity is synchronously tuned. In Tables E-1 and E-2 the electronic efficiencies are taken, respectively, as  $\eta_e = 84$  percent and 75 percent, giving curves A and B of Figure 4-25. A more detailed calculation would involve deriving  $\eta_e$  from the large-signal computer model and optimizing  $V_1/V_0$  at the output. The calculations proceed as follows:

Column 1: beam power

Column 2: column 1  $\times \eta_e$  = power delivered to output cavity

$$\text{Column 3: } \left(\frac{V_1}{V_0}\right)^2 \frac{1}{2(R/Q)Q_u} \frac{(\text{beam power})^{0.8}}{(\text{beam perveance})^{0.8}}$$

This is the skin heating and excludes intercepted power (Equation (D-12)).

Column 4:  $1 - \frac{\text{column 3}}{\text{column 2}} =$  circuit efficiency,  $\eta_{cct}$

Column 5: output power =  $\eta_{cct} \times$  column 2

Column 6: net efficiency from beam power alone:  $\eta_{cct} \times \eta_e$

Column 7:  $\frac{\text{column 6} \times \text{beam power}}{(\text{beam power} + \text{solenoid power} + \text{heater power})}$

If a depressed collector were added, column 7 would be multiplied by:

$\frac{\text{beam power}}{(\text{beam power}) - (\text{recovered power})}$

to give the new efficiency.

TABLE E-1

## KLYSTRON OUTPUT POWER WITH 84 PERCENT ELECTRONIC EFFICIENCY ASSUMED

1	2	3	4	5	6	7
Beam Power (kW)	Power to Output Cavity (kW)	Heating of Walls of Output Cavity (W)	$\eta_{cct}$	Output Power (W)	DC-RF Conversion Efficiency	Net Efficiency (with 1 kW Solenoid Power and 60 W Heater Power)
2	1.68	120	0.93	1560	0.78	0.501
6	5.04	288	0.94	4752	0.792	0.673
10	8.4	434	0.95	7966	0.796	0.720
20	16.8	756	0.96	16044	0.802	0.762
30	25.2	1045	0.96	24155	0.805	0.778
60	50.4	1820	0.96	48580	0.81	0.796

TABLE E-2

## KLYSTRON OUTPUT POWER WITH 75 PERCENT ELECTRONIC EFFICIENCY ASSUMED

1	2	3	4	5	6	7
Beam Power (kW)	Power to Output Cavity (kW)	Heating of Walls of Output Cavity (W)	$\eta_{cct}$	Output Power (W)	DC-RF Conversion Efficiency	Net Efficiency (with 1 kW Solenoid Power and 60 W Heater Power)
2	1.5	120	0.92	1380	0.69	0.450
6	4.5	288	0.94	4212	0.702	0.597
10	7.5	434	0.94	7066	0.707	0.639
20	15.0	756	0.95	14244	0.712	0.676
30	22.5	1045	0.95	21460	0.715	0.691
60	45.0	1820	0.96	43180	0.72	0.708

APPENDIX F  
KLYSTRON THERMAL CONTROL SYSTEM

F.1 HEAT CONDUCTION

Consider a cavity end wall as a hollow cylinder with:

- inner radius,  $R_1$
- outer radius,  $R_2$
- axial length,  $d$  and
- thermal conductivity,  $k$ .

If  $W$  watts are conducted radially outwards, the temperature drop  $\Delta T$  is given by:

$$\Delta T = \frac{W \ln (R_2/R_1)}{2\pi dk} \quad (F-1)$$

assuming a uniform distribution of the heat across wall (parallel to the axis of the tube). For example, in the 43 kW klystron, it is seen that

- $R_1 = 0.36$  cm
- $R_2 = 3$  cm
- $d = 1$  cm (walls 1 cm thick)
- $k = 3.67$  W/cm/K for copper, and
- $\Delta T = 92^\circ\text{C}$  per kilowatt.

The total heat dissipated in the output cavity is 2420 watts (adding 600 watts to the skin heat of Table E-2 to account for interception), giving a temperature rise of 111 degrees in each wall.

If the outer temperature is  $300^\circ\text{C}$ , the inner temperature is  $411^\circ\text{C}$  and the tunnel tips would be even hotter. With thicker walls, the heat flow would be concentrated near the cavity. Hence fluid or heat-pipe cooling is necessary.

Similar estimates for pyrolytic graphite radiators, for which  $k$  is 2.8 or less, show that heat pipes are needed there also to distribute the heat evenly over the radiating surface. Assume that half the heat flows halfway out (the rest being radiated); then it is seen that

$$R_2 = 43 \text{ cm}$$

$$R_1 = 8 \text{ cm (or less)}$$

$$d = 1 \text{ cm (for an acceptably low weight)}$$

$$W = 2100 \text{ W (half the body heat from the 43 kW tube), and}$$

$$\Delta T = 142 \text{ degrees; if the body were at } 300^\circ\text{C the midpoints of the radiator would be cooler than } 158^\circ\text{C with normal conduction.}$$

## F.2 TEMPERATURE, AREA AND WEIGHT OF RADIATORS

Let the emissivity be  $\epsilon$ , the temperature  $T^\circ\text{K}$  and the heat power to be removed  $Q$  watts. Then the area is:

$$A = \frac{Q}{F_1 \epsilon \sigma T^4} \text{ cm}^2 \text{ (one side only)} \quad (\text{F-2})$$

where  $\sigma = 5.67 \times 10^{-12} \text{ w/cm}^2/\text{K}^4$  (Stefan's constant) and  $F_1$  is a "view factor" depending on other bodies in the vicinity.  $F_1 \epsilon \sigma T^4$  is the radiation rate averaged over the surface; it is assumed that with heat pipes to aid conduction the temperature is nearly uniform.

Let the incident solar radiation be  $S$  watts/sq. cm. Let the radiator have a view factor  $F_2$  for a parallel beam and an absorptivity  $\alpha$  for solar radiation. The power absorbed is then  $\alpha F_2 S$  and this must be radiated together with the heat power  $W$  produced in the klystron. Thus in Equation (F-2) it is seen that:

$$Q = \alpha F_2 S + W \quad (\text{F-3})$$

so that the area required is:

$$A = \frac{W}{F_1 \epsilon \sigma T^4 - F_2 \alpha S} \quad (\text{F-4})$$

Outside the atmosphere the total solar energy for the mean distance between the sun and the earth is  $0.14 \text{ W/cm}^2$  (10 percent in ultraviolet, 40 percent visible, and 50 percent infrared)<sup>5</sup>. Assume that the absorptivity,  $\alpha$ , equals 0.9 throughout; then  $\alpha S$  equals  $0.126 \text{ W/cm}^2$ .

The following sections use Equation (F-4) to estimate the size, and hence the weight, of body and collector radiators.

### F.2.1 COLLECTOR

The PPM tube has a multistage reflex collector with electrodes radiating at  $900^\circ\text{C}$  and emissivity 0.92. The temperature is chosen conservatively because of the insulation needed to separate the depressed stages. Radiation from the rear electrodes is absorbed and reradiated by those in front. For the weight estimate each square centimeter is assumed to weigh 1 gram. The high-power tube has a radiating tungsten envelope (reference 4-3, Addendum E) at  $1400^\circ\text{C}$  with emissivity 0.55 and thickness 0.002 cm. The weight estimate is treated as a sphere; density of tungsten equals  $19.2 \text{ g/cm}^3$ . The view factor  $F$  is unity since the collector "sees" open space. Using Equation (E-3) and the power estimates of Appendix D and Table 2-1 gives the following:

<u>Tube</u>	<u>Collector Heat (W)</u>	<u>Area (<math>\text{cm}^2</math>)</u>	<u>Radius (cm)</u>	<u>Weight (g)</u>
5.6 kW PPM	979	99	5.60	99
16 kW with Solenoid	5090	209	8.16	32
43 kW with Solenoid	13680	562	13.40	88

Notice that the multistage depressed collector weighs more per watt radiated.

The length required to spread the beam is estimated to be:

5.65 kW PPM tube = 10 cm  
 16 kW tube = 18 cm  
 43 kW tube = 30 cm.

The last two estimates are based on beam-spread curves (reference 25 of Section 4) allowing for residual angular velocity due to cathode flux and increased charge density in a beam of 25 percent its initial energy.



### F.2.2 COLLECTOR REFLECTOR AND HEAT SHIELD

For all tubes, this is a molybdenum cone with thickness 0.002 cm and density 10.2 g/cm<sup>3</sup>, extending back to the collector entrance:

base radius  $\approx$  1.5 x collector radius;

length = collector length.

The actual shield may be more complex (reference 4-4, Addendum E), but this simple design gives a useful weight estimate.

	<u>Reflector Radius (cm)</u>	<u>Length (cm)</u>	<u>Weight (g)</u>
PPM tube	8.5	10	7
16 kW tube	13.0	18	21
43 kW tube	20.0	30	42

### F.2.3 BODY RADIATOR

This is a circular surface of pyrolytic graphite ( $\epsilon = 0.92$ ) backed by heat pipes to insure good conduction and near uniform temperature. The 250°C chosen allows for 50°C temperature rise between the radiator and the heat source. The radiator must "see past" the collector, and the view factors  $F_1$  and  $F_2$  are themselves functions of the area A. But it is assumed here for simplicity that  $F_1 = F_2 = 2/3$ . As before, the radiator weight is taken as one gram per square centimeter, a reasonable figure since the density of pyrolytic graphite is only 2.2 g/cm<sup>3</sup>. The heat figures of Tables E-1 and E-2 (interpolated for 16 kW) then give the following radiator weights:

<u>Tube</u>	<u>Body Heat (including Solenoid Power Where Applicable)</u>	<u>Radiator Area (cm<sup>2</sup>)</u>	<u>Radius (cm)</u>	<u>Weight (g)</u>
5.6 kW PPM	1201	6816	46.6	6816
16 kW with Solenoid	2415	13705	66.0	13705
43 kW with Solenoid	4200	23835	87.0	23835

#### F. 2. 4 BODY REFLECTOR AND HEAT SHIELD

This is needed in the solenoid tube to protect the waveguides and surrounding structure from heat generated in the solenoid. The reflector is a second molybdenum core extending from the start of the tube to the body radiator, and at its base is 5 cm larger in radius from the body. Using lengths 80.7 cm and 66.2 cm, respectively, the weight is thus 442 g (16 kW tube) and 714 g (43 kW tube).

#### F. 3 WEIGHT OF HEAT PIPES

The assumptions made are:

- a. Heat pipes surround all the cavities in the solenoid-focused tube (length 62 cm) and the output cavity only in the PPM tube (length 4 cm).
- b. The inner radius equals 3 cm and the outer radius equals 4 cm (cross-sectional area = 22 cm<sup>2</sup>).
- c. Heat pipes line the back of the body radiator: total length 10 x the radiator radius; cross-sectional area 2 sq. cm.
- d. Density equals 2.2 g/cm<sup>3</sup> as for cesium.
- e. Linear body dimensions for the 16 kW tube scale down by a factor (16/43)<sup>0.2</sup> (since proportional to beam speed) from the 43 kW tube. Then the following weights are calculated.

<u>Tube</u>	<u>Body Heat Pipes (g)</u>	<u>Radiator Heat Pipes (g)</u>	<u>Total (g)</u>
5.6 kW PPM	158	2050	2208
16 kW with Solenoid	2013	2904	4917
43 kW with Solenoid	2454	3828	6282

## APPENDIX G

### CONFINED-FLOW FOCUSING OF A RELATIVISTIC BEAM

The equilibrium condition for a relativistic beam (reference 26 of Section 4) is:

$$\omega_c^2 = \frac{2\omega_p^2}{p_o(1-K)} \quad (G-1)$$

where

$\omega_c = \eta B$  is the radian cyclotron frequency,

$\omega_p^2 = \eta \rho_o / \epsilon_o$  is the radian plasma frequency, and

$\eta = |e|/m_o$ , where  $m_o$  is the rest mass of the electron.

$K$  is the cathode flux parameter

$$K = \left(\frac{r_c}{r_o}\right)^4 \left(\frac{B_c}{B_o}\right)^2 \quad (G-2)$$

where the subscripts  $c$  and  $o$ , respectively, denote the cathode and the entrance to the interaction region.  $p_o$  is the relativistic factor  $1/[1 - (u_o^2/c^2)]^{1/2}$ , where  $u_o$  is the beam speed and  $c$  is the speed of light, so that the focusing field and corresponding solenoid power are reduced by a factor  $[1 - (u_o^2/c^2)]^{1/4}$  from the non-relativistic value.

In the derivation of Equation (G-1) the self-magnetic field of the beam increases the focusing force by a factor  $p_o^2$ , but the angular velocity of the beam also falls, by a factor  $1/p_o$ .

In a 60 kW 0.2-micropervance beam, for example, the voltage is 39 kV,  $u_o/c$  is 0.37, and  $(1/p_o)^{1/2}$  is 0.963, so that nearly 4 percent of the solenoid power is saved in comparison with a nonrelativistic beam of the same length and charge density.